STRONGLY NONLINEAR AXION DYNAMICS

A DISSERTATION
SUBMITTED TO THE DEPARTMENT OF PHYSICS
AND THE COMMITTEE ON GRADUATE STUDIES
OF STANFORD UNIVERSITY
IN PARTIAL FULFILLMENT OF THE REQUIREMENTS
FOR THE DEGREE OF
DOCTOR OF PHILOSOPHY

David Cyncynates
May 2022

This dissertation is online at: https://purl.stanford.edu/dm114rr1586

I certify that I have read this dissertation and that, in my opinion, it is fully adequate in scope and quality as a dissertation for the degree of Doctor of Philosophy.

Savas Dimopoulos, Primary Adviser

I certify that I have read this dissertation and that, in my opinion, it is fully adequate in scope and quality as a dissertation for the degree of Doctor of Philosophy.

Peter Graham

I certify that I have read this dissertation and that, in my opinion, it is fully adequate in scope and quality as a dissertation for the degree of Doctor of Philosophy.

Robert Wagoner

Approved for the Stanford University Committee on Graduate Studies.

Stacey F. Bent, Vice Provost for Graduate Education

This signature page was generated electronically upon submission of this dissertation in electronic format. An original signed hard copy of the signature page is on file in University Archives.

Abstract

Axions and axion-like particles are well-motivated candidates for Beyond-the-Standard-Model (BSM) physics. While the present-day dynamics of axions are typically well approximated as nearly-free massive particles, their production in the early universe via the misalignment mechanism can allow them to access strong self-interactions. This thesis focuses on the consequences of these strong self-interactions for astrophysics and cosmology. In the first part of this thesis, we consider the dynamics of quasi-bound states called oscillons, and construct a new formalism to calculate their structure and properties. We use this formalism to construct a family of scalar field theories whose oscillons are cosmologically long-lived and can lead to present-day astrophysical signatures. The second part of this thesis focuses on coupled axion systems, and we show how the kinds of potentials that naturally arise in models of the axiverse can lead to a new kind of resonant energy transfer between axions. This resonance causes energy to flow from the axions with larger decay constants to those with smaller decay constants, generically enhancing direct detection signatures. Further, this resonance enhances density perturbations, leading to the formation of dense galactic substructure and oscillons. We explore the possible signatures of this resonance in direct detection experiments such as ADMX and DM Radio, as well as astrophysical signatures in astrometric and photometric probes of galactic substructure.

Acknowledgments

I would like begin by thanking my advisor Savas Dimopoulos for guiding, supporting, and encouraging me throughout my Ph.D. Over the years, I have benefited greatly from Savas's example of how to conduct research: his judicious choice of research problems, his integrity for uncovering the truth, and his unwavering enthusiasm to learn new physics. I am extremely grateful to Savas for providing me with the freedom to explore my own research ideas and to develop my own research style and interests.

It has been a great pleasure to interact with many wonderful faculty over my time at Stanford: Asimina Arvanitaki, Peter Graham, David Reis, Glenn Starkman, Robert Wagoner, and many others, all of whom have generously shared some of their wisdom with me. In particular, I would like to thank Peter and Bob for many interesting physics conversations over the years, and for their generosity in serving on my reading committee.

I also want to thank my fellow students Tudor Giurgica-Tiron, Olivier Simon, Jedidiah O. Thompson, with whom I have had the pleasure of collaborating on several exciting papers. I also thank fellow students Alexander Bogorad, Marios Galanis, Saarik Kalia, Amalia Madden, Anirudh Prabhu, Samuel Wong, and Dmitriy Zhigunov as well as postdocs and now-faculty Sebastian Baum, Masha Baryakhtar, Horng Sheng Chia, Michael Fedderke, Alexander Gußmann, Junwu Huang, Robert Lasenby, Krista Lynne Smith, Daniel Wilkins, and many others whom I have interacted with over the years for interesting physics discussions, answering my questions, and contributing to the exciting atmosphere during my time at Stanford.

A special thank you to my family for their support, during my Ph.D. and otherwise, and for believing in me and my work. In particular, I would like to thank my parents, who during the spring of 2020 bought me a one way plane ticket back home where I would end up spending the next one-and-a-half years. I credit their decision for my productivity, which would have certainly suffered without their company.

Finally, I would like to thank my partner Teresa Jones, whose support and encouragement helped me through the toughest times during my Ph.D., and for the many hours that she spent reading my papers and listening to me practice my talks.

Contents

List of Figures

Chapter 1

Introduction

In the present epoch, axions and scalar fields in general are often well approximated as massive particles whose interactions with the Standard Model (SM) are firmly perturbative and whose self-interactions are equally weak. The early universe, however, was a much more energetic place, and the initial conditions set by inflation can allow axions to experience strong self-interactions that cannot be treated by perturbation theory in the coupling. This thesis explores various axion dynamics made accessible by cosmology and explores their observational signatures.

The first chapter contains results published in the journal Physical Review D [65]. The original concept of this project was my own, and this paper is the result of a collaboration with Tudor Giurgica-Tiron, with whom I share equally the intellectual and writing credit. The focus of the paper is to introduce a novel method for computing the properties of oscillons, quasi-bound states of real scalar fields with attractive self-interactions. Crucially, our formalism simultaneously retains physical boundary conditions and non-perturbative self-interactions, and has allowed us to show why certain oscillon ansatz solutions in the literature yield extremely accurate predictions, thus placing these techniques on solid theoretical footing. Further, our method improves on the accuracy of existing ansatz methods and other semi-analytic techniques in the literature, while also enhancing computational efficiency. Finally, we use our insight to construct a new infinite family of scalar field theories that contain extremely long-lived oscillons, which may realistically live into the present day and lead to astrophysical signatures.

The second chapter contains results published in the journal Physical Review D [66]. The original concept of this project was my own, and this paper is the result of a collaboration with Tudor Giurgica-Tiron, Olivier Simon, and Jedidiah Thompson, with whom I share equally the intellectual and writing credit. In this project, we study consequences of the existence of a large collection of axions predicted by string theory, commonly known as a string axiverse. Axions have a natural cosmological production mechanism, vacuum misalignment, making them well-motivated dark matter (DM) candidates, and much existing work on axion production has considered the case of a single

free axion. In a realistic axiverse, however, string axions are expected to be distributed densely over many orders of magnitude in mass, and to interact with one another through their joint potential. In this paper, we show that non-linearities in this potential lead to a new type of resonant energy transfer between axions with nearby masses. This resonance generically transfers energy from axions with larger decay constants to those with smaller decay constants, and leads to a multitude of signatures. These include enhanced direct detection prospects for a resonant pair comprising even a small subcomponent of dark matter, and boosted small-scale structure if the pair is the majority of DM. Near-future iterations of experiments such as ADMX and DM Radio will be sensitive to this scenario, as will astrophysical probes of DM substructure.

Chapter 2

Structure of the Oscillon

Axions are real scalar fields predicted to exist in many extensions of the Standard Model. One of the best-motivated is the QCD axion, which emerges as the pseudo-Nambu-Goldstone boson of a broken $U(1)$-axial symmetry, known as Peccei-Quinn (PQ) symmetry [67]. The PQ breaking scale f_a, known as the axion decay constant, suppresses the axion's self-interactions and its coupling to the Standard Model (SM). To avoid impacting stellar cooling rates, axion-SM interactions must be highly suppressed, forcing f_a to be in the deep UV, $f_a \gtrsim 10^{10}$ GeV [68–70]. As the universe cools below the QCD scale $\Lambda_{\rm QCD} \approx 200$ MeV, strong dynamics generate a periodic potential for the axion, whose VEV cancels the strong sector's CP-violating phase, thus resolving the strong-CP problem. The separation between the QCD scale and the PQ scale forces the axion's mass $m_a \sim \Lambda_{\rm QCD}^2/f_a$ to be smaller than 1 meV, potentially by many orders of magnitude [71, 72].

Furthermore, axionic degrees of freedom emerge in great numbers from realistic string compactifications, collectively known as the Axiverse. Like the QCD axion, these axion-like particles (ALPs) are generally described by two parameters: their mass m and the decay constant f. Generic ALPs are also expected to have naturally small masses, which are exponentially suppressed by the string instanton action. The precise form of the ALP potential depends on the specifics of the UV theory it descends from, leaving its low-energy dynamics effectively unconstrained [73].

Axions (both the QCD axion and ALPs) come equipped with natural production mechanisms, such as the vacuum misalignment mechanism, making them well-motivated dark matter candidates [59,74–81]. Of particular phenomenological interest are ultralight axions, whose masses can be as low as 10^{-21} eV [5,8,82–87]. Such ultralight axions lead to novel wave dark matter signatures, including effects on the matter power spectrum and structure formation [59, 88–91], CMB observables [20, 92], and the formation of compact scalar structures such as axion minihalos [93–95], gravitationally bound solitons and axion stars [96–98], and self-interaction bound oscillons [1, 64, 99–123], the latter of which is the subject of this paper.

As the densest object in this family of bound axionic structures, oscillons promise dramatic

astrophysical signatures, and have therefore been the subject of intense scrutiny [124–130]. Oscillons have a finite lifespan, and such phenomena crucially rely on oscillons that are cosmologically long-lived. Since dark matter axions are constrained by Lyman-α forest measurements to be at least 10^{-21} eV in mass, their oscillation period is at most 0.1 years [5,8,82–84,86,87]. Therefore, oscillons that survive 14 Gyr until the present day must be stable for at least 10^{11} oscillations. Simulating an oscillon this long-lived is at the upper limit of current computational capabilities [1, 118], and thus indirect methods are required to study longer-lived oscillons.

Significant progress has been made towards understanding the structure and evolution of oscillons in the last two decades, building on improved computational resources and theoretical understanding [1, 64, 106–123]. Of central theoretical importance are artificial, exactly-periodic solutions of the equations of motion, which have been used to approximate the oscillon's instantaneous profile and radiation rate. In rare instances, in which the oscillon is known to be infinitely long-lived, this approximation is exact, and the solution is called a *breather*: a finite energy periodic solution of the equations of motion. The most famous such example is the 1+1 dimensional sine-Gordon breather, which is stabilized by an infinite set of conserved quantities [131]. Breathers are not known to exist in 3+1 dimensions. Relaxing the breather's finite energy constraint, we find the periodic solutions known as *quasibreathers*. These constructions have an infinite amount of energy residing in their standing-wave tails. These radiative tails can be understood as an approximation of the oscillon's classical radiation amplitude, which can be used to estimate the oscillon's lifetime.

In this paper, we further develop the quasibreather technique into a framework for understanding the classical properties of oscillons, unifying several observations made in the literature, and addressing key conceptual questions about the harmonic structure and stability of oscillons. By imposing realistic boundary conditions, we introduce the *physical quasibreather* (PQB) as the member of the quasibreather family closest to a radiating oscillon, and arrive at an improved method for calculating oscillon properties, such as lifetime, radial profile, linear stability, and frequency content. In the limit of long lifetimes, our method becomes especially efficient, since semi-perturbative techniques may be employed to rapidly compute oscillon radiation. We apply our new methods to systematically study oscillon lifetimes in periodic axion potentials, allowing us to probe the genericity of long-lived oscillons. Moreover, we apply our framework to expand on existing studies of long-lived oscillons in monodromy potentials.

We summarize our study of oscillon lifetimes in periodic potentials with parity in the form of *longevity landscapes*, such as the one depicted in figure 2.1a. There, we scan the coefficients $\mathcal{V}_n$ of the axion potential $V(\phi)$ defined as

$$V(\phi) = m^2 f^2 \sum_{n=1}^{\infty} \frac{\mathcal{V}_n}{n^2} \left(1 - \cos\left(\frac{n\phi}{f}\right)\right), \qquad \sum_{n=1}^{\infty} \mathcal{V}_n = 1\,. \tag{2.1}$$

Here, the field ϕ is the axion field, m its mass, and f its decay constant. The particular slice through

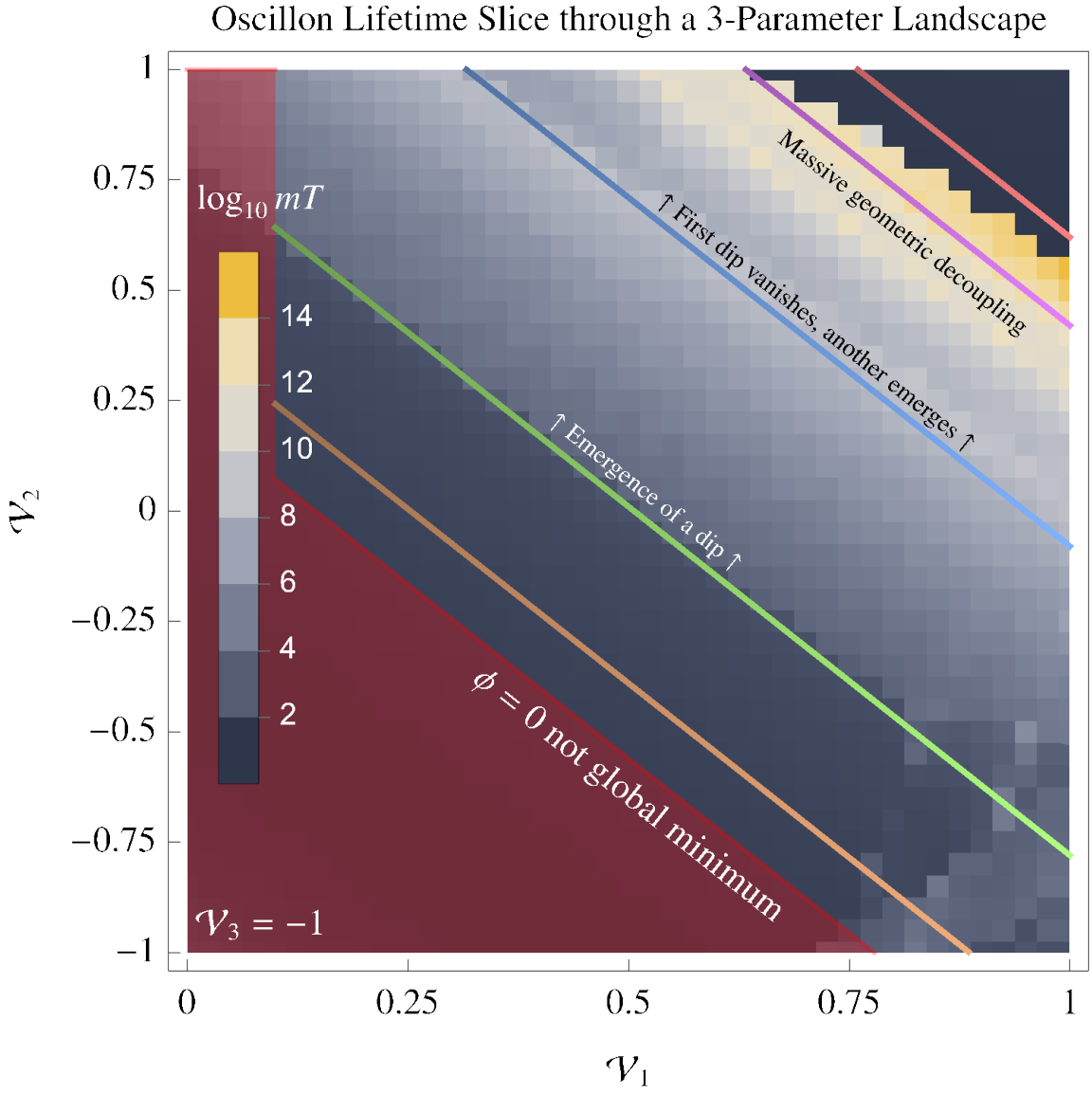

Figure 2.1a: A slice through the oscillon lifetime landscape of parity symmetric periodic potentials with three free parameters (2.1) (see text for details). The lifetime T is calculated in units of the scalar mass m for oscillons starting with a fundamental frequency of $\omega = 0.8m$. The result is a glimpse into the structure of the oscillon lifetime landscape, revealing islands of longevity, separated by valleys. These features correspond to the location of exceptional 'dip' frequencies, where the third harmonic experiences totally destructive interference. We plot the families of potentials along the important colored contours in figure 2.1b.

the space of coefficients in figure 2.1a is defined by the choice to treat $\mathcal{V}_1$ and $\mathcal{V}_2$ as free parameters, while fixing $\mathcal{V}_3 = -1$, and forcing $\mathcal{V}_4$ to satisfy the mass constraint, with all other $\mathcal{V}_n$ set to zero. Our

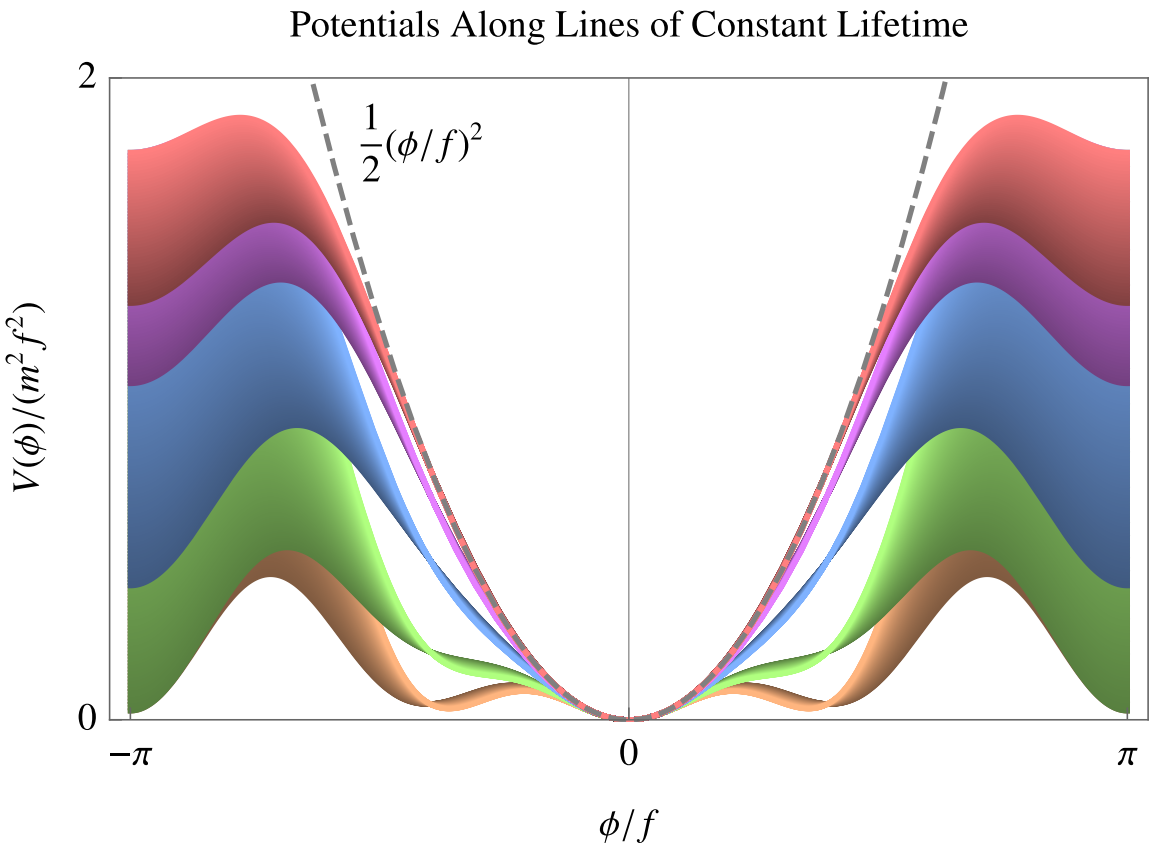

Figure 2.1b: The potentials along the lines of constant lifetime in figure 2.1a. To interpret this figure, we recognize that each color corresponds to approximately a single lifetime. Therefore, thin regions contain the most significant features, while broad regions, such as the value of the potential near $\phi/f = \pm\pi$, are the least significant for determining the lifetime. As the central part of the potential approaches a free theory, the oscillon must grow in spatial extent because of weak self-interaction, leading to decoupling of the large bound oscillon from the short wavelength radiation (see section 2.2.1). On the other hand, some self-interaction is necessary to delay energetic death, which is why the purple potentials are much longer-lived than the red ones (see sections 2.2.3 and 2.3).

numerical techniques based on the PQB formalism have allowed us to perform this parameter sweep in 96 CPU-hours, parallelized down to a few hours of wall-clock time. We see that the landscape is broken down into "islands of longevity," where neighboring potentials sustain oscillons that are similarly long-lived. While most of this space supports oscillons in the range $10^2 - 10^4$ oscillations, these few tunable parameters in the potential are enough to allow for oscillons that may live up to 10^{14} cycles.

The distinct islands in figure 2.1a correspond to the action of two mechanisms that suppress oscillon radiation, which we identify as *totally destructive self-interference* and *geometric decoupling*. Together, these two effects comprise the *form-factor* of the oscillon coupling to radiation, but we separate them because of their distinct imprints on the oscillon life-cycle, as depicted in figure 2.2. Further, the cliffs in figure 2.1a represent destructive interference peaks entering unreachable frequencies beyond the point of *energetic death*, where the oscillon is forced to dissipate because of energy conservation. Here, we briefly review these three effects.

Destructive interference: The bound bulk of the oscillon is a nearly coherent object, oscillating at frequency ω. Through the interaction terms of integer order ϕ^{n+1}, the oscillon bulk behaves as a nearly coherent source of radiation at multiples of the fundamental frequency $n\omega$. Similar to a diffraction experiment, certain geometries lead to totally destructive interference, exponentially confining certain radiation channels at exceptional frequencies. When the dominant radiation channel destructively interferes, the radiated power experiences a sudden 'dip.'

Geometric decoupling: The size of the oscillon is inversely proportional to the momentum $\sqrt{m^2 - \omega^2}$, which blows up as the binding energy per particle $m - \omega$ goes to zero, i.e. as ω approaches the rest mass m (see figure 2.3). In this limit, the oscillon grows much larger than the wavelengths of radiation $2\pi/n\omega$, causing a separation of scales. As this separation grows, the smooth oscillon bulk decouples from radiation, which manifests as an exponential decrease in radiated power towards the end of the oscillon's lifetime.

Energetic death: As the oscillon radiates away its energy, the binding energy per particle decreases, reducing the oscillon's central amplitude and increasing its radius. In three or more spatial dimensions, weak self-interactions result in a volume growing faster than can be accommodated by the decreasing central amplitude. Therefore, at frequencies ω approaching the mass m, there is a point past which an external energy source is necessary for the oscillon to remain bound. At this point, the oscillon is forced to undergo a rapid process of dissipation, which we call energetic death.

These mechanisms explain the structure of the longevity landscape observed in figure 2.1a. An island of longevity starts when a point of destructive interference (a 'dip') emerges from low

frequencies (green contour). As the dip migrates toward higher frequencies, its effect is enhanced by geometric decoupling, causing lifetime to increase until the dip moves beyond the frequency of energetic death, resulting in a longevity 'cliff' (blue contour).

In order to obtain these results, we have applied our PQB formalism to estimate the evolution of extremely long-lived spherically symmetric oscillons in isolation. In doing so, we have made the implicit assumption that the physical oscillon has relaxed into a state near the PQB. In order to check that this assumption is valid, we have performed a detailed linear stability analysis of the PQB to spherical and non-spherical perturbations, and we have presented evidence that unstable modes remain small enough that our procedure stays predictive (appendix 4.3).

This paper is structured as follows. Section 2.1 introduces the main object of study, the physical quasibreather. The oscillon is identified as living in the basin of attraction of the PQB, which naturally captures notions of oscillon stability. Section 2.2 uses the PQB formalism to understand the mechanisms of longevity briefly discussed above, and derives the minimum radiation condition. Section 2.3 applies the mechanisms of oscillon longevity and death to construct a family of potentials supporting ultra-long-lived oscillons. Section 2.4 applies our techniques to study the genericity of long-lived oscillons, and introduces local and global measures of fine-tuning. Section 2.5 applies our formalism to well-known potentials in the literature, re-deriving and expanding on previous results. Finally, the appendices provide a detailed technical overview of our formalism, and contain an exhaustive treatment of linear stability, as well as our numerical workflow. Appendix 4.1 provides the mathematical basis of the PQB. Appendix 4.2 details the numerical procedure for obtaining the PQB. Appendix 4.3 details our linear and nonlinear stability analysis of the PQB. Appendix 4.4 provides technical formulae relevant for computing the PQB and its linear stability. Appendix 4.5 details our explicit numerical simulations.

2.1 The physical quasibreather

The nonlinear wave equation we study in this paper is of the generic form

$$0 = \ddot{\phi} - \nabla^2\phi + V'(\phi/f)\,. \tag{2.2}$$

Here, f is the scale of self-interaction, known as the axion decay constant. The overdot represents time differentiation, ∇^2 is the usual flat-space Laplacian, and V' represents differentiation of the potential $V(\phi/f)$ with respect to the field ϕ. An oscillon is a finite-energy solution of (2.2) that is quasibound by self-interactions. In 3+1 dimensions, which is the focus of our study, all known oscillons have a finite lifetime because they radiate classical scalar waves. To understand whether a potential hosts cosmologically relevant oscillons, one needs a robust computational formalism for obtaining these classical radiation rates. Here, we introduce the physical quasibreather formalism for computing the oscillon radiation and lifetime, while leaving the more technical details to appendix

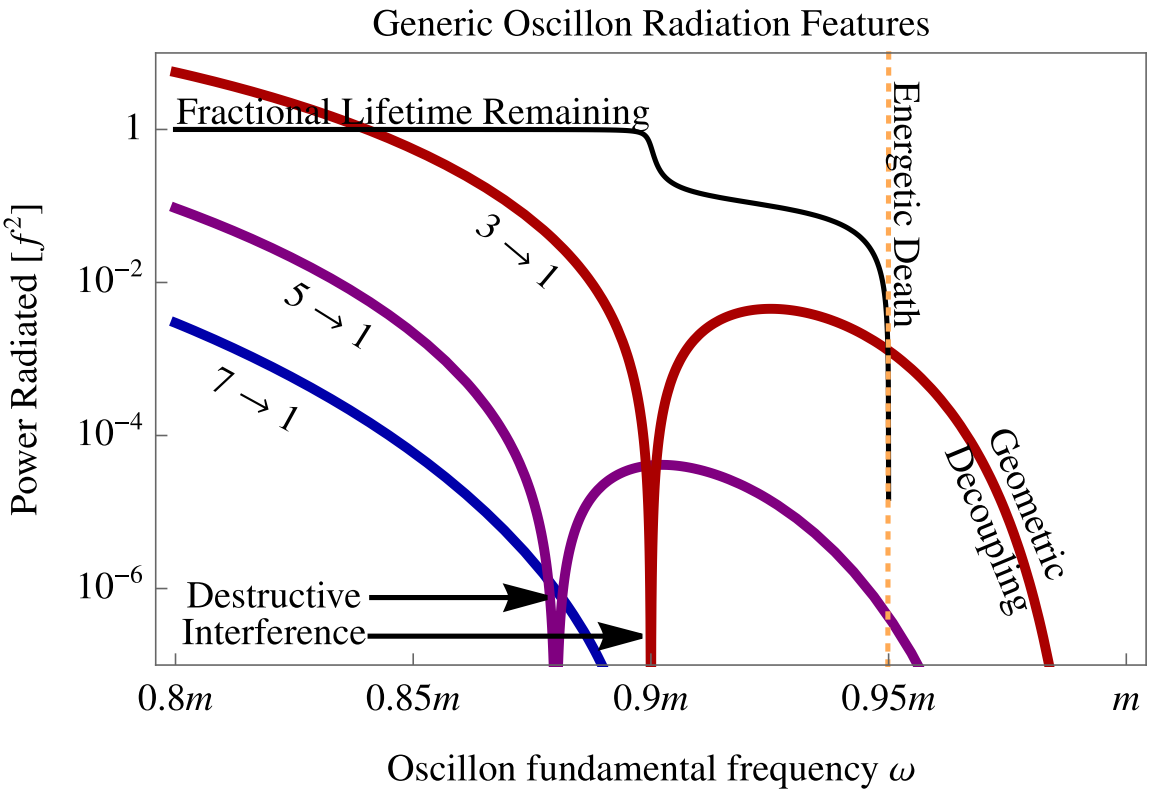

Figure 2.2: This plot illustrates the mechanisms of oscillon longevity and death described in section 2.2. Here, we plot the power carried out of the oscillon in the dominant radiating harmonics as a function of the oscillon frequency ω. The fundamental frequency ω increases with time, and therefore may be interpreted as a time coordinate (see figure 2.3). For simplicity, we consider a scalar potential with parity symmetry, leading to radiation at odd multiples of ω due to $n \to 1$ processes. Towards higher frequencies, the size of the oscillon $2\pi/\sqrt{m^2 - \omega^2}$ is much larger than the radiation wavelength $2\pi/(n\omega)$, leading to the geometric decoupling of radiation. As the oscillon becomes more diffuse, its volume grows faster than its amplitude shrinks, forcing an early energetic death. At exceptional frequencies, certain radiative harmonics vanish as a consequence of destructive self-interference.

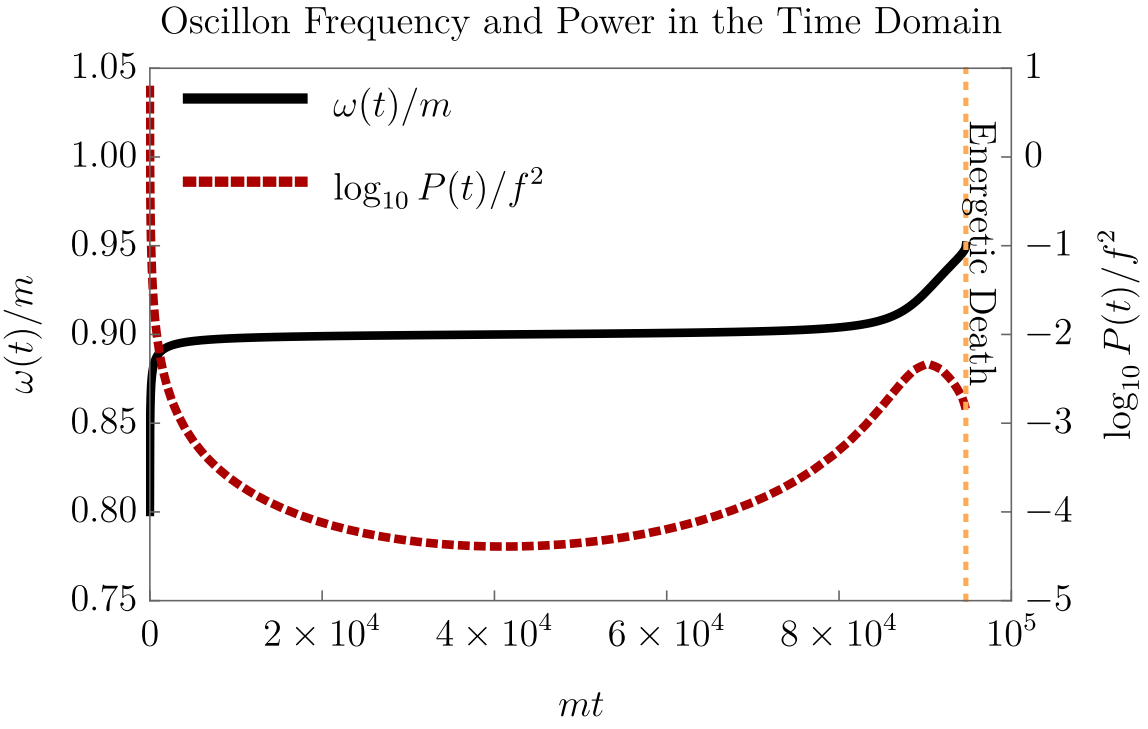

Figure 2.3: The oscillon's instantaneous frequency $\omega(t)$ and radiated power $P(t)$ plotted as explicit functions of time. These curves correspond to the generic scenario in figure 2.2. This plot illustrates how the oscillon spends most of its life at the exceptional frequency where the dominant radiating harmonic vanishes through destructive self-interference.

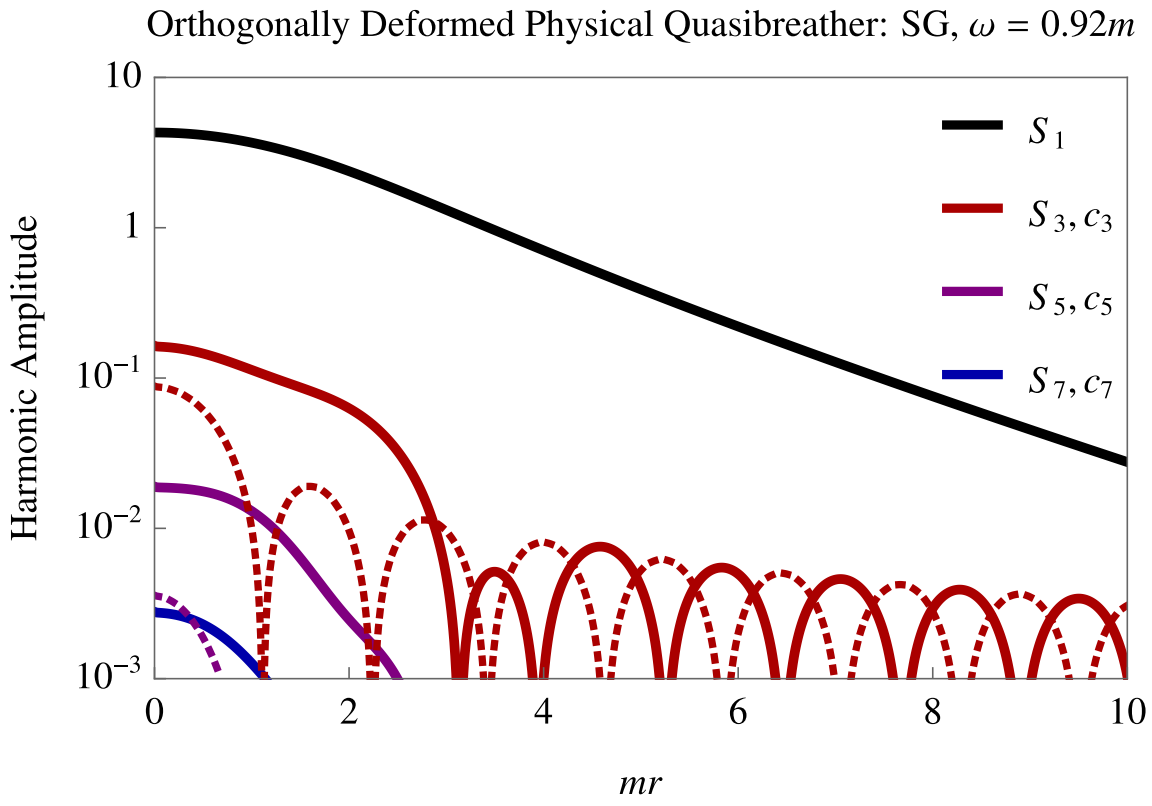

Figure 2.4: The radial profile of the physical quasibreather (PQB) (solid) and its orthogonal deformation (OD) (dashed) for the sine-Gordon (SG) oscillon at $\omega = 0.92m$, plotted against radius in units of the mass m^{-1}. In the limit where the radiation tails are small, this serves as an instantaneous approximation of the internal structure of the oscillon. The first quasibreather harmonic S_1 is exponentially bound, defining the oscillon bulk. The third harmonic S_3 is the dominant radiation mode, followed by the fifth, seventh, and so on. The spatial and temporal phase of the OD are 90 degrees out of phase with the PQB in the radiative region, representing outgoing radiation.

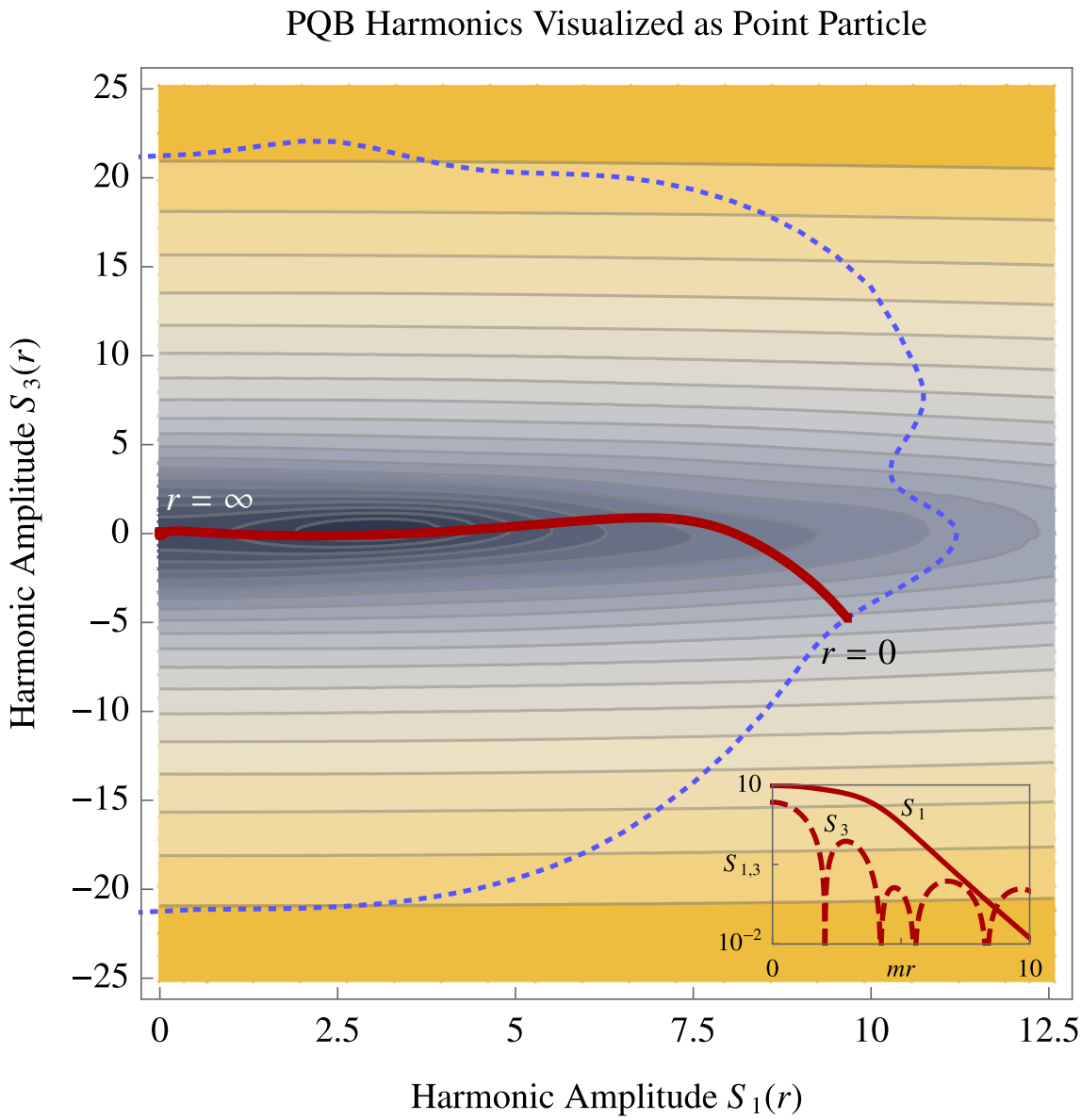

Figure 2.5: The PQB trajectory of the harmonic amplitudes S_1 and S_3 (red) is plotted on top of the level sets of the effective potential. The set of all initial conditions corresponding to quasibreathers is outlined in dotted blue. The particular example plotted here is of the sine-Gordon equation for $\omega = 0.5m$.

4.1.

A physical potential V represents interactions between an integer number of particles, and therefore possesses a well defined Taylor series. Consequently, a field oscillating at fundamental frequency ω will only couple to integer multiples of ω. Thus, one may look for quasibreather solutions: spherically symmetric, exactly periodic solutions of the equation of motion (2.2) of the form

$$\theta_{\rm QB}(t, r, \vartheta, \varphi) \equiv \frac{\phi}{f} = \sum_{n \in \mathbb{N}_0} S_n(r, \omega) \sin(n\omega t + \delta_n) \,, \tag{2.3}$$

where δ_n are constant phases, with $\delta_1 = 0$ by the choice of a time coordinate. The harmonic profiles $S_n(r, \omega)$ divide into bound modes $n < m/\omega$ and radiative modes $n > m/\omega$. Solutions of this form were first introduced in [132] and have since been used throughout the oscillon literature to obtain approximate oscillon solutions (see [115] for a complete review). Although (2.3) is a periodic solution of the equations of motion, it is not an infinitely long-lived oscillon; the far-field tails of the radiative harmonics $S_{n>m/\omega}$ decay like r^{-1}, and therefore contribute infinite energy.

These unphysical, infinite energy radiative tails have been problematic when interpreting quasibreathers as approximate oscillons. Furthermore, finding a quasibreather of a specific frequency is underdetermined: there are as many different quasibreathers of frequency ω as there are radiative degrees of freedom, representing the choice of central amplitudes $S_{n>m/\omega}(r = 0, \omega)$. One proposal to resolve this ambiguity is to pick the quasibreather with the minimum radiation amplitude, in an attempt to minimize the influence of the unphysical radiation tails (see e.g. [115]). Here, we introduce a different criterion for choosing the quasibreather closest to a physical oscillon. Instead of demanding that the radiative tails are minimized, we will require that the quasibreather is perturbatively close to a radiating solution of (2.2).

To this end, we introduce the *orthogonal deformation* (OD)

$$\theta_{\rm OD}(t, r, \vartheta, \varphi) \equiv \sum_{n\omega > m} c_n(r, \omega) \cos(n\omega t + \delta_n) \,, \tag{2.4}$$

whose temporal phase is 90 degrees offset from that of the quasibreather (2.3). Note that the sum over n only includes the frequencies corresponding to modes with radiative tails, $n\omega > m$. When added to the standing wave quasibreather (2.3), the orthogonal deformation allows for travelling modes (see figure 2.4). We then define the family of *physical quasibreathers* (PQB), $\theta_{\rm PQB}$, parametrized by ω, as those quasibreathers which may be orthogonally deformed $\theta_{\rm PQB} \to \theta_{\rm PQB} + \theta_{\rm OD}$ to satisfy purely outgoing boundary conditions at leading order in $\theta_{\rm OD}$ (i.e. $\theta_{\rm PQB} + \theta_{\rm OD}$ must satisfy the Sommerfeld radiation condition [133]). Note, we will use subscripts to refer either to a general quasibreather $\theta_{\rm QB}$ or to a physical quasibreather $\theta_{\rm PQB}$ with an OD partner that together satisfy the Sommerfeld radiation condition.

The radiative boundary conditions are enforced at spatial infinity, where the wave equation (2.2)

is well approximated by the Klein-Gordon equation. In this region, the OD and the radiative tails of the PQB are of the same amplitude because they represent purely outgoing radiation. Because θ_{PQB} is a solution of the equations of motion, the perturbation θ_{OD} must backreact at second order $\mathcal{O}(\theta_{\mathrm{OD}}^2)$, *and* it must obey a homogeneous linear equation to the same order [1]. Therefore, a PQB with small radiative tails must have an OD that is small *everywhere*, compared to the PQB central amplitude. The infinite lifetime limit is the limit of no radiation, and in this case, the PQB approaches a finite energy oscillon. Therefore, the PQB will be the central object in our study of long-lived oscillons.

To summarize, the following three objects are pointwise close to one another: the finite energy oscillon, the PQB, and the orthogonally deformed PQB. This proximity forms the basis of an expansion of the oscillon, which we fully develop in appendix 4.1, where the oscillon is understood to be a stable perturbation of the orthogonally deformed PQB. As such, oscillon properties (instantaneous frequency, stability, radiation, etc.) may be understood as originating from the nearest PQB. Furthermore, we develop the Floquet analysis of linear perturbations to the deformed PQB in appendix 4.3. Although linear stability turns out to be a sufficient criterion for the existence of an oscillon, it is not a necessary condition, since stable orbits can (and do) emerge at higher orders. In other words, linear instability does *not* imply the dissolution of the oscillon, since nonlinearities control the size of the linearly unstable perturbations. This effect has important phenomenological consequences for the nature of the oscillon evolution (for examples, see figures 2.11,2.13,4.4a,4.4b). Specifically, slow quasiperiodic oscillations around the PQB profile emerge in linearly unstable regions, with amplitude that depends strongly on initial conditions.

Below, section 2.1.1 provides a minimal technical review of our framework, which will be useful in understanding the qualitative features of oscillon evolution in section 2.2. Afterwards, section 2.1.2 outlines the steps in the numerical workflow of computing the PQB and OD, as well as the associated oscillon properties such as lifetime.

2.1.1 The mode equations

At each stage of its life-cycle, the oscillon may be viewed as close to a particular physical quasibreather. This description becomes increasingly precise in the infinite lifetime limit, where radiation goes to zero and the oscillon evolves slowly. Because the oscillon spends a long time in the vicinity of a particular physical quasibreather, the notion of the instantaneous frequency ω becomes well defined. Physically, ω then behaves like an adiabatic parameter, although formally it serves as an index to label which physical quasibreather the oscillon is closest to at a given time. The fact that the oscillon does remain close to the physical quasibreather family is a consequence of its attractive properties, which we make precise in appendix 4.3.

We are now in position to introduce the mode equations, which describe the spatial profile of

[1] This is technically only true once one introduces $\delta\theta$ in appendix 4.1.

the physical quasibreather at a given frequency ω. In the interest of a pedagogical introduction, we will consider the particularly simple case of a single bound harmonic S_1 for a potential with parity $V(\theta) = V(-\theta)$, and we will keep only the first radiative harmonic S_3.

As outlined above, the potential V is Taylor expandable, and therefore factorizes into a sequence of integer harmonics of the fundamental frequency ω. By restricting to $V(\theta) = V(-\theta)$, only the odd harmonics are coupled to one another, allowing for the following decomposition

$$V'(\theta_{\rm PQB}) \equiv m^2 f \sum_{n=1,3} V'_n(S_1, S_3) \sin(n\omega t) + \dots \,, \tag{2.5}$$

$$V''(\theta_{\rm PQB}) \cos(n'\omega t) \equiv m^2 \sum_{n=1,3} V''_{n,n'}(S_1, S_3) \cos(n\omega t) + \dots \,, \tag{2.6}$$

where the dots refer to terms proportional to higher frequencies $n\omega$, and terms that contain the small harmonics S_n, $n \geq 5$. Inserting the quasibreather and the orthogonal deformation into the equations of motion, we arrive at the orthogonally deformed mode equations

$$\begin{aligned} 0 &= S_1'' + \frac{2}{r} S_1' + \omega^2 S_1 - m^2 V_1'(S_1, S_3) \,, \\ 0 &= S_3'' + \frac{2}{r} S_3' + (3\omega)^2 S_3 - m^2 V_3'(S_1, S_3) \,, \\ 0 &= c_3'' + \frac{2}{r} c_3' + \left((3\omega)^2 - m^2 V''_{3,3}(S_1, S_3)\right) c_3 \,. \end{aligned} \tag{2.7}$$

To fully specify the solution to this system, we must provide 6 boundary conditions: regularity at the origin

$$0 = S_1'(0) = S_3'(0) = c_3'(0) \,, \tag{2.8}$$

regularity at spatial infinity

$$0 = S_1(\infty) \,, \tag{2.9}$$

and radiative boundary conditions [133]

$$\begin{aligned} 0 &= \lim_{r\to\infty} \partial_r r S_3(r) - \sqrt{(3\omega)^2 - 1}\, r c_3(r) \,, \\ 0 &= \lim_{r\to\infty} \sqrt{(3\omega)^2 - 1}\, r S_3(r) + \partial_r r c_3(r) \,. \end{aligned} \tag{2.10}$$

To understand these equations, it is helpful to visualize the evolution of S_1 and S_3 as the coordinates of a point particle rolling down a hill, where r is now the time coordinate, and the initial stationary particle is placed so that it arrives at the saddle located at the origin when $r \to \infty$ (see figure 2.5). Out of the continuum of quasibreather initial conditions $S_1(0), S_3(0)$ satisfying this constraint, the

orthogonal deformation selects only one, corresponding to the PQB.

2.1.2 Calculation workflow

Here we review the workflow of estimating the oscillon lifetime in the physical quasibreather framework, leaving a more detailed presentation to the appendices.

1. The harmonics S_n of the PQB may be thought of as existing in two categories. The perturbative harmonics are those S_n whose amplitude is everywhere small enough that self-interaction can be safely neglected. Those S_n for which this is not true are called non-perturbative. Typically, only a few non-perturbative harmonics are needed to achieve numerical convergence. The physical intuition for whether a harmonic may be treated perturbatively or not is whether it contributes significantly to the bound energy compared to the flux radiated per cycle. In other words, a good rule of thumb for whether a harmonic is perturbative is whether its central amplitude is significantly larger than the leading orthogonal deformation at the origin.

2. The non-perturbative harmonics (which must include S_1) are calculated using a shooting technique, in which the S_n's are propagated from the origin to an outer boundary at $r = r_{\text{out}}$. At this point, the Sommerfeld radiation condition (2.10) is used to calculate the OD, $c_n(r_{\text{out}})$ and $c_n'(r_{\text{out}})$. From these final conditions, the c_n are propagated back to the origin in the background of the non-perturbative S_n. One then checks whether the backwards propagated c_n's satisfy regularity at the origin. We perform a search over initial conditions $S_n(0)$ until regularity is satisfied for all c_n's.

3. Having computed the non-perturbative harmonics, an arbitrary number of perturbative harmonics may be computed to linear order by solving a sparse matrix equation. In other words, once the hard work of computing the non-perturbative harmonics is done, one may compute the full spectrum of the oscillon to arbitrary harmonic order with little computational cost. One may then re-shoot the non-perturbative harmonics in the background of the perturbative harmonics to account for linear back-reaction, repeating until converged.

4. The result of these calculations is a semi-non-perturbative expression for the physical quasibreather S_n and its orthogonal deformation c_n. The radiation power in each harmonic is easily computed as $P_n = 2\pi r^2 (n\omega)\sqrt{(n\omega)^2 - 1}\left(S_n^2 + c_n^2\right)$ evaluated at the outer boundary. The sum $\sum_n P_n$ is the PQB approximation to the total power P radiated by the oscillon.

5. Having calculated the outgoing power P as a function of the PQB frequency ω, we may approximate the lifetime of the oscillon near the physical quasibreather trajectory as $T = \int \mathrm{d}\omega (dE_B/d\omega)/P$, where E_B is the *bound* energy in the oscillon, defined as the difference between the PQB and OD energy (see appendix 4.1.4).

We provide a public implementation of this protocol for the case of a single non-perturbative harmonic in potentials with parity — a fast and easy-to-use tool to obtain ballpark estimates of oscillon properties at larger frequencies [2].

2.2 The oscillon life-cycle

Here we review and expand upon previous literature results [1, 64, 98, 99, 107–118] in order to identify the main mechanisms responsible for oscillon longevity and death. We point out two distinct effects contributing to oscillon longevity: *geometric decoupling* and *destructive interference*, both of which may be thought of together as the *form-factor* of the oscillon coupling to radiation. It is important to separate form-factor into these two effects because they intervene at different times, and have different consequences for oscillon evolution. Often, an oscillon's lifetime is dominated by one mechanism or the other, while the longest lived oscillons take advantage of both simultaneously. Separately, as the oscillon ages and grows more diffuse, it will inevitably undergo an *energetic death*, beyond which its energy would be forced to unphysically increase. These three effects are all pointed out in figure 2.2, which depicts the typical radiation history of an oscillon. Below, we provide a semi-quantitative overview of these three effects.

2.2.1 Geometric decoupling

Recall that the oscillon is a smooth, nearly coherent object, coupling to integer multiples n of its fundamental frequency ω through many-to-one interactions at leading order ϕ^{n+1}. As the oscillon radiates bound energy throughout its life, its fundamental frequency increases towards m (see figure 2.3), and its typical size $2\pi/\sqrt{m^2-\omega^2}$ blows up, where $m-\omega$ is the binding energy per particle. Therefore, a natural separation of scales occurs between the length scale of radiation $2\pi/n\omega$ and the size of the oscillon, leading to an exponential suppression of the oscillon's coupling to radiative modes $n\omega$, $n \geq 2$. According to a standard Riemann-Lebesgue suppression argument, the ratio of the $n\omega$ harmonic amplitude to the fundamental harmonic central value scales as γ^n, with

$$\gamma \approx \exp\left[-G\frac{\omega}{\sqrt{m^2-\omega^2}}\right], \tag{2.11}$$

where G is an order 1 geometrical factor, used here as a stand-in for the exact shape of the oscillon. The fact that the geometrical factor G is in the exponent shows that even modest changes in the oscillon's shape can dramatically change its lifespan, emphasizing the importance of accurately resolving the oscillon geometry. Moreover, because the factor $\omega/\sqrt{m^2-\omega^2}$ becomes larger as ω approaches m, the differences between potentials will be exaggerated in this limit, while low-frequency oscillons will typically be similar to one another (see figures 2.11 and 2.12 for an example). As a

[2] Simple oscillon code.

consequence of this growing separation of scales, oscillons whose frequency ω approaches the mass m radiate at increasingly suppressed rates, so that the last phase of the oscillon's life is often the longest. We refer to this general trend as geometric decoupling.

2.2.2 Destructive interference and the minimum radiation condition

Throughout the oscillon lifetime, radiative harmonics are subject to self-interference, which is totally destructive at exceptional frequencies. At these points, destructive interference completely confines specific harmonics, and subverts the expected radiation hierarchy implied by geometric decoupling. When the leading harmonic is confined, the overall radiation amplitude shrinks by another global factor of γ. For many especially long-lived oscillons, a period near harmonic confinement dominates the total lifetime. In principle, it is possible to imagine engineering ultra-long-lived oscillons by aligning the destructive interference of multiple harmonics, leading to additional suppression by γ^ℓ, where ℓ is the number of aligned exceptional points. In practice, these constructions are necessarily fine tuned, since each resonance must be aligned to order $\gamma^{\ell-1}$.

Interferometric analogue The basic physics of oscillon radiation is captured by the physical model in figure 2.6, which describes an interference experiment reminiscent of the classic Lloyd's mirror. In this simple one-dimensional setup, a coherent, finite-sized, optical source at $r > 0$, representing the oscillon's coupling to the radiative harmonic, is placed in front of a mirror at $r = 0$, representing the spherical symmetry of the oscillon. Each point in the source experiences interference both from its reflection, and from its neighbors. Let the spatial location and magnitude of the source be described by $\tilde{\mathcal{J}}(r)$. The direct radiation reaching the observer is therefore

$$A_{\text{direct}}(t,r) = \int_0^\infty \mathrm{d}x\, \tilde{\mathcal{J}}(x)\, e^{i[\omega t - k(r-x)]}\,. \tag{2.12}$$

On the other hand, the reflected light paths sum up to an amplitude:

$$A_{\text{reflected}}(t,r) = \int_0^\infty \mathrm{d}x\, \tilde{\mathcal{J}}(x)\, e^{i[\omega t - k(r+x)+\pi]}\,, \tag{2.13}$$

where, crucially, a half-wavelength path difference is picked up upon reflection at the mirror. This is equivalent to enforcing the usual regularity conditions at the origin in a spherically symmetric field solution. Finally, the observer adds up these contributions coherently, which explicitly leads to an amplitude equal to the sine-transform of the source:

$$\begin{aligned} A_{\text{obs}}(t,r) &= A_{\text{direct}}(t,r) + A_{\text{reflected}}(t,r)\,, \\ &= 2e^{i[\omega t - kr + \pi/2]} \int_0^\infty \mathrm{d}x\, \tilde{\mathcal{J}}(x)\, \sin(kx)\,. \end{aligned} \tag{2.14}$$

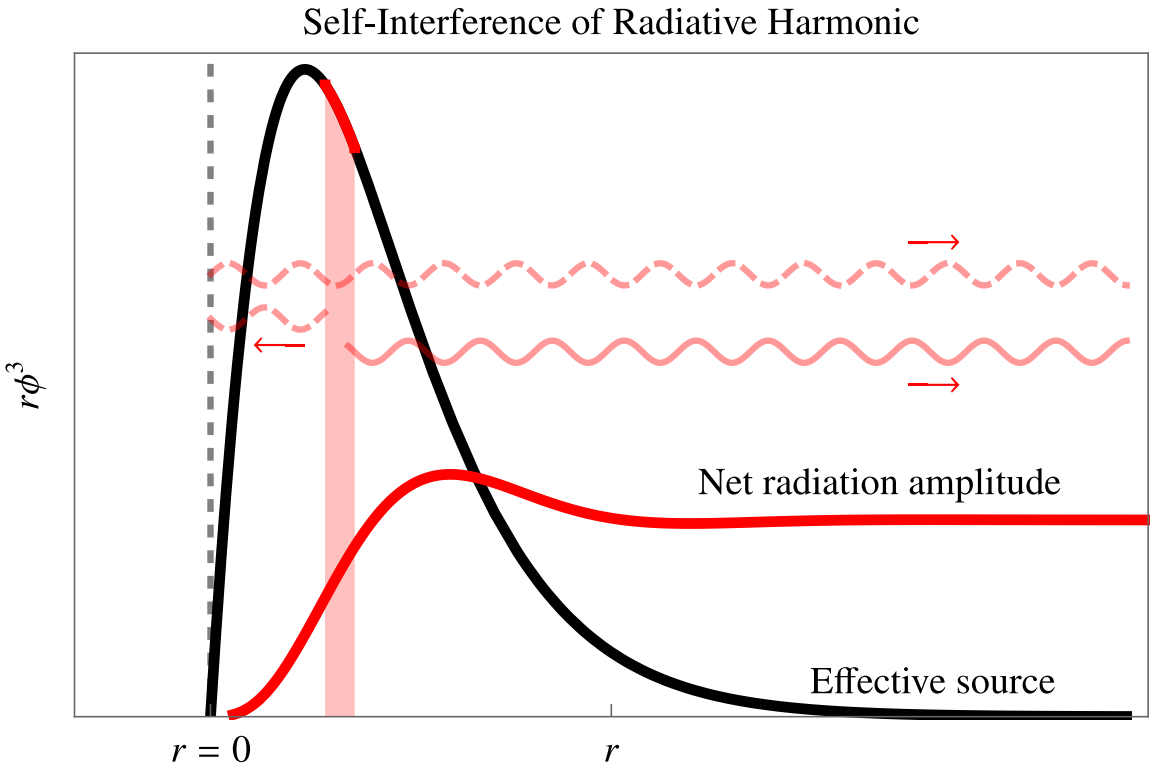

Figure 2.6: A physical model for an oscillon radiating into the third harmonic. The black line represents the background oscillon source ϕ^3, while the red lines represent the amplitude of the radiated field. The spherical symmetry of the oscillon imposes boundary conditions at the origin which behave like an optical mirror: an inward propagating spherical wave is reflected at the origin, propagating back outward with the opposite phase. The result is that the oscillon radiation may experience two kinds of self-interference: interference from the physical extent of the source, analogous to diffraction of a laser beam through a finite-width slit, and interference due to the spherical symmetry of the oscillon, represented by the mirror. At certain oscillon frequencies, these two effects conspire to destructively interfere, trapping a nominally free harmonic.

In the following section, we derive a similar result from the mode equations of the PQB, and quantify corrections to this simplified picture.

The physical quasibreather picture In the previous section, we introduced a simple interpretation of the oscillon radiation in terms of the interference of a coherent source with its own reflection. Here we study the mode equations (2.7), in which the first radiative harmonic S_3 and the orthogonal deformation c_3 are treated as a perturbation of the fundamental S_1. Under this perturbative assumption, the mode equations for the radiative harmonic $\tilde{S}_3 \equiv rS_3$ and its orthogonal deformation $\tilde{c}_3 \equiv rc_3$ further simplify to the frictionless linear system

$$\tilde{S}_3''(r) + k_S^2(r)\tilde{S}_3(r) = r\mathcal{J}_3(r)\,, \tag{2.15}$$

$$\tilde{c}_3''(r) + k_c^2(r)\tilde{c}_3(r) = 0\,. \tag{2.16}$$

Here, k_S and k_c represent the r-dependent wavenumbers of the third harmonic S_3 and c_3 in the background of the fundamental harmonic S_1, and $r\mathcal{J}_3(r)$ corresponds to the $3 \to 1$ processes generating the radiation. Note, the wavenumber is different for the third harmonic S_3 and its orthogonal deformation c_3, a distinction explicitly derived in the appendix result (4.40). There, we find that the difference between k_S and k_c appears at sixth order in a Bessel expansion of the background, and therefore is typically small, making the approximation $k_S = k_c$ quantitatively good in most circumstances. We can solve the linear system analytically in terms of two linearly independent solutions $y_{1,2}^S(r)$ and $y_{1,2}^c(r)$ of the *homogeneous* equations. In this case, the expression for the Green's function is simple and the full solution becomes a sum of homogeneous (defined by initial conditions) and inhomogeneous contributions, of the form:

$$\begin{aligned}
\tilde{S}_3(r) =& a_1^{\mathrm{H}} y_1^S(r) + a_2^{\mathrm{H}} y_2^S(r) + y_1^S(r)\int_0^r \mathrm{d}r'\, r'\,\mathcal{J}_3(r')\,\frac{y_2^S(r')}{W^S(r')} - y_2^S(r)\int_0^r \mathrm{d}r'\, r'\,\mathcal{J}_3(r')\frac{y_1^S(r')}{W^S(r')}\,,\\
\tilde{c}_3(r) =& b_1^{\mathrm{H}} y_1^c(r) + b_2^{\mathrm{H}} y_2^c(r)\,,
\end{aligned} \tag{2.17}$$

where $W^S(r) \equiv y_1^S(r)y_2^{S\prime}(r) - y_1^{S\prime}(r)y_2^S(r)$ is the Wronskian. Let $y_1^{S,c}$ be the sine-like solution (nonzero derivative at $r = 0$) and let $y_2^{S,c}$ be the cosine-like solution (zero derivative at $r = 0$). Regularity at the origin requires that only sine-like initial conditions are allowed, constraining the cosine-like terms to be zero $b_2^{\mathrm{H}} = a_2^{\mathrm{H}} = 0$.

In the far-field region, all solutions $y_{1,2}^{S,c}$ are simple combinations of sines and cosines of frequency $k_3 = \sqrt{(3\omega)^2 - m^2}$. However, orthogonality between y_1 and y_2 is generally not maintained into the

far-field. Without loss of generality, we can introduce phase-shifts to express these misalignments,

$$y_1^S = \sin(k_3 r)\,, \tag{2.18}$$
$$y_2^S = \cos\big(k_3 r + \varphi_2^S\big)\,, \tag{2.19}$$
$$y_1^c = \sin(k_3 r + \varphi_1^c)\,, \tag{2.20}$$

with the understanding that when these phase-shifts are zero, we regain the simple constant-wavenumber Helmholtz solutions. These phase-shifts can in principle be computed in the WKB approximation. Furthermore, we define the orthogonal components $y_s = \sin(k_3 r)$ and $y_c = \cos(k_3 r)$ against which we can project the shifted solutions, leading to

$$y_1^S = y_s\,, \tag{2.21}$$
$$y_2^S = y_c \cos\varphi_2^S - y_s \sin\varphi_2^S\,, \tag{2.22}$$
$$y_1^c = y_c \sin\varphi_1^c + y_s \cos\varphi_1^c\,. \tag{2.23}$$

Substituting, we collect the orthogonal contributions to the radiative tails as

$$\begin{aligned} S_3(r) r &\xrightarrow[r\to\infty]{} y_s(a_1^{\mathrm{H}} + a_1^{\mathrm{I}} + a_2^{\mathrm{I}} \sin\varphi_2^S) - y_c a_2^{\mathrm{I}} \cos\varphi_2^S\,, \\ c_3(r) &\xrightarrow[r\to\infty]{} y_s b_1^{\mathrm{H}} \cos\varphi_1^c + y_c b_1^{\mathrm{H}} \sin\varphi_1^c\,, \end{aligned} \tag{2.24}$$

where a_1^{I} and a_2^{I} are fixed, representing the total inhomogeneous contribution from the oscillon background

$$a_1^{\mathrm{I}} = \int_0^\infty \mathrm{d}r'\, r'\, \mathcal{J}_3(r')\, \frac{y_2^S(r')}{W^S(r')}\,, \tag{2.25}$$
$$a_2^{\mathrm{I}} = \int_0^\infty \mathrm{d}r'\, r'\, \mathcal{J}_3(r') \frac{y_1^S(r')}{W^S(r')}\,. \tag{2.26}$$

Radiative boundary conditions (2.10) match the coefficients of y_s and y_c between S_3 and c_3, which uniquely determines the homogeneous degrees of freedom,

$$\begin{aligned} b_1^{\mathrm{H}} &= a_2^{\mathrm{I}} \cos\varphi_2^S \sec\varphi_1^c \\ a_1^{\mathrm{H}} &= -a_1^{\mathrm{I}} + a_2^{\mathrm{I}}(-\sin\varphi_2^S + \cos\varphi_2^S \tan\varphi_1^c). \end{aligned} \tag{2.27}$$

Consequently, the solution simplifies to

$$S_3(r) r = a_2^{\mathrm{I}} \cos\big(\varphi_2^S\big)(y_s \tan\varphi_1^c - y_c)\,, \tag{2.28}$$
$$c_3(r) r = a_2^{\mathrm{I}} \cos\big(\varphi_2^S\big)(y_s + y_c \tan\varphi_1^c)\,. \tag{2.29}$$

In other words, the amplitude of the radiation is always proportional to the inhomogeneous contribution a_2^{I}. At exceptional frequencies, this contribution is exactly zero and the harmonic experiences totally destructive interference; this is visible in the power versus frequency plots as a sudden drop (see figures 2.11 and 2.12 for example). Therefore, in this linear model the condition for totally destructive interference is

$$0 = \int_0^\infty \mathrm{d}r'\, r'\, \mathcal{J}_3(r') \frac{y_1^S(r')}{W^S(r')}\,. \tag{2.30}$$

In the case of a flat wave-number, i.e. Helmholtz system, this is precisely the sine-transform of the source, as predicted by the simple interferometric model. Because totally destructive interference is equivalent to a single constraint on one free parameter ω, we conclude this effect is *generic*, and not the result of some fine tuning.

To reach this result, we have effectively solved for the physical quasibreather, defined by the choice of a_1^{H} in (2.27), at the level of the third harmonic and in a linear approximation. In previous literature (e.g. [115]), a different quasibreather was highlighted as relevant in approximating the oscillon, namely the *minimum-radiation quasibreather*. This corresponds to a different choice of homogeneous parameters; in this case, the construction of c_3 is irrelevant and the value of a_1^{H} is chosen such that S_3 is minimized at the level of (2.24), specifically by picking:

$$a_1^{\mathrm{H}} = -a_1^I - a_2^I \sin\varphi_2^S\,. \tag{2.31}$$

We see that this differs from the physical quasibreather answer (2.27) by an additional $a_2^{\mathrm{I}} \cos\varphi_2^S \tan\varphi_1^c$, which is zero in the case when $\varphi_1^c = 0$, i.e. when the wavenumbers $k_S(r)$ and $k_c(r)$ are identical functions of r. While typically small, differences between $k_S(r)$ and $k_c(r)$ appear at higher-orders in the background, and are not guaranteed to be perturbative — as derived below in appendix 4.4.1. Therefore, the minimum-radiation quasibreather and the physical quasibreather are generally close but distinct, and are identical only at the exceptional 'dip' frequency where both predict zero radiative tails.

2.2.3 Energetic death

As explained in section 2.2.1, the spatial extent of the oscillon increases as it radiates away its binding energy. On the other hand, the balance between self- and binding-energy demands that the oscillon's central amplitude decreases. Depending on the number of spatial dimensions, one effect or the other dominates the oscillon's total energy as ω approaches m. In particular, in three or more spatial dimensions, the volume turns out to grow faster than the central amplitude shrinks. The oscillon's parent PQB also obeys the same scaling relation, and at some point the bound energy in the PQB will necessarily begin to increase. To keep up, the oscillon would need a source of energy; in its absence, the oscillon is forced off the PQB trajectory, in a process we call energetic death.

To make these ideas precise, we can invoke the mode equations (2.7), in the limit of small central amplitude $S_1(0)$. Note, because the oscillon's volume is large, it is geometrically decoupled from radiation according to the argument in section 2.2.1, and therefore it is safe to neglect backreaction from the radiative harmonics. Keeping only the leading quartic nonlinearity in the potential, S_1 is described by

$$0 = S_1'' + \frac{d-1}{r} S_1' - (m^2 - \omega^2) S_1 + \frac{3}{4} m^2 \lambda S_1^3 \,. \tag{2.32}$$

Here, d is the number of spatial dimensions. To extract the scaling of $S_1(0)$, we match the bound energy of the oscillon to its self-energy, leading to

$$(m^2 - \omega^2) S_1^2 \sim m^2 \lambda S_1^4 \,. \tag{2.33}$$

Therefore, the scaling of the central amplitude is independent of dimensions, namely

$$S_1(0) \propto \sqrt{m^2 - \omega^2} \,. \tag{2.34}$$

On the other hand, since the spatial extent of the oscillon scales like scale $1/\sqrt{m^2 - \omega^2}$ (as seen in section 2.2.1), its volume must increase according to

$$V \sim \left(m^2 - \omega^2\right)^{-d/2} \,. \tag{2.35}$$

Combining these two scalings results in the oscillon's total energy

$$E \propto V S_1(0)^2 \propto \left(m^2 - \omega^2\right)^{1-d/2} \,, \tag{2.36}$$

which grows as ω approaches m for spatial dimension $d \geq 3$. In other words, the expectation that the oscillon energy decreases as a function of ω is only true up to a specific frequency strictly less than m. Beyond this point, the oscillon energy is forced to increase as a result of weak self-interaction. Such an increase is unphysical, and the value of ω at which the PQB's energy is minimized sets the moment of death. For an earlier argument along these lines, see [109, 115].

For an explicit comparison, take the $d = 1$ sine-Gordon oscillon, which has a simple analytic form

$$\phi = 4 \arctan \left[\frac{\sqrt{m^2 - \omega^2} \cos \omega t}{\omega \cosh \sqrt{m^2 - \omega^2} x} \right] \,. \tag{2.37}$$

In the $\omega \to m$ limit, the energy of the sine-Gordon oscillon is exactly $16\sqrt{m^2 - \omega^2}$, which matches our predicted scaling.

All the examples of oscillons studied in sections 2.3, 2.4 and 2.5 live in three spatial dimensions,

and therefore exhibit an energetic death. In other words, for each oscillon there is a specific frequency strictly less than m beyond which the scalar field may no longer exist close to a PQB. After this point, our formalism no longer applies, and the oscillon is considered "dead." Afterwards, gravity may take over leading to the formation of much more diffuse configurations such as axion stars [97,98]. In our numerical simulations, this moment of death is distinctly visible as a "loop," representing the rapid conversion of the oscillon into radiation through $3 \to 1$ processes (see figures 2.11, 2.13, and 2.14).

2.3 A prescription for oscillon longevity

Here we provide a procedure for generating potentials that support cosmologically long-lived oscillons. In section 2.2, we explained how the longest-lived oscillons exhibit a combination of geometric decoupling and destructive interference. Geometric decoupling refers to the suppression of radiation when the oscillon size is much larger than the radiation wavelengths, which is especially pronounced at large frequencies ω close to m. For a large oscillon, the interferometric 'fringe pattern' also occurs more rapidly, leading to more instances of destructive interference which further suppresses radiation. Thus, we may find long-lived oscillons by searching for potentials that support large oscillons at frequencies ω close to m. An apparent obstacle to this goal is due to energetic death (see section 2.2.3), which limits the frequencies for which the oscillon can have decreasing energy as a function of ω. In the following, we identify a feature in the scalar potential that can stave off energetic death *and* produce large oscillons.

In section 2.1, we introduced the mode equations (2.7) obeyed by the radial profiles of the PQB harmonics $S_n(r)$, and the sense in which these harmonics may be thought of as the coordinates of a point particle, whose initial condition is tuned so that $(S_1, S_3, \dots) = \vec{0}$ at $r = \infty$. Here we aim to study the longest-lived oscillons, whose radiation is necessarily small. Moreover, we will focus on large frequencies $\omega \approx m$, for which higher harmonics are further suppressed by a natural separation of scales $\omega \gg \sqrt{m^2 - \omega^2}$. Therefore, we will drop the higher harmonics $n \geq 3$ in this section's analysis, and work with a simplified 1-dimensional point-particle picture, representing the radial profile of the fundamental mode, $S_1(r)$.

We now introduce the equations that govern S_1 from first principles, using an effective action technique, equivalent to the PQB formalism for a single bound harmonic. The Lagrangian describing the real scalar ϕ is

$$L[\phi] = \int \mathrm{d}^3x \left[\frac{1}{2}\dot{\phi}^2 - \frac{1}{2}\nabla^2\phi^2 - V(\phi) \right] . \tag{2.38}$$

Because both V and ϕ are proportional to f^2 (as in (2.1)), f is an overall factor in the action, and therefore does not contribute to the dynamics. Hence, for the rest of this section, we will work in units of $f = 1$. Since we are looking for quasiperiodic, spherically symmetric solutions dominated

by the fundamental mode, we substitute $\phi = S_1(r)\sin\omega t$ and integrate out time, leading to the effective action for S_1:

$$S_{\text{eff}}[S_1] = \int_0^{\frac{2\pi}{\omega}} \mathrm{d}t L[S_1 \sin\omega t] = -\frac{\pi}{\omega}\int 4\pi r^2\,\mathrm{d}r\left[\frac{1}{2}S_1'(r)^2 - V_{\text{eff}}(S_1)\right]. \tag{2.39}$$

By integrating out time, we arrive at an action for a point particle $S_1(r)$, where r acts like a time coordinate, and the resulting effective potential is

$$V_{\text{eff}}[S_1] \equiv \frac{1}{2}\omega^2 S_1(r)^2 - \frac{\omega}{\pi}\int_0^{\frac{2\pi}{\omega}} \mathrm{d}t\, V(S_1\sin\omega t)\,. \tag{2.40}$$

Finally, the equation of motion for S_1 arising from this effective action carries a $2/r$ friction term from the spherical Jacobian

$$0 = S_1'' + \frac{2}{r}S_1' + V_{\text{eff}}'(S_1)\,, \tag{2.41}$$

where V_{eff}' represents the derivative of V_{eff} with respect to S_1.

A solution of these equations which describes an oscillon profile needs to respect regularity conditions at $r = 0$ and $r = \infty$, corresponding to $S'(0) = 0$ and $S(\infty) = 0$. All solutions which respect regularity at $r = \infty$ must exponentially decay, since V_{eff} behaves like a quadratic hilltop $-\frac{1}{2}(m^2 - \omega^2)S_1^2$ for small S_1. From the perspective of the point particle, this means that initial conditions are tuned such that S_1 has just enough energy to climb up the hilltop at 0.

In order to engineer large oscillons, we need the particle S_1 to stay at small velocities so that the oscillon interior spreads out. Initializing on a hillside of V_{eff} is detrimental to this goal, since the slope of V_{eff} controls the speed of S_1, typically leading to a small oscillon core. On the other hand, releasing S_1 close to a hilltop allows S_1 to remain at low velocities for a time inversely proportional to the initial displacement of S_1 from the hilltop.

Therefore, we need to connect hilltop-initialized solutions (i.e. low central velocity) to physical solutions (i.e. which arrive at $S_1(\infty) = 0$). To compensate for the energy lost by $2/r$ friction, a physical solution must be initialized with positive potential energy (where we've normalized $V_{\text{eff}}(0) = 0$). Effective potentials which satisfy these two conditions will have non-trivial local maxima, whose hilltop is higher than 0 (see figure 2.7).

Here we reverse engineer a class of scalar potentials $V(\phi)$ which generate effective potentials $V_{\text{eff}}(S_1)$ with the aforementioned hilltops. This construction makes use of the fact that the mass term in the effective potential $V_{\text{eff}}(S_1)$ acquires an ω^2 offset compared to the mass term in the scalar potential $V(\phi)$. Based on this observation, we introduce the family of *frustrated quadratics*, whose Fourier coefficients (in the basis expansion (2.1)) are chosen as the solution to the following

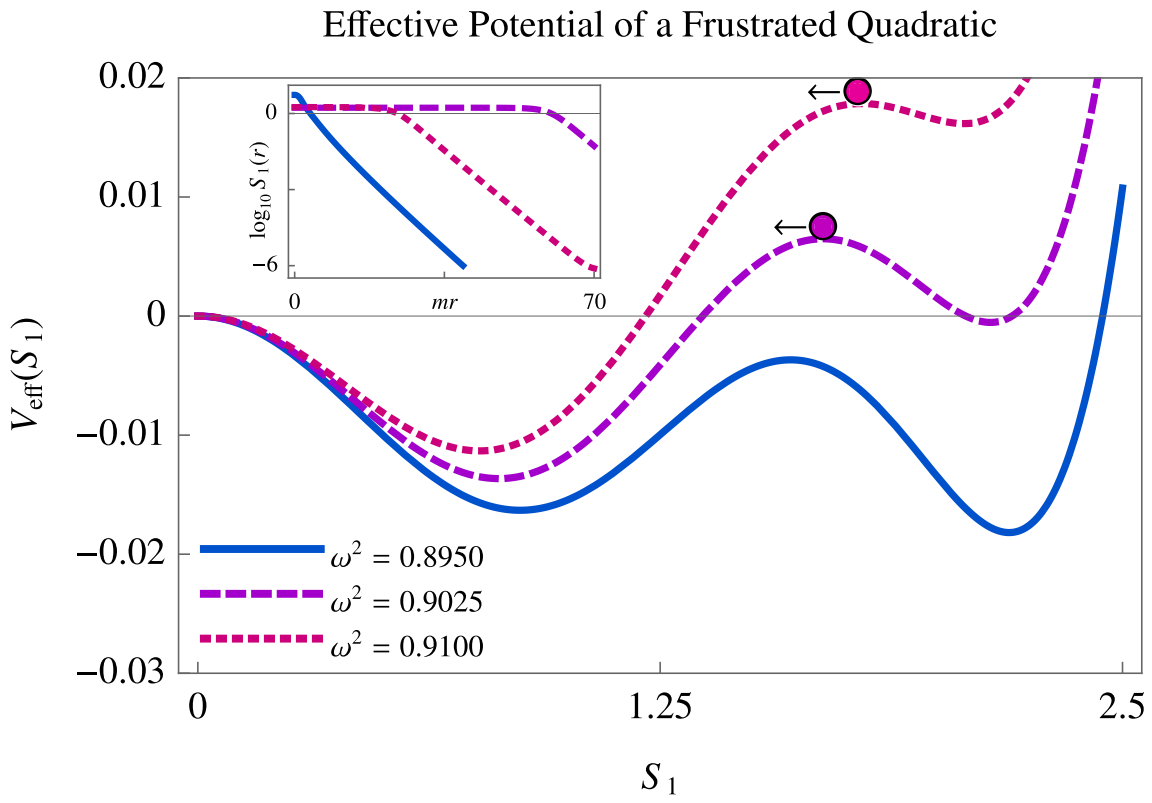

Figure 2.7: Effective potential $V_{\text{eff}}(S_1)$ for a long-lived oscillon, at three nearby frequencies. The example is obtained using the frustrated quadratic method defined in (2.42) with $m_f^2 = 0.9m^2$ and $b = 2$, computed using three Fourier coefficients $\mathcal{V}_{1,2,3}$ with $\mathcal{V}_3$ forced to satisfy the mass constraint in (2.1). We see that as ω passes through the frustrated mass m_f, new solutions to the equations of motion (2.41) emerge, specifically when the local maximum of the effective potential increases to positive values. The balls are placed at the values $S_1(0)$ which initialize physical oscillon solutions at the respective frequencies ω. The inset figure shows the trajectories of the smallest-amplitude solutions of (2.41) for each of the three potentials plotted.

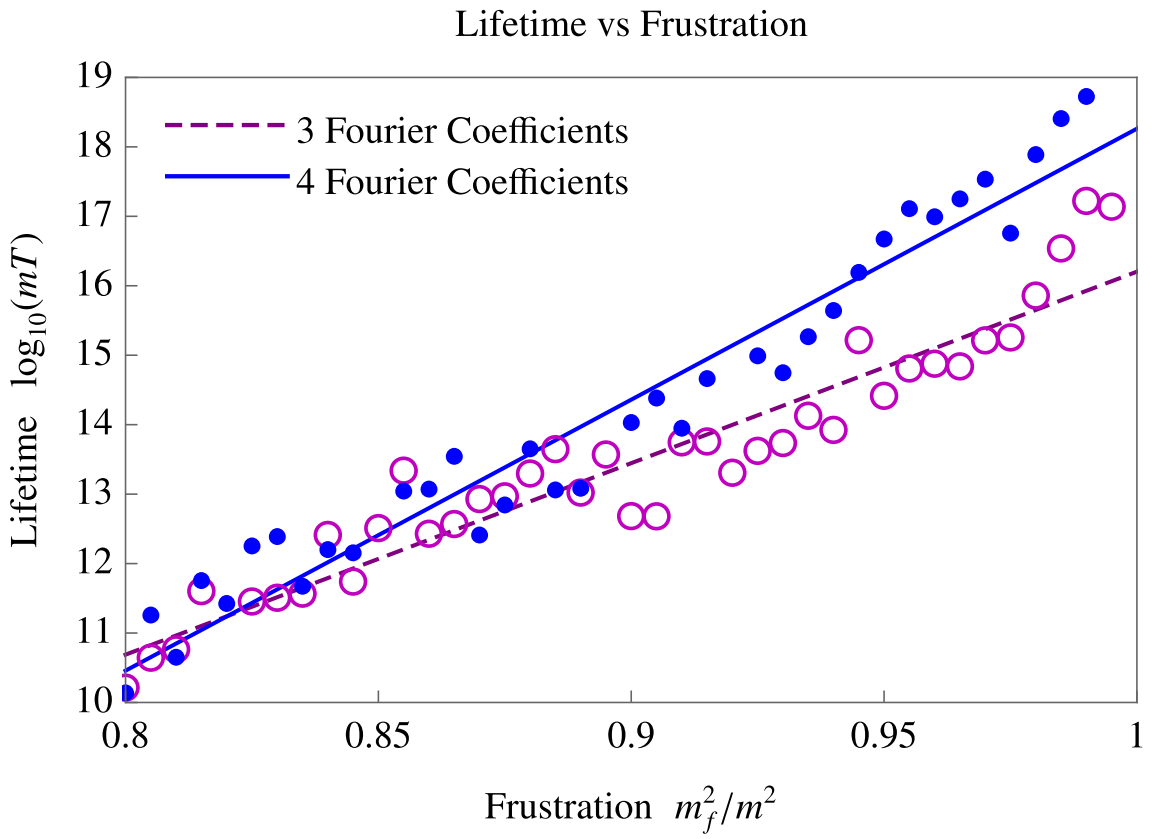

Figure 2.8: Lifetime versus frustration for oscillons in frustrated quadratic potentials, computed using three and four Fourier coefficients (see equation (2.42)). The lifetimes are integrated over the interval $\omega \in [0.8, 0.999]$ in the one-non-perturbative harmonic PQB formalism. We speculate that introducing more Fourier coefficients leads to longer-lived oscillons, since the frustration mass can be closer to m before self-interactions become repulsive, leading to enhanced geometric decoupling. The line of best fit for three coefficients (dashed purple) is $\log_{10}(mt) = 28(m_f/m)^2 - 11$, and the best fit with four coefficients (solid blue) is $\log_{10}(mT) = 39(m_f/m)^2 - 21$.

optimization problem:

$$\begin{aligned} \text{minimize} \quad & \max_{\phi\in[-b,b]} \left| V(\phi) - \frac{1}{2}m_f^2\phi^2 \right| , \\ \text{subject to} \quad & V''(\phi=0) = m^2 , \end{aligned} \tag{2.42}$$

where $0 < b < \pi$, and $0 < m_f < m$ is the frustrated mass. In other words, we are forcing the potential to have mass m at small ϕ, and a different, smaller mass m_f at larger ϕ. For frequencies ω close to m_f, the effective potential V_{eff} will consist of a series of hills and valleys inside the interval $S_1 \in [-b, b]$, whose amplitude is controlled by how tightly the objective (2.42) is optimized.

As local hilltops in such potentials rise above the zero-potential line, new oscillon solutions emerge. When the hilltop is precisely at the zero-line, this new solution is wholly unphysical, carrying infinite energy. As ω increases, this hilltop is pushed upwards, and $S_1(0)$ starts with more potential energy that needs to be dissipated through friction. As a consequence, $S_1(0)$ starts further from the hilltop so that it begins rolling earlier while the $2/r$ friction is still active, corresponding an oscillon with a smaller radius and less energy (see the inset of figure 2.7). Even though this branch may appear at very large ω close to m, this effect guarantees there is some finite range of frequencies over which the energy of these solutions decreases, meaning a physical oscillon can be supported.

In figure 2.8, we plot the lifetime of oscillons in frustrated quadratics as a function of the frustration m_f^2/m^2. The frustration mass m_f controls the frequency at which new hilltop solutions emerge. As m_f increases towards m, the appearance of these new branches occurs at larger frequencies, taking advantage of enhanced geometric decoupling and leading to longer lifetime. Increasing the number of Fourier coefficients in the potential reduces the height of the hilltops in the effective potential, allowing them to emerge at larger frequencies. Further, higher frequencies in the potential pushes the hilltops closer to $S_1 = 0$, allowing for lower-energy oscillons. We speculate that a fixed number of Fourier coefficients in the potential implies an upper bound on oscillon lifetimes, although we leave this question to future work.

2.4 Is longevity fine-tuned?

There are many known examples of potentials which support very long-lived oscillons, including those identified in section 2.3. However, the precise form of these potentials remains largely unconstrained by a UV theory, and therefore it is not clear how to assess whether their longevity is a result of fine-tuning, since the distribution from which the potential coefficients are sampled strongly influences the lifetime. Therefore, we introduce two notions of tuning that attempt to quantify the difficulty of constructing a theory with a long-lived oscillon:

1. *Global Tuning* asks what fraction of parameter space hosts long-lived oscillons. A typical object of study is the probability distribution of lifetimes, sampled with minimal priors over the potential coefficients in some natural basis.

2. *Local Tuning* asks whether a given long-lived oscillon is sensitive to variation in its potential parameters. The typical objects of study are the local gradient and curvature of the lifetime with respect to the parameter space at the point in question.

In sections 2.4.1 and 2.4.2, we address the genericity of long-lived oscillons in periodic potentials with parity. The advantage of studying periodic potentials is that they are naturally expanded in the Fourier basis. Without any theoretical priors, a natural scale for the Fourier coefficients is $m^2 f^2$, and variations will be of the same size.

One may also be interested in studying the genericity of long-lived oscillons in monodromy potentials [134–136]. Since an oscillon has a finite amplitude, one may restrict the aperiodic monodromy potentials to a compact interval, which is fully described by a Fourier expansion. However, any realistic model of axion monodromy is asymptotically a power law, meaning the high frequency modes of the potential are perfectly correlated. To sample the full space of monodromy potentials, one must sample from a distribution that imposes this correlation. In the absence of a reliable way to select coefficients from this distribution, we leave this question to future work. Instead, in section 2.5.1, we scan the one-parameter family of monodromy potentials studied in [1, 111, 118].

2.4.1 Global tuning

In this section, we study the distribution of oscillon lifetimes as a function of the potential coefficients in the Fourier basis. In particular, we will consider periodic potentials with parity

$$V(\theta) = m^2 f^2 \sum_{n=1}^{\infty} \frac{\mathcal{V}_n}{n^2} \left(1 - \cos n\theta\right) , \qquad \sum_{n=1}^{\infty} \mathcal{V}_n = 1 , \tag{2.43}$$

where the sum of the coefficients $\mathcal{V}_n$ constrains the mass of ϕ to be m. In Figure 2.9, we plot the lifetime versus the free variation of the first two coefficients $n = 1, 2$ with the third constrained so that the sum in (2.43) is satisfied, with all other $\mathcal{V}_n$ set to zero. The mass constraint in (2.43) naturally sets the typical scale of $\mathcal{V}_n$ to 1. Therefore, we restrict our study to $\mathcal{V}_n$ in the range $[-1, 1]$, inspired in part by the fact that the QCD axion potential has order 1 coefficients in this basis (see equation (2.49)).

Figures 2.9 and 2.10 provide illustrative examples of some important qualitative features of the distribution of oscillon lifetimes. First, we observe islands of longevity, seen in figure 2.9 as localized regions of exceptionally long lifetimes. In figure 2.10, this feature is manifested as plateaus in the distribution of lifetimes. We observe that each successive degree of freedom introduces a new longer-lived island of longevity which we observe to be exponentially more long-lived than the last. The probability of landing on one of these islands decreases with a scaling expected to be exponential in the number of degrees of freedom.

With these observations in mind, we introduce a notion of global tuning based on the cumulative

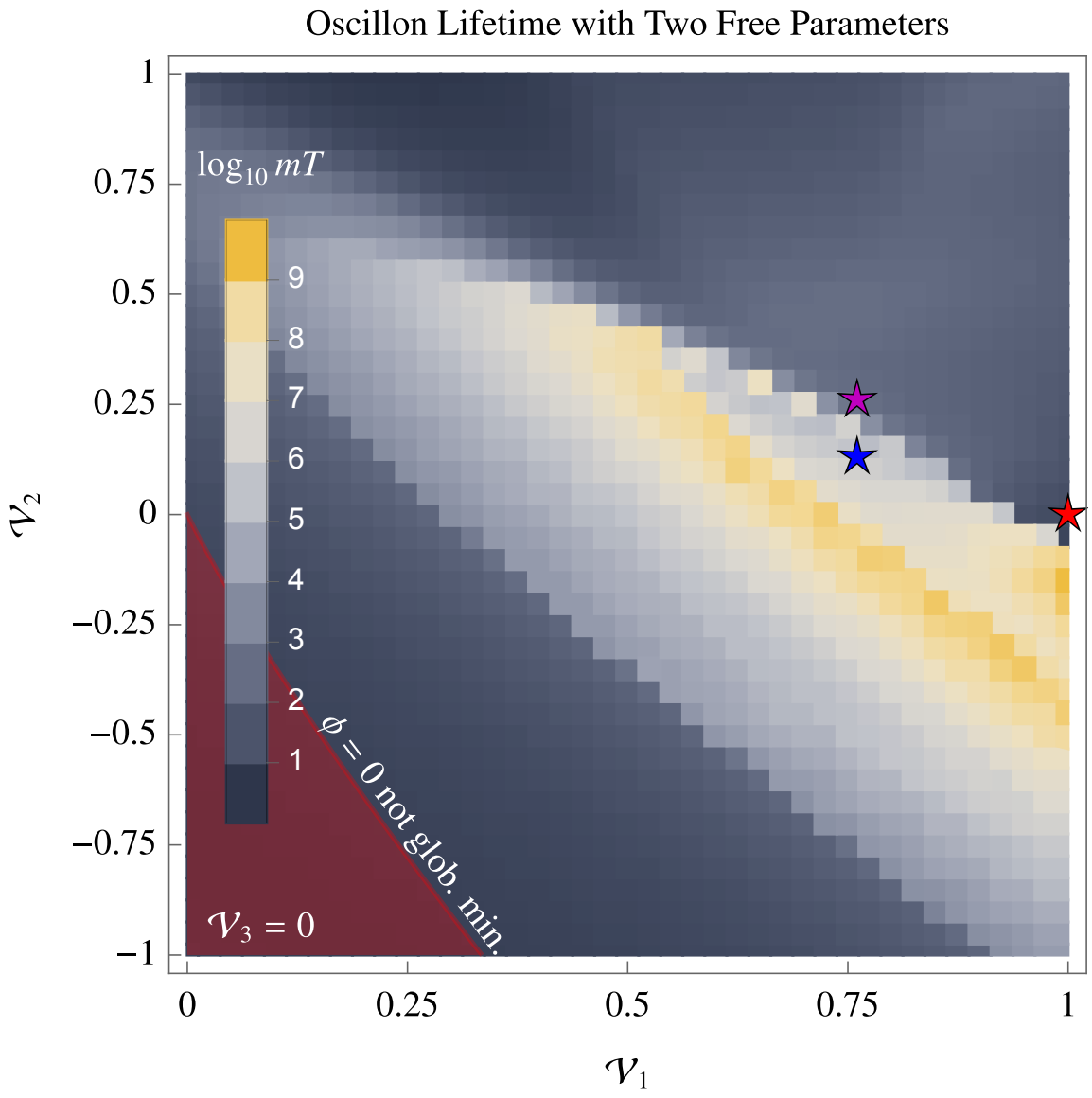

Figure 2.9: Accessible oscillon lifetimes in a periodic potential with two degrees of freedom $\mathcal{V}_1, \mathcal{V}_2$. Here $\mathcal{V}_3$ is constrained such that the mass is fixed to m, with all other $\mathcal{V}_{n\geq 4} = 0$. The red region indicates parts of the parameter space where $\phi = 0$ is not a global minimum of the potential, and has significantly shorter lifetimes. The stars indicate potentials for which we have compared our formalism with multiple non-perturbative harmonics to direct numerical simulation (see Figure 2.11). The peninsula of longevity corresponds to the emergence of a frequency at which the third harmonic experiences totally destructive interference at 'dips.' The yellow banding corresponds to the migration of dips to higher frequencies, where geometric decoupling suppresses the fifth harmonic, increasing the impact of the dip. At the upper right of these bands, the dip migrates to frequencies higher than that of energetic death, creating a longevity cliff.

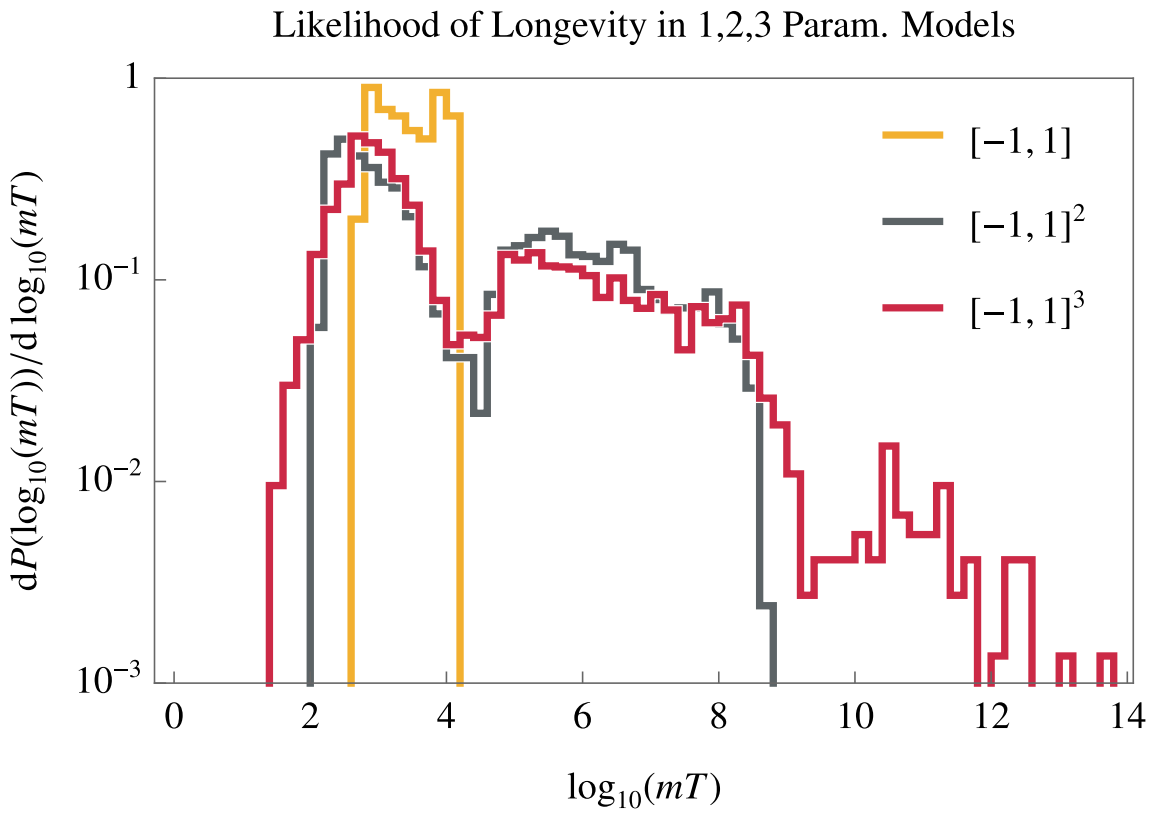

Figure 2.10: The distribution of oscillon lifetimes for 1 (yellow), 2 (gray), and 3 (red) degrees of freedom in a periodic potential. We uniformly sample the n_{DOF}-dimensional cube $\mathcal{V}_1, \ldots \mathcal{V}_{n_{\mathrm{DOF}}} \in [-1, 1]$ restricting the potential such that $\phi = 0$ is a global minimum, and $\mathcal{V}_{n_{\mathrm{DOF}}+1}$ is fixed such that the mass is m, with the remaining $\mathcal{V}_n$ set to 0. Lifetimes are computed in the interval $\omega/m \in [0.8, 0.995]$ in the single-non-perturbative-harmonic approximation. The geometric suppression of the radiative modes means that these frequencies likely dominate the oscillon lifetime, and that the perturbative radiation approximation is typically good. We see that each new degree of freedom is observed to introduce a new island of longevity (island 1 $\log_{10} mT \in [0, 4]$, island 2 $\log_{10} mT \in [4, 9]$, island 3 $\log_{10} mT \in [9, 14]$).

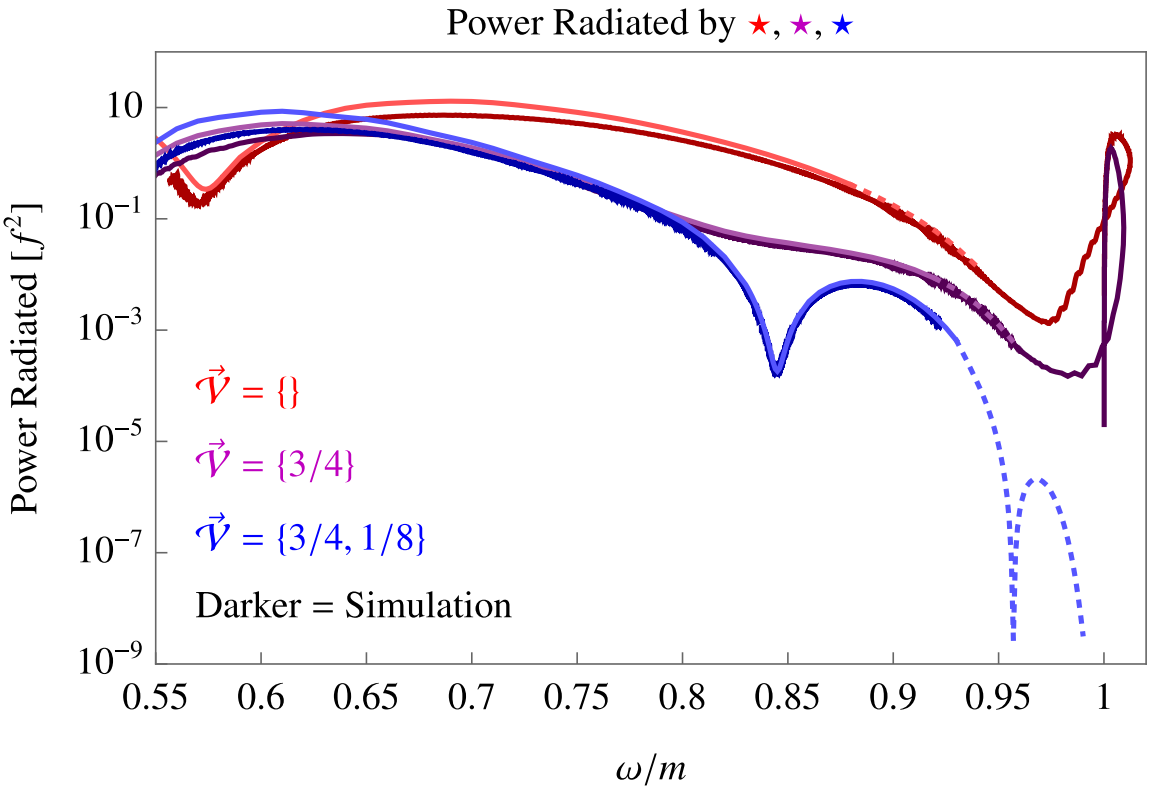

Figure 2.11: The power radiated by the oscillons in the potentials denoted by stars in figure 2.9. The dark curves are data from explicit numerical simulations (see appendix 4.5), while the lighter curves are computed in the PQB formalism. The PQB predictions become dotted in regions of linear instability, as computed using the methods described in appendix 4.3. Notice that at low frequencies, the oscillon power curves are of similar magnitude, diverging at larger frequencies due to geometric decoupling, as explained in section 2.2.1. The loops at the end of the simulations correspond to the oscillon rapidly converting into 3ω modes past the point of energetic death, causing the measured frequency at the origin to briefly grow larger than 1.

probability of finding an oscillon at least as long-lived. Therefore, smaller values of this probability mean more extreme outliers, and thus higher degrees of global tuning. For example, according to our PQB simulations, summarized by figure 2.10, an oscillon of lifetime $\log_{10} mT = 3$ is tuned to one part in 2 (or 50%). Oscillons of lifetime $\log_{10} mT = 7$ are tuned to one part in 8 (or 10%), and oscillons of lifetime $\log_{10} mT = 12$ are tuned to one part in 400 (or 0.2%). Finally, the longest lived potential we observe in our search lives roughly $\log_{10} mT = 14$, and its tuning is roughly one part in 3000, or 0.03%, although longer-lived oscillons may still reside further up the distributional tail.

2.4.2 Local tuning

As opposed to global tuning, which deals with the statistics over large volumes of parameter space, local tuning attempts to quantify the sensitivity of an oscillon's lifetime to variations in its potential coefficients. If we understand the lifetime mT as a function of the potential coefficients $\vec{\mathcal{V}} \equiv \{\mathcal{V}_1, \dots\}$, we can naturally introduce a local approximation of mT as a function of its gradient and curvature, writing $\vec{\mathcal{V}} = \vec{\mathcal{V}}_0 + \delta\vec{\mathcal{V}}$, and $mT(\vec{\mathcal{V}}_0) = mT_0$,

$$\begin{aligned} G_i = \frac{\partial \log_{10} mT}{\partial \mathcal{V}_i}\,, \qquad \mathbf{K}_{ij} = \frac{\partial^2 \log_{10} mT}{\partial \mathcal{V}_i \partial \mathcal{V}_j}\,, \\ \log_{10} mT = \log_{10} mT_0 + \vec{G}\cdot\delta\vec{\mathcal{V}} + \frac{1}{2}\delta\vec{\mathcal{V}}\cdot\mathbf{K}\cdot\delta\vec{\mathcal{V}}\,. \end{aligned} \tag{2.44}$$

In terms of this local approximation, we may quantify the sensitivity of the lifetime to local variations in $\vec{\mathcal{V}}$, as the minimum relative displacement of the potential coefficients $||\delta\vec{\mathcal{V}}||/||\vec{\mathcal{V}}_0||$ necessary to change the lifetime by an order of magnitude $\log_{10} mT_0 \pm 1$. In other words, our local tuning metric is the solution to the following constrained optimization problem,

$$\text{minimize } ||\delta\vec{\mathcal{V}}||/||\vec{\mathcal{V}}_0|| \text{ subject to } \left|\vec{G}\cdot\delta\vec{\mathcal{V}} + \frac{1}{2}\delta\vec{\mathcal{V}}\cdot\mathbf{K}\cdot\delta\vec{\mathcal{V}}\right| > 1\,. \tag{2.45}$$

We denote the minimal value $\nu \equiv ||\delta\vec{\mathcal{V}}||/||\vec{\mathcal{V}}_0||$.

Consider the potential $\vec{\mathcal{V}} = (1, 1/2, -1)$, for which an oscillon lives approximately $\log_{10} mT = 14$. Using the above measure of tuning, and a grid based approximation to the gradient and Hessian, we calculate $\nu \approx 0.03$. In other words, a 3% variation in the potential parameters corresponds to an order of magnitude change in the lifetime of the oscillon. This is substantially *less* tuned than one would expect from our global metric, in which this potential is 0.03% tuned. This is a reflection of the structure of the lifetime landscape, which contains islands of stability seen in figures 2.1a, 2.9 and 2.10.

2.5 Illustrative examples

Here we apply our framework to a series of potentials that have been studied extensively in previous literature, with the aim to reproduce and expand upon known results. The main goal is to show how our methods can accommodate a wide variety of potentials: both with or without parity, and with or without periodicity. We compare the results of our PQB framework to explicit numerical simulation. When simulating the equations of motion explicitly (as in appendix 4.5), the wall-clock time is at least proportional to the oscillon lifetime, which becomes computationally prohibitive for lifetimes beyond $10^{10}/m$. Our framework can bypass this scaling since time has been explicitly integrated out, allowing us to predict the existence of very long-lived oscillons, well in excess of the lifetimes we can simulate explicitly.

The results of this section are presented in the form of "power vs frequency" curves, which represent the instantaneous flux radiated by the oscillon at a particular fundamental frequency ω. The oscillon fundamental frequency ω monotonically increases with time, and can therefore be thought of as a time coordinate. For a detailed review of how to interpret these plots and their features, see figure 2.2.

2.5.1 Axion monodromy

Monodromy refers to the non-trivial winding of an axionic degree of freedom, which effectively endows the axion with an aperiodic potential at low energies [73, 134, 135]. In general, the resulting monodromy potentials share the property that they asymptote to a power law at large field values. A common family of potentials which interpolate between the asymptotic power-law and the small-field mass m is

$$V(\phi) = \frac{m^2 f^2}{p}\left(\left[\left(\frac{\phi}{f}\right)^2 + 1\right]^{p/2} - 1\right), \tag{2.46}$$

where p scans the asymptotic power-law. The potential (2.46) has been widely studied, and has been shown to support very long-lived oscillons, in excess of 10^{10} cycles [1, 111, 113, 118].

In figure 2.12, we summarize our study of the oscillon life-cycles as we scan p from -8 to -1. In general, we find good agreement with the results of [1]: the power versus frequency curves and lifetimes broadly match the predictions of [1] in the cases we have mutually studied $p = -8, -5, -4, -1$ although there are minor differences.

As p increases from -8 to -1, the lifetime of the corresponding oscillon increases dramatically, from 10^6 to 10^{10} cycles. This is due to the simultaneous action of the two longevity mechanisms identified in section 2.2. Specifically, the third harmonic experiences totally destructive interference at an exceptional frequency that is larger with increasing p. Therefore, as p grows, the third harmonic dip moves deeper into the frequencies where geometric decoupling dominates, which further

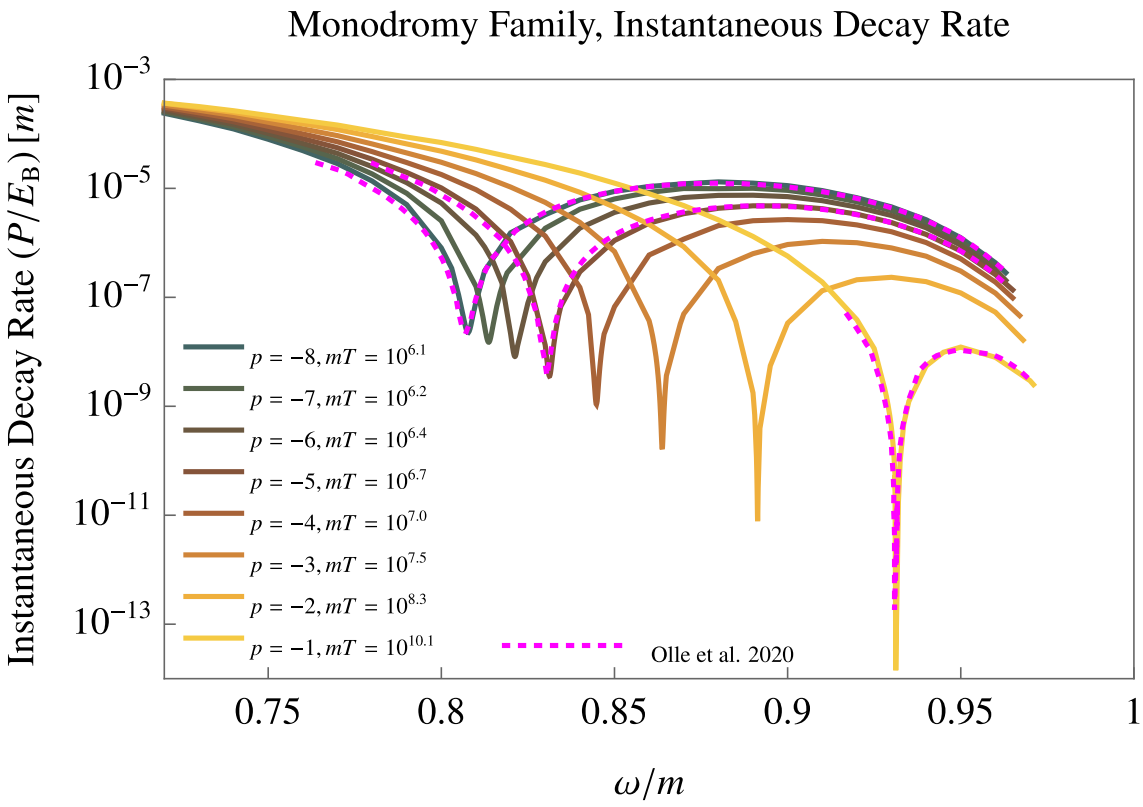

Figure 2.12: The instantaneous decay rate P/E_{B} of the oscillons in the monodromy potentials (2.46) for $p = -1, \ldots, -8$, calculated in the PQB formalism, versus the results of Olle et al. [1]. Here, the power P and bound energy E_{B} are computed as in section 2.1. As p scans from -8 to -1, the third harmonic dip migrates to larger frequencies where the fifth harmonic is further suppressed by geometric decoupling, leading to increased lifetime. To obtain the PQB results, we start with a two-non-perturbative harmonic approximation and used three non-perturbative harmonics to obtain better accuracy near the dips. At frequencies below the dip frequency, we see a small shift in the PQB formalism vs [1], which may arise from the need to use more non-perturbative harmonics at lower frequencies or because the Fourier series representation of (2.46) converges slowly.

suppresses the fifth harmonic.

A natural conjecture is that the oscillons of (2.46) are unusually long-lived because of the asymptotic power law in the potential. However, our results in figure 2.12 indicate that longevity is dominated by large frequencies, where field amplitudes are too small for the asymptotic behavior to take over. In particular, for $p = -1$, the field amplitude at the origin is roughly $\phi(0) \approx 1.5f$, far too small to be sensitive to the flatness of the potential at large ϕ/f. Therefore, we conjecture that it is *not* the asymptotic form, but the details of the connection between $\frac{1}{2}m^2\phi^2$ and ϕ^p that determine the oscillon lifetime.

In the oscillon literature, many examples of extremely long-lived oscillons are obtained with monodromy potentials. Thus, a natural question is whether all monodromy potentials share a common feature leading to longevity, or whether simple examples such as (2.46) happen to live in a tuned island of longevity. In the language we introduced in section 2.4.1, in order to quantify the link between monodromy and longevity we would need to know the probability distribution from which monodromy potentials are chosen. In the absence of this non-trivial construction, we are left with a case-by-case analysis of particular potentials, which, in this probabilistic view, may suffer from sampling bias.

2.5.2 ϕ^4 theory

ϕ^4 theory is the quintessential example of spontaneously broken parity symmetry. It is well known to host moderately long-lived oscillons, which have been studied in previous work [99,106,112,113,116]. Shifting to the broken vacuum and fixing the mass of $\phi = \theta/f$ to be m, we arrive at the following parity-violating potential

$$V(\theta) = m^2 f^2 \left(\frac{1}{2}\theta^2 - \frac{1}{2}\theta^3 + \frac{1}{8}\theta^4 \right) . \tag{2.47}$$

In order to properly compute the physical quasibreather in this potential, the first three harmonics C_0, S_1, C_2 must be treated non-perturbatively. As is evident from the numerical simulation (figure 2.13), the ϕ^4 physical quasibreathers are linearly unstable over the entire range of ω for which the oscillon is long lived. The instability that occurs at linear order in the PQB background is, however, stabilized by self-interaction, leading to quasiperiodic oscillations. These nonlinear oscillations are visible as dense curly-Q's in the Power vs Frequency plot (figure 2.13).

Our explicit numerical simulation yields an approximate lifetime of $6000/m$, which is close to the PQB prediction of $5900/m$. This confirms the earlier results in [99].

2.5.3 The QCD axion

The QCD axion is the best studied example of a scalar field described by a periodic potential, and could allow for oscillons with cosmological observables. At low temperatures, the QCD axion

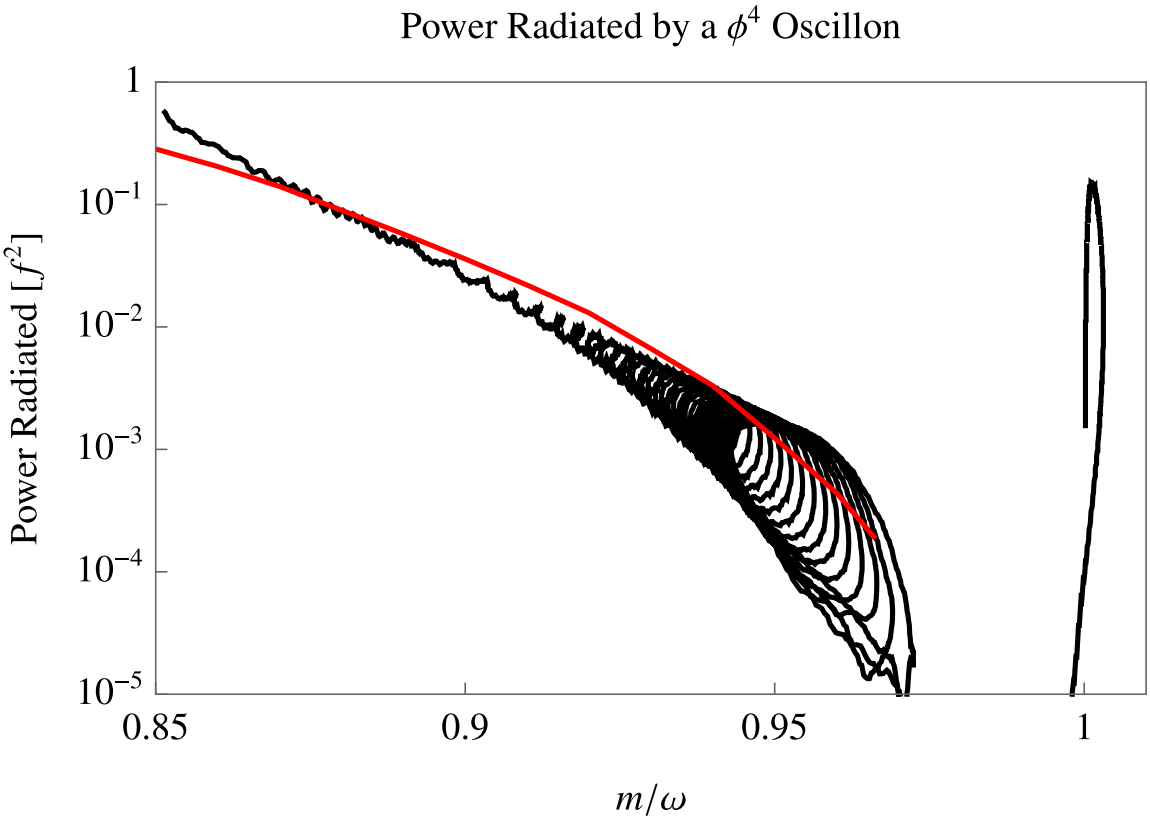

Figure 2.13: Comparison of the explicitly simulated ϕ^4 oscillon (black) with the physical quasi-breather trajectory (red) truncated to the leading three harmonics C_0, S_1, C_2 (in the notation of appendix 4.1), all treated non-perturbatively. The oscillating behavior is a symptom of linear instability, although crucially, it does not destroy the oscillon, since the size of the oscillations is controlled by nonlinearity. For technical details of the explicit simulation, see appendix 4.5.

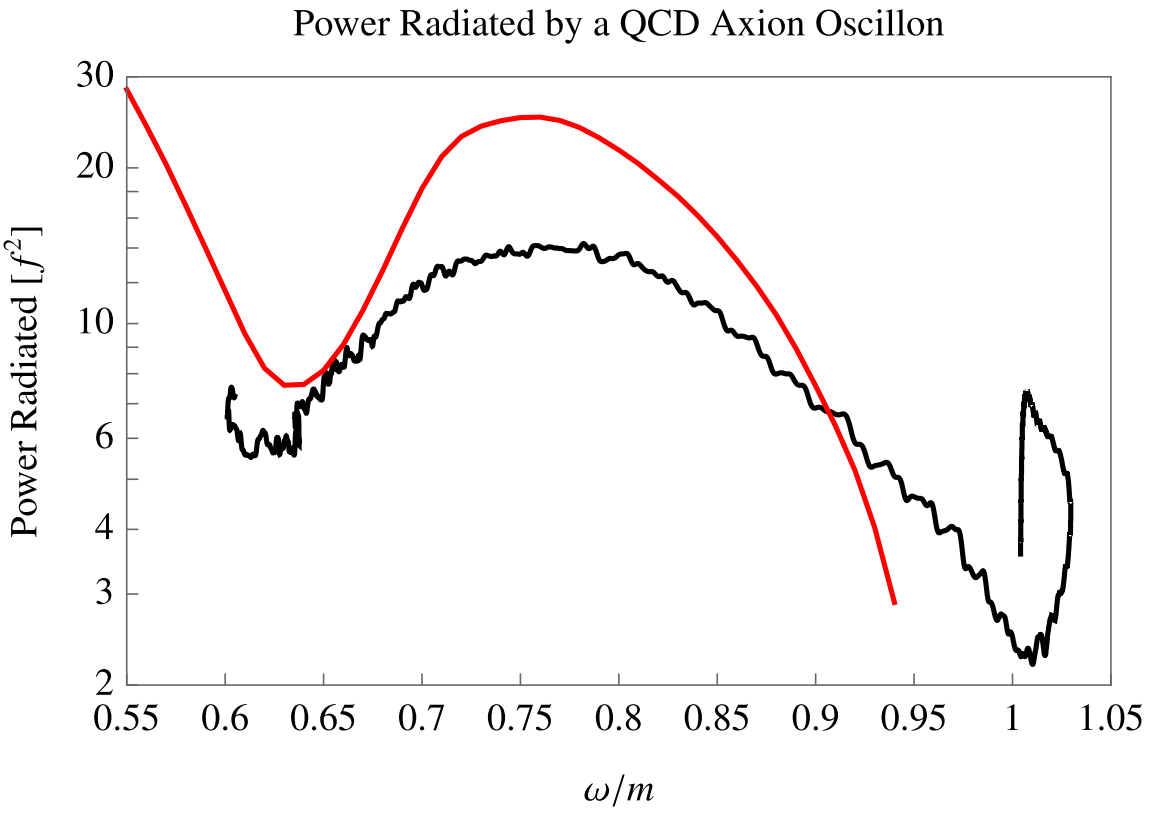

Figure 2.14: Comparison of the explicitly simulated QCD axion oscillon (black) to the PQB formalism (red) with three non-perturbative harmonics. The radiated power is so large that the orthogonal deformation is non-perturbative, leading to disagreement within a factor of a few, although the shape of the physical quasibreather curve still captures the qualitative features of the simulated oscillon. Namely, it shows that there is a dip around $\omega = 0.6m$ where the fifth harmonic is dominant. This region, in which the third harmonic is confined and non-perturbatively large, constitutes most of the oscillon's lifetime.

potential is dominated by strong dynamics, giving rise to the potential [80, 98],

$$V(\phi) = -m_\pi^2 f_\pi^2 \sqrt{1 - \frac{4 m_u m_d}{(m_u + m_d)^2} \sin^2\left(\frac{\phi}{2f}\right)}\,. \tag{2.48}$$

A simple Taylor expansion about $\theta = 0$ reveals that (2.48) has a smaller quartic term than the simple cosine potential, which leads us to expect the oscillons in (2.48) to be shorter-lived than the sine-Gordon oscillon. Indeed, this expectation is confirmed by the physical quasibreather framework and explicit numerical simulation (see figure 2.14 and appendix 4.5).

In order to compute the lifetime in the physical quasibreather formalism, we calculate the potential's Fourier coefficients

$$\vec{\mathcal{V}} = \{1.427, -0.648, 0.336, \dots\} \tag{2.49}$$

Our formalism can accommodate many non-zero Fourier coefficients, although only the first three (and a fourth to normalize the mass) are necessary to converge within 1% of the true potential; adding more terms has a negligible impact on the results of explicit simulation and on the result of our PQB formalism.

The result of this analysis is that the QCD axion oscillon is relatively short-lived compared to the average oscillon, living about $400/m$. However, it is interesting to observe that this oscillon spends most of its life with a confined third harmonic, undergoing very large central-amplitude oscillations of order $15f$. Although the short lifespan of the QCD axion oscillon means that it will only leave its cosmological imprint shortly after formation, the large amplitude and violent deaths of these oscillons may have observational implications.

2.6 Conclusion

Real scalar fields play a central role in many theories of early universe cosmology and dark matter. Many of these theories predict attractive self-interactions that allow the scalars to form quasistable oscillons. Understanding oscillon lifetime is necessary for determining whether oscillons only play a role in early universe cosmology, or whether they may also survive until the present day and lead to dramatic astrophysical signatures.

In this work, we have expanded the quasibreather approximation into a formalism for computing the properties of oscillons that naturally incorporates realistic boundary conditions. We defined the physical quasibreather by finding initial conditions of the nonlinear wave equation that simultaneously obey radiative boundary conditions *and* specify a quasibreather solution. As the closest quasibreather to a physical oscillon, the PQB provides a raw approximation for the oscillon profile (see e.g. figure 2.4) which is increasingly accurate in the limit of long lifetimes. Furthermore,

the PQB represents the solutions to which the oscillon is instantaneously and locally attracted to during its evolution. When understood as a stable perturbation to a PQB, the oscillon borrows its properties from its PQB partner, including its radial profile and radiation rate [3]. When the PQB becomes linearly unstable, nonlinear quasiperiodic oscillations emerge, whose size is controlled by higher-order terms, as depicted in figures 2.13, 4.4a, and 4.4b. In other words, linear instability often does not result in the death of the oscillon. Further, we have demonstrated that the PQB and the minimum radiation quasibreather differ at 6th order in the background, explaining the success of the 'minimum radiation quasibreather ansatz.'

Since the PQB offers an accurate description of the oscillon structure, we have used it to understand the oscillon's form-factor and the resulting mechanisms which control longevity. Specifically, as the oscillon radiates its energy away, its central amplitude decreases, causing self-interactions to become weaker; as a result, the oscillon becomes much larger than the radiation wavelengths, suppressing the radiated power (see figure 2.2). At these high frequencies ($\omega \to m$), the large oscillon core naturally leads to the rapid self-interference of radiation. When the self-interference is destructive, the total radiation is suppressed by another power of the form-factor. While both these effects, geometric decoupling and destructive interference, are generic features of oscillon evolution, the longest-lived oscillons are a consequence of these two effects occurring simultaneously at large oscillon frequencies close to m (as in figure 2.12). Finally, we have understood the physics of oscillon death as a further consequence of weak self-interaction: past a certain critical frequency the energy of the PQB is forced to increase, and the oscillon cannot sustain its proximity to its PQB partner. Using our understanding of the mechanisms responsible for oscillon longevity and death, we have constructed the family of *frustrated quadratic* potentials which support extremely long-lived oscillons, living more than 10^{18} cycles (see section 2.3).

There are several computational advantages provided by our methodology. First, the oscillon evolution is computed in a time-independent way, separating the physical lifetime of the oscillon from the computational wall-clock time it takes to evolve numerically. Second, our formalism naturally incorporates non-perturbative harmonics, and potentials without even parity. Third, all perturbative harmonics may be efficiently computed by taking advantage of sparse linear algebra. Fourth, we have introduced the Fourier basis as the natural basis for expanding potentials when studying oscillons. In this basis, the form of the mode equations is especially simple, allowing us to write down analytical expansions for the mode potentials that converge everywhere. Fifth, our formalism provides a natural language for studying the stability of oscillons. Finally, the speed of our numerical techniques has enabled us to study extremely long-lived oscillons, and has yielded the first prediction of cosmologically long lived periodic potentials (see figure 2.8).

Using our efficient numerical techniques, we scan over degrees of freedom in axionic potentials (see figures 2.1a and 2.9), allowing us to probe the genericity of long-lived oscillons (see figure 2.10).

[3] Although, see appendix 4.1 for a full explanation of the sense in which the oscillon is a stable perturbation of a PQB

Important outcomes of this parameter scan include the identification of features in the lifetime landscape with the mechanisms of longevity (see section 2.2), and the realization that extremal lifetimes may scale at least exponentially in the number of potential degrees of freedom. At the same time, long lifetimes are not particularly fine-tuned, since as few as three degrees of freedom are enough to generate oscillons that survive until last-scattering (4×10^6 cycles) with only 15% global tuning (as defined in section 2.4.1), and oscillons that live until today (10^{11} cycles) with 0.5% global tuning.

2.7 Acknowledgments

We thank Savas Dimopoulos, Asimina Arvanitaki, Sebastian Baum, Robert Lasenby, Horng-Sheng Chia, Anirudh Prabhu, and Dmitriy Zhigunov for stimulating conversations and helpful comments on the manuscript. D.C. is grateful for the support of the National Science Foundation under grant number PHY-1720397, and for the support of the SITP. T.G.T. is grateful for the support of the Department of Energy under grant number DE-SC0020266. Some of the computing for this project was performed on the Sherlock and Farmshare clusters. We would like to thank Stanford University and the Stanford Research Computing Center for providing computational resources and support that contributed to these research results.

Chapter 3

Friendship in the Axiverse

Among the best-motivated extensions of the Standard Model (SM) are *axions*, periodic pseudoscalar fields with an approximate shift symmetry that protects their mass from radiative corrections.[1] The most well-known example is the *QCD axion*, which was originally proposed as a solution to the puzzling smallness of the neutron's electric dipole moment [137–140]. This is not the only type of axion that can exist though: axions can be quite generic in UV completions of the SM with compact extra dimensions and nontrivial topologies, the principle example of which is string theory [141–143]. The combined motivation of the QCD axion and string theory lead to predictions of a plenitude of string axions with mass scales spanning many orders of magnitude, a possibility referred to as the *String Axiverse* [73].

A light axion ϕ with potential $V(\phi)$ has a natural production mechanism known as the *misalignment mechanism* [144–147], whereby the axion field is effectively initialized at some finite displacement from the minimum of its potential, and undergoes subsequent classical evolution.[2] These potentials are generally expected to be periodic and at leading order are often well-approximated by a cosine:

$$V(\phi) = m^2 f^2 \left(1 - \cos\left(\frac{\phi}{f}\right)\right) . \tag{3.1}$$

Here f is the axion's *decay constant*, which is expected to suppress all couplings of the axion field to the SM [155–157]. The periodicity of the axion potential provides a natural measure on the space of initial conditions. In the absence of any dynamic [81,158–163] or anthropic [164,165] considerations,

[1] The term "axion-like particles" is also used in the literature.

[2] In the sub-eV axion mass range we consider, and because the axion is a bosonic particle, phase-space occupation numbers are very large and the cosmological axion field can be described by solving the classical equations of motion of a condensate [148–151]. This is the mean-field approximation in which one replaces the quantum field operator $\hat{\phi}$ by its central value (i.e. $\hat{\phi} \to \langle\hat{\phi}\rangle \equiv \phi$) in the Heisenberg equations of motion, resulting in the classical field equations. As stressed in [150], one does the same thing when using Maxwell's equations to describe the electromagnetic field as the collective behavior of a large number of photons, and indeed the mean-field approximation constitutes the standard treatment in scalar field models of inflation and dark matter (see for example [148–154] and the many references therein).

a reasonable expectation is that the initial condition ϕ_0 is drawn effectively randomly from the interval $[-\pi f, \pi f)$. Defining $\Theta_0 \equiv \phi_0/f$ we can then compute the present-day energy density in the axion field, yielding:

$$\Omega_{\rm ax} \approx 0.4 \left(\frac{\Theta_0}{\pi/2}\right)^2 \left(\frac{m}{10^{-17}\ {\rm eV}}\right)^{1/2} \left(\frac{f}{10^{16}\ {\rm GeV}}\right)^2 , \tag{3.2}$$

which receives corrections as $|\Theta_0|$ gets very close to π [59, 166–171]. At these large misalignments, self-interactions from the cosine potential can play a significant role in the field's evolution at early times, leading in extreme cases to exponential growth of spatial perturbations and a plethora of associated signatures [59, 166–171].

The above discussion of the misalignment mechanism applies to the case of a single axion uncoupled from all other particles in the spectrum. However the generic prediction of the axiverse is actually many axions, spanning orders of magnitude in both mass m and decay constant f. A more realistic picture of the axiverse is then a sector consisting of N pseudoscalar fields that pick up nonperturbative contributions to their collective potential from M instantons. We typically expect $M \gg N$ [172], so no axion is expected to be massless. This results in a generic potential of the form:

$$V(\phi_1, \ldots, \phi_N) = \sum_{i=1}^{M} \Lambda_i^4 \left[1 - \cos\left(\sum_{j=1}^{N} \mathcal{Q}_{ij} \frac{\phi_j}{f_j} + \delta_i\right)\right] , \tag{3.3}$$

where δ_i are arbitrary constant phases, f_i are the various decay constants, and $\mathcal{Q}_{ij}$ are rational numbers associated with the axion charges under each instanton [172–178]. The energy scales Λ_i are typically exponentially suppressed relative to the UV string scale $\Lambda_{\rm str}$ by instanton actions S_i: $\Lambda_i \sim \Lambda_{\rm str} e^{-\lambda S_i}$ where λ is an $\mathcal{O}(1)$ coupling constant.

In the absence of strong priors on the instanton actions, the axions are expected to have an approximately log-flat distribution in mass [73], an expectation that has been confirmed in specific orientifold compactifications of type IIB string theory [172, 179]. The range of axion masses can easily span several dozen orders of magnitude, from smaller than the current Hubble rate H_0 to order $M_{\rm Pl}$. The decay constants, meanwhile, are typically more narrowly distributed but can still range over a few orders of magnitude $f \sim 10^{12} - 10^{19}$ GeV [73, 172, 180]. The number of axions in these compactifications is proportional to the Hodge number of the orientifold and thus can easily be $\mathcal{O}(100s)$, making "coincidences" in axion mass a common occurrence: $\mathcal{O}(100)$ axions distributed log-flat over $\mathcal{O}(60)$ orders of magnitude in mass imply that each axion is on average only a factor of a few away from an axion with a similar mass. By chance some pairs of axions will be even closer, and as we will show, these coincident pairs can be significantly more visible than other axions in the axiverse.

For concreteness, in this paper we consider a sector consisting of two axions receiving two instanton contributions to their potential:

$$V(\phi_L, \phi_S) = \Lambda_1^4 \left(1 - \cos\left(\frac{\phi_S}{f_S} + \frac{\phi_L}{f_L}\right)\right) + \Lambda_2^4 \left(1 - \cos\frac{\phi_L}{f_L}\right) , \tag{3.4}$$

where we will focus on the case where the axion masses are within a factor of $\mathcal{O}(2)$ from each other but the decay constants are not necessarily close. This potential can be shown in a nicer form by transforming to angular variables $\theta_S \equiv \frac{\phi_S}{f_S}$ and $\theta_L \equiv \frac{\phi_L}{f_L}$ and then writing the instanton scales as $\Lambda_1^4 \equiv m^2 f^2$, $\Lambda_2^4 \equiv \mu^2 \mathcal{F}^2 m^2 f^2$, yielding

$$V(\theta_L, \theta_S) = m^2 f^2 \left[(1 - \cos(\theta_S + \theta_L)) + \mu^2 \mathcal{F}^2 (1 - \cos\theta_L)\right] . \tag{3.5}$$

Letting $f \equiv f_S$ and $\mathcal{F} \equiv \frac{f_L}{f_S}$, the mass of ϕ_S is $m_S \equiv m$, and that of ϕ_L is $m_L \equiv \mu m$. We will focus on the case where the parameters are in the range $0.75 \lesssim \mu < 1$ and $\mathcal{F} \gg 1$. We term such a similar-mass pair "friendly" and will refer to ϕ_L and ϕ_S as the "long" and "short" axion respectively in reference to the size of their decay constants. We note that ϕ_L and ϕ_S are not exact mass eigenstates, but as discussed in App. 4.6 they are very nearly mass eigenstates when $\mathcal{F} \gg 1$. We will thus neglect this subtlety for the current qualitative discussion but correctly account for it in the main text below.

In the absence of the axion interactions, Eq. 3.2 would suggest that for similar masses and $\mathcal{O}(1)$ misalignments, the long axion will always dominate the late-time energy density of the pair because of its larger decay constant. This is true for $\mu \lesssim 0.75$, but when the axion masses get within roughly 25% of each other, a new effect occurs and can result in highly efficient energy transfer from the long axion to the short axion. We identify this new phenomenon as an instance of *autoresonance*, a well-known effect in the mechanics of classical oscillators which has found broad applications across the nonlinear sciences.[3]

Near the bottom of the potential, both axions oscillate with a frequency approximately given by their mass: the long axion at μm and the short axion at m. However, because the short axion has a nonlinear potential, its oscillation frequency receives corrections depending on its amplitude. At $\mathcal{O}(1)$ amplitudes (such as those that may be expected from a random initial misalignment angle), its oscillation frequency can become so detuned from m that it lines up instead with μm. At this point the small interaction with the long axion can resonantly drive the short axion and hold it at this fixed amplitude, effectively counteracting the damping effects of Hubble friction. Locking onto this autoresonance is not a guaranteed process and does depend on the initial misalignment angles,

[3]Autoresonance in nonlinear systems is a fascinating topic in its own right. Although the concept can be traced to the first sychrotron accelerators [181–183], it has of late received little attention in the high-energy theory community. First principles treatments are in [184–187]. Refs. [188, 189] review modern scientific applications. Specific applications exist for atomic and molecular systems [190, 191], rigid rotators [190], plasmas [192–195], Bose-Einstein condensates [196], planetary systems [188], and control theory and sensing [197–201].

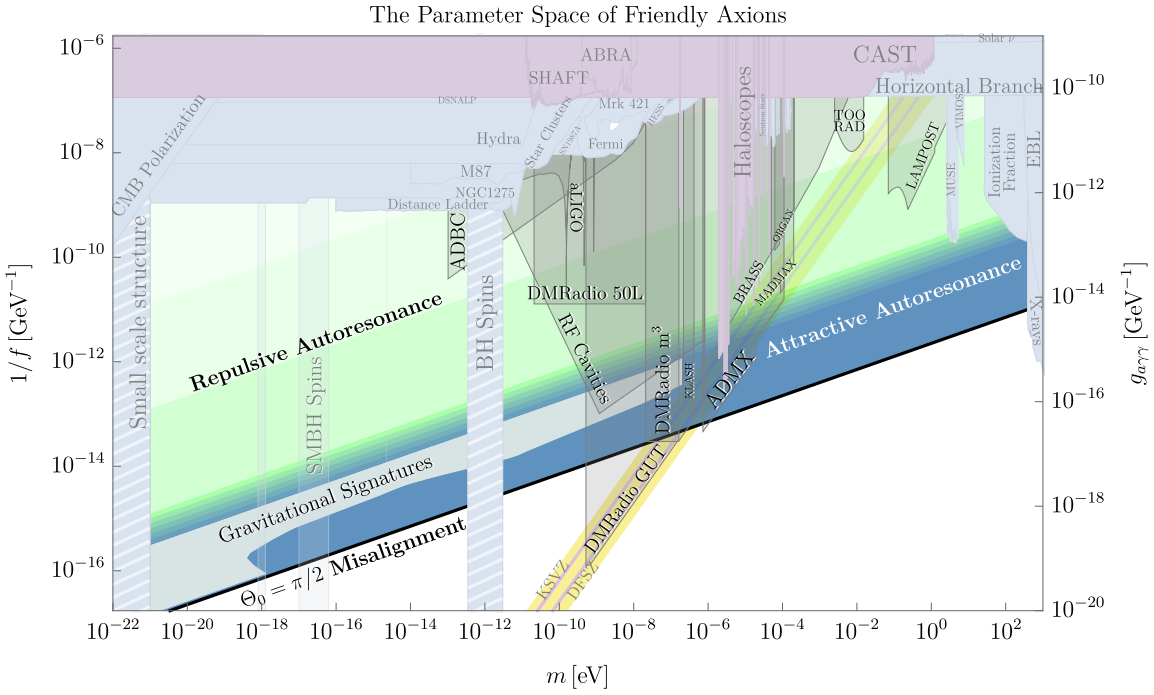

Figure 3.1: Summary of parameter space, constraints, and signatures for a pair of friendly axions undergoing autoresonance. The lower black solid line ("$\Theta_0 = \pi/2$ Misalignment") corresponds to the decay constant that produces the correct relic abundance for an initial misalignment angle of $\pi/2$ with the simple cosine potential of Eq. 3.1. Autoresonance allows an axion whose parameters lie near this line (i.e. an axion that would produce the proper DM abundance in the absence of interactions via misalignment) to efficiently transfer its energy to an axion with a much smaller decay constant. The blue region ("Attractive Autoresonance") labels the parameter space accessible to the simple model of Eq. 3.5. For even smaller values of f, nonperturbative structure growth quenches the autoresonant energy transfer in this simple model (see Sec. 3.2), but axion DM with these parameters can still be generated for slightly more complicated axion potentials that include repulsive self-interactions to prevent structure growth (Sec. 3.4). These regions of parameter space are labeled "Repulsive Autoresonance." We also show constraints and projections for various experimental efforts to detect axions and axion DM through the axion-photon coupling $g_{a\gamma\gamma}$ [2–9, 9, 10, 10–16, 16–58], where we have assumed $g_{a\gamma\gamma} \simeq \frac{\alpha}{4\pi f}$. In the friendly scenario, axion DM can be produced with untuned initial misalignment angles and with much stronger couplings to the SM than would be expected based on the decay constant predicted by Eq. 3.2. We note that these direct detection signatures persist even when the friendly axions make up only a subcomponent of DM (Sec. 3.3.1). The region labeled "Gravitational Signatures" can be probed using DM substructures generated during autoresonance (Sec. 3.3.2). The horizontal axis of this plot refers to the overall mass scale of the two axions (i.e. the parameter m in our potential Eq. 3.5), while the precise axion masses in the mass basis have additional small dependence on the parameters μ and $\mathcal{F}$. As explained in Sec. 3.3.3, the exclusions from black hole spin measurements extend to arbitrarily small values of f only when viewed as constraints on the specific scenario of the pair of axions being $\mathcal{O}(1)$ of dark matter.

but once it has been established it is extremely stable and persists until nearly all energy has been transferred out of the long axion and into the short axion. This is by no means a tuned occurrence: As a representative example, for $\mu \sim 0.8$ and $\mathcal{F} \sim 20$, roughly half of the possible combinations of initial misalignment angles result in autoresonance, leading to the late-time energy density of the sector being dominated by the short axion.

The signatures of a period of autoresonance are quite dramatic. Axion couplings to the SM are generically suppressed by their decay constant, for example they are expected to have couplings to the photon of the form [155–157, 202–205]:

$$\mathcal{L} \supset -\frac{g_{a\gamma\gamma}}{4}\phi F_{\mu\nu}\tilde{F}^{\mu\nu}\,, \tag{3.6}$$

where $g_{a\gamma\gamma} \sim \frac{\alpha}{4\pi f}$ with $\alpha \equiv \frac{e^2}{4\pi}$ the QED fine structure constant. The short axion (with the smaller decay constant) is thus typically coupled more strongly to the SM than the long axion. Autoresonance efficiently transfers an axion sector's energy density into a form more easily probed experimentally. As we summarize in Fig. 3.1, much of the short axion parameter space will be probed with existing and upcoming experiments. We emphasize that this enhancement can be observable regardless of whether the friendly pair in question comprises the totality of the DM or only a subcomponent.

In addition, a long period of autoresonance means that the short axion spends a long time under the influence of its nonlinearities. As shown in Ref. [59] in the context of a single axion model, this can lead to a parametric resonant enhancement in the growth of spatial inhomogeneities of the axion field. If the axion makes up all of the DM, such inhomogeneities eventually collapse into gravitationally-bound dark matter minihalos that can be probed purely through their gravitational effects. For simple axion potentials such as Eq. 3.1, Ref. [59] found that this required initial misalignments of the order $|\Theta_0 - \pi| \lesssim 10^{-5}$. Such a tuning can be motivated by anthropics or dynamical mechanisms [162, 163], and in broader classes of axion potentials it can be avoided entirely [59], but similar minihalo phenomenology and signatures can also be reproduced by a friendly autoresonating pair of axions with untuned initial conditions provided the friendly pair comprises the entirety of the DM.

The structure of the rest of this paper is as follows: In Sec. 3.1 we outline the dynamics of autoresonance for the spatially homogeneous components of the axion fields in greater detail. In Sec. 3.2 we extend our analysis to inhomogeneities in both fields and show that those in the short axion grow due to a parametric resonance instability. In extreme cases, inhomogeneities can grow nonperturbatively large during autoresonance, quenching the transfer of energy between the axions. We then move to discussing signatures of autoresonance in Sec. 3.3, going over both the significant effects on direct detection parameter space and the astrophysical and cosmological probes of dense minihalos. In Sec. 3.4 we broaden our scope somewhat to potentials with repulsive self-interactions, which do not lead to structure growth but can still support autoresonance. Finally, in Sec. 3.5 we summarize the results of this paper and discuss its implications and future directions.

To streamline the presentation we have placed several useful results and derivations in the appendices. In App. 4.6 we discuss the difference between the mass and interaction bases for the coupled axion system and show that it has only marginal effects on our analysis. In App. 4.7 we give a lengthier analytic treatment of autoresonance for a pair of friendly axions, and we do the same for aspects of perturbative structure growth in App. 4.8. App. 4.9 concludes with a detailed description and discussion of the numerical simulations used to study the case of nonperturbative structure growth.

Throughout this paper we work in units where $\hbar = c = 1$, and we use the reduced Planck mass $M_{\rm Pl} \equiv (G/8\pi)^{-1/2} \approx 2.4 \times 10^{18}$ GeV. We use the Planck 2018 results [206] for our cosmological parameters, taking the dark matter fraction of the universe to be $\Omega_{\rm DM} = 0.23$, the scale factor at matter radiation equality $a_{\rm eq} = 1/3388$, the present-day Hubble parameter $H_0 = 67.66$(km/s)/Mpc, and the Hubble parameter at matter-radiation equality $H_{\rm eq} = 2.2 \times 10^{-28}$eV. We work with a mostly negative metric signature $(+,-,-,-)$.

3.1 Friendly zero-mode dynamics

At energies well below its instanton scale, an axion in an expanding universe is well-approximated by a damped harmonic oscillator. Its amplitude decays because of Hubble friction as $a^{-3/2}$, while its energy density falls as a^{-3}. The dynamics of our model (Eq. 3.5) differ from this simple picture in two important ways. First, at early times, the axion field has enough energy that attractive self-interactions of the cosine potential are important, and each axion behaves as a damped *nonlinear* oscillator, with oscillation frequency that is *smaller* than its rest mass. Second, the axions are coupled to one another, allowing energy to flow between them. These two facts lead to the possibility of *autoresonance*, wherein a driven axion may dynamically adjust its frequency to match that of a driver axion. During autoresonance, the driven axion can receive most of the driver's energy, leading to new late time signatures.

We begin by taking appropriate limits of the two-axion model (Eq. 3.5) to reduce to the equation for a single driven pendulum, which exhibits the same essential behavior. The equations of motion for the axions θ_S and θ_L specified by the potential Eq. 3.5 in an FLRW background are

$$\frac{\Box}{m^2}\theta_L + \frac{1}{\mathcal{F}^2}\sin(\theta_S + \theta_L) + \mu^2 \sin\theta_L = 0\,, \tag{3.7a}$$

$$\frac{\Box}{m^2}\theta_S + \sin(\theta_S + \theta_L) = 0\,, \tag{3.7b}$$

where $\Box \equiv \partial_t^2 + 3H\partial_t - \frac{\boldsymbol{\nabla}^2}{a^2}$ for a scalar field in FLRW and $H = \frac{1}{2t}$ during radiation domination. In this section we are focused on the homogeneous component of both fields, so we will neglect the spatial derivatives and denote the homogeneous components of the fields by Θ_S and Θ_L. In addition,

we will measure time in units of m^{-1}, allowing us to write these in a simpler form:

$$\partial_t^2\Theta_L + \frac{3}{2t}\partial_t\Theta_L + \frac{1}{\mathcal{F}^2}\sin(\Theta_S+\Theta_L) + \mu^2\sin\Theta_L = 0\,, \tag{3.8a}$$

$$\partial_t^2\Theta_S + \frac{3}{2t}\partial_t\Theta_S + \sin(\Theta_S+\Theta_L) = 0\,. \tag{3.8b}$$

In the large-$\mathcal{F}$ limit, the equation of motion for Θ_L decouples from Θ_S, causing the Θ_L field to behave as an independent nonlinear oscillator subject only to Hubble friction. The solution to such an equation for an $\mathcal{O}(1)$ initial misalignment $\Theta_{L,0}$ and $t \gg 1$ is well-known: $\Theta_L(t) \propto \Theta_{L,0}t^{-3/4}\cos(\mu t)$, and at late times this becomes small. If we expand the Θ_S equation of motion in small Θ_L we obtain:

$$\partial_t^2\Theta_S + \frac{3}{2t}\partial_t\Theta_S + \sin\Theta_S \approx -\Theta_L\cos\Theta_S\,. \tag{3.9}$$

Provided the amplitude of Θ_S is not too large, $\cos\Theta_S$ will be reasonably close to 1, and we can approximate[4]

$$\partial_t^2\Theta_S + \frac{3}{2t}\partial_t\Theta_S + \Theta_S - \frac{1}{6}\Theta_S^3 \approx -\Theta_L\,, \tag{3.10}$$

which is the equation of motion for a damped, driven pendulum in the small amplitude limit, formally known as a Duffing oscillator.

We first consider the left hand side of Eq. 3.10 in isolation and in the absence of damping,

$$\partial_t^2\Theta_S + \Theta_S - \frac{1}{6}\Theta_S^3 = 0\,. \tag{3.11}$$

With an oscillatory ansatz $\Theta_S(t) \approx \sigma_S\cos(\omega t+\delta)$, we find that, due to the attractive self-interactions, the oscillation frequency ω of the pendulum is a decreasing function of its amplitude σ_S:

$$\omega(\sigma_S) \approx 1 - \frac{\sigma_S^2}{16} + \mathcal{O}(\sigma_S^4). \tag{3.12}$$

This fact is key to autoresonance. Because of this effect, the range of frequencies below the fundamental frequency 1 is now accessible to possible resonances. As we will see below, by driving the pendulum at a frequency μ below the fundamental, the system can automatically evolve to a new equilibrium amplitude at which $\omega(\sigma_S) \approx \mu$.

We now move to the next stage of complexity by re-introducing constant damping and driving terms,

$$\partial_t^2\Theta_S + \gamma\partial_t\Theta_S + \Theta_S - \frac{1}{6}\Theta_S^3 = \sigma_d\cos(\mu t)\,, \tag{3.13}$$

where γ and σ_d are the damping and driving coefficients respectively. The long-term effect of the

[4]This formally corresponds to the limit $\Theta_S \gg (1/6)\Theta_S^3 \gg (1/2)\Theta_S^2\Theta_L$. In practice, this approximation appears to work quite well even when the hierarchy is not very large.

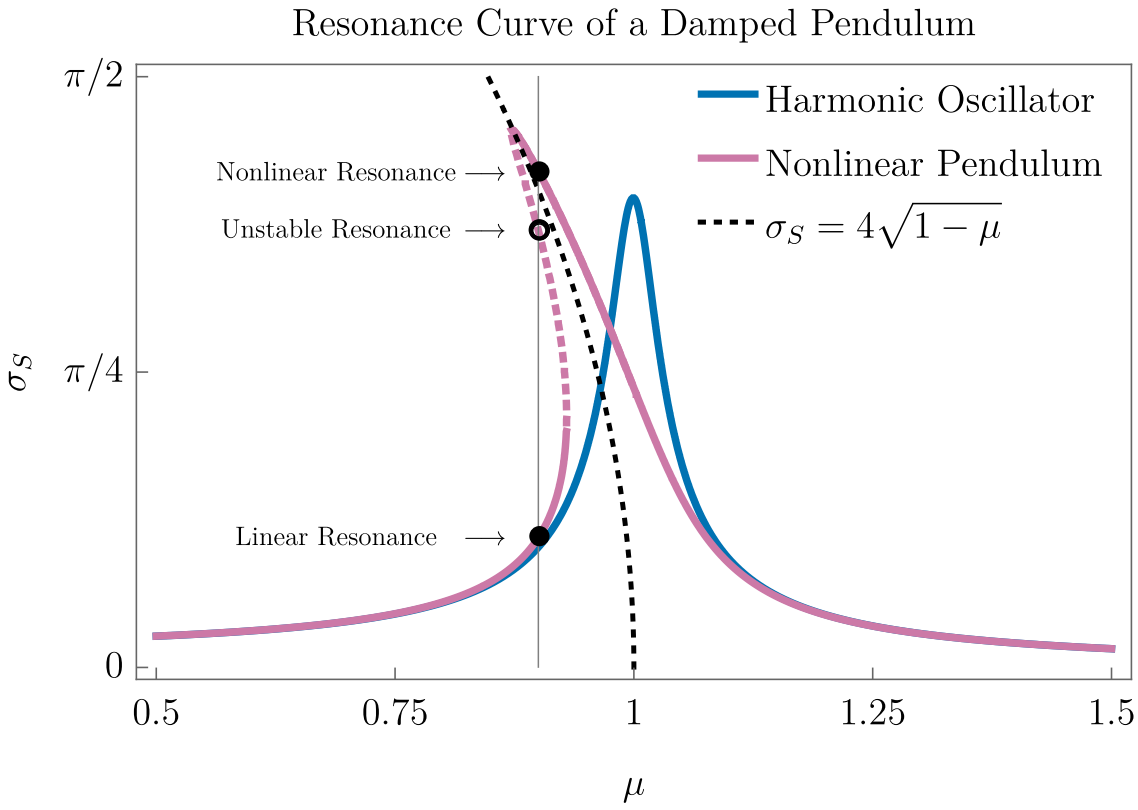

Figure 3.2: Resonance curve (Eq. 3.15) for a pendulum of fundamental frequency $m = 1$ driven at an amplitude of $\sigma_d = 4 \times 10^{-3}$ at a damping of $\gamma = 2.5 \times 10^{-3}$ (Magenta). The vertical line is drawn for a driving frequency of $\mu = 0.9$ and intersects the resonance curve at the three equilibrium solutions. The bottom solution (the linear branch) is stable and well-approximated by the harmonic oscillator resonance curve (Blue). The intermediate solution living on the dashed segment is unstable. The top solution is once again stable, and corresponds to the autoresonant solution for the short axion (with amplitude σ_S). The Dashed Black curve represents the frequency curve of a free pendulum.

driver is best depicted by a *resonance curve*, which shows the possible equilibrium amplitudes σ_S as a function of the driver's frequency μ. In the absence of the nonlinear term $-\frac{1}{6}\Theta_S^3$, the oscillator's equilibrium amplitude is unique:

$$\sigma_S = \frac{\sigma_d}{\sqrt{\left(1-\mu^2\right)^2 + \gamma^2\mu^2}}\,, \tag{3.14}$$

where $1-\mu^2$ represents the difference between the squares of the oscillator frequency 1 and the driver μ. An intuitive trick to extend this resonance curve to the nonlinear oscillator is to replace the fundamental frequency 1 in Eq. 3.14 with its amplitude-dependent version in Eq. 3.12:

$$\sigma_S = \frac{\sigma_d}{\sqrt{\left(\omega(\sigma_S)^2-\mu^2\right)^2 + \gamma^2\mu^2}}\,. \tag{3.15}$$

By introducing amplitude dependence to the resonance condition, there can now be up to three equilibrium amplitudes for Θ_S as a function of the driver frequency μ, which we show in Fig. 3.2. The smallest amplitude corresponds to the regime of linear excitation of the pendulum and is stable to perturbations; we will refer to this solution as the *linear branch*. The intermediate amplitude solution is unstable to small perturbations. The third and largest amplitude equilibrium, which we will refer to as the *nonlinear branch*, is again stable and, as we will show below, corresponds to autoresonance.

We now return to cosmological scenario of Eq. 3.10, where friction and driving are decaying functions of time. In particular, the damping is given by the Hubble parameter $\gamma \to 3H(t) \propto t^{-1}$, and the amplitude of the driver follows the cosmological evolution of the long axion, namely $\sigma_d \to \sigma_L(t) \propto t^{-3/4}$. In spite of this time dependence, the notion of a resonance curve is still useful in the cosmological scenario since both damping and driving vary slowly compared to the rapid oscillatory timescale when $t \gg 1$, allowing σ_S to arrive at a quasi-equilibrium.

Remarkably, it is the cosmological evolution of γ and σ_d that is responsible for autoresonance. We show this effect in Fig. 3.3, where we plot the instantaneous equilibrium of σ_S at each point in time for two different initial Θ_L amplitudes $\sigma_L(0)$ and fixed driving frequency μ. Early on, the system is dominated by friction, and the equilibrium value of σ_S is small. At late times, Hubble friction decays faster than the driver, resulting in equilibrium solutions on both the linear branch near zero, and on the nonlinear branch at large amplitude. Whether the short axion is smoothly carried up to the nonlinear branch $\sigma_S \to 4\sqrt{1-\mu}$, or left on the linear branch where $\sigma_S \to 0$ depends on whether the initial driving amplitude $\sigma_L(0)$ is large enough. The same reasoning can be applied to Eq. 3.9 with only slight modifications, which we discuss in App. 4.7.

Thus we have identified a cosmological mechanism for arriving at the nonlinear branch of the resonance curve. This instance of autoresonance is not unique. For example, Ref. [188] showed that autoresonance can be induced by sweeping the driver's frequency and applied this effect to a variety

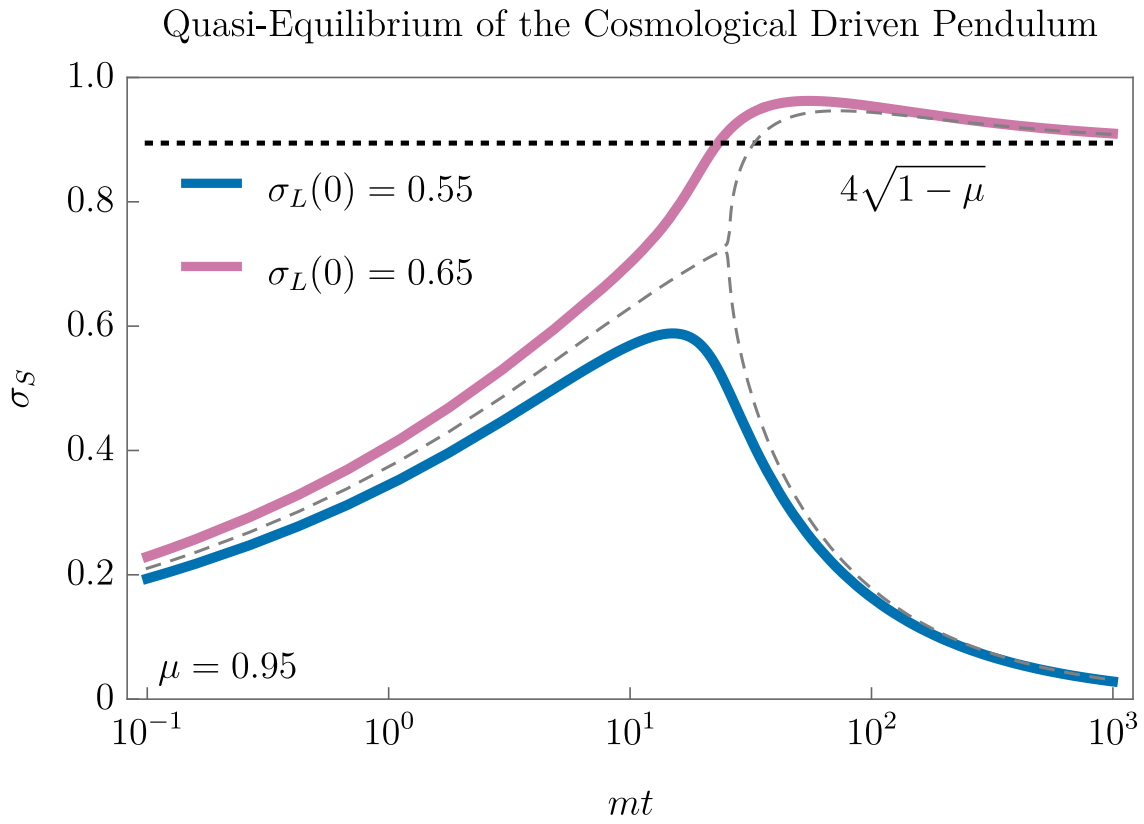

Figure 3.3: Quasi-equilibrium trajectories of the short amplitude σ_S as it tracks the time-dependent resonance curve, for two values of the initial driver amplitude $\sigma_L(0)$ and a fixed driver frequency $\mu = 0.95$. For small driver amplitudes (Blue), the short axion never leaves the linear branch of the resonance curve. For large enough driver amplitudes (Magenta), the short axion is smoothly lifted from zero amplitude to the stable nonlinear branch, which converges to the undamped pendulum solution ($\omega(\sigma_S) = \mu$ with $\omega(\sigma_S)$ given by Eq. 3.12). At the critical driving, the two branches are equally accessible as a bifurcation (Gray, Dashed). See App. 4.7.1, and in particular Fig. 4.9 for further details.

of systems, including planetary dynamics and plasma physics. In other words, autoresonance is a generic feature of many driven nonlinear systems where some external parameter varies, and may be a generic feature of the axiverse as well.

We now return to the full system of Eq. 3.8, which describes the homogeneous part of the coupled axion system of Eq. 3.5 in an FLRW background. For some range of values of μ, $\mathcal{F}$, and initial misalignment angles Θ_S and Θ_L, the system autoresonates, with Θ_S dynamically adjusting its amplitude so that its frequency matches the driver frequency μ, and then remaining at this amplitude until backreaction onto Θ_L eventually cuts off the autoresonance. For a representative choice of parameters this can be seen concretely in Fig. 3.4. The physics of this autoresonance is quite rich, and in App. 4.7 we develop a formalism that lets us quantitatively understand many details about it, but for the remainder of this section we focus on three questions. First, at what amplitude is the short field held during autoresonance? Second, assuming the system begins to autoresonate, what eventually cuts it off (i.e. how long does it last) and what is the final energy density in the short axion field? And third, what range of parameters (μ, $\mathcal{F}$, and the initial misalignment angles) lead to autoresonance?

The first question is also the simplest to answer. If a nonlinear oscillator is being autoresonantly driven in its steady state, its amplitude will be chosen such that its frequency approximately matches the driver frequency. In the case of two friendly axions discussed here, the short axion is driven by the long axion, which oscillates with frequency μ in its linear regime (i.e. once $\Theta_L \ll 1$). As discussed above, the frequency of a cosine oscillator as a function of its amplitude σ_S is given by Eq. 3.12. During autoresonance, the amplitude of Θ_S will remain fixed at $\omega(\sigma_S) \approx \mu$. For $\mu = 0.8$ for example, this evaluates to $\sigma_S \approx 1.82$.

This "locking" of the Θ_S amplitude has important cosmological effects. Hubble friction operates to steadily dilute the total axion energy density, but because Θ_S is autoresonantly held at fixed amplitude, its energy density does not decrease. As a result, there is a steady transfer of energy from the long axion to the short axion, and the relative partition of energy between the two fields shifts as the universe evolves. If both axions have $\mathcal{O}(1)$ initial misalignment angles, then at $H \sim m$ we have that $\rho_S \sim m^2 f^2$ and $\rho_L \sim \mu^2 \mathcal{F}^2 m^2 f^2$. As time goes on, ρ_S remains roughly constant but ρ_L decreases $\propto a^{-3} = t^{-3/2}$. Thus after approximately a time

$$t_{\rm eq} \equiv \frac{C_{\rm eq}}{m} (\mu \mathcal{F})^{4/3} \,, \tag{3.16}$$

the short and long axion energy densities will have equalized, where $C_{\rm eq}$ is an order 1 constant. Autoresonance is still maintained for some time after this, although from this point on the energy loss in the long field is dominated by the transfer to the short field rather than Hubble friction. This continues until autoresonance is cut off.

That autoresonance must eventually be cut off is clear from energetics; the short axion amplitude cannot remain constant forever. Our second principal question is what causes this cutoff, and the

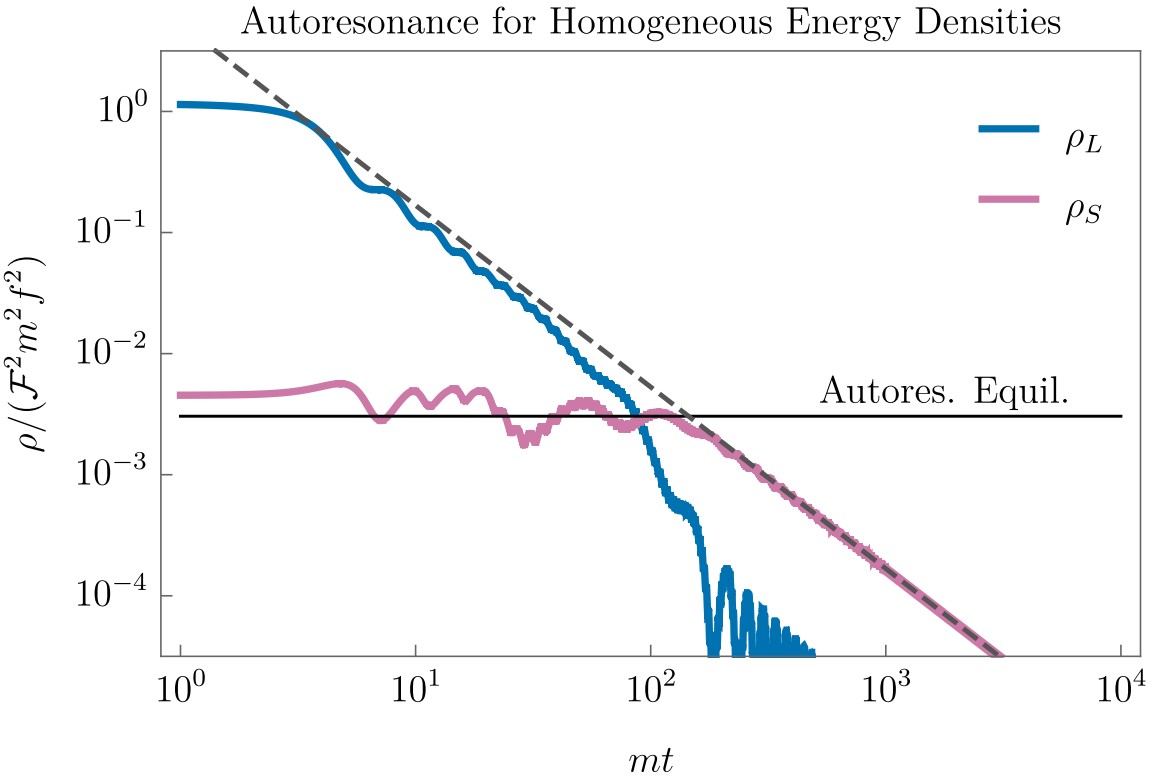

Figure 3.4: Evolution of energy densities in the short and long axions for generic initial conditions that lead to autoresonance. The parameters taken here are $\mu = 0.8$, $\mathcal{F} = 20$, $\Theta_{S,0} = 0.4\pi$, $\Theta_{L,0} = 0.8\pi$, although the qualitative features are similar for broad ranges of initial conditions within the "friendly" band $0.75 \lesssim \mu < 1$. $\mathcal{F}$ sets the rough initial ratio of energy densities in the short and long modes but does not play any significant role in determining whether the system lands on autoresonance provided it is somewhat large ($\mathcal{F} \gtrsim 5$). The short axion energy density is held approximately constant at a value determined by the equilibrium amplitude of Eq. 3.12 (labeled "Autores. Equil.") until the long axion no longer has enough energy density to drive the autoresonance. Note that the final energy densities are not equal, but rather the short axion ends up with virtually all of the system's energy density. At late times, the mass mixing of the two axions leads to rapid flavor oscillations in the long axion's energy density. Rotating to the mass basis (see App. 4.6) removes these.

answer lies in the equation of motion for Θ_L (Eq. 3.8a). In our above first pass, we neglected the $\mathcal{F}^{-2}\sin(\Theta_S+\Theta_L)$ term in the large-$\mathcal{F}$ limit, but in truth this approximation is only valid when the amplitude of Θ_L remains somewhat large. If we expand in small Θ_L and retain the first-order contribution from the $\mathcal{F}^2$ term we obtain:

$$\partial_t^2\Theta_L + \frac{3}{2t}\partial_t\Theta_L + \Theta_L(\mu^2 + \frac{1}{\mathcal{F}^2}\cos\Theta_S) + \frac{1}{\mathcal{F}^2}\sin\Theta_S = 0\,, \tag{3.17}$$

and so we can see that when $\mathcal{F}^{-2}\sin\Theta_S \sim \mu^2\Theta_L$, backreaction will significantly affect the frequency of Θ_L. This is a somewhat decent proxy for when autoresonance ends, which predicts a maximum ratio of the amplitudes σ_S and σ_L of the short and long axions:

$$\left.\frac{\sigma_S}{\sigma_L}\right|_{\text{late-time}} \sim \mu^2\mathcal{F}^2 \gg 1\,. \tag{3.18}$$

Defining the homogeneous energy density in each axion by

$$\rho_S = f^2\left(\frac{1}{2}(\partial_t\Theta_S)^2 + m^2\left(1-\cos(\Theta_S+\Theta_L)\right)\right) \approx \frac{1}{2}m^2f^2\sigma_S^2\,, \tag{3.19}$$

$$\rho_L = \mathcal{F}^2f^2\left(\frac{1}{2}(\partial_t\Theta_L)^2 + \mu^2m^2\left(1-\cos\Theta_L\right)\right) \approx \frac{1}{2}\mu^2m^2\mathcal{F}^2f^2\sigma_L^2\,, \tag{3.20}$$

where the approximations are only valid when $\Theta_L \ll \Theta_S$ (the expectation after a period of autoresonance), we then have,

$$\left.\frac{\rho_S}{\rho_L}\right|_{\text{late-time}} \sim \mu^2\mathcal{F}^2 \gg 1\,. \tag{3.21}$$

Once autoresonance ends, the two axions behave as uncoupled fields with the exception of a small mass mixing, which can be rotated away by shifting to the mass basis. The details of this transformation are discussed in App. 4.6, but the important result is that for $\mathcal{F} \gg 1/\left(1-\mu^2\right)$ the rotation angle is quite small. The resulting flavor oscillations, however, do have a small effect, which we take into account in App. 4.7. This yields a more precise estimate for the final energy density ratio which is given in App. 4.7. For $\mathcal{F} \gg 1/(1-\mu^2)$ this ratio is well-approximated by:

$$\left.\frac{\rho_S}{\rho_L}\right|_{\text{late-time}} \sim 4\mathcal{F}^2(1-\mu)^2 \gg 1\,. \tag{3.22}$$

This ratio then remains approximately constant as the universe evolves, since both ρ_S and ρ_L redshift $\propto a^{-3}$.

Although it is a simple heuristic, Eq. 3.22 is extremely important, and highlights one of the main results of this paper: if autoresonance occurs, Θ_L transfers nearly all of its energy density into Θ_S, which then dominates the late-time axion energy density. The short axion can thus have far more energy density than would seem possible using the misalignment mechanism with $\mathcal{O}(1)$

misalignments for all fields. Because Θ_S has a smaller decay constant, it will also generically have larger couplings to the SM. As we will discuss in Sec. 3.3, these larger couplings can be probed by direct detection experiments even when the friendly pair makes up only a subcomponent of the dark matter.

In actuality Eq. 3.22 is a decent heuristic but there are a few additional effects which can modify the final result significantly. The first is the fact that when the initial conditions of the axions cause an autoresonance to occur, they typically also excite oscillations about the steady-state autoresonance. These lead to a variance of the final ratio in Eq. 3.22 of up to a few orders of magnitude. We devote App. 4.7 to a more detailed study of autoresonance that touches on such effects, although analytic results are limited in precision by the nonlinearity of the dynamics. In all such cases, however, the vast majority of the axion energy density ends up in the short field, so this effect only significantly affects the final abundance of the long field (a small subcomponent of the total axion energy density). The second and by far most significant effect is that of spatial inhomogeneities in the short field. These can be resonantly amplified during autoresonance and, if they grow large enough, can cut off the autoresonance before the full $\mathcal{O}(\mathcal{F}^2)$ ratio of Eq. 3.22 is achieved. We discuss these effects in Sec. 3.2.

With this central result we can pass onto our third principal question: what range of parameters (μ, $\mathcal{F}$, and the initial misalignment angles) lead to autoresonance? Let us first consider the effect of the decay constant ratio $\mathcal{F}$. Because the dynamics of autoresonance are mainly determined by the $\mathcal{F} \to \infty$ limit of the axion equations of motion (Eq. 3.8), the precise value of $\mathcal{F}$ does not play a big role in determining whether autoresonance will occur, although it must be somewhat large ($\mathcal{F} \gtrsim 5$) to trust the above analytic results. Numerically, we find that there are potentially-observable effects on gravitationally-bound structures for $\mathcal{F} \gtrsim 3$, which we discuss further in Sec. 3.2.

The mass ratio μ of the axions plays a much larger role. For the attractive self-interactions of Θ_S discussed in the bulk of this paper, autoresonance requires $\mu < 1$, since the driving frequency must be less than the fundamental frequency of the driven field (i.e. the long axion's mass must be slightly smaller than the short axion's). However if the hierarchy of masses is too large, autoresonance ceases to be possible. Intuitively, this is because as the masses get further apart, the amplitude of the short axion predicted by Eq. 3.12 gets larger and larger. Eventually, the approximation $\cos\Theta_S \sim 1$ in Eq. 3.10 fails, and the effects of this destroy the possibility of autoresonance. As we discuss in App. 4.7, this predicts a minimum value of $\mu \gtrsim 0.64$ to achieve autoresonance. In practice, very few initial conditions lead to autoresonance for $\mu \lesssim 0.75$ (see inset of Fig. 3.5), so the range $0.75 \lesssim \mu < 1$ is a useful notion of how "friendly" two axions must be to see significant effects of the kind we have described. We have studied this question numerically in the finite $\mathcal{F}$ limit, and summarize our results in Fig. 3.5 and in particular its inset. We find that for μ in the "friendly" band $0.75 \lesssim \mu < 1$, $\mathcal{O}(50\%)$ of the space of initial misalignment angles result in autoresonance, which leads to the short axion dominating the late-time energy density whenever it happens.

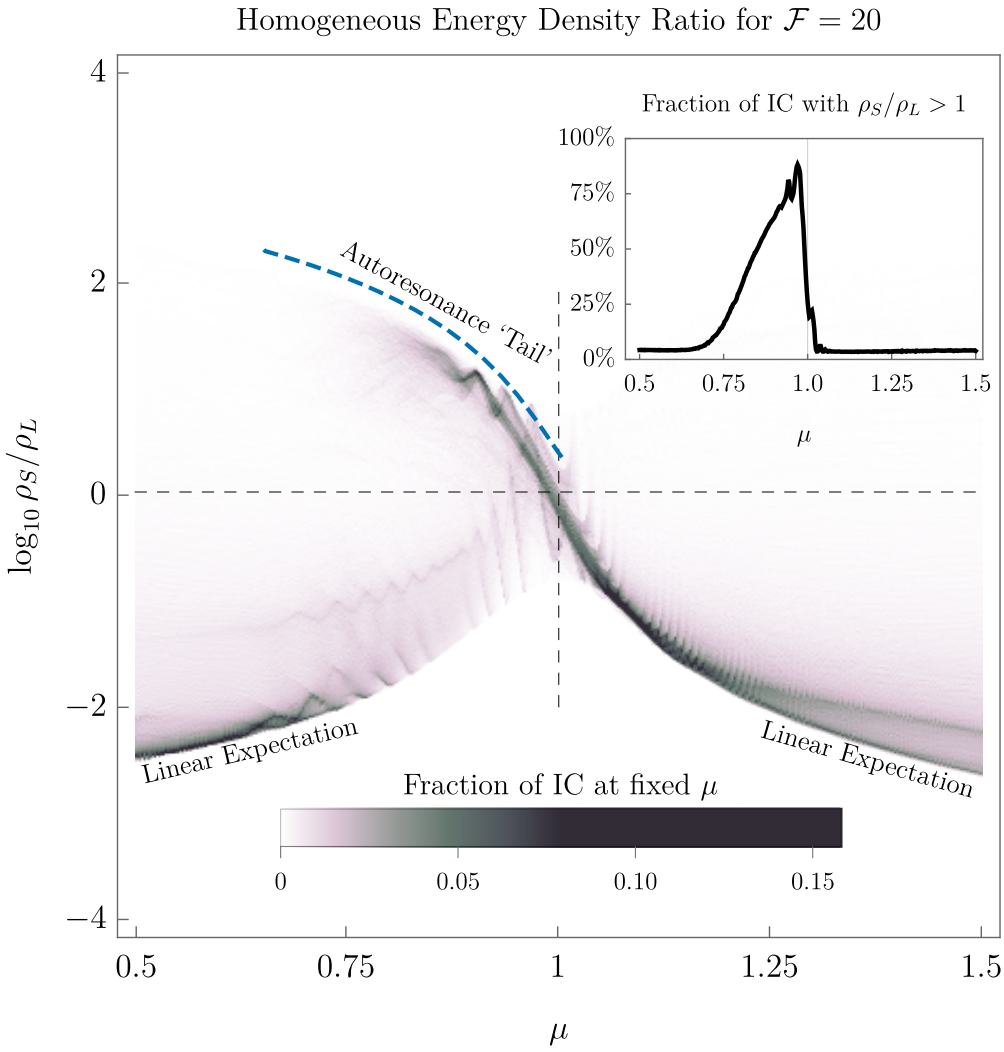

Figure 3.5: The relic density ratio of the short axion ρ_S to the long axion ρ_L in the model two-axion system of Eq. 3.5. A vertical slice of this plot at fixed μ should be read as a histogram, with darker colors representing a higher likelihood of choosing initial conditions (IC) uniformly sampled from $(\Theta_S(0), \Theta_L(0)) \in [-\pi, \pi] \times [-\pi, \pi]$ corresponding to that density ratio. For $\mu \geq 1$ and $\mu \leq 0.75$, most initial conditions lead to $\rho_S \ll \rho_L$ (lower dark bands), as naïvely expected for two uncoupled axions. For $0.75 \lesssim \mu < 1$, a period of autoresonance causes ρ_S to dominate the relic abundance (wispy dark features pointing towards the upper left). We plot the analytical estimate for the shape of the autoresonance tail in dashed blue (see App. 4.7). **Inset:** An integrated version of this plot that shows, for each value of μ, the total fraction of initial misalignment angles that result in the short axion dominating the late-time energy density in the axion sector.

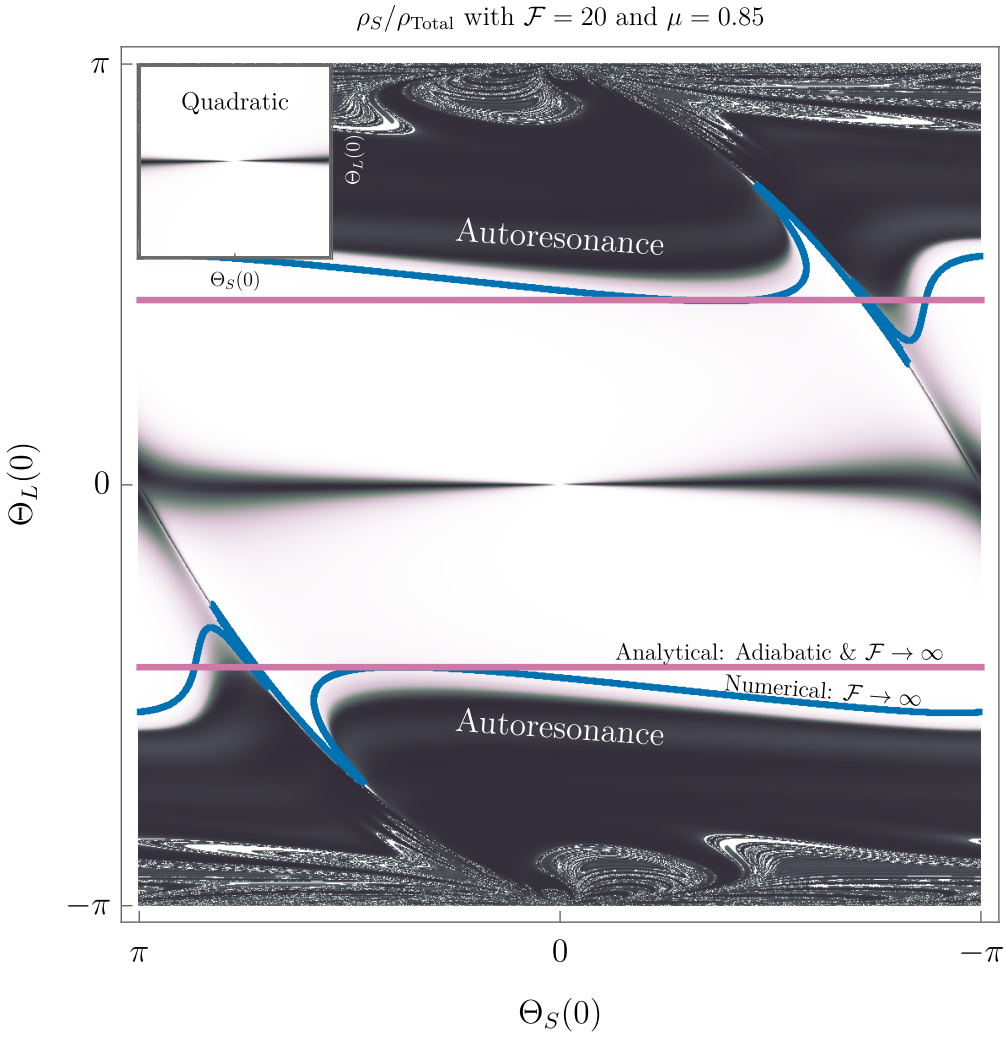

Figure 3.6: A representative plot of the late-time relative abundance of the short axion Θ_S compared to the total axion energy density, as a function of initial misalignment angles for both Θ_S and Θ_L. Black regions correspond to initial angles for which Θ_S dominates the final relic abundance. It is clear that this happens in two qualitatively distinct regions: when $\Theta_L(0)$ is tuned close to zero and when $|\Theta_L(0)|$ is above some threshold, which for these parameters is roughly $\pi/2$. The latter corresponds to those initial misalignment angles which land on autoresonance and thus lead to a nearly complete transfer of energy density from Θ_L to Θ_S. The former is simply explained by the linearized dynamics, as shown in the inset. The autoresonance cutoff predicted in the adiabatic $\mathcal{F} \to \infty$ limit (Eq. 4.80) is displayed in Magenta. The numerical $\mathcal{F} \to \infty$ cutoff is displayed in Blue, which differs from the adiabatic prediction in that it accounts for transient Θ_S motion (see main text for details). At very large initial long axion misalignments, a fractal-like structure emerges due to chaotic dynamics in the coupled system, which we discuss in App. 4.7.4. **Inset:** The same plot obtained by discarding all terms in the potential $V(\Theta_L, \Theta_S)$ of Eq. 3.5 higher than quadratic order in the fields. In this case, the upper and lower regions completely disappear because autoresonance relies on the self-interactions of the short axion to achieve frequency-matching between the long and short fields.

For fixed μ and $\mathcal{F}$, we can gain a better understanding of which initial misalignment angles lead to autoresonance by using the resonance curve techniques discussed above. In App. 4.7 we show that all $\Theta_S(0)$ will be brought to autoresonance by sufficiently large $\Theta_L(0)$ in the large $\mathcal{F}$ and small $1-\mu$ limits (see Eq. 4.80 and surrounding discussion). In Fig. 3.6, we show a representative scan over initial misalignment angles for the parameters $\mu = 0.85$ and $\mathcal{F} = 20$. For initial $|\Theta_{L,0}| \gtrsim \pi/2$, nearly all values of $\Theta_{S,0}$ end up autoresonating, directing nearly all the axion energy density into the short field. Fig. 3.6 also displays the large-$\mathcal{F}$ autoresonance thresholds: the Magenta contour represents the adiabatic prediction (Eq. 4.80), which one should compare to the numerical Blue contour. These thresholds differ because the numerical contour accounts for initial transient Θ_S oscillations that depend mildly on the misalignment angles, while the analytical approximation assumes that all transients have died out. These differences vanish as we take μ closer to 1, where the adiabatic approximation becomes exact.

3.2 Spatial fluctuations

In the previous section, we described the phenomenon of autoresonance in the two-axion potential of Eq. 3.5. Autoresonance causes the short axion to undergo sustained, large-amplitude oscillations by drawing energy from the long axion. At these large amplitudes, θ_S experiences strong attractive self-interactions which can lead to the growth of large density perturbations in the axion field during radiation domination. If the friendly pair comprises a sizable fraction of DM, these perturbations collapse early during matter domination, leading to a multitude of present-day astrophysical signatures. The mechanism at play is a form of parametric resonance, quite similar to that studied in Ref. [59]. In this section we generalize that study to our case of coupled axions. We begin in Sec. 3.2.1 by considering a one-axion analogue of the friendly axion system that contains most of the relevant physics of perturbation growth. We then show in Sec. 3.2.2 that the results of this analogue model apply almost without modification to the case of friendly axions, and we arrive at analytic expressions for the growth rate of the short axion perturbations. In Sec. 3.2.3 we proceed to a preliminary numerical study of autoresonance in the presence of non-perturbative θ_S fluctuations. Our $3+1d$ numerical simulations provide evidence that the autoresonant energy transfer of Sec. 3.1 can be cut off early if θ_S fluctuations grow sufficiently large, significantly changing the predictions of the homogeneous theory. Finally, in Sec. 3.2.4 we conclude by describing the Newtonian formalism to evolve the density perturbations to the present day and discuss the late-time axion halo spectrum. In this final section we treat only the case where the friendly axions constitute all of the DM. We expect qualitatively similar effects if the pair constitute a significant ($\gtrsim \mathcal{O}(1\%)$) fraction of the DM, but we leave this case to future work.

3.2.1 Invitation: A single axion model of perturbation growth

In the standard misalignment picture, the axion ϕ starts out displaced by order f from its vacuum expectation value. The axion begins oscillating at $H \sim m$ and quickly loses energy to Hubble friction, diluting to approximately one fifth of its initial amplitude over a single oscillation. At such small amplitudes, self-interactions are weak, and the axion's potential is well-approximated by a free quadratic. If, however, the axion starts very close to the top of the cosine, then oscillations are delayed, and Hubble friction is tiny by the time the axion starts oscillating. It thus takes a long time for the axion to damp down from its large initial amplitude. The consequence of this *large misalignment* is that the axion probes the nonlinear part of the potential for an extended period of time. The now-accessible many-to-one interactions convert the non-relativistic spectrum of axion fluctuations into semi-relativistic modes through parametric resonance. The resulting density fluctuations can then collapse into small scale structure, leading to an abundance of late-time signatures [59,207,208].

It turns out that fine-tuned initial conditions are not necessary for such effects if the axion has a more complicated potential. For example, Ref. [59] also studied monodromy-inspired potentials that flatten at large field values, effectively extending the cosine plateau. We can obtain a similar effect if a single axion's potential receives contributions from two instantons:

$$V(\phi) = m^2 f^2 \left[\left(1 - \cos\left(\frac{\phi}{f} + \delta \right) \right) + \mu^2 \mathcal{F}^2 \left(1 - \cos\left(\frac{\phi}{\mathcal{F} f} \right) \right) \right] , \tag{3.23}$$

where in this setup $\mathcal{F}$ is an integer[5] and $\delta \in [0, 2\pi)$ is a generic phase offset. Like the two-axion potential of Eq. 3.5, this potential is comprised of a "short" and a "long" instanton (first and second lines respectively), whose ratio of periods is $\mathcal{F}$. For parameters $\mathcal{F} \gtrsim 3$ and $\mu \sim 1$, the resemblance goes further. Since the fundamental period of the field is $(-\pi\mathcal{F}f, \pi\mathcal{F}f)$, an untuned initial misalignment angle is $\phi/f \sim \mathcal{O}(\mathcal{F})$. After a time $t_{\rm osc} \sim \frac{1}{m}(\mu\mathcal{F})^{4/3}$, the axion amplitude will have diluted to the scale of the small instanton ($\phi/f \sim \mathcal{O}(1)$) and it will feel strong self-interactions. This delay is completely analogous to the time it takes for θ_S to fall off the autoresonance (Eq. 3.16). In addition, Hubble friction has already decreased significantly by this time, and $t_{\rm osc}$ is thus functionally equivalent to the delay time of oscillations during large misalignment [59]. At this point the self-interactions can lead to rapid perturbation growth.

We study the axion perturbations in the background of the perturbed FLRW metric

$$\mathrm{d}s^2 = (1 + 2\Phi)\,\mathrm{d}t^2 - a^2(1 - 2\Phi)\delta_{ij}\,\mathrm{d}x^i\,\mathrm{d}x^j \,, \tag{3.24}$$

where $\Phi(t, \mathbf{x}) = \sum_{\mathbf{k}} \Phi_k(t) e^{\mathrm{i}\mathbf{k}\cdot\mathbf{x}}$ is the adiabatic scalar perturbation generated by inflation. Planck

[5] A potential of this form can naturally arise from a general axiverse potential such as that of Eq. 3.3, and in that context $\mathcal{F}$ is just the ratio of the axion's integer charges $\mathcal{Q}$ under two different instantons. $\mathcal{F}$ can thus in general be any rational number rather than only an integer, but this does not change any of the qualitative features of the analysis and so we neglect it here.

measurements of the CMB are consistent with a nearly scale-invariant dimensionless power spectrum $\mathcal{P}_\Phi(t \to 0) = \langle \Phi_{k,0}\Phi_{k,0}\rangle \approx 2.1\times 10^{-9}(k/k_\star)^{n_s-1}$, where $n_s \approx 1-0.03$ is the spectral tilt and $k_\star \approx 0.05\mathrm{Mpc}^{-1}$ is the pivot scale [206]. Because we lack measurements below $k = 1\ \mathrm{Mpc}^{-1}$, and for simplicity, we assume a scale-invariant power spectrum for the remainder of the text $\langle \Phi_{k,0}\Phi_{k,0}\rangle = 2.1\times 10^{-9}$.

We separate the axion field $\theta(t,\mathbf{x}) \equiv \phi/(\mathcal{F}f)$ into a homogeneous component and a spatially varying perturbation

$$\theta(t,\mathbf{x}) = \Theta(t) + \sum_{\mathbf{k}} e^{i\mathbf{k}\cdot\mathbf{x}}\delta\theta(t,\mathbf{k})\,, \tag{3.25}$$

where $\mathbf{k}$ is the comoving wavenumber. To make our notation simpler, we re-scale the comoving wavenumber by defining

$$\tilde{k}^2 \equiv \frac{1}{2mH_{\rm rad}(t)}\frac{k^2}{a(t)^2}\,, \tag{3.26}$$

where $a(t)\propto t^{1/2}$ is the scale-factor during radiation domination, $H^2_{\rm rad} = 8\pi G^2\rho_{\rm rad}$, and $\rho_{\rm rad}\propto a(t)^4$ is the energy density in radiation. Note that with this definition $\tilde{k}$ is dimensionless and constant in time, and $\tilde{k}\sim 1$ corresponds to those modes that enter the horizon at $H\sim m$. The zero-mode obeys the equation

$$\partial_t^2\Theta + \frac{3}{2t}\partial_t\Theta + \frac{1}{(\mathcal{F}f)^2}V'(\mathcal{F}f\Theta) = 0\,, \tag{3.27}$$

and the perturbation obeys the linearized equation

$$\partial_t^2\delta\theta(t,\tilde{k}) + 3H\partial_t\delta\theta(t,\tilde{k}) + \left(\frac{m}{t}\tilde{k}^2 + \frac{1}{(\mathcal{F}f)^2}V''(\mathcal{F}f\Theta(t))\right)\delta\theta(t,\tilde{k}) = \mathcal{S}(t,\tilde{k})\,, \tag{3.28}$$

where primes indicate differentiation with respect to Θ, and the perturbation initial conditions are set by inflation, which after many e-folds has flattened the axion field so that $\delta\theta(0,\mathbf{x}) = 0$ to high precision. $\mathcal{S}(t,\tilde{k})$ is a small source representing the effect of the adiabatic scalar perturbations to the metric on the axion field:

$$\mathcal{S}(t,\tilde{k}) = 2\left[\frac{t_k}{t}\frac{d\Phi_k}{dt_k}\partial_t\Theta + \Phi_k V'(\Theta)\right]\,, \tag{3.29}$$

where

$$\Phi_k = 3\Phi_{k,0}\left(\frac{\sin t_k}{t_k^3} - \frac{\cos t_k}{t_k^2}\right)\,, \qquad t_k^2 \equiv \frac{2}{3}\frac{m}{H_{\rm rad}}\tilde{k}^2\,. \tag{3.30}$$

Unlike misalignment in the cosine potential (Eq. 3.1), the two scales of Eq. 3.23 mean that

misalignment takes place in two parts. In the first epoch, the axion has a large amount of energy coming from the larger of the two instantons (the long instanton). These initial oscillations have kinetic energy density many times larger than the small instanton, and the axion rolls over the short instanton's wiggles without noticing them. The second epoch begins once the axion's energy matches the small instanton scale at a time $t = t_{\rm osc}$. At this point, strong self interactions from the short instanton lead to the parametric resonant growth of perturbations.

More quantitatively, the story of misalignment in the two-instanton potential (Eq. 3.23) is as follows. At early times when $H \gg m$, the axion remains fixed at its untuned initial condition $\Theta = \Theta_0 = \mathcal{O}(1)$, where it acts as a cosmological constant. After Hubble friction dilutes below the mass scale, the zero-momentum mode starts oscillating and the axion energy density dilutes like matter. After just one oscillation, Θ is small enough that the self-interactions caused by the large instanton are negligible, and we can approximate the equation for $\delta\theta$ as

$$\partial_t^2 \delta\theta + 3H\partial_t \delta\theta + m^2 \left(\frac{\tilde{k}^2}{mt} + \mu^2 + \cos(\mathcal{F}\Theta + \delta) \right) \delta\theta \approx \mathcal{S} \,. \tag{3.31}$$

Although the self-interactions of the long instanton are no longer relevant, it still dominates the energy density of Θ, $\rho \sim \frac{1}{2}\mu^2 m^2 \mathcal{F}^2 f^2$. Thus, when the axion is rolling past the bottom of the potential, we can approximate $\dot{\Theta} \sim \mu m$, and the short instanton acts as a parametric driver at integer multiples of the fundamental frequency $\mathcal{F}\dot{\Theta} \approx \mathcal{F}\mu m$. Because the mass of $\delta\theta$ is order $\mu m \ll \mathcal{F}\dot{\Theta}$, these rapid parametric oscillations do *not* induce parametric resonance, and $\delta\theta$ remains small during this early phase.

The axion does not begin to feel strong self-interactions until its energy density has diluted to the scale of the small instanton,

$$\rho(t) \approx (\mu m)^2 (\mathcal{F} f)^2 \Theta_0^2 (mt)^{-3/2} = m^2 f^2 \Theta_0^2 \left(\frac{t}{t_{\rm osc}} \right)^{-3/2} , \tag{3.32}$$

at a time $t = t_{\rm osc} \approx (\mu\mathcal{F})^{4/3}/m$. At this point, the amplitude of the zero mode oscillations has damped to $\Theta \sim 1/\mathcal{F}$, and Θ acts as a parametric driver with frequency at integer multiples of $\mathcal{F}\dot{\Theta} \sim m$. Now that the parametric driver and the perturbation frequency are both order m, $\delta\theta$ will experience a period of exponential growth due to a parametric resonance instability.

As we will derive in App. 4.8, the growth rate of the axion perturbations is controlled by a single parameter, the frequency shift $\delta\omega$ of the zero-mode oscillations, defined by the relationship

$$\delta\omega(\sigma) \equiv \omega(\sigma) - \omega(0) \,, \tag{3.33}$$

where σ and $\omega(\sigma)$ are the amplitude and frequency of the homogeneous mode Θ. The sign of $\delta\omega$ characterizes the net-repulsive or attractive interactions of the potential over the range of a

complete Θ oscillation. Consider, for example, the case of a repulsive (positive) quartic interaction. The interaction increases the potential at larger amplitudes, causing the axion to turn around faster than it would have in a quadratic potential, reducing the period of oscillation. Similar reasoning applies to attractive quartic and to cubic interactions, which both work to increase the oscillation period.[6] Thus, net-repulsive interactions have $\delta\omega > 0$ and net-attractive interactions have $\delta\omega < 0$.

The instantaneous exponential growth rate $\Gamma(t, \tilde{k})$ of the axion perturbation $\delta\theta(t, \tilde{k})$ amplitude at comoving wavenumber $\tilde{k}$ is (see App. 4.8):

$$\Gamma(t, \tilde{k}) = \mathrm{Re}\left[-\frac{3}{4t} + |\delta\omega|\sqrt{1 - \left(1 + \frac{\tilde{k}^2}{2t\delta\omega}\right)^2}\right], \tag{3.34}$$

where the $-3/4t$ is due to Hubble friction. We can see that for repulsive self-interactions ($\delta\omega > 0$), the growth rate is always negative, and thus density perturbations do not grow through parametric resonance. Consequently, the late-time signatures of repulsive interactions are completely characterized by the analysis of Sec. 3.1, offering a clean benchmark model of autoresonant dark matter which we describe further in Sec. 3.4. On the other hand, attractive self-interactions, for which $\delta\omega < 0$, *do* grow density perturbations, which we describe below and calculate in detail in App. 4.8.

We can estimate the size of the $\delta\theta$ by integrating the growth rate

$$\langle\delta\theta(t, \tilde{k})^2\rangle \approx \langle\delta\theta(t_{\rm init}, \tilde{k})^2\rangle \exp\left[2\int_{t_{\rm init}}^{t} \mathrm{d}t'\Gamma(t', \tilde{k})\right] \tag{3.35}$$

where $t_{\rm init} \approx t_{\rm osc}$ is the earliest time where $\Gamma \geq 0$, and

$$\langle\delta\theta(t, \tilde{k})^2\rangle \approx \frac{\Phi_{k,0}^2}{\left(1 + \frac{mt\tilde{k}^2}{\pi^2}\right)^2}, \tag{3.36}$$

is an empirical formula for the amplitude of $\delta\theta$ before perturbations start growing [59]. Because the leading-order frequency shift is always quadratic in the zero-mode amplitude $\delta\omega \propto \sigma^2$, we can parametrize the frequency shift's time evolution as $\delta\omega(t) = \delta\omega_{\rm osc}(t/t_{\rm osc})^{-3/2}$. As we show in App. 4.8, the resulting scalar perturbations are maximized at $\tilde{k} = \tilde{k}_{\rm max}$, with corresponding integrated growth rate

$$\tilde{k}_{\rm max}^2 \approx -0.622\delta\omega_{\rm osc}t_{\rm osc}, \tag{3.37}$$

$$\lim_{t\to\infty}\int_{t_{\rm osc}}^{t} \mathrm{d}t'\Gamma(t', \tilde{k}_{\rm max}) \approx -1.45\delta\omega_{\rm osc}t_{\rm osc} - 2.8, \tag{3.38}$$

where we have taken $t_{\rm init} = t_{\rm osc}$, and -2.8 corresponds to the suppression from Hubble damping.

[6] Cubic interactions are always net-attractive, since the axion always spends more time on the attractive side of the potential.

To summarize, the axion only starts to experience parametric resonance once it has damped to the short instanton scale. The early period of large-amplitude oscillations only serves to delay parametric resonance to a late-enough time that it is not immediately quenched by Hubble friction. In the following section, we will study perturbations in the two-axion model Eq. 3.5, and we will find that the results of this section carry over to the period after autoresonance ends, and in addition that autoresonance provides a mechanism for mode growth even during the early phase of large amplitude oscillations, leading to enhanced total perturbation growth.

3.2.2 Perturbation growth during autoresonance

In this section, we quantify mode growth during the early phase of autoresonance, where the zero-mode physics is quite different from that of Sec. 3.2.1. Nonetheless, the single-axion model (Eq. 3.23) introduced in the previous section shares important features with the friendly axion model (Eq. 3.5), and the same framework for parametric resonance is easily extended to this case. Importantly, we will find that autoresonance is a period of significant parametric resonance, which accounts for exactly one third of the total mode growth, lasting only 2% of the total growth time. This is the consequence of the large, constant amplitude oscillations that are the hallmark of autoresonance.

The equations of motion for the density perturbations of the short and long axion are

$$\partial_t^2\delta\theta_S + 3H\partial_t\delta\theta_S + m^2\left(\frac{1}{mt}\tilde{k}^2 + \cos(\Theta_S+\Theta_L)\right)\delta\theta_S + m^2\cos(\Theta_S+\Theta_L)\delta\theta_L = \mathcal{S}_S\,, \tag{3.39a}$$

$$\partial_t^2\delta\theta_L + 3H\partial_t\delta\theta_L + m^2\left(\frac{1}{mt}\tilde{k}^2 + \mathcal{F}^{-2}\cos(\Theta_S+\Theta_L) + \mu^2\cos\Theta_L\right)\delta\theta_L + m^2\mathcal{F}^{-2}\cos(\Theta_S+\Theta_L)\delta\theta_S = \mathcal{S}_L\,. \tag{3.39b}$$

where $\mathcal{S}_{S,L}$ represent how the metric fluctuations source the scalar perturbations of θ_S and θ_L respectively (see App. 4.8). In the large-$\mathcal{F}$ limit, we can see that $\delta\theta_L$ will behave just as in ordinary misalignment in a single cosine potential. Therefore, we approximate $\delta\theta_L \to 0$ and consider $\delta\theta_S$ in isolation. We further approximate $\Theta_S + \Theta_L \approx \Theta_S$, since Θ_L damps quickly to small amplitudes while Θ_S is locked by autoresonance. Thus, the equation for the short axion perturbation becomes

$$\partial_t^2\delta\theta_S + 3H\partial_t\delta\theta_S + m^2\left(\frac{1}{mt}\tilde{k}^2 + \cos\left(\Theta_S\right)\right)\delta\theta_S \approx \mathcal{S}_S\,. \tag{3.40}$$

This is of the same form as Eq. 3.28, and therefore our expression for the growth rate is exactly Eq. 3.34, where the frequency shift is now given by the condition for autoresonance $\delta\omega(\sigma_S(t)) = \delta\omega_{\rm osc} = \mu - 1$ for $t < t_{\rm osc}$. In this case, $t_{\rm osc} = C_{\rm osc}(\mu\mathcal{F})^{4/3}/m$ is the time at which autoresonance ends and nearly-harmonic decaying Θ_S oscillations begin. $C_{\rm osc}$ is an $\mathcal{O}(1)$ constant that depends on initial conditions. We now integrate the growth rate to arrive at the magnitude of $\delta\theta_S$ at the end of

autoresonance

$$\langle \delta\theta_S(t_{\rm osc},k)^2\rangle \approx \langle \delta\theta(t_{\rm init},k)^2\rangle \exp\left[2\int_0^{t_{\rm osc}} {\rm d}t'\Gamma(t',k)\right]. \tag{3.41}$$

The fastest growing mode starts growing at $t_{\rm init}\approx 0.155 t_{\rm osc}$, with comoving wave number $\tilde{k}_{\rm max}$ and integrated growth rate

$$\tilde{k}_{\rm max}^2 \approx -0.622\delta\omega_{\rm osc}t_{\rm osc}\,, \tag{3.42}$$

$$\int_{t_{\rm init}}^{t_{\rm osc}} {\rm d}t'\Gamma(t',\tilde{k}_{\rm max}) \approx -0.725\delta\omega_{\rm osc}t_{\rm osc} - 1.4\,, \tag{3.43}$$

where -1.4 originates from Hubble damping.

After the end of autoresonance, σ_S decays as $t^{-3/4}$ and $\delta\omega(\sigma_S(t)) = \delta\omega_{\rm osc}(t/t_{\rm osc})^{-3/2}$, just as in Sec. 3.2.1. At this point, we have reduced the two-axion perturbation equations Eq. 3.39 to a single-axion equation Eq. 3.40, and we may directly apply the results of Sec. 3.2.1, leading to the post-autoresonance integrated growth rate

$$\tilde{k}_{\rm max}^2 \approx -0.622\delta\omega_{\rm osc}t_{\rm osc}\,, \tag{3.44}$$

$$\lim_{t\to\infty}\int_{t_{\rm osc}}^{t} {\rm d}t'\Gamma(t',\tilde{k}_{\rm max}) \approx -1.45\delta\omega_{\rm osc}t_{\rm osc} - 2.8\,. \tag{3.45}$$

Notice that the spectrum of axion perturbations produced during autoresonance is peaked in the same location as the post-autoresonance perturbations. As a result, the total growth from both the fixed-amplitude autoresonance and the subsequent decaying-Θ_S oscillations is just the sum of Eq. 3.43 and Eq. 3.45

$$\lim_{t\to\infty}\int_{0}^{t} {\rm d}t'\Gamma(t',\tilde{k}_{\rm max}) \approx -2.175\delta\omega_{\rm osc}t_{\rm osc} - 4.2\,. \tag{3.46}$$

The linear analysis of this section allows us to predict a late-time spectrum of DM halos provided all perturbations remain small (Sec. 3.2.4). However, it is possible that a density perturbation grows non-perturbatively large, at which point this analysis breaks down. We treat this numerically in the next section, where we find that non-perturbative structures can also quench the autoresonant transfer of homogeneous energy density described in Sec. 3.1. We summarize the distinction between the perturbative and non-perturbative regions in Fig. 3.7, where the colors indicate the time at which modes become nonlinear. In the white regions, all modes remain linear and the conclusions of Sec. 3.1 go through unchanged. In the colored regions, the various contours indicate the different stages of parametric resonance at which modes become nonlinear. For modes becoming nonlinear after the end of autoresonance, we can safely apply the results of Sec. 3.1. For parameters where modes become nonlinear before the end of autoresonance, we must instead turn to the techniques

of Sec. 3.2.3.

3.2.3 Nonperturbative structures during autoresonance

Autoresonance holds the homogeneous field Θ_S at large amplitudes for a long time, causing the spatial perturbations $\delta\theta_S$ to undergo a long period of exponential growth through parametric resonance. When these perturbations become $\mathcal{O}(1)$, the notion of the homogeneous mode Θ_S breaks down, and the conclusions of Sec. 3.1 no longer apply. In order to get a sense of what happens in this nonlinear regime, we have performed a preliminary numerical investigation for a small set of Lagrangian parameters and initial conditions, which we describe in detail in App. 4.9. Here we summarize our early results, which suggest that non-perturbative structure shuts down autoresonance, generically leading to a smaller final energy density in θ_S than predicted by Sec. 3.1.

We simulate two axions in the potential Eq. 3.5 in the background of the perturbed FLRW metric Eq. 3.24 where all fields are required to satisfy periodic boundary conditions. The results of one such simulation are given in Fig. 3.8. Because of the non-perturbative fluctuations in θ_S, there is no unique way to partition the energy densities between θ_S and θ_L, so we make the following choice:

$$\bar{\rho}_S = \frac{f^2}{V}\int \mathrm{d}V\left[\frac{1}{2}(\partial_t\theta_S)^2 + \frac{1}{2}(\nabla\theta_S)^2 + m^2(1-\cos(\theta_S+\theta_L))\right], \tag{3.47}$$

$$\bar{\rho}_L = \frac{f^2\mathcal{F}^2}{V}\int \mathrm{d}V\left[\frac{1}{2}(\partial_t\theta_L)^2 + \frac{1}{2}(\nabla\theta_L)^2 + m^2\mu^2(1-\cos\theta_L)\right]. \tag{3.48}$$

where V is the simulation volume. Even after the onset of non-perturbative θ_S fluctuations (marked by the vertical gray line), the θ_S energy density only deviates slightly from the homogeneous prediction. This deviation remains small until the perturbations begin collapsing under their own attractive self-interaction, which we mark with a vertical black line. The objects nucleating from this nonlinear collapse are *oscillons*: long-lived spherically symmetric scalar configurations held together by attractive self-interaction [1, 65, 100, 101, 103, 104, 111, 113, 118, 119]. At this point, both ρ_S and ρ_L diverge from the prediction of Sec. 3.1, and simultaneously begin diluting (almost) like cold matter. Unexpectedly, we observe the final energy density ratio ρ_S/ρ_L to scale like $t^{0.17}$, although it is unclear whether this scaling persists until the energy densities equalize, or whether it is a numerical artifact. In our later estimates of direct detection prospects, we assume that the energy density ratio is fixed after oscillon nucleation, which is conservative since we are mainly interested in the detection of ρ_S.

In spite of this numerical uncertainty, there is a possible physical explanation for why oscillon nucleation may end autoresonance. Consider that for θ_S to sustain autoresonance in any given region of space, θ_S's amplitude must remain locally large enough that its frequency can remain locked to μ. At early times, θ_S fluctuations are dominated by a single momentum mode $\tilde{k} = \tilde{k}_{\mathrm{max}}$, whose wavelength is typically much longer than the Compton wavelength of the axion field. As this mode

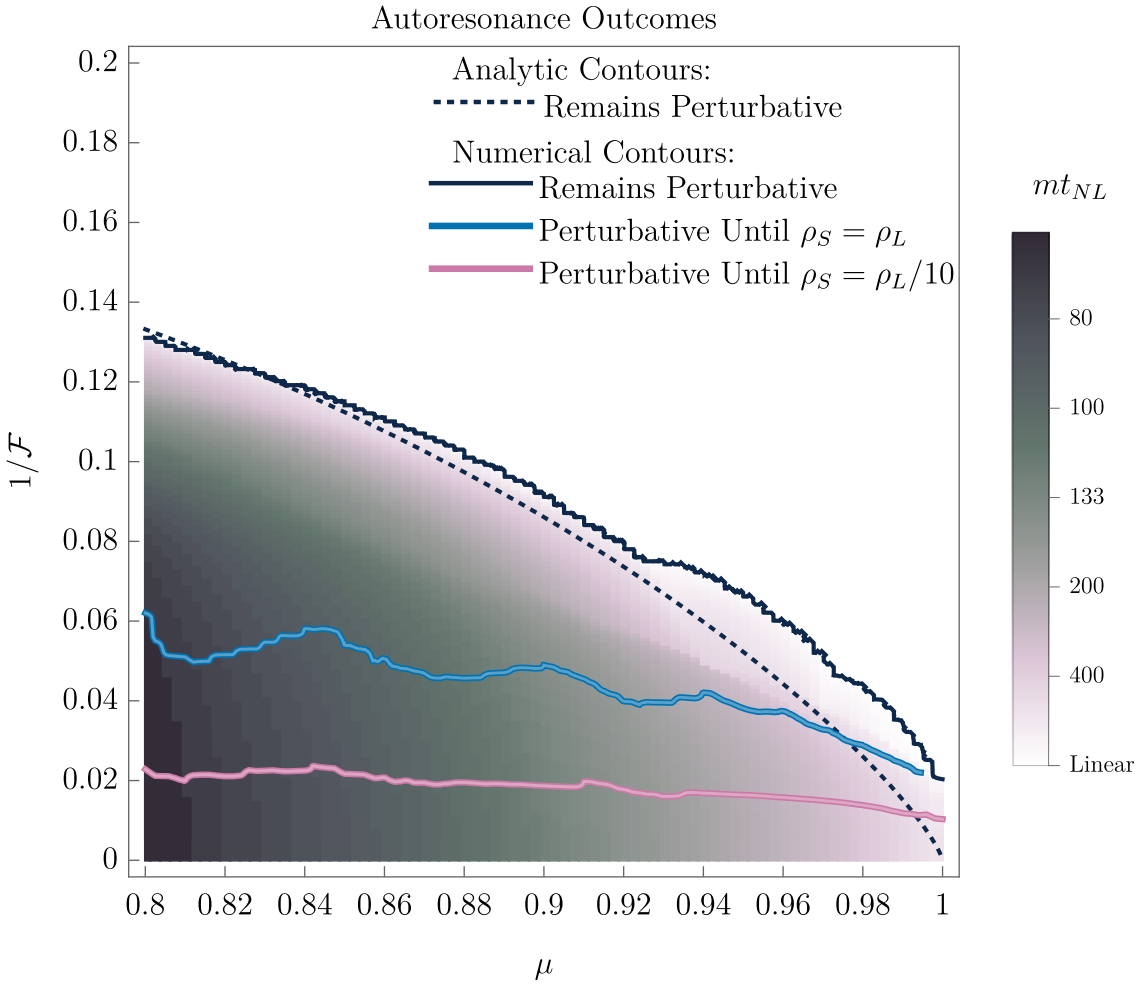

Figure 3.7: The time until the onset of nonlinearity, obtained for the specific initial conditions $\theta_S(0) = 0, \theta_L(0) = 0.8\pi$, chosen because they lead to autoresonance for the entire set of scanned $(\mu, \mathcal{F})$. The criterion for nonlinearity is that a single mode crosses $\delta\theta_S \geq 1$. Above the Solid Black contour, the axion remains perturbative indefinitely. The Dotted Black contour is the corresponding analytical estimate using the techniques of Sec. 3.2.2. Above the Blue contour, the axion only becomes non-perturbative after the energy densities of θ_S and θ_L have equalized. Below this, modes become nonlinear even earlier, but above the Magenta contour modes remain linear until θ_S has at least 1/10 the energy density of θ_L.

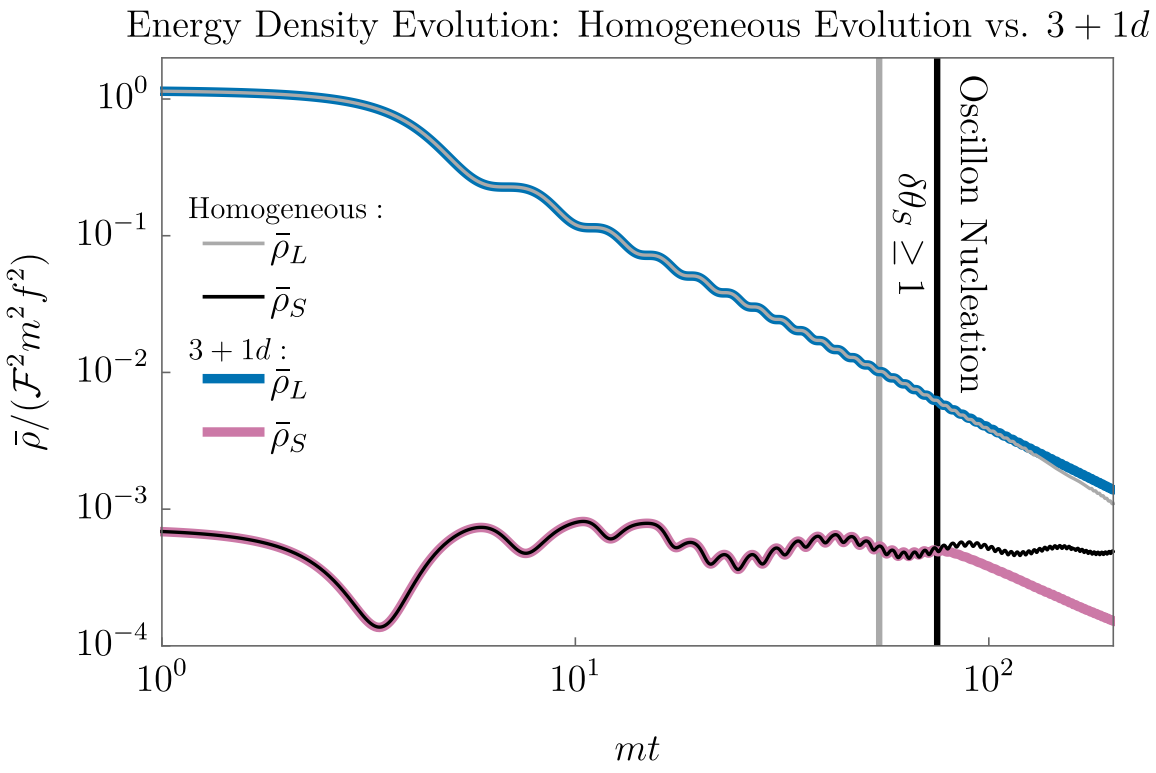

Figure 3.8: Comparison of the energy densities of the long and short axions from a homogeneous calculation (Sec. 3.1) versus the corresponding $3+1$ dimensional lattice simulation (see App. 4.9 for details). Here, $\mathcal{F} = 50$ and $\mu = 0.8$, with initial conditions $\theta_L(0) = 0.8\pi$ and $\theta_S(0) = 0$ chosen to lie in the autoresonance band. The vertical gray line represents the point beyond which θ_S fluctuations become non-perturbative, although ρ_S does not yet deviate significantly from the homogeneous expectation. Once these large θ_S fluctuations collapse under their own attractive self-interactions at the vertical black line, the autoresonant energy transfer stops, and both species dilute approximately like cold matter.

grows, a fixed fraction of the comoving volume is at a large enough amplitude for autoresonance, even after $\delta\theta_S(\tilde{k}_{\rm max})$ becomes much larger than unity. After a short time, these comoving regions of space collapse into oscillons with a fixed physical size much smaller than the scale of $\tilde{k}_{\rm max}$. At this point the long-wavelength perturbations at $\tilde{k}_{\rm max}$ have lost much of their amplitude to gradient energy and to radiation production, and most of space is below the autoresonance threshold. While the large-amplitude oscillons may in principle still remain autoresonant with θ_L, the θ_S energy density now dilutes like matter, since the comoving number density of oscillons is approximately conserved, and the non-autoresonant parts of space cannot become autoresonant.

We do, however, emphasize the need for higher resolution simulations to confirm our results and intuition. Even though it is physically reasonable that non-perturbative structure cuts off autoresonance, the opposite possibility also offers exciting observational prospects. If autoresonance is not cut off, then the short axion may become even more visible at smaller f_S (larger $\mathcal{F}$), offering enhanced direct detection prospects. On the other hand, if our numerics are confirmed, then the resulting oscillons may have parametrically enhanced lifetimes, leading to interesting present-day signatures of their own. We do not perform a full analysis of this possibility here, but we do discuss it further in Sec. 3.5.

3.2.4 Newtonian evolution and gravitational collapse

A long time after parametric resonance has concluded, the axion field is firmly non-relativistic and can be well-approximated by its Newtonian evolution. If the friendly pair comprises a majority of the dark matter, the over-dense regions begin to collapse under their own gravity and virialize at the onset of matter domination, leading to the formation of axion minihalos, which eventually comprise galactic substructure. In this section, we extend the formalism of Ref. [59] to describe this process in the case of two friendly axions. For concreteness, in this section we assume the friendly pair makes up all of the dark matter.

After parametric resonance, the axion fields are best described in the mass basis

$$\nu_h \equiv \phi_S \cos\eta + \phi_L \sin\eta\,, \tag{3.49}$$

$$\nu_l \equiv \phi_L \cos\eta - \phi_S \sin\eta\,, \tag{3.50}$$

where the ν basis is related to the old basis by the rotation angle η, and the states ν_h and ν_l have corresponding heavy and light masses m_h and m_l, all defined in App. 4.6. When $\mathcal{F} \gg (1-\mu^2)^{-1}$, the mass-eigenstates ν_h and ν_l are *mostly* comprised of ϕ_S and ϕ_L respectively. The fields ν_h and ν_l may be broken down into a homogeneous background and perturbations

$$\nu_{h,l} = N_{h,l}(t) + \sum_{\mathbf{k}} e^{i\mathbf{k}\cdot\mathbf{x}} \delta\nu_{h,l}(t,\mathbf{k}) \tag{3.51}$$

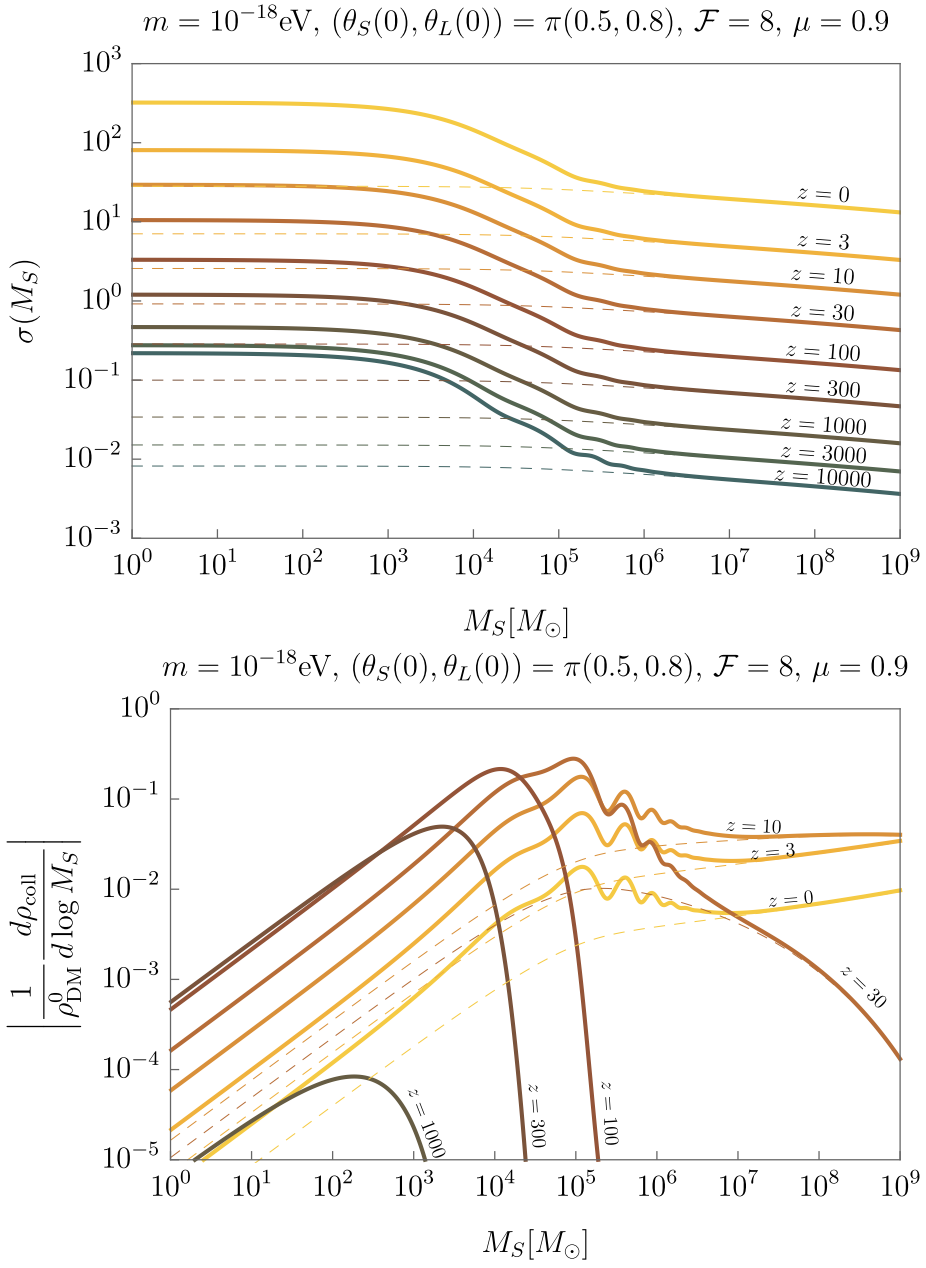

Figure 3.9: The standard deviation of the density perturbations (top) and the differential fraction of collapsed structures (bottom) at a given smoothing mass M_S. The mass scale $m = 10^{-18}$ eV is chosen to enable direct comparison with Fig. 7 of Ref. [59], where a 10^{-10} tuning of the initial misalignment angle is necessary to achieve comparable density fluctuations. The thin dashed lines correspond to the same density fluctuations and collapsed fraction for a non-self-interacting scalar of the same mass $m = 10^{-18}$ eV.

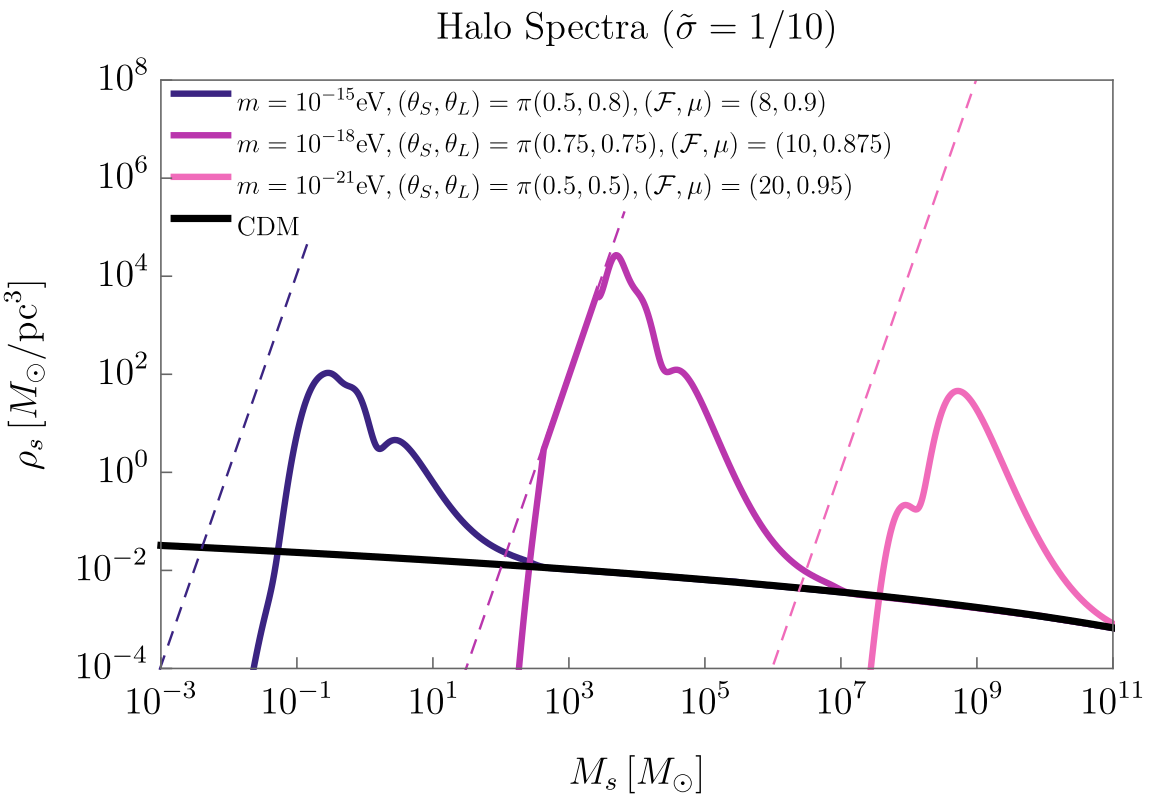

Figure 3.10: The halo spectrum ρ_s versus scale mass M_s in the friendly axion model with initial misalignments and Lagrangian parameters chosen to be representative of what one might expect to find in the axiverse. The three masses m chosen for this plot match those of Fig. 8 in Ref. [59] in order to allow for direct comparison. Note the large enhancement of subhalo density relative to the CDM expectation. The dashed lines correspond to the density of a soliton, a gravitationally-bound scalar field configuration supported by kinetic pressure, which represents the densest stable collapsed axion structure of a given mass. The soliton mass-density relationship is given by $\rho_s \approx 0.067 G^3 m^6 M_s^4$ [60].

yielding the corresponding relative density perturbations $\rho_{h,l} = \bar{\rho}_{h,l}(1 + \delta_{h,l})$,

$$\delta_{h,l} = \frac{\partial_t N_{h,l} \partial_t \delta\nu_{h,l} + m_{h,l}^2 N_{h,l} \delta\nu_{h,l}}{\frac{1}{2}(\partial_t N_{h,l})^2 + \frac{1}{2} m_{h,l}^2 N_{h,l}^2} \,. \tag{3.52}$$

where $\bar{\rho}_{h,l}$ is the average density of $\nu_{h,l}$ respectively.

Following Ref. [59], we now change variables from t to $y \equiv a(t)/a_{\rm eq}$, where $a_{\rm eq}$ is the scale factor at matter-radiation equality. The density fluctuations deep inside the horizon $\tilde{k}^2 \gg H/m$ then obey the Newtonian equations of motion

$$\begin{aligned} 0 = (1+y)\delta'' + \left(\frac{3}{2} + \frac{1}{y}\right)\delta' \\ - \left(\frac{3}{2y} F_G - \frac{1}{y^3}\tilde{k}^2 C_s^2 - \frac{1}{y^2}\tilde{k}^4 C_Q^2\right)\delta \,, \end{aligned} \tag{3.53}$$

where we have defined the vector of relative density perturbations $\delta \equiv (\delta_h, \delta_l)^T$, and primes denote differentiation with respect to y. The matrices of Eq. 3.53 are defined

$$C_s^2 = \frac{3\sqrt{2} m H_{\rm eq} M_{\rm Pl}^2}{\bar{\rho}_h + \bar{\rho}_l} \begin{pmatrix} \frac{\lambda_{hh}\bar{\rho}_h}{16 m_h^4} & \frac{\lambda_{hl}\bar{\rho}_l}{8 m_h^2 m_l^2} \\ \frac{\lambda_{hl}\bar{\rho}_h}{8 m_h^2 m_l^2} & \frac{\lambda_{ll}\bar{\rho}_l}{16 m_l^4} \end{pmatrix} , \tag{3.54}$$

$$C_Q^2 = \begin{pmatrix} m^2/m_h^2 & 0 \\ 0 & m^2/m_l^2 \end{pmatrix} , \tag{3.55}$$

$$F_G = \frac{1}{\bar{\rho}_h + \bar{\rho}_l} \begin{pmatrix} \bar{\rho}_h & \bar{\rho}_l \\ \bar{\rho}_h & \bar{\rho}_l \end{pmatrix} , \tag{3.56}$$

where $\lambda_{hh,hl,ll}$ are the quartic interactions in the mass basis of even parity (corresponding to interactions with even numbers of both species), whose full expressions are given in App. 4.6. The matrices C_s and C_Q are coefficients representing the strength of self-interactions and kinetic pressure respectively, which together comprise the effective speed of sound. The matrix F_G represents the attractive force of gravity. These equations may then be numerically integrated to late times.

Having solved for the full history of the linear density perturbations, we can now describe the nonlinear collapse of these density perturbations into small-scale structures. The formalism to describe nonlinear gravitational collapse is well-known [209] and worked out in detail in Ref. [59], which we summarize here for completeness.

In the extended Press-Schechter formalism, a local overdensity is considered to have collapsed if it exceeds the critical overdensity $\delta_c = 1.686$ [210]. In the two-axion model, the total DM overdensity in momentum space is

$$\delta(t, \mathbf{k}) \equiv \frac{\bar{\rho}_h(t)\delta_h(t, \mathbf{k}) + \bar{\rho}_l(t)\delta_l(t, \mathbf{k})}{\bar{\rho}_h(t) + \bar{\rho}_l(t)} \,. \tag{3.57}$$

To obtain a distribution for the density perturbations in position space, we smooth the density field $\delta(t,\mathbf{x}) \equiv (2\pi)^{-3}\int \mathrm{d}^3k e^{\mathrm{i}\mathbf{k}\cdot\mathbf{x}}\delta(t,\mathbf{k})$ over a radius R_S using the spherical top-hat window function $W(R_S,\mathbf{x}) = \Theta(R_S - |\mathbf{x}|)(3/(4\pi R_S^3))$:

$$\delta(t,\mathbf{x},R_S) \equiv \int \mathrm{d}^3x' W(R_S,\mathbf{x}-\mathbf{x}')\delta(t,\mathbf{x}')\,. \tag{3.58}$$

The mass contained within the smoothing radius is $M_S = (4\pi/3)\rho^0_{\mathrm{DM}}R_S^3$, where $\rho^0_{\mathrm{DM}} = 3.3\times 10^{-8}M_\odot/\mathrm{pc}^3$ is the average dark matter density in the present-day universe.

Assuming that the density perturbations obey a Gaussian distribution, the differential collapsed fraction of energy density per unit mass is

$$\frac{1}{\rho^0_{\mathrm{DM}}}\frac{d\rho_{\mathrm{coll}}}{d\log M_S} = \sqrt{\frac{2}{\pi}}\frac{\delta_c}{\sigma(M_S)}\left|\frac{d\log\sigma(M_S)}{d\log M_S}\right| e^{-\frac{\delta_c^2}{2\sigma^2(M_S)}}\,, \tag{3.59}$$

where the density fluctuation variance is $\sigma^2(M_S) = \langle\delta(t,\mathbf{x},R_S)^2\rangle$. We plot the variance and differential collapsed fraction in Fig. 3.9 for a representative set of initial conditions and Lagrangian parameters for a mass scale $m \approx 10^{-18}$eV to allow for direct comparison to figure 7 of Ref. [59]. We see that an early period of autoresonance has enhanced structure at the mass scale $M_S \approx 10^5 M_\odot$, which collapses significantly earlier than the larger-scale structure comprising entire galactic halos.

In Ref. [59], the authors point out two downsides of Press-Schechter theory. First, $\delta(t,\mathbf{x},R_S)$ can be large even if there is no structure at the scale R_S, so long as there is structure at larger scales. Second, the differential collapsed fraction does not count substructure. To remedy this, they propose the use of a smoothing function in momentum space which isolates structures of scale R,

$$W(\mathbf{k},R) = \frac{1}{(2\pi\tilde{\sigma}^2)^{1/4}}\exp\left[-\frac{\log(|\mathbf{k}|R/\pi)^2}{4\tilde{\sigma}^2}\right]\,. \tag{3.60}$$

Using Eq. 3.58 with this new window function, we compute the variance $\sigma^2(M_S)$,

$$\sigma^2(M_s) = \int \mathrm{d}\log k\,|\delta(t,k)|^2|W(\mathbf{k},R_s)|^2\,. \tag{3.61}$$

Structures at a given mass scale M_s are considered to have collapsed at a time corresponding to the scale factor $a_{\mathrm{coll}}(M_s)$ when a 1-σ overdensity exceeds δ_c, where $M_s = \rho^0_{\mathrm{DM}}(4\pi/3)R_s^3$. The resulting collapsed structure has a well-known density roughly 200 times the ambient density at the time of collapse $\rho_s \approx 200\times\rho^0_{\mathrm{DM}}a_{\mathrm{coll}}^{-3}$. We plot the resulting halo spectra in Fig. 3.10 for three representative sets of initial conditions and Lagrangian parameters, where we have chosen mass scales that match those in Fig. 8 of Ref. [59] to enable direct comparison. This halo spectrum peaks at a scale mass

determined by the $\tilde{k}_{\rm max}$ in Sec. 3.2.2, which is well-approximated by:

$$M_s \sim \frac{4}{3}\pi\rho_{\rm DM}(H=m/2)\left(\frac{2\pi}{m\tilde{k}_{\rm max}}\right)^3 \sim 1.2\times10^4 M_\odot \left(\frac{10^{-19}\ {\rm eV}}{m}\right)^{3/2}\left(\frac{5}{\tilde{k}_{\rm max}}\right)^3 . \tag{3.62}$$

3.3 Signatures

So far, we have primarily focused on the early-time dynamics of a pair of friendly axions, but in this section we turn to the late-time observable effects of these dynamics. Broadly they fall into two categories.

First, autoresonance can facilitate a significant transfer of energy density from an axion with a large decay constant to an axion with a much smaller decay constant. Since the axion's couplings to the SM are generically suppressed by its decay constant, axions produced via autoresonance can be coupled significantly more strongly to the SM than axions produced via the usual misalignment mechanism, and can be observable even if they make up only a small subcomponent of DM. We discuss this point and outline future detection prospects in Sec. 3.3.1.

The second broad class of observable effects are indirect gravitational signatures. As discussed in Sec. 3.2, an era of autoresonance can lead to significant growth of density fluctuations that can collapse into gravitationally-bound structures earlier than would be predicted by ΛCDM, as shown in Fig. 3.9. This collapse requires that the pair of friendly axions make up the entirety of dark matter, but if this happens such structures can be detectable through their gravitational effects. The halo substructure turns out to be quite similar to that produced by the mechanism of Ref. [59], so the techniques discussed therein for detecting such structures apply here as well. We briefly review these in Sec. 3.3.2. Finally, both the long and short axions can potentially be constrained by black hole superradiance; we comment on this in Sec. 3.3.3. The reach of all signatures discussed in this section are summarized in Fig. 3.12 for the case where the friendly axions are the DM, and in Fig. 3.11 for the case where they are only a subcomponent.

3.3.1 Enhanced direct detection prospects

The most striking effect of axion friendship to significantly improve the prospects of probing an axiverse in direct detection experiments. In the absence of interactions, all axions with similar masses would be equally detectable provided they all started at similarly untuned initial misalignment angles. An axion with a smaller decay constant f will have a smaller present-day abundance, but its stronger coupling to the SM precisely cancels this out when it comes to observability. Quantitatively, haloscope experiments couple to the combination $g_{a\gamma\gamma}^2\rho_{\rm ax}$, where the axion-photon coupling is expected to be of order $g_{a\gamma\gamma} \simeq \alpha/4\pi f$ with α the QED fine-structure constant. An axion of a

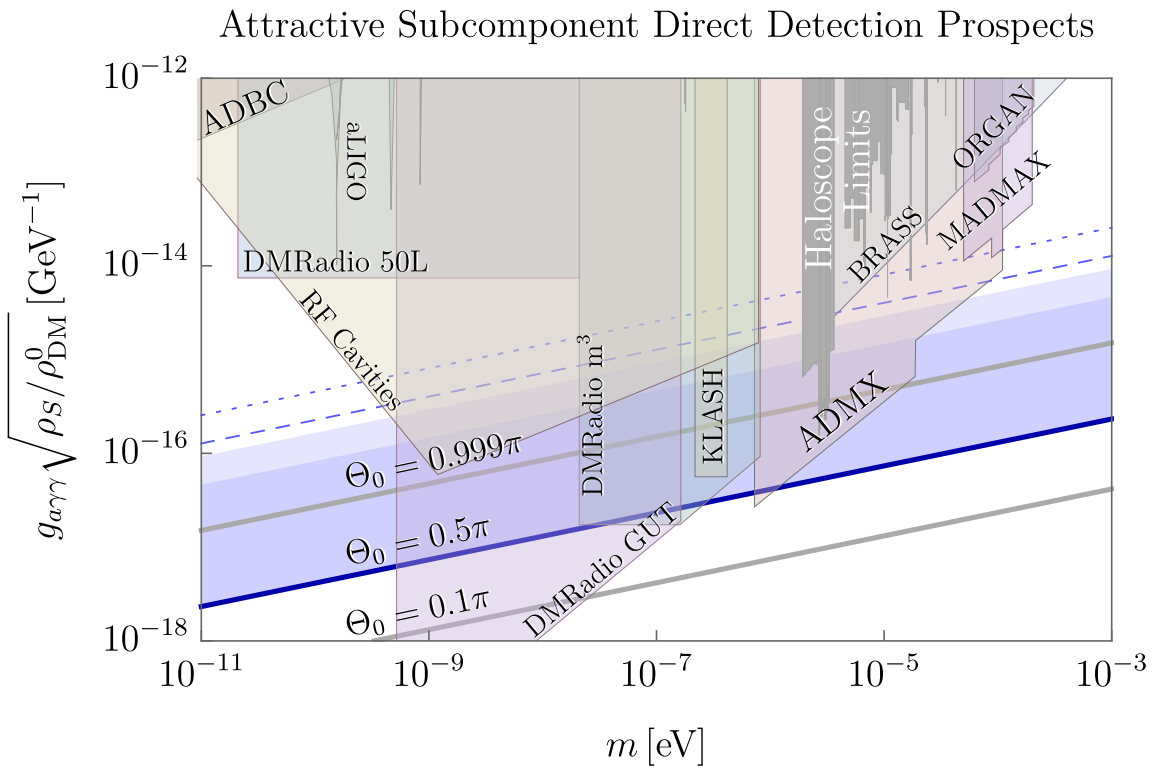

Figure 3.11: Enhanced direct detection prospects for a short axion, assuming that the friendly pair comprises a small fraction of the total dark matter energy density. The darker blue band shows the prospects for $\mu = 0.8$ and $\Theta_L(0) = 0.5\pi$ in the large $\mathcal{F}$ limit, where the possible enhancement saturates for $\mathcal{F} \gtrsim 20$ due to the formation of nonperturbative structure (Sec. 3.2.3). For $\mu = 0.99$, the possible enhancement saturates for $\mathcal{F} \gtrsim 40$ (light blue band). As $\mathcal{F}$ decreases below the saturation value, the visibility decreases linearly with $\mathcal{F}$. This enhanced visibility should be compared to that of a single free axion with initial misalignment $\Theta_0 = 0.5\pi$ (middle solid blue line). The dashed and dotted blue lines are the sensitivity prospects for $\mu = 0.8$ and $\mu = 0.99$ respectively in the large $\mathcal{F}$ limit with $\Theta_L(0) = 0.9\pi$. Because the friendly pair makes up only a subcomponent of DM, its overdensities do not collapse under self-gravity, and minihalos never form. Thus, an $\mathcal{O}(1)$ fraction of ρ_S in the galaxy is ambient (as opposed to clumped) and will pass through direct detection experiments. As a result, the direct detection prospects are improved relative to those in Fig. 3.12. This plot was made using prospects compiled in [2, 3, 21–28, 30, 31, 33, 34].

given mass m will thus be detectable to an experiment with sensitivity:[7]

$$\left(g_{a\gamma\gamma}^2 \frac{\rho_{\rm ax}}{\rho_{\rm DM}^0}\right)_{\rm naïve}^{1/2} \sim 2.3 \times 10^{-17}\ {\rm GeV}^{-1} \left(\frac{\Theta_0}{\pi/2}\right) \left(\frac{m}{10^{-7}\ {\rm eV}}\right)^{1/4}, \tag{3.63}$$

where we have normalized to the current universe-average DM density, Θ_0 is its initial misalignment, and this formula receives logarithmic corrections near $\Theta_0 = \pi$. Note importantly that Eq. 3.63 is independent of the decay constant. For this reason, in this naive scenario, an axion haloscope experiment sensitive to a wide range of masses is unlikely to see any axiverse axion until it reaches the sensitivity threshold of Eq. 3.63. However, once it does reach this point it may see several axion signals at the same time, even from axions which make up only a small subcomponent of the DM.

In contrast, we have seen that for a pair of friendly axions in the axiverse, autoresonance can transfer nearly all of the energy density from the long axion (with the larger decay constant f_L) to the short axion (with the smaller decay constant f_S). This results in a "best of both worlds" scenario: if autoresonance completes, the short axion's energy density is set by f_L while its coupling to the SM is set by f_S. This makes the short axion much more observable, enhancing its signal strength relative to Eq. 3.63:

$$\begin{aligned}\left(g_{a\gamma\gamma}^2 \frac{\rho_{\rm ax}}{\rho_{\rm DM}^0}\right)_{\rm friendly}^{1/2} &= \mathcal{F} \left(g_{a\gamma\gamma}^2 \frac{\rho_{\rm ax}}{\rho_{\rm DM}^0}\right)_{\rm naïve}^{1/2} \\ &\sim 4.6 \times 10^{-16}\ {\rm GeV}^{-1} \left(\frac{\mathcal{F}}{20}\right) \left(\frac{\Theta_0}{\pi/2}\right) \left(\frac{m}{10^{-7}\ {\rm eV}}\right)^{1/4}\end{aligned} \tag{3.64}$$

where Θ_0 refers to the long axion's initial misalignment angle. Although there may only be a few pairs of friendly axions in the axiverse which end up autoresonating, these few pairs (or, more precisely, the short axion in each of these pairs) may become the one most visible to direct detection experiments.

For fixed $\mathcal{F}$, the enhancement to the signal strength (Eq. 3.64) does not depend on whether the friendly pair makes up all of DM or only a subcomponent, but this distinction can still matter for direct detection due to the formation of spatial structure. The subcomponent case is simpler, and we summarize the enhancement to direct detection prospects in Fig. 3.11. Any experiment whose projected sensitivity intersects the blue regions (set by different values of $\mathcal{F}$) will be able to probe any friendly axion pair in their mass range with large-enough $\mathcal{F}$. Attractive autoresonance may thus be visible to many proposed experiments such as ADMX [23], DM Radio [21, 30], HAYSTAC [61], KLASH [22], superconducting RF cavities [25–27], and, optimistically, BRASS [24] and MADMAX [31].

If the friendly pair comprises the totality of DM, the situation is slightly more complicated. In

[7] This expression and the analysis of this section refer to experiments that probe the axion through its coupling to photons. There are other potential axion couplings that can be probed which are subject to similar analyses, but we do not discuss them here.

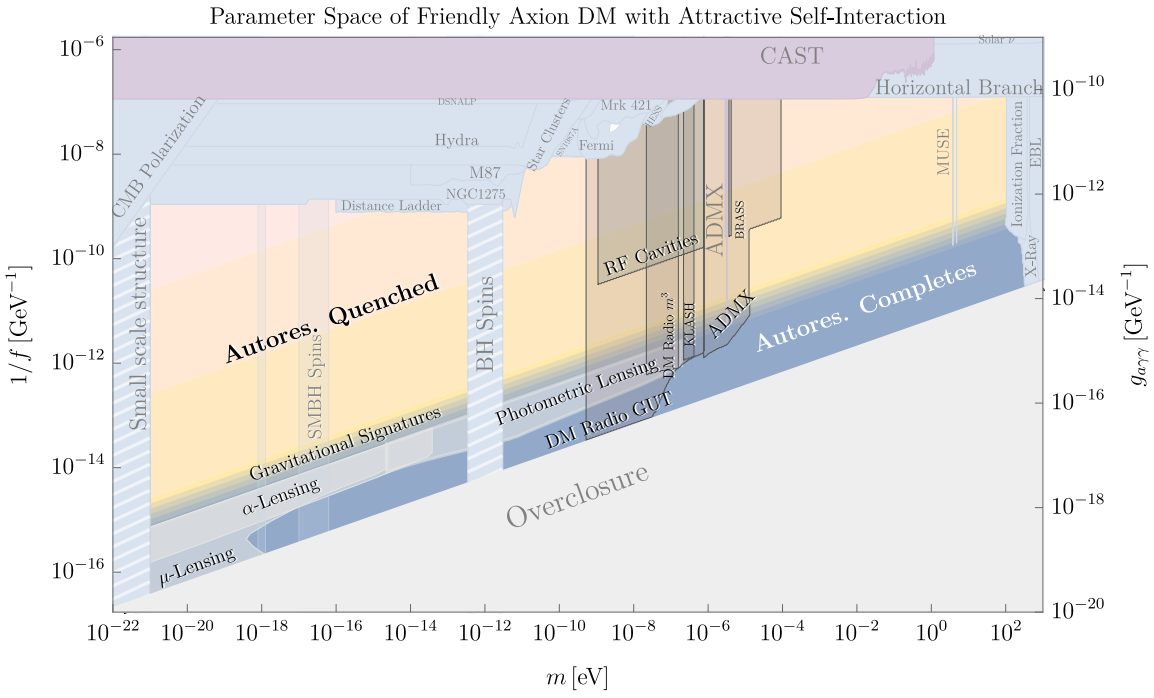

Figure 3.12: Summary of parameter space, constraints, and signatures for friendly axions in the concrete model of Eq. 3.5 for $\mu = 0.8$ and representative initial conditions that result in autoresonance. This plot is for the case where the friendly pair makes up the entirety of DM, and the axes m and f refer to the mass and decay constant of the short axion specifically. In the region labeled "Autores. Completes," autoresonance lasts long enough that nearly all of the axion energy density is in the form of θ_S, while in the region labeled "Autores. Quenched," nonperturbative structure halts autoresonance early and the short axion makes up only a subcomponent. Throughout, we assume that the short axion has a coupling to photons of size $g_{a\gamma\gamma} \simeq \frac{\alpha}{4\pi f}$ and we plot direct detection constraints and projections based on this coupling. Even when θ_S is only a subcomponent, it can be a very visible subcomponent due to its enhanced coupling to the SM. The regions labeled "Gravitational Signatures" are discussed in Sec. 3.3.2 and elaborated on in Fig. 3.13. The regions labeled "BH Spins" and "SMBH Spins" refer to BH superradiance constraints discussed in Sec. 3.3.3. This plot was made using limits compiled in [2–9, 9, 10, 10–16, 16, 17, 19–27, 30, 36–52, 54–58, 61].

this case, as discussed in Sec. 3.2, the self-interactions of θ_S can result in the growth of density perturbations that gravitationally collapse earlier than they would have in ΛCDM and thus form dense axion minihalos. The region where these structures remain perturbative until most of the axion energy density is in the short axion is labeled "Autores. Completes" in Fig. 3.12, but even in this case anywhere from 95–99% of the dark matter can reside in these minihalo structures.[8] If the minihalos are numerous enough that one may expect at least one encounter with a detector during its experimental runtime, then the experimental sensitivity is not significantly changed by such substructure, although for a resonant experiment the scanning strategy may need to be modified to maximize the likelihood of scanning the correct frequency during a minihalo encounter [59]. This is generally the case for axions with mass $m \gtrsim 10^{-3}$ eV, where the minihalos are light and therefore extremely numerous. For smaller axion masses, where the minihalos are heavy and fewer in number, direct detection experiments are sensitive only to the ambient background fraction of DM. To be conservative, we assume an ambient fraction of only 1% when computing the projected sensitivity of experiments to short axions lighter than 10^{-3} eV.

For larger decay constant ratios $\mathcal{F} \gtrsim 20$, θ_S can grow nonperturbative fluctuations during autoresonance. In this case, detailed simulations are required to understand the full dynamics of autoresonance, but our initial numerical explorations provide tentative evidence that the autoresonant energy transfer is quenched shortly after the θ_S field becomes nonperturbative. Most of the friendly pair's energy density remains in the long axion, but the short axion's energy density is still boosted compared to the "single axion misalignment" expectation of Eq. 3.2. In addition, if autoresonance is quenched, the overall density fluctuations in the dark sector cease their parametric resonant growth before becoming $\mathcal{O}(1)$. The large fluctuations in the θ_S energy density only lead to $\mathcal{O}(\mathcal{F}^{-2}(mt_{\rm NL})^{3/2})$ fluctuations in the total axion energy density, where $t_{\rm NL}$ is the time it takes for $\delta\theta_S$ to become $\mathcal{O}(1)$. These fluctuations can in principle still seed early collapse during matter domination, but computing their precise effects is difficult due to the uncertainties inherent in the nonlinear collapse of the θ_S field.

We adopt a conservative strategy to estimating the sensitivity of future direct detection experiments in the event that autoresonance is quenched. We take the short axion energy density ρ_S to be given by its value at the point that autoresonance ends (i.e. the point at which the θ_S perturbations become nonlinear), redshifted as matter to late times. Nonperturbative θ_S fluctuations at the end of autoresonance correspond to $\mathcal{O}(\rho_S/(\rho_S+\rho_L))$ perturbations in the total matter energy density, which remain approximately frozen during radiation domination and grow linearly with the scale factor during matter domination. They then undergo Newtonian collapse at a scale factor a given

[8] We estimate the ambient dark matter fraction by computing the collapsed fraction in structures whose mass is smaller than that of the Milky Way, and subtracting that from the total collapsed fraction at the present day. This calculation neglects several important effects, including tidal stripping, which may boost the ambient dark matter component. The resulting ambient fractions we found were all between 1% and 30%, and we quote 1% to be conservative.

by:

$$\frac{\rho_S}{\rho_S + \rho_L} \frac{a}{a_{\rm eq}} = \delta_{\rm c} \,. \tag{3.65}$$

If these structures collapse before the present-day ($a < 1$), some of the θ_S and θ_L energy densities will reside in dense minihalo structures that may transit an experiment only rarely. To be conservative, we quote an ambient fraction of only 1% (see Footnote 8). If these structures have not yet collapsed by the present-day ($a > 1$), we consider an $\mathcal{O}(1)$ fraction of our local halo's θ_S density to reside in an ambient component. This occurs for a density ratio at least as small as

$$\frac{\rho_S}{\rho_S + \rho_L} \lesssim \delta_{\rm c} a_{\rm eq} \approx \frac{1}{2000} \,. \tag{3.66}$$

The effects of substructure can thus be viewed as occurring for three distinct ranges of $\mathcal{F}$. For $\mathcal{F} \lesssim 20$, autoresonance completes and ρ_S dominates the dark matter density, although its fluctuations suppress the ambient component, reducing overall direct detection sensitivity relative to the case where the friendly pair collectively makes up only a DM subcomponent. For $\mathcal{F} \gtrsim 20$, ρ_S begins to drop by $\mathcal{F}^{-2}$, but this is exactly counteracted by its enhanced coupling $\propto \mathcal{F}^2$. For even larger $\mathcal{F} \gtrsim 20\sqrt{2000} \approx 900$, ρ_S comprises an $\mathcal{O}(1/2000)$ subcomponent or less, and its fluctuations no longer lead to early collapse, boosting overall detectability relative to when $\mathcal{F} \lesssim 900$. Altogether, these effects result in the direct detection prospects of Fig. 3.12 for the case where the friendly pair makes up all of DM.

3.3.2 Gravitational signatures of substructure

As discussed in Sec. 3.2, if the friendly axion pair makes up a majority of the dark matter then autoresonance can lead to DM substructures that are denser than predicted by ΛCDM. In this respect it is quite similar to the mechanism of Ref. [59], and indeed the halo mass spectrum predicted by that mechanism is quite similar to the one that emerges from a period of autoresonance. We are thus able to adapt their subhalo detection projections to the case studied here, and we summarize the results in Fig. 3.13. We dedicate the rest of this section to a brief review of the two most relevant signatures, suppressing others which are interesting but slightly less sensitive. For a more complete treatment we refer the reader to Ref. [59] and the references cited therein.

The first class of indirect signatures we focus on are *astrometric lensing signatures*. A dense, heavy halo passing through our line-of-sight weakly lenses all background stars, and the lensing pattern is correlated across all stars behind the halo. A telescope with good angular resolution and a wide field-of-view can in principle look for such correlated deflections and infer the presence of an intervening weak lens. In practice, since the true positions of individual stars are unknown, it is impossible to observe the correlations of the stars' angular positions on the sky, but as the lens moves

it will induce correlated proper motion and proper acceleration of the background star field. A high-angular-resolution experiment that periodically measures the positions of a large number of stars can search for such correlated motions, either with templates or by looking for global correlations. Several such astrometric experimental efforts either exist (*Gaia* [211], HST [212]) or are planned (*Theia* [213], WFirst [214], SKA [215], TMT [216]). Ref. [62] worked out dense subhalo sensitivity projections for *Gaia* and *Theia*, and we report these in Fig. 3.13 for the halo mass spectrum predicted in Sec. 3.2.

Another potential class of observable signatures are those associated with *photometric microlensing*. The basic idea is to monitor a distant star and look for changes in its brightness that would indicate a gravitational lens passing through the line of sight. This technique has been used to place constraints on extremely compact objects (such as primordial black holes), but in general it is harder to use it for dilute, gravitationally-bound subhalos because they only lens weakly and thus have minute effects on a star's observed brightness. To deal with this, Ref. [63] has proposed using highly-magnified stars that are only observable because they lie close to a critical gravitational lensing caustic of a galaxy cluster. If the DM in the galaxy cluster is composed of subhalos, the virial motion of these subhalos will add Poissonian noise to the position of the star, which has an amplified impact on the star's brightness. This noise has a characteristic frequency and amplitude that depends on the DM halo mass spectrum, and Ref. [63] suggests the observation of this noise can probe DM substructure. Ref. [59] has made projections of the sensitivity of such a technique for gravitationally-bound subhalos and we report these in Fig. 3.13 for the halo spectrum calculated in this paper. It should be noted that these projections are subject to potentially significant uncertainties associated with the galactic evolution (and tidal stripping) of such gravitationally-bound subhalos, and we caution that proper simulations must be done to confirm them.

For $\mathcal{F} \gtrsim 20$, perturbations in the short axion field can grow nonperturbative and quench the autoresonance before the majority of the axion energy density is transferred to θ_S. In this case, even though there are large fluctuations in the short axion field, the overall density fluctuations are small because the majority of the axion energy density is still in θ_L. Structures thus collapse gravitationally at roughly the same time they would have in ΛCDM, and all gravitational signatures of autoresonance disappear. We show this in Fig. 3.12, where the gravitational signatures appear only in the region where θ_S can compose the totality of dark matter.

3.3.3 Superradiance signatures and constraints

The phenomenon of black hole superradiance (SR), by which the angular momentum of an initially rapidly rotating black hole (BH) is transferred to a cloud of bound axions generated around the BH, can be used to constrain axions at ultralight masses by measuring the age and spin of astrophysical BHs [73, 165, 172, 217–222]. SR bounds are quite unique in that they are more constraining for an axion which has *small* interactions, as interactions tend to slow down the extraction of angular

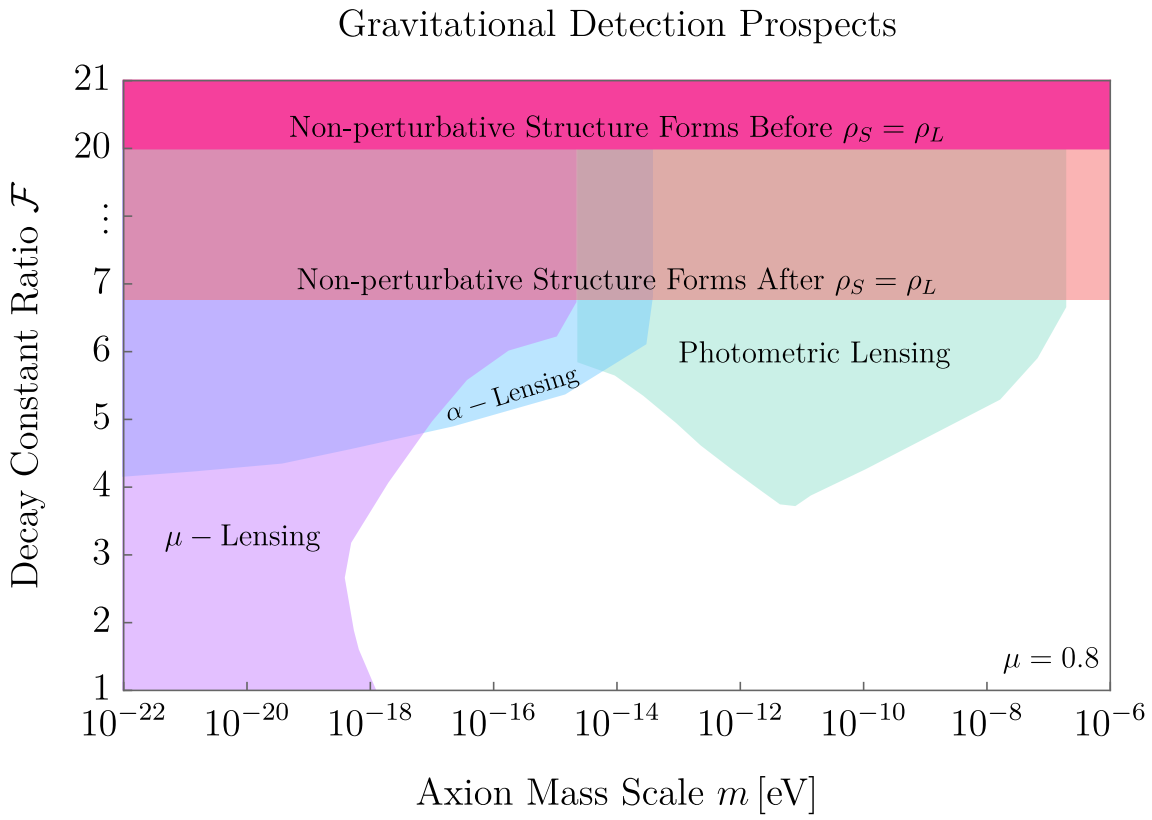

Figure 3.13: Gravitational detection prospects for short-axion DM substructure. This plot was generated for $\mu = 0.8$, but does not have significant dependence on μ or the initial misalignment angles (provided they result in autoresonance). The Purple "μ-lensing" and Blue "α-lensing" regions show projected sensitivities of future telescopes to weak astrometric lensing of local stars (correlated distortions in their velocities with SKA and their accelerations with *Theia* respectively) [62]. The Teal "photometric lensing" region may be probed through brightness fluctuations of a critically-lensed distant star [59,63]. Inside the Peach region, nonperturbative structures form during radiation domination, making this region subject to theoretical uncertainties about how this substructure will resolve today. Nonetheless, we expect that $\mathcal{O}(1)$ density fluctuations will collapse immediately after matter-radiation equality and lead to similar direct detection prospects as for the perturbative region below. In the Hot Pink region at the top, nonperturbative structure quenches autoresonance before the two axion energy densities equalize; in this region the short axion is a subcomponent and gravitational detection prospects die off quickly as $\mathcal{F}$ increases.

momentum from the BH into the cloud. Even a single axion with a potential typified by Eq. 3.1 inevitably has *self*-interactions, which at leading order are quartic with dimensionless coupling $\lambda \sim m^2/f^2$. As one moves towards values of f smaller than $\sim 10^{15}$ GeV in axion parameter space, the growth of the SR cloud is cut off at perturbative values of θ and angular momentum can no longer efficiently be extracted from the BH [222].

For the case of the coupled short and long axions studied here, as long as the evolution remains perturbative in θ_S, θ_L, SR is better studied in the mass basis in which flavor oscillations are removed (App. 4.6). For $\mathcal{F} \gg (1-\mu^2)^{-1}$, the heavy state $\nu_h \approx \phi_S$ has quartic self-interactions $\lambda_{hh} \approx m^2/f^2$, while the light state $\nu_l \approx \phi_L$ has quartic self-interactions $\lambda_{ll} \approx (\mu/\mathcal{F})^2 \lambda_{hh}$. As emphasized previously, in the scenario in which the friendly axion pair is DM, the light state (i.e. the long axion) must fall within the region of parameter space that would yield the correct present-day DM density in the absence of friendly interactions (i.e. within a band centered on the "$\Theta_0 = \pi/2$ Misalignment" line of Fig. 3.1). The coupling λ_{ll} is therefore fixed. Depending on the value of $\mathcal{F}$, the self-coupling λ_{hh} of the heavy state (i.e. the short axion) may or may not be small enough that the SR bounds apply to the short axion directly. If $\mathcal{F}$ is large enough that the short axion cannot be constrained by SR, then the scenario of two friendly axions being DM is still constrained by SR bounds on the long axion (one can check that cross-couplings do not change those bounds in that limit). For this reason, we have shown the SR bounds from astrophysical BHs on Figs. 3.1 and 3.12 as extending to arbitrarily large $\mathcal{F}$, since they exclude a long axion living near the "$\Theta_0 = \pi/2$ Misalignment" line within that mass range.

Because of the complicated merger history of supermassive BHs and the larger uncertainties on their measured parameters, it is difficult to make a definite claim that a lack of spindown implies the absence of an axion in the spectrum. A more detailed understanding of merger histories and better measurements could make supermassive BHs robust probes of axions in the $10^{-18} - 10^{-16}$eV mass range in the future. We show this region on Fig. 3.1 and Fig. 3.12 in a lighter shade to reflect this uncertainty.

We note that there is a somewhat tuned—but not entirely excluded—scenario in which *neither* DM axion can be constrained by SR bounds on BH spins. If μ is close enough to unity that $\mathcal{F} \ll (1-\mu^2)^{-1}$, one can have that $\lambda_{ll} \simeq \lambda_{hh} \simeq m^2/f^2$ and all mass states have comparable self-interactions. In the interaction basis, this can be explained by observing that strong mixing between the two axions causes the long axion to inherit the strong self-interactions of the short axion via flavor oscillations. One might view this as the spindown signatures of an axion with a nominally large decay constant being masked by the presence of a closely resonant axion with a small decay constant.

If the friendly axion pair is a subcomponent of DM, the long axion is not required to live near the "$\Theta_0 = \pi/2$ Misalignment" line of Fig. 3.1. In this case, both axions can have small enough decay constants to evade SR spin bounds. Rather than rapidly extracting the angular momentum from a

BH and storing it in a SR cloud, axions with small decay constants form smaller clouds that slowly transfer angular momentum directly from the BH to spatial infinity in the form of coherent axion waves that could be detected on Earth by planned nuclear magnetic resonance experiments [222]. The signal strength on Earth of these small clouds scales as the axion mass to the fourth power, but does not scale with the decay constant. It is therefore possible that small clouds of both short and long axions exist simultaneously around a BH and emit axion waves at nearby frequencies $\sim m$ and $\sim \mu m$ that are similarly detectable. A more detailed study of cross-cloud interactions would be necessary to fully understand this scenario.

3.4 Repulsive self-interactions

So far our analysis has been focused on the axion potential of Eq. 3.5, which has attractive self-interactions for θ_S. This is often the case in the most minimal axion potentials, because instanton contributions typically enter the potential as cosines, which have negative (i.e. attractive) quartic interactions. However this is not a universal rule, and repulsive self-interactions can exist in axion models [172, 223]. In this section we summarize the phenomenology when the short axion has repulsive self-interactions. As we will see, autoresonance can occur with few differences from the attractive case. Importantly, however, repulsive self-interactions can prevent all structure growth during autoresonance, implying that autoresonance cannot be cut off early by non-perturbative structures. Therefore, if the system lands on autoresonance, it is guaranteed to complete the energy transfer, further enhancing signatures at large decay constant hierarchies $\mathcal{F} \gg 20$, for which attractive self-interaction signatures would be saturated (see Fig. 3.11). Future direct detection experiments such as ADBC [28], DANCE [29], DM Radio 50L [30], LAMPOST [32], aLIGO [33], ORGAN [34], and TOORAD [35] may therefore see a self-repulsive short axion, even though they cannot access the parameter space relevant to an attractive theory.

To make our discussion concrete, consider the following axiverse-inspired potential with repulsive θ_S self-interactions

$$V(\theta_S, \theta_L) = m^2 f^2 \left(\zeta^2(1-\cos(\theta_S+\theta_L)) + (1-\cos(\mathcal{Q}\theta_S+\delta)) + \mu^2\mathcal{F}^2(1-\cos\theta_L)\right) . \tag{3.67}$$

For small θ_S amplitudes, interactions are repulsive if $1 < \mathcal{Q} \lesssim \zeta \lesssim \mathcal{Q}^2$ and $3\pi/4 \lesssim \delta \lesssim 5\pi/4$, and repulsive autoresonance may occur if $\mu^2 \gtrsim \zeta^2 - \mathcal{Q}^2$, and $\mathcal{F} \gg \zeta$.

A good diagnostic of autoresonance is to measure the late-time energy density ratio of θ_S and θ_L as in Fig. 3.5. As before, it is often helpful to think about the energy density ratio in the interaction basis, since it is this quantity that late-time signatures depend on. However, the partition of energy between the two fields becomes ambiguous beyond the scale of flavor oscillations. A useful choice is

the time-average of the corresponding kinetic term

$$\rho_S \approx \langle (\partial_t \Theta_S)^2 \rangle \,, \qquad \rho_L \approx \mathcal{F}^2 \langle (\partial_t \Theta_L)^2 \rangle \,. \tag{3.68}$$

This estimate generalizes easily to theories with a large number of fields and instantons, provided the mass matrix is close to diagonal. We plot the late time energy density ratios in Fig. 3.14 for a representative set of parameters, which is meant to be compared to Fig. 3.5. This plot shows two important distinguishing features. First, autoresonance occurs for driver frequencies above the short rest mass $\mu > \omega_S(0)$, and not below as in the case of attractive self-interactions. This is a consequence of repulsive self-interactions, which cause the short axion's frequency to increase with an increase in its amplitude (see inset of Fig. 3.14). Second, there are two apparent autoresonance bands in Fig. 3.14 as opposed to the single band in Fig. 3.5. This is again a consequence of the nontrivial dependence of frequency on amplitude. Because Θ_S is a periodic variable, the repulsive self-interactions that take place at small amplitudes cannot continue to arbitrary field displacements. Thus, the positive frequency shift that occurs at small amplitudes must eventually turn around and decrease, ultimately passing through zero as shown in the inset of Fig. 3.14. Therefore, every possible positive frequency shift in the potential Eq. 3.67 is achieved at two separate amplitudes σ_S. Depending on the initial conditions, the driver Θ_L of a particular frequency μ may drive Θ_S at one of two possible amplitudes, giving rise to the two autoresonant tails.

These two tails, while both the consequence of repulsive self-interactions, lead to very different phenomenology. Let us first consider the small amplitude tail (Blue). Here, the result of the small-amplitude formalism for computing the perturbation growth rate Eq. 3.34 goes through unchanged: perturbations do not grow because the frequency shift $\delta\omega$ is positive (see App. 4.8).

At larger amplitudes (Magenta), the motion of the zero-mode Θ_S is no longer well approximated by its motion near the bottom of the potential, and the formalism of App. 4.8 no longer applies. Even though we cannot analytically quantify the growth rate of modes beyond the small amplitude approximation, we may gain some qualitative intuition through the following considerations. Recall from our discussion in Sec. 3.2.1 that perturbations are agnostic to features in the potential below the kinetic energy of Θ_S. Therefore, the relevant features of the potential for perturbation growth occur near the turnaround points where kinetic energy vanishes. At these points, the potential behaves as locally attractive if increasing σ_S decreases $\omega(\sigma_S)$, and locally repulsive if it increases $\omega(\sigma_S)$. In other words, the relevant quantity for mode growth is $\omega'(\sigma_S)$. This argument predicts that autoresonance on the large amplitude tail (Magenta) of Fig. 3.14 for which $\omega'(\sigma_S) < 0$, representing net-attractive self-interactions, drives the growth of large perturbations. We have confirmed this intuition with numerical simulations.

The observational prospects for repulsive autoresonance are striking. Spatial perturbations to the axion field do not grow, and so autoresonance is not quenched even for $\mathcal{F} \gg 20$. This implies that the boost to direct detection signal strength (Eq. 3.64) can be quite large if such large hierarchies

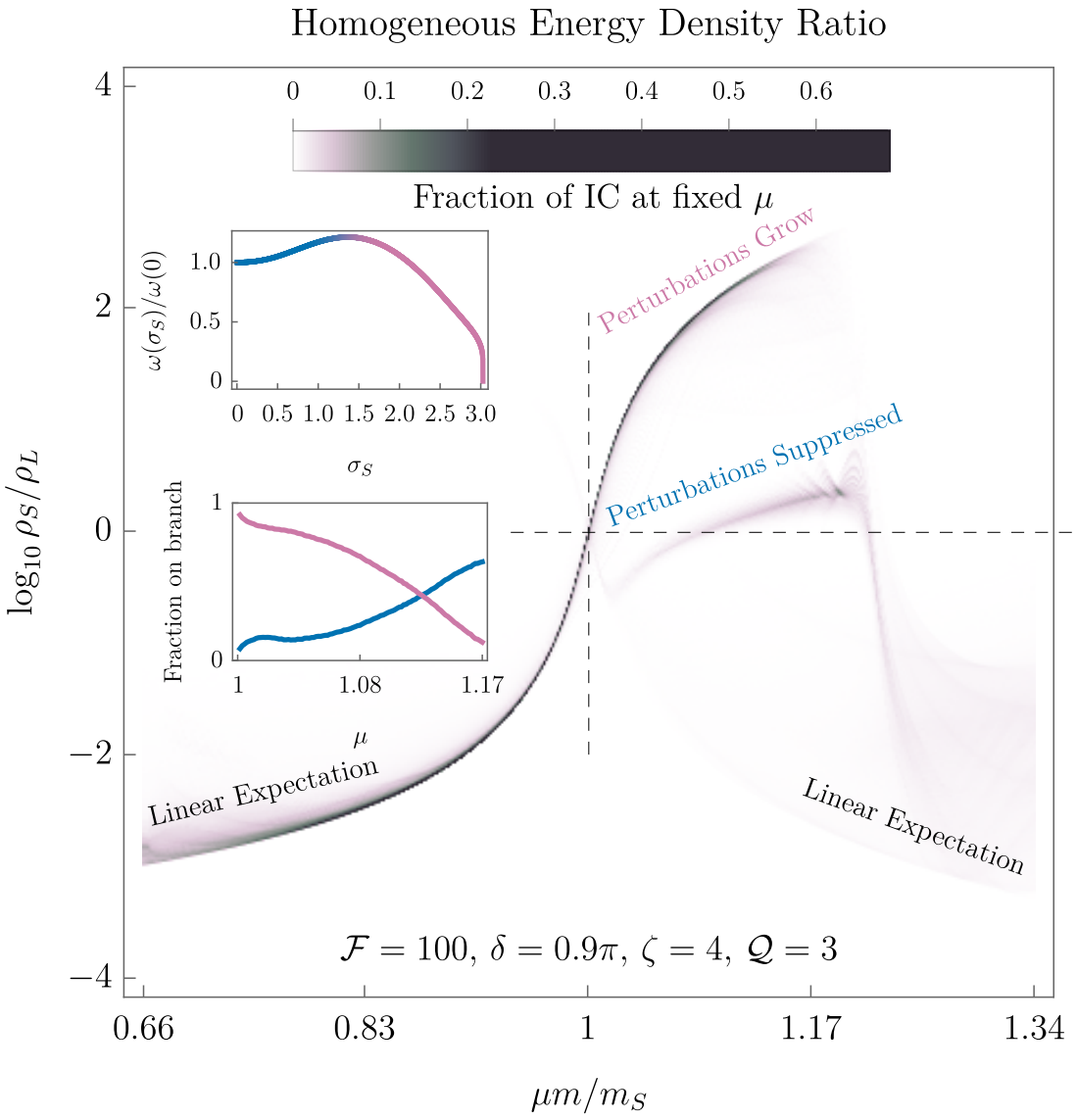

Figure 3.14: The distribution of late-time energy density ratios ρ_S/ρ_L, as defined by Eq. 3.68 in the potential Eq. 3.67. For each choice of μ, the initial conditions $(\Theta_S(0), \Theta_L(0)) \in [-\pi, \pi] \times [-\pi, \pi]$ are sampled uniformly, and the results are binned by the final density ratio $\log \rho_S/\rho_L$. This figure should be compared to Fig. 3.5. For $m_S \leq \mu m \lesssim 1.17 m_S$, (note, $m_S \approx 3m$ is the short axion mass) there are two Θ_S amplitudes that can autoresonate with Θ_L, corresponding to the upper and lower tails visible in the upper right. **Top Inset:** The frequency versus amplitude curve for Θ_S, showing that small amplitudes experience net-repulsive self-interactions, which suppress perturbation growth (Blue), and larger amplitudes experience net-attractive self-interactions, which enhance growth (Magenta). The two autoresonant tails correspond to the two solutions σ_S of the equation $\omega(\sigma_S) = \mu$ for $\mu \geq \omega(0)$. **Bottom Inset:** The fraction of initial misalignment angles landing on each branch. Note, the total probability of landing on either nonlinear branch does not equal 1 because one may also land on the linear branch, where the short axion does not autoresonate.

of decay constants exist in the axiverse.[9] Such strongly coupled relics provide important targets for direct detection experiments probing mass ranges where both the expectation Eq. 3.63 and that of attractive autoresonance are out of reach. These observational implications motivate us to take the possibility of repulsive autoresonance seriously, even though the potential Eq. 3.67 is repulsive over a relatively small range of parameters. Whether repulsive interactions remain relatively rare in realistic axiverse potentials is an open question, and our model serves as motivation to study this question further.

3.5 Discussion and future directions

In this paper, we have studied the dynamics of coupled axion dark matter, and in particular the case of a pair of axions with nearby masses. We have shown that one axion can dynamically adjust its amplitude so that its frequency matches that of another and then remain fixed at this amplitude for cosmologically-relevant times, avoiding the damping effects of Hubble friction long enough to dominate the energy density in the axion sector. This frequency-matching is a form of autoresonance, and within the concrete model of this paper, it is a common phenomenon provided the long axion mass m_L is within around 25% of the short axion mass: $0.75 m_S \lesssim m_L < m_S$. This gives a good notion of how "friendly" two axions must be to see the effects we have described, and such a coincidence of masses is unsurprising in an axiverse with $\mathcal{O}(100s)$ of axions distributed log-flat in mass.

If autoresonance does occur, the energy transfer typically runs from the axion with a larger ("long") decay constant to the axion with a smaller ("short") decay constant, meaning that the effect on the axion sector is generally to make it more detectable by direct detection experiments. This alone is a very exciting prospect, and various experiments such as ADMX, DM Radio, and HAYSTAC will probe significant regions of parameter space of friendly axions, independent of the friendly pair's total energy density. In addition, if the pair makes up all of DM, we have shown that autoresonance for a potential with attractive self-interactions can lead to a parametric-resonance-driven growth of spatial perturbations in the axion field, which can then collapse at early times and form dense axion minihalos. For axion masses $m \lesssim 10^{-7}$ eV, these have gravitational signatures that can be probed with near-future experiments. If autoresonance lasts for a long time (which occurs for large hierarchies of axion decay constants), spatial perturbations can grow nonperturbative and the analytic formalism developed here breaks down, but our preliminary numerical results suggest that the autoresonance is quenched. Still in this case, the short axion receives a significant boost to its energy density. The various signatures discussed are complementary, and in some parts of parameter space multiple signatures may be observed, allowing a concrete identification of the friendly axion scenario from other mechanisms which may predict similar minihalo spectra.

[9] This itself is a question worthy of future study. At least some concrete realizations of the axiverse result in decay constant distributions that are spread only $1-2$ orders of magnitude about a central value [172].

There remain several natural questions about this mechanism. The first is whether the QCD axion, which has a temperature-dependent mass, can receive an energy density enhancement due to resonances with an axiverse. It turns out that autoresonant (i.e. nonlinear) energy transfer to the QCD axion is impossible: by the time the QCD axion nears its zero-temperature mass m_a, any would-be friend has already lost too much energy for the nonlinear interactions in the QCD potential to be accessible, putting autoresonance out of reach.

On the other hand, linear resonances are accessible to the QCD axion: as the QCD axion mass increases through the masses of other axions in an axiverse, an level-crossing may lead to energy transfer to or from the QCD axion. The possibility of the QCD axion generating a cosmological abundance of axiverse axions has been explored in Refs. [224–227]. We note that it is similarly possible for an axiverse axion to transfer its initial energy density to the QCD axion, leading to QCD axion DM signatures at large masses $m_a \gtrsim$ meV, well above the range expected from an $\mathcal{O}(1)$ initial misalignment angle.

A second natural question is what happens if the decay constant hierarchy $\mathcal{F}$ is large enough that spatial fluctuations grow nonperturbative during autoresonance and collapse into oscillons—compact axion structures bound by self-interactions. We have performed numerical simulations in this regime that indicate autoresonance is quenched by oscillon formation, but they are limited in their resolution. Further simulations are necessary to verify our results, but it is worth pointing out that oscillons can potentially have intriguing signatures of their own which we have not worked out here. Oscillons in general do not have very long lifetimes, but may live significantly longer in the background of a long axion condensate that can resonantly drive them (see Refs. [228, 229] for examples of driven nonlinear field equations). Energy conservation suggests that in this case the oscillon's lifetime may be extended parametrically to:

$$mT_{\rm driven} \propto (mT_{\rm vacuum})^{4/3}\,, \tag{3.69}$$

where m is the axion mass and $T_{\rm vacuum}$ is the lifetime of an oscillon with fundamental frequency μm. For potentials with somewhat long-lived oscillons already (see e.g. Refs. [1, 65, 111, 113, 118, 119]), this enhancement would allow them to survive to matter-radiation equality even at larger axion masses $m \gtrsim 10^{-15}$ eV for the longest lived oscillons [65]. At late times, if such an oscillon is in a galactic halo of θ_L DM and it can remain locked to the virialized ρ_L background, then the only upper bound on its lifetime comes from exhausting the entire halo energy density. Since even a small subcomponent of oscillons can be detected [125, 126, 130], this is an important case to study further.

The example of autoresonance we have studied in this paper is not the only type of nonlinear resonance possible in a coupled oscillator system, and future work is needed to understand whether other types of resonance can show up in the axiverse. For example, even a pendulum can resonate in a qualitatively different way than we have studied so far: at energies above the potential barrier, it can make complete circuits about its pivot, which opens up a large window of higher frequencies

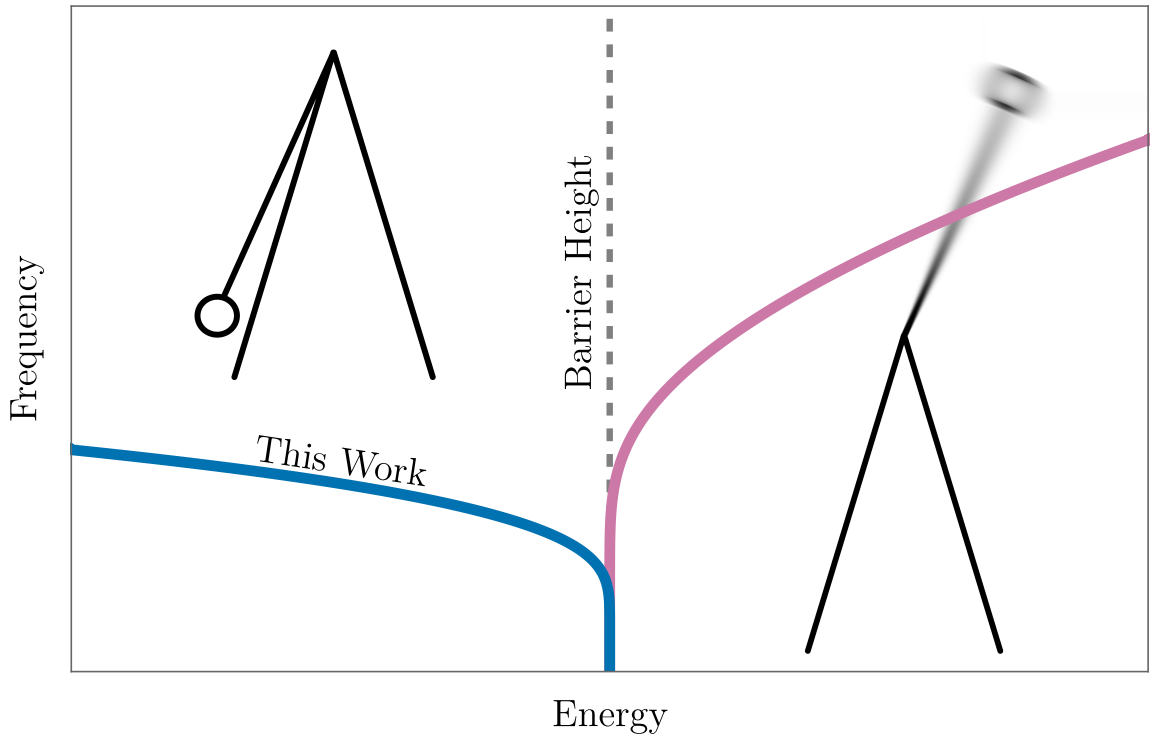

Figure 3.15: The frequency of a classical pendulum versus its energy. There are two distinct regimes. First, at energies below the barrier height, the pendulum oscillates around its equilibrium angle, at a frequency which decreases with energy (Blue). At energies above the potential barrier height, the pendulum completes full rotations. In this regime, it is the pendulum's velocity which oscillates around an 'equilibrium value,' and the oscillation frequency increases with energy (Magenta). In this paper, we have described how a driver can lock onto the low-energy branch of this curve through autoresonance. The high-energy branch opens up the possibility of autoresonance and associated signatures over a larger frequency range.

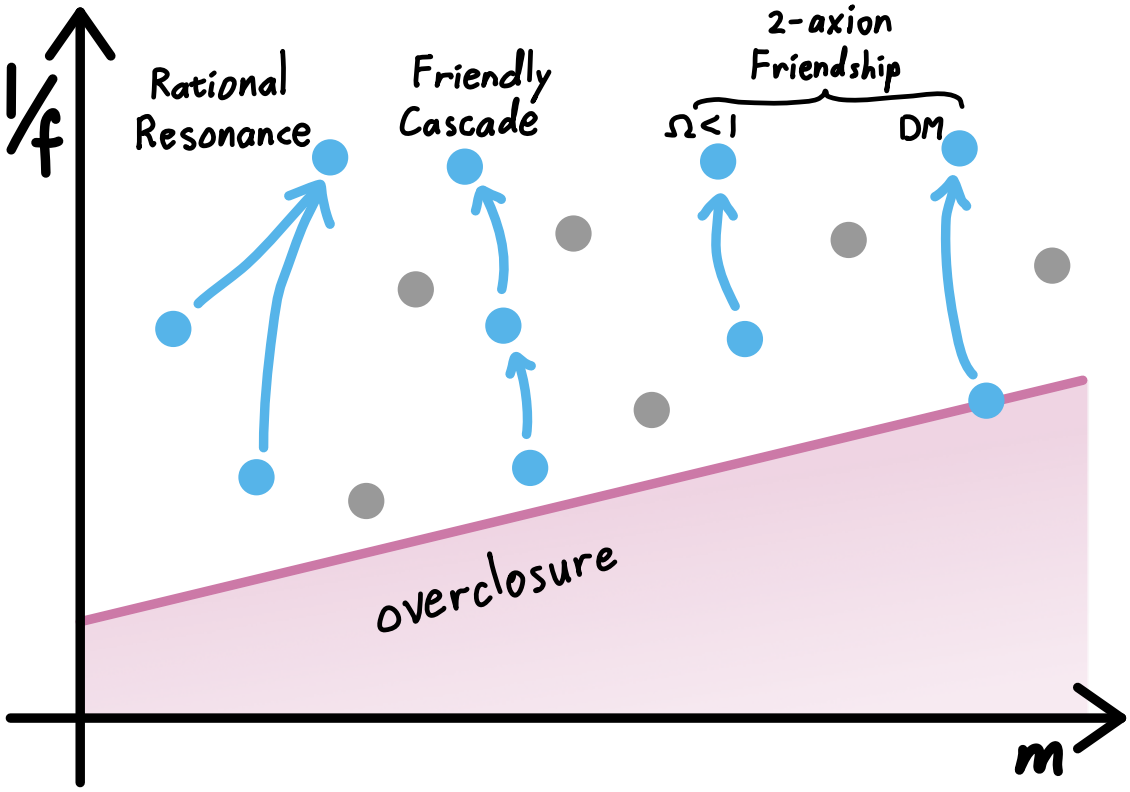

Figure 3.16: Some possibilities for energy redistribution in the axiverse. Each axion in the axiverse is represented as a point in the mass-decay constant plane. The magenta line represents those values of m and f that lead to the proper relic abundance of DM for $\mathcal{O}(1)$ initial misalignment if the axions are treated independently. As we have shown here, energy density can be resonantly transferred to axions with smaller decay constants (illustrated by blue arrows). We have studied the case of two axions with nearby masses ("2-axion Friendship"), both when the pair comprise the totality of DM ("DM") and when they are only a subcomponent ("$\Omega < 1$") but there are other possibilities in a realistic axiverse. For example multiple axions with nearby masses could transfer energy in a sequence ("Friendly Cascade") or collections of axions could dynamically synchronize and lock onto a rational resonance, where no two frequencies match identically but they are related rationally. These latter possibilities are likely to be less common than the two-axion case discussed in this work because they require more coincidences, but with $\mathcal{O}(100\text{s})$ of axions they may still be possible and further work is necessary to understand them.

to autoresonance due to the nonlinearities of the oscillator. This is illustrated in Fig. 3.15. These circular resonances may be accessed if one axion obtains an approximately constant velocity, which may occur because of the complicated geometry of multi-axion potentials or because of an explicit breaking of PQ symmetry in the early universe [81,230].[10] We illustrate some of the other possibilities for axiverse axions in Fig. 3.16, but further work is needed to understand which of these can be realized in realistic models.

String theory remains the most successful attempt at a unified theory of quantum gravity, but unfortunately we lack many experimental probes of this possibility. Nearly all new effects (particles, forces, nonlocality, etc.) within the theory are suppressed by the string scale, which in principle can lie quite close to the Planck scale, making it virtually impossible to test with current technology. String theory axions are a notable exception, and observing several distinct axions in the particle spectrum would hint at string theory as a UV completion for the SM. In many scenarios, string axions can be accurately approximated as weakly-interacting massive fields. However, this approximate picture of axions as a collection of perturbatively-coupled oscillators misses something important: in such a system, *exact* resonances are necessary for appreciable energy transfer between normal modes [231]. Since there is no reason to expect that axion masses obey simple integer relations (assuming the masses are temperature-independent and remain fixed as the universe evolves), such exact resonances are impossible, and one would conclude that no significant transfer of energy can happen between axions in an axiverse. As we have shown here, quite the opposite is true: in a realistic system, exact resonance can be obtained *dynamically*, because the frequency of a nonlinear oscillator is a function of its amplitude. In other words, perturbative treatments can miss important features if they do not account for the full nonlinearity of the axiverse potential. The two-axion case studied here should be considered a minimal example of the effects of nonlinear couplings in the axiverse, and it already provides exciting signatures in the reach of near-future experiments.

3.6 Acknowledgments

We would like to thank Mustafa Amin, Asimina Arvanitaki, Savas Dimopoulos, Robert Lasenby, Viraf Mehta, Glenn Starkman, Harikrishnan Ramani for many useful discussions. We thank Asimina Arvanitaki, Sebastian Baum, Alexander Gußmann, Robert Lasenby, and Viraf Mehta for helpful comments on the draft, and in particular we thank Masha Baryakhtar for her detailed and thoughtful comments. D.C. is grateful to Dmitriy Zhigunov for the initial conversations that led to this line of research, and for helpful conversations about pseudospectral methods. Some of the computing for this project was performed on the Sherlock cluster. We would like to thank Stanford University and the Stanford Research Computing Center for providing computational resources and support that contributed to these research results. D.C. is grateful for the support of the Stanford Institute

[10] Mechanisms like [81,230] would also result in large density perturbations because the axion kinetic energy delays the onset of harmonic oscillations (see Sec. 3.2).

for Theoretical Physics (SITP), the National Science Foundation under Grant No. PHY-2014215, and the Gordon and Betty Moore Foundation under Grant No. GBMF7946. T.G.-T. is grateful for the support of the Department of Energy under Grant No. DE-SC0020266. O.S. is supported by a DARE fellowship from the Office of the Vice Provost for Graduate Education at Stanford University. J.O.T. is supported by a William R. Hewlett Stanford Graduate Fellowship.

Chapter 4

Appendix

4.1 The physical quasibreather formalism

In this appendix, we outline the precise definition of the physical quasibreather (PQB) and its orthogonal deformation (OD) introduced in section 2.1. We will see that the orthogonally deformed PQB is an instantaneous solution of the equations of motion that satisfies outgoing boundary conditions. We then find oscillonic solutions of the equations of motion that are perturbations of the orthogonally deformed PQB. By studying the evolution and stability of these perturbations, we arrive at a sense in which the orthogonally deformed PQB can be an attractor, which we apply to study oscillon stability in appendix 4.3.

4.1.1 Quasibreathers

Physical potentials may be interpreted in terms of n-particle interactions, and therefore possess Taylor expansions around their vacua. Consequently, a periodic field configuration with fundamental frequency ω will only couple to modes oscillating with integer multiples of this fundamental frequency. In other words, physical non-linear wave equations possess periodic orbits, which may be interpreted as a Fourier series in time. This is in contrast to unphysical potentials that may not be interpreted in terms of integer-number particle interactions, which can at best possess quasiperiodic orbits.

For the remainder of the appendix, we move into dimensionless units with $m = f = 1$. The non-linear wave equation for the field θ in a potential V is then

$$0 = \ddot{\theta} - \nabla^2\theta + V'(\theta)\,. \tag{4.1}$$

As we have argued above, V must possess a Taylor series, and therefore θ may be expanded as a

series of integer harmonics

$$\theta = \sum_{n\in\mathbb{N}_0} S_n(r,\omega)\sin(n\omega t + \delta_n)\,, \tag{4.2}$$

where δ_n is a phase, and we have taken spherical symmetry for simplicity. Without loss of generality, we may take $\delta_1 = 0$. We say that a solution of the form (4.2) is generated by the frequency ω if S_1 is non-zero, and the only non-zero higher harmonics S_n are those that couple to S_1, consistent with closure of the equations of motion. We then define the quasibreather as the solution generated by ω.

Using this definition, we may compute the generic form of the quasibreather. Consider the generic potential

$$V(\theta) = \frac{1}{2}\theta^2 + \frac{1}{3}\lambda_3\theta^3 + \frac{1}{4}\lambda_4\theta^4 + \dots\,. \tag{4.3}$$

From the symmetries of sine and cosine, we observe that

$$(\sin\omega t)^n = \begin{cases} \sum_k a_k \sin n_k\omega t,\ n_k \in \mathbb{N}_{\text{odd}}, & n \text{ is odd},\\ \sum_k b_k \cos m_k\omega t,\ m_k \in \mathbb{N}_{\text{even}}, & n \text{ is even}, \end{cases}$$
$$(\cos\omega t)^n = \begin{cases} \sum_k c_k \cos n_k\omega t,\ n_k \in \mathbb{N}_{\text{odd}}, & n \text{ is odd},\\ \sum_k d_k \cos m_k\omega t,\ m_k \in \mathbb{N}_{\text{even}}, & n \text{ is even}. \end{cases}$$

The case of parity $V(\theta) = V(-\theta)$ offers a pleasant simplification, decopling the even harmonics and the odd harmonics from one another. Thus, potentials with parity have quasibreathers of the form

$$\theta_{\text{QB}} = \sum_{n\in\mathbb{N}_{\text{odd}}} S_n(r,\omega)\sin n\omega t\,, \tag{4.4}$$

and a periodic solution of the form $\theta = \sum_{n\in\mathbb{N}_{\text{even}}} S_n(r,\omega)\sin n\omega t$, although it is not a quasibreather because it is not generated by ω. Quasibreathers in potentials without parity possess expansions

$$\theta_{\text{QB}} = \sum_{n\in\mathbb{N}_{\text{odd}}} S_n(r,\omega)\sin n\omega t + \sum_{n\in\mathbb{N}_{\text{even}}} C_n(r,\omega)\cos n\omega t\,, \tag{4.5}$$

where $\mathbb{N}_{\text{even}}$ contains 0. Thus, we have identified the form of the quasibreathers of the non-linear wave equation when V represents a physical interaction.

Inserting the form (4.5) into (4.1), one arrives at the set of mode equations

$$\begin{aligned} 0 &= -(n\omega)^2 C_n - C_n'' - \frac{d-1}{r}C_n' + V_n'(C,S)\,, n \in \mathbb{N}_{\text{even}}\,,\\ 0 &= -(n\omega)^2 S_n - S_n'' - \frac{d-1}{r}S_n' + V_n'(C,S)\,, n \in \mathbb{N}_{\text{odd}}\,, \end{aligned} \tag{4.6}$$

where d is number of spatial dimensions, and V_n is defined through the equation

$$V'(\theta_{\mathrm{QB}}) = \sum_{n\in\mathbb{N}_{\mathrm{odd}}} V_n(C,S)\sin n\omega t + \sum_{n\in\mathbb{N}_{\mathrm{even}}} V_n(C,S)\cos n\omega t\,. \tag{4.7}$$

Equation (4.6) is a system of second order ordinary differential equations, and therefore each degree of freedom S_n, C_n must be constrained by two boundary conditions.

In order to discuss boundary conditions, we define the number n_0 as the least integer such that $n_0\omega > 1$, so that bound harmonics have $n < n_0$ and radiative harmonics have $n \geq n_0$. Regularity at the origin places a non-trivial constraint on all harmonics, that all S_n and C_n must have zero first derivative at the origin. However, regularity at spatial infinity is only a constraint on the bound modes, $n < n_0$; all radiative harmonics decay geometrically as they propagate to spatial infinity. Thus, for a quasibreather, the radiative harmonics are only constrained by regularity at the origin, and the space of possible quasibreathers has dimension equal to the number of radiative modes. In other words, one has the freedom to pick the amplitude of the radiative modes at the origin, and the result will still be a quasibreather. The authors of [115] have alleviated this ambiguity by picking a specific quasibreather out of this manifold: the *minimum radiation quasibreather*, whose radiative tails are the smallest. Instead, we pick the physical quasibreather (PQB), defined below, which is perturbatively close to a radiating solution.

4.1.2 The deformed mode equations

A localized field configuration with a finite lifetime necessarily radiates its energy to spatial infinity, and therefore satisfies radiative boundary conditions at spatial infinity. In this section, we introduce the concept of the *physical quasibreather* (PQB), which is, in a precise sense, the quasibreather closest to a physical configuration satisfying radiative boundary conditions.

First, we define the *orthogonal deformation* (OD) of the quasibreather (4.5), which consists of adding 90° out-of-phase components s_n and c_n to the radiative harmonics in order to satisfy radiative boundary conditions

$$\begin{aligned}\theta = &\sum_{n\in\mathbb{N}_{\mathrm{odd}}} S_n(t,r,\omega)\sin n\omega t + \sum_{n\in\mathbb{N}_{\mathrm{even}}} C_n(t,r,\omega)\cos n\omega t \\ &\sum_{n\in\mathbb{N}^{\geq n_0}_{\mathrm{even}}} s_n(t,r,\omega)\sin n\omega t + \sum_{n\in\mathbb{N}^{\geq n_0}_{\mathrm{odd}}} c_n(t,r,\omega)\cos n\omega t\,.\end{aligned} \tag{4.8}$$

Notice that here we've introduced a time dependence to the modes, which accounts for the fact that a radiating solution cannot have a stationary profile. This formulation will be useful for studying initial conditions of interest, namely, those which specify a quasibreather and orthogonal deformation that together satisfy outgoing boundary conditions. Although (4.8) is a vast overparametrization of

a single field, we recognize that a solution of the *deformed mode equations* (4.9)

$$\begin{aligned}
0 &= \ddot{S}_n - 2n\omega\dot{c}_n - (n\omega)^2 S_n - S_n'' - \frac{d-1}{r}S_n' + V_{S_n}' \,, \\
0 &= \ddot{c}_n + 2n\omega\dot{S}_n - (n\omega)^2 c_n - c_n'' - \frac{d-1}{r}c_n' + V_{c_n}' \,, \\
0 &= \ddot{C}_n + 2n\omega\dot{s}_n - (n\omega)^2 C_n - C_n'' - \frac{d-1}{r}C_n' + V_{C_n}' \,, \\
0 &= \ddot{s}_n - 2n\omega\dot{C}_n - (n\omega)^2 s_n - s_n'' - \frac{d-1}{r}s_n' + V_{s_n}' \,,
\end{aligned} \tag{4.9}$$

is also a solution of the full equation of motion (4.1). Equation (4.9) is obtained from the equations of motion (4.1) by substituting (4.8) and collecting the terms proportional to $\sin n\omega t$ or $\cos n\omega t$ for a given n, setting them independently to zero. Intuitively, when the time dependence of the harmonic functions S, C, s, c is slow, they have the usual interpretation as the profiles of quasistationary modes. Here the functions $V_X' = V_X'(S_n, C_n, s_n, c_n)$, are the *mode potentials*, in which we have suppressed functional dependence for brevity. The mode potentials are defined by the equation

$$V'(\theta) = \sum_{n\in\mathbb{N}_{\text{odd}}} V_{S_n}' \sin n\omega t + \sum_{n\in\mathbb{N}_{\text{even}}} V_{C_n}' \cos n\omega t + \sum_{n\in\mathbb{N}_{\text{even}}} V_{s_n}' \sin n\omega t + \sum_{n\in\mathbb{N}_{\text{odd}}} V_{c_n}' \cos n\omega t \,, \tag{4.10}$$

where θ is written in the form of equation (4.8), and $V_{S_n}', V_{C_n}', V_{s_n}', V_{c_n}'$ are pure functions of S_n, C_n, s_n, c_n.

During the evolution of equation (4.9), ω is treated as a constant. This is not in contradiction to the usual understanding that the fundamental frequency of the oscillon increases with time. For the purpose of the mode equations (4.9), ω is understood as a choice of a fixed parameter, independent of the time variation of the modes S, C, s, c themselves. For certain initial conditions, and for certain choices of ω, there will be periods of time over which S, C, s, c vary slowly, and it is during these periods that ω may be interpreted as the instantaneous frequency of the oscillon.

In other words, there is no a priori reason to choose a particular ω for a particular field configuration, and one may only think of ω as an instantaneous frequency in the context of certain initial conditions. Thus, the following paragraphs are dedicated to specifying initial conditions which allow ω to be interpreted as the instantaneous frequency of an oscillon, where the oscillon is perturbatively close to a quasibreather. The smaller the orthogonal deformation, the better this interpretation is, and the longer it holds. In this sense, ω may be conceptualized as an adiabatic parameter, although one should not confuse it with an externally controlled parameter — in our framework, it is a constant that parametrizes the decomposition (4.8) of solutions to (4.1).

We now specify the following consistent set of initial and boundary conditions, in which we treat s_n and c_n as linear perturbations. Here, we take $V_X' = V_X'(S_n(0,r), C_n(0,r), 0, 0)$, and we define $\delta V_X' \equiv \sum_{n\geq n_0} s_n(0,r)\partial_{s_n} V_X' + c_n(0,r)\partial_{c_n} V_X'$ (note the absence of a constant term in $\delta V_X'$ is a consequence of (a), below). A complete and consistent set of initial and boundary conditions

associated with (4.9), that exactly specify a quasibreather and orthogonal deformation at $t = 0$ is

(a) **Initial Quasibreather:**

$$0 = -(n\omega)^2 S_n(0,r) - S_n''(0,r) - \frac{d-1}{r} S_n'(0,r) + V_{S_n}' \,,$$
$$0 = -(n\omega)^2 C_n(0,r) - C_n''(0,r) - \frac{d-1}{r} C_n'(0,r) + V_{C_n}' \,,$$

(b) **Initial Deformation:**

$$0 = -(n\omega)^2 c_n(0,r) - c_n''(0,r) - \frac{d-1}{r} c_n'(0,r) + \delta V_{c_n}' \,,$$
$$0 = -(n\omega)^2 s_n(0,r) - s_n''(0,r) - \frac{d-1}{r} s_n'(0,r) + \delta V_{s_n}' \,,$$

(c) **Maximally stationary:**

$$0 = \dot{S}_{n\geq n_0}(0,r) = +2n\omega \dot{S}_{n<n_0}(0,r) + \delta V_{c_n}' \,,$$
$$0 = \dot{C}_{n\geq n_0}(0,r) = -2n\omega \dot{C}_{n<n_0}(0,r) + \delta V_{s_n}' \,,$$
$$0 = \dot{s}_n(0,r) = \dot{c}_n(0,r) \,,$$

(d) **Regularity:**

$$0 = S_n'(t,0) = C_n'(t,0) = s_n'(t,0) = c_n'(t,0) \,,$$
$$0 = S_{n<n_0}'(t,\infty) = C_{n<n_0}'(t,\infty) \,,$$

(e) **Radiative:**

$$0 = \lim_{r\to\infty} r^{\frac{1-d}{2}} (r^{\frac{d-1}{2}} c_n(t,r))' + \sqrt{(n\omega)^2 - 1} S_n(t,r) \,,$$
$$0 = \lim_{r\to\infty} r^{\frac{1-d}{2}} (r^{\frac{d-1}{2}} S_n(t,r))' - \sqrt{(n\omega)^2 - 1} c_n(t,r) \,,$$
$$0 = \lim_{r\to\infty} r^{\frac{1-d}{2}} (r^{\frac{d-1}{2}} C_n(t,r))' + \sqrt{(n\omega)^2 - 1} s_n(t,r) \,,$$
$$0 = \lim_{r\to\infty} r^{\frac{1-d}{2}} (r^{\frac{d-1}{2}} s_n(t,r))' - \sqrt{(n\omega)^2 - 1} C_n(t,r) \,.$$

Our initial condition (a) selects S_n and C_n which specify a quasibreather. This quasibreather is one which may be orthogonally deformed to satisfy radiative boundary conditions, and it is this quasibreather which we call the PQB.

Because we have broken the time translation symmetry of the quasibreather by satisfying radiative boundary conditions, the modes S, C, s, c are endowed with an irreducible time dependence. The maximally stationary condition (c) shows that this time dependence is proportional to the pointwise small deformations s and c. Since s and c obey a homogeneous system of equations (b), their amplitude everywhere must uniformly go to zero as their amplitude at $r = \infty$ goes to zero. From (e), we see that $c_n \propto S_n$ and $s_n \propto C_n$ at spatial infinity. Thus we conclude that if S_n and C_n possess small radiative tails, then s_n and c_n become pointwise small everywhere, and the time variation of the modes uniformly approaches zero. This is the limit in which the oscillon is long-lived, and

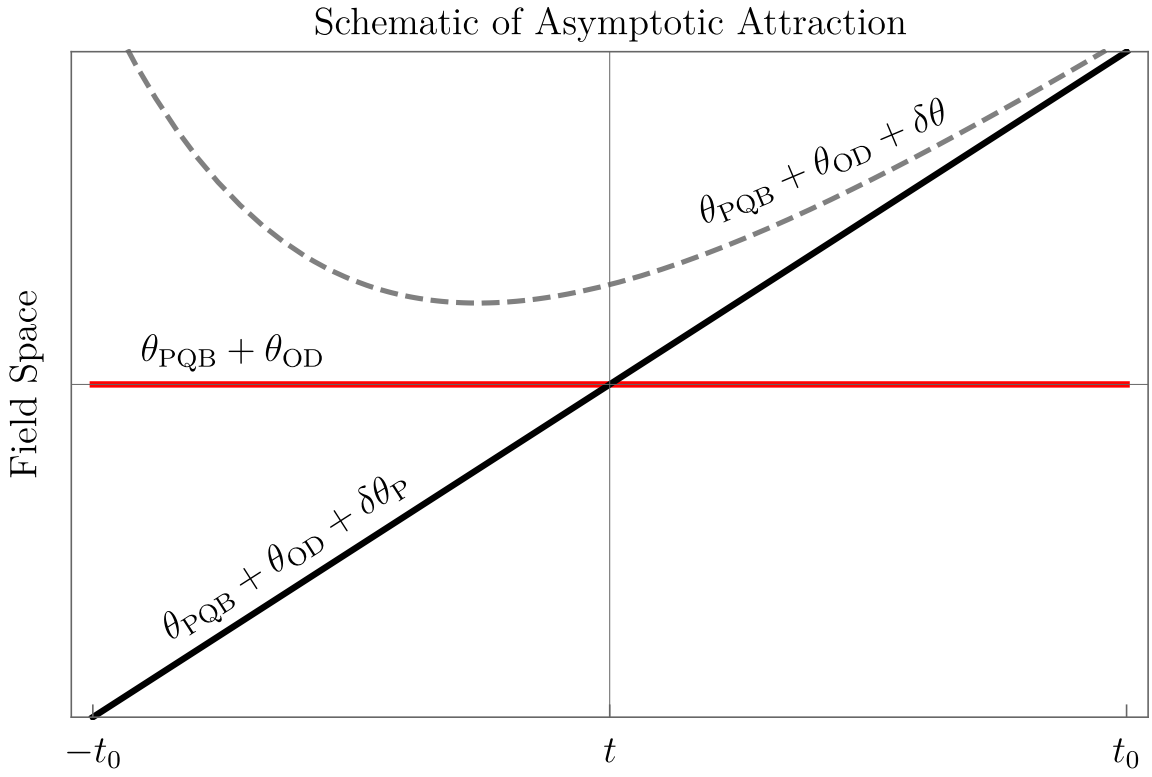

Figure 4.1: The asymptotic attractor (red) is approached as the inhomogeneous solution goes to zero. The homogeneous terms, representing the initial conditions at $t = -t_0$ cannot converge exactly to zero by the time the inhomogeneous solution passes through zero, and therefore the perturbation never exactly reaches the asymptotic attractor.

approaches the quasibreather; in this same limit, the interval over which this approximation is valid, during which ω may be thought of as an instantaneous frequency, becomes longer.

4.1.3 The asymptotic attractor

The initial conditions (a-e) specify a solution to the nonlinear wave equation that, at $t = 0$ is exactly an orthogonally deformed physical quasibreather (to linear order in the deformation). More practically, we want to understand the evolution of the oscillon in the neighborhood of this deformed physical quasibreather, before and after this particular point. To this end, we introduce the perturbation $\delta\theta(t, r)$, which simultaneously absorbs the time dependence of the modes in (a-e), and deviations from the orthogonally deformed physical quasibreather. Specifically, a field configuration θ describing a physical oscillon can be expanded as

$$\theta = \theta_{\rm PQB} + \theta_{\rm OD} + \delta\theta\,, \tag{4.11}$$

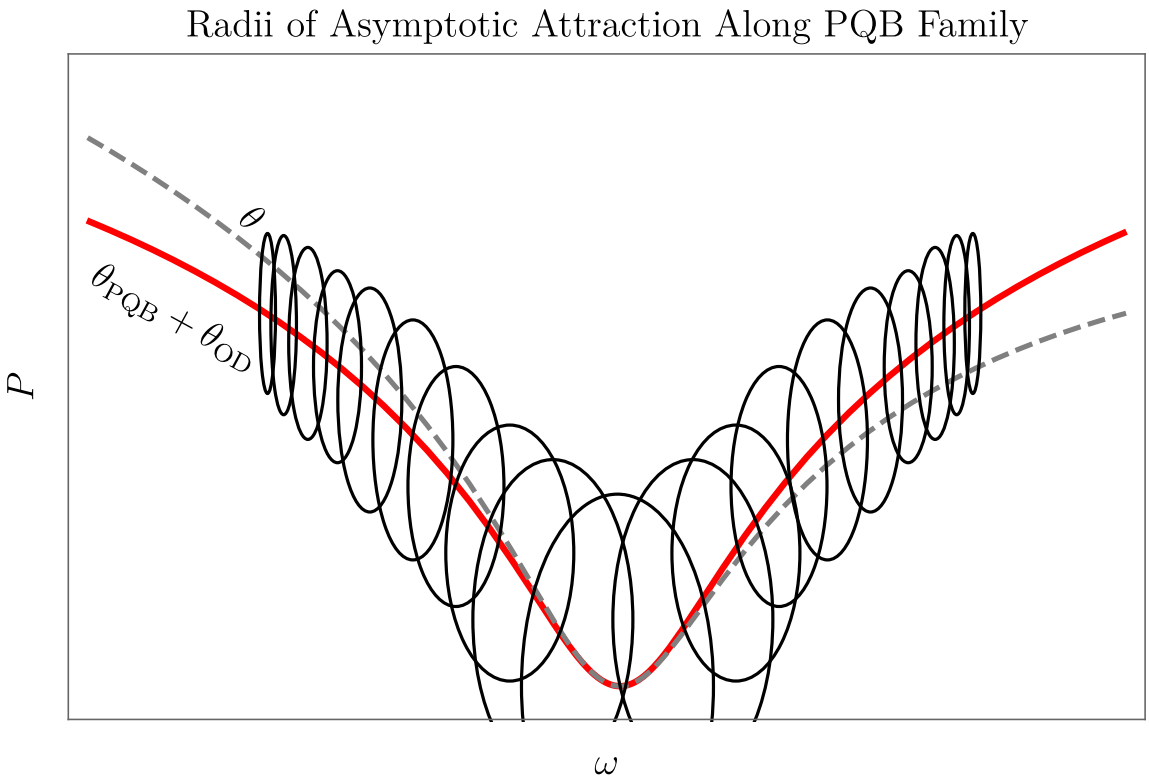

Figure 4.2: Here we have a schematic Power Radiated (as a proxy for field-space) vs Oscillon Frequency plot for the family of deformed PQB (red) and an oscillon trajectory (dashed grey). Each ellipse centered on a deformed PQB represents the domain of frequencies and field values over which that specific quasibreather is an asymptotic attractor. As the oscillon trajectory enters an attractive region, it moves closer to the attractive deformed PQB. Consequently, it is also drawn into the attractive vicinity of the neighboring PQBs. Therefore, the oscillon is forced to approach the red trajectory as the radii of attraction get larger and larger towards the bottom of the dip. After traversing the dip, the deformed PQB radii of attraction begin to shrink, and the oscillon trajectory begins to diverge from the deformed PQB trajectory. In this latter half of the evolution, we see how the deformed PQB trajectory does not act as a standard attractor, but can still be described as an asymptotic attractor. To see this, notice how the oscillon instantaneously moves closer to the quasibreather when entering each new attractive bubble.

with

$$\theta_{\rm PQB} = \sum_{n\in\mathbb{N}_{\rm odd}} S_n(0,r,\omega)\sin n\omega t + \sum_{n\in\mathbb{N}_{\rm even}} C_n(0,r,\omega)\cos n\omega t\,, \tag{4.12}$$

$$\theta_{\rm OD} = \sum_{n\in\mathbb{N}^{\geq n_0}_{\rm even}} s_n(0,r,\omega)\sin n\omega t + \sum_{n\in\mathbb{N}^{\geq n_0}_{\rm odd}} c_n(0,r,\omega)\cos n\omega t\,. \tag{4.13}$$

Crucially, $\theta_{\rm PQB}$ is exactly a quasibreather solution, and $\theta_{\rm OD}$ is exactly periodic in time, as opposed to $\delta\theta$, which characterizes the secular evolution of the oscillon in the vicinity of the physical quasibreather at ω. Inserting (4.11) into (4.1), we arrive at the following equation for $\delta\theta$ at linear order,

$$0 = \delta\ddot{\theta} - \nabla^2\delta\theta + V''(\theta_{\rm PQB})\delta\theta + \sum_{n<n_0}(\delta V'_{c_n}\cos n\omega t + \delta V'_{s_n}\sin n\omega t)\,. \tag{4.14}$$

This is a sourced equation, representing the fact that the physical quasibreather with orthogonal deformation does not conserve energy on its own. As a linear equation, $\delta\theta$ may be decomposed into a sum of homogeneous terms, which obey the homogeneous equation

$$0 = \delta\ddot{\theta}_H - \nabla^2\delta\theta_H + V''(\theta_{\rm PQB})\delta\theta_H\,, \tag{4.15}$$

and one particular solution $\delta\theta_P$, that obeys the sourced equation (4.14), which we take to be identically zero at $t = 0$. In the absence of homogeneous terms, it is this particular solution $\delta\theta_P$ which satisfies the initial conditions (a-e). Therefore, the homogeneous terms represent perturbations around those initial conditions. If the homogeneous solutions of (4.14) are stable, then we say that $\theta_{\rm PQB} + \theta_{\rm OD}$ is an *asymptotic attractor*.

The usefulness of the construction $\delta\theta$ is that it contains all information about the linear stability of the oscillon [1]. Just like in a standard damped oscillator, linear stability represents an exponential approach to the inhomogeneous solution. In other words, it is enough to study the stability of the homogeneous equation (4.15) with the tools of Floquet theory. The full picture of how the one-parameter family of deformed physical quasibreathers, parametrized by the frequency ω, acts like an attractor may be understood in the following picture. Before $t = 0$, the particular solution $\delta\theta_P$ is approaching 0 (see Figure 4.1). If the homogeneous terms are stable, then the field θ is approaching the deformed physical quasibreather at frequency ω. However, past $t = 0$, $\delta\theta_P$ begins to grow again, causing the field to diverge from this temporary quasibreather partner. This story repeats by choosing the next physical quasibreather to expand around at a nearby frequency $\omega + d\omega$, such that the attractive region of this new quasibreather has some overlap with the repulsive region of

[1] This is an oversimplification, since equation (4.15) cannot be stable in the sense that it only has decaying modes. Stability will emerge out of nonlinear corrections, but for the sake of a simple discussion, we save this technicality for appendix 4.3.

the previous quasibreather at ω (see figure 4.2). The term "asymptotic attractor" is chosen because of its likeness to the concept of asymptotic series, in which increasing the order of an expansion increases its precision until, at some point, it begins to diverge.

4.1.4 Energetic instability

The physical quasibreather background around which we expand the perturbation $\delta\theta$ is one among a continuum of quasibreathers, parametrized by their fundamental frequency ω. Thus, when we talk about a perturbation $\delta\theta$, we introduce the notation $\delta\theta^\omega$ in order to talk about "the perturbation relative to (the deformed physical quasibreather of frequency) ω," where we may omit the parenthetical when it is unambiguous to do so.

In the previous section, we introduced the concept of asymptotic attraction, in which an oscillon may be viewed as approaching a physical quasibreather for a finite period of time. For each quasibreather, there is an epoch of attraction, during which the particular solution $\delta\theta_P$ is shrinking towards zero, and an epoch of repulsion, during which $\delta\theta_P$ is growing away from zero. Neighboring quasibreathers at ω and $\omega + d\omega$ have particular solutions that cross zero at different absolute times $t = t_\omega$ and $t = t_{\omega+d\omega}$ respectively; whether $t_\omega < t_{\omega+d\omega}$ determines whether $\omega + d\omega$ is attractive for some time after ω becomes repulsive. Because the particular solution $\delta\theta_P$ encodes the energy flow out of the oscillon, the relative timing of the zero crossings of $\delta\theta_P^\omega$ and $\delta\theta_P^{\omega+d\omega}$ may be viewed as a reflection of energy conservation, defining an arrow of time. That is, the oscillon at $\omega + d\omega$ is energetically accessible from ω if $t_\omega < t_{\omega+d\omega}$.

This time ordering implies the existence of a relative energy function, whose local monotonicity encodes whether $\omega + d\omega$ is accessible from ω. In other words, the physical quasibreather at $\omega + d\omega$ is energetically accessible from ω if there is a time when $\delta\theta^\omega$ is a negative energy perturbation relative to ω and $\delta\theta^{\omega+d\omega}$ is a positive energy perturbation relative to $\omega + d\omega$. However, the energy of the total field configuration is ill-behaved because of the divergent radiative tails. Strictly speaking, because the quasibreather at ω has a different amplitude radiative tail than the quasibreather at $\omega + d\omega$, $\delta\theta$ cannot be a finite energy perturbation of both quasibreathers. However, the tails are decoupled and do not influence the dynamics of the oscillon bulk. Therefore, our measure of the perturbation energy must be agnostic to the radiation tails.

One might be inclined to count only the energy inside some finite box containing the oscillon bulk. However, such a measure still grows polynomially with the size of the box. One may also try to subtract the radiative tails by removing the $1/r$ (in $d = 3$) asymptotic, although again, this depends on an explicit cutoff between the bulk and the tails. Our framework provides a natural resolution to this ambiguity. Specifically, the orthogonal deformation θ_{OD} provides a measure of the radiative tail of θ_{PQB} valid everywhere. It is the energy associated with this orthogonal deformation

that we subtract, leading to our definition of the bound energy in the PQB

$$E_B \equiv \lim_{r\to\infty}\left[\int_0^r \mathrm{d}V\left(\frac{1}{2}\dot{\theta}^2_{\mathrm{PQB}}+\frac{1}{2}(\nabla\theta_{\mathrm{PQB}})^2+V(\theta_{\mathrm{PQB}})\right)-\int_0^r \mathrm{d}V\left(\frac{1}{2}\dot{\theta}^2_{\mathrm{OD}}+\frac{1}{2}(\nabla\theta_{\mathrm{OD}})^2+V(\theta_{\mathrm{OD}})\right)\right]. \tag{4.16}$$

Note, because θ_{OD} and θ_{PQB} are out of phase, this difference will oscillate around an average value, reflecting the uncertainty principle. This definition has the virtue of converging to the deformed physical quasibreather energy when the oscillon is infinitely long-lived, i.e. when all harmonics are confined.

Having provided an unambiguous measure of the bound energy of the physical quasibreather, we may now address the question of when the perturbation $\delta\theta$ may flow between nearby quasibreathers. Because the frequency of the quasibreather, ω, is a decreasing function of the bound energy, a family of physical quasibreathers is energetically stable where

$$\frac{dE_B}{d\omega}<0\,. \tag{4.17}$$

Inside a region of asymptotic attraction, the radiation power P of the physical quasibreathers is a good approximation for the radiation power of the oscillon. This leads to a standard approximation for the oscillon lifetime, under the assumption that the perturbation $\delta\theta$ may completely relax (the adiabatic assumption)

$$T\approx\int\frac{\mathrm{d}E_B}{P(E_B)}\,. \tag{4.18}$$

As the oscillon becomes increasingly long-lived, and thus approaches the physical quasibreather, this prediction becomes increasingly precise.

4.2 Quasibreather numerical methods

In the previous section, we arrive at the physical quasibreather as the main object of study which may be used to derive the properties of oscillons in a physical potential. In this section, we develop the numerical tools which enable the efficient calculations of physical quasibreathers and their orthogonal deformations.

4.2.1 Linear radiation

Let us begin by supposing that S_n and C_n are known for $n<n_{\mathrm{pert}}$, and that the remaining S_n and C_n are perturbatively small everywhere, so that they obey linear equations. Define the perturbation

vector and the deformation vector respectively

$$\vec{C} = r^{(d-1)/2} \begin{pmatrix} C_{n_{\rm pert}} \\ S_{n_{\rm pert}+1} \\ \vdots \end{pmatrix}, \qquad \vec{s} = r^{(d-1)/2} \begin{pmatrix} s_{n_{\rm pert}} \\ c_{n_{\rm pert}+1} \\ \vdots \end{pmatrix}, \tag{4.19}$$

the diagonal matrix of frequencies

$$\mathbf{\Omega} = \begin{pmatrix} n_{\rm pert}\omega & & \\ & (n_{\rm pert}+1)\omega & \\ & & \ddots \end{pmatrix}, \tag{4.20}$$

the source vector $\vec{\mathcal{J}}(S_1, C_2, \dots)$ and the mass matrices $\mathbf{V}_{\vec{C}}(S_1, C_2, \dots), \mathbf{V}_{\vec{s}}(S_1, C_2, \dots)$, which are functions of the non-perturbative harmonics. Finally, we define the Sommerfeld operator $\mathbf{S}$, which together with the Dirichlet-Neumann 1D flat Laplacian acting on each diagonal block $\boldsymbol{\nabla}^2$ [2], contains the Sommerfeld radiation condition (e), provided in appendix 4.4.1. In this notation, the equations of motion for the perturbation and the deformation can be written as a sparse linear system

$$\begin{pmatrix} \vec{\mathcal{J}}_{\vec{C}} \\ \vec{\mathcal{J}}_{\vec{s}} \end{pmatrix} = \begin{pmatrix} -\mathbf{\Omega}^2 - \boldsymbol{\nabla}^2 + \mathbf{V}_{\vec{C}} & \mathbf{S} \\ -\mathbf{S} & -\mathbf{\Omega}^2 - \boldsymbol{\nabla}^2 + \mathbf{V}_{\vec{s}} \end{pmatrix} \begin{pmatrix} \vec{C} \\ \vec{s} \end{pmatrix}. \tag{4.21}$$

This form, in which $\vec{C}$ and $\vec{s}$ only couple through the boundary term $\mathbf{S}$, is guaranteed because $\vec{C}$ on its own solves the equations of motion, and hence any backreaction from a perturbation $\vec{s}$ must come at second order. The explicit forms of $\mathbf{S}$, $\mathbf{V}_{\vec{C}}$, $\mathbf{V}_{\vec{s}}$ and $\mathcal{J}_{\vec{C}}$, $\mathcal{J}_{\vec{s}}$ are provided for several cases of interest in the appendix 4.4.1. Note, $\mathcal{J}_{\vec{s}}$ is proportional to the orthogonal deformation of the non-perturbative modes, and is therefore zero when all radiative modes are perturbative.

The fact that we may write the equations for the perturbative modes as a well-determined system of equations is a reflection of the fact that the radiative boundary conditions and regularity conditions completely (and uniquely, for the linear modes) specify the physical quasibreather.

4.2.2 Nonlinear harmonics

The perturbative method in the previous section amounts to solving a sparse linear system, a process that is computationally efficient. Thus, given the knowledge of the non-perturbative background harmonics, we can compute the contribution of arbitrarily many additional harmonics at almost no computational cost.

Now we must do the dirty work of computing the nonlinear harmonics. Computing $n_{\rm pert} - 1$ non-perturbative harmonics will amount to shooting a point particle in $n_{\rm pert} - 1$ dimensions, and

[2] In $d \neq 1, 3$ one must remember to add $(d-1)(d-3)/(4r^2)$ to account for the change of variables.

tuning its initial condition so that it lands on the saddle-top at the origin.

The physical quasibreather only feels the orthogonal deformation at second order, and therefore we may use the following procedure to compute the deformed PQB to leading order:

1. Choose $S_n(0)$ and $C_n(0)$ from the $n_{\text{pert}} - 1$ dimensional space of initial conditions.
2. Shoot the harmonics S_n, C_n from $r = 0$ to some large finite radius r_{out} by evolving the mode equations (a).
3. Use the radiative boundary conditions (e) to convert the S_n to c_n and C_n to s_n at $r = r_{\text{out}}$.
4. Shoot the c_n, s_n back to the origin in the background resulting from step 2.
5. Check for regularity at the origin for the c_n and s_n, and regularity at r_{out} for the bound harmonics. If not regular, adjust $S_n(0)$ and $C_n(0)$ and repeat from step 2. Since regularity is equivalent to minimizing the first derivative, this can be implemented by a variant of a binary search procedure, e.g. golden section search.
6. Compute any number of perturbative harmonics using the procedure from the previous section in the background of the non-perturbative harmonics.
7. To account for linear backreaction of the perturbative harmonics, re-shoot the non-perturbative harmonics in the background of the perturbative harmonics. This last step is repeated until convergence.

In practice, it is helpful to break down the $n_{\text{pert}} - 1$ dimensional search into $n_{\text{pert}} - 1$ linear searches that are performed hierarchically. The process of nonlinear shooting is sped up by precomputing the potential functions and using table-lookup. This kind of optimization is especially important when dealing with periodic potentials where repeatedly computing Bessel functions is costly.

4.2.3 Branching of the fundamental mode

In section 2.1, we reduce the problem of finding the radial profile of the oscillon to a classical-mechanical 'shooting' problem. In its simplest case of one non-perturbative harmonic S_1, the problem further simplifies to the rolling of a massive ball in a double-welled potential $V_{S_1}(S_1)$ in the presence of $2/r$ friction. A shooting solution is one which starts at rest at an initial displacement $S_1(0)$ and ends at $S_1 = 0$ at $r = \infty$.

In linear equations, such as the radial hydrogen atom problem, there is exactly one solution for each integer number of nodes (i.e. zero-crossings) of the radial profile S_1. In our PQB mode equations, strong nonlinearities break this intuition, as depicted in figure 4.3. Specifically, a small change in the oscillon frequency ω can change the number of solutions with zero nodes by an increment of two, introducing new branches of oscillon solutions (or eliminating them) when the

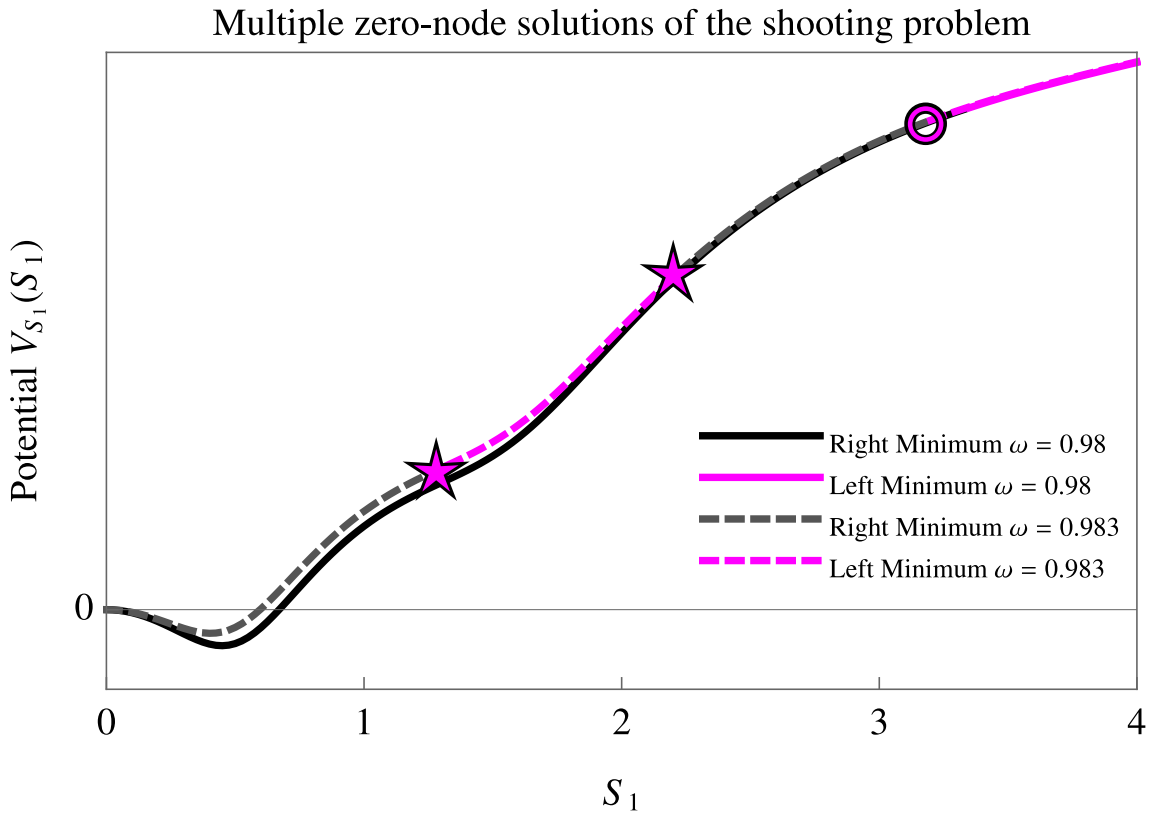

Figure 4.3: The emergence of two new zero-node solutions in the potential defined by Fourier coefficients $\vec{\mathcal{V}} = \{1, 0.5, -1, 0.5\}$ at large oscillon frequencies. The plot shows the effective potential $V_{S_1}(S_1)$ as a function of S_1 for positive values of S_1; since the potential is parity-symmetric, the $S_1 < 0$ region is the mirror opposite with respect to the $S_1 = 0$ axis. We have adjusted the vertical axis to better illustrate the qualitative features of the potential. Different regions are colored according to the sign of $S_1(\infty)$ when launched from that location. A shooting solution is represented by a point on the boundary between a black and magenta region. Whereas initially there was only one zero-node shooting solution (marked by the circle), the new potential adds two more zero-node solutions, marked by the stars. Intuitively, the higher the starting point, the further the particle will travel, causing successive solutions to have an increasing number of nodes. However, the combination of $2/r$ friction and nonlinearities in the potential breaks this intuition. Depending on the potential's convexity at the initial point, the oscillon may lose a widely variable amount of energy to friction. Therefore, it is at these regions of varying curvature that we expect these new solutions to emerge.

potential possesses non-trivial convexity. If this new branch consists of quasibreathers with lower bound energy, then the original branch may jump to the low-energy branch after the original branch experiences energetic death. In the reverse scenario, oscillons may form on the high-energy branch but the low-energy branch is energetically forbidden from reaching the high-energy branch.

In the oscillons that we study in e.g. figure 2.1a, many of the longer-lived potentials contain a high-energy branch of very large, low-amplitude oscillons which only exists in a small range of frequencies close to m. One such example is shown in figure 4.3. All the examples studied in section 2.3 are the result of purposefully introducing these branches at a specific frequency $\omega \approx m_f$.

4.3 Floquet analysis

In appendix 4.1 we introduced the notion of asymptotic attraction to describe physical oscillons as perturbations of PQBs. From this expansion, we have reduced the problem of oscillon stability to the study of the linear stability of equation (4.15). Standard Floquet theory tells us that the result of this analysis can have two outcomes: the equation is linearly unstable, or it possesses oscillatory states exclusively (modulo boundary effects). In other words, the existence of a stable decaying mode implies the existence of a growing mode, and stability must emerge at higher order in perturbation theory, if at all. Here, we address the linear stability of perturbations $\delta\theta$, and later argue that nonlinear terms stabilize linearly oscillatory modes.

4.3.1 Linear stability analysis

Let us begin by reproducing equation (4.15) for ease of reference: the linearized homogeneous equation for the perturbation $\delta\theta$ in the background of $\theta_{\rm PQB}$ is,

$$0 = \delta\ddot{\theta} - \nabla^2\delta\theta + V''(\theta_{\rm PQB})\delta\theta\,. \tag{4.22}$$

Recall that $\theta_{\rm PQB}$ is a periodic solution of the equations of motion, and therefore can induce parametric resonances. Substituting in the form of the quasibreather (4.5), we find

$$V''(\theta_{\rm PQB}) = \sum_{m\in\mathbb{N}_{\rm even}} V''_m(S,C)\cos m\omega t + \sum_{m\in\mathbb{N}_{\rm odd}} V''_m(S,C)\sin m\omega t\,, \tag{4.23}$$

which, under parity symmetry of V, further simplifies to

$$V''(\theta_{\rm PQB}) = \sum_{m\in\mathbb{N}_{\rm even}} V''_m(S)\cos n\omega t\,, \tag{4.24}$$

where V''_m is defined by (4.23). We will leave specific formulae for V''_m to appendix 4.4.3.

Since (4.15) is linear, we may Fourier transform $t \to \Omega$, and decompose $\delta\theta$ in spherical harmonics.

Because the quasibreather background is periodic, it induces couplings between frequencies separated by integer multiples of the fundamental frequency ω. Therefore, let us restrict our analysis to the values of the Fourier transform $\delta\theta(\Omega, r)$ at the discrete tower of harmonics defined as $\Omega_n \equiv \Omega_0 + n\omega$, $n \in \mathbb{Z}$, where the base frequency Ω_0 can be assumed to lie in the interval $(0, \omega)$. Therefore, the Fourier components on this tower, denoted $\delta\theta_n(\Omega_0, r) \equiv \delta\theta(\Omega_n, r)$, will respect a matrix-differential equation:

$$0 = -(\Omega_0 + n\omega)^2\delta\theta_n - \delta\theta_n'' - \frac{d-1}{r}\delta\theta_n' + \frac{\ell(\ell+d-2)}{r^2}\delta\theta_n + V_0''(S,C)\delta\theta_n + \\ + \frac{1}{2}\sum_{m\in\mathbb{N}^{>0}_{\text{even}}} V_m''(S,C)(\delta\theta_{n+m} + \delta\theta_{n-m}) + \frac{1}{2\mathrm{i}}\sum_{m\in\mathbb{N}_{\text{odd}}} V_m''(S,C)(\delta\theta_{n+m} - \delta\theta_{n-m})\,, \tag{4.25}$$

where ℓ is the angular momentum number. This is apparently a quadratic eigenvalue problem in the fundamental frequency Ω_0 [232], although as we will see, it becomes an irrational eigenvalue problem upon imposing transparent boundary conditions [233, 234]. The eigenvalue solutions Ω_0 characterize the stability or instability of the system: real eigenvalues corresponding to oscillatory motion; if solutions pick up an imaginary part, the mode will be exponentially growing (if $\mathrm{Im}(\Omega_0) < 0$) or exponentially decaying (if $\mathrm{Im}(\Omega_0) > 0$). In the absence of transparent boundary conditions, the solutions come in pairs of complex conjugates; in this closed-box scenario, the existence of a stable (i.e. decaying) mode implies the existence of an unstable mode.

An instructive example We may gain some insight into the eigenvalues Ω_0 by studying the simpler case of perturbations inside a box for a potential with parity. The matrix differential equation simplifies such that only the sum over even terms in (4.25) survives. At leading order we only include the first harmonic's $n = \pm 1$ terms; the reason is that large-n harmonics both decouple from the fundamental and become unbound. This allows us to keep only the V_0'' and V_2'' terms in the equation. Moreover, we make the assumption that Ω_0 is small compared to ω, representing solutions to the perturbation equations with a separation between the fast and slow timescales; this is relevant when we focus on the boundary between periodicity and instability, where Ω_0 will be small in magnitude. This assumption will be supported by the result of the analysis.

The result is the following 2×2 matrix-differential equation

$$0 = \left[2\omega\Omega_0\boldsymbol{\sigma}_z + \boldsymbol{\sigma}_x V_2'' + \mathbf{I}(\omega^2 - \nabla^2 + V_0'')\right]\delta\vec{\theta}\,, \tag{4.26}$$

where we have suppressed the argument of V_0'', V_2'' for brevity and $\boldsymbol{\sigma}_i$ are the Pauli matrices with entries of magnitude 1. We may phrase this as a typical eigenvalue problem in Ω_0 by multiplying through with $\boldsymbol{\sigma}_z/2\omega$, leading to

$$0 = \det\left(\mathbf{H} + \mathbf{A} - \Omega_0\mathbf{I}\right)\,, \tag{4.27}$$

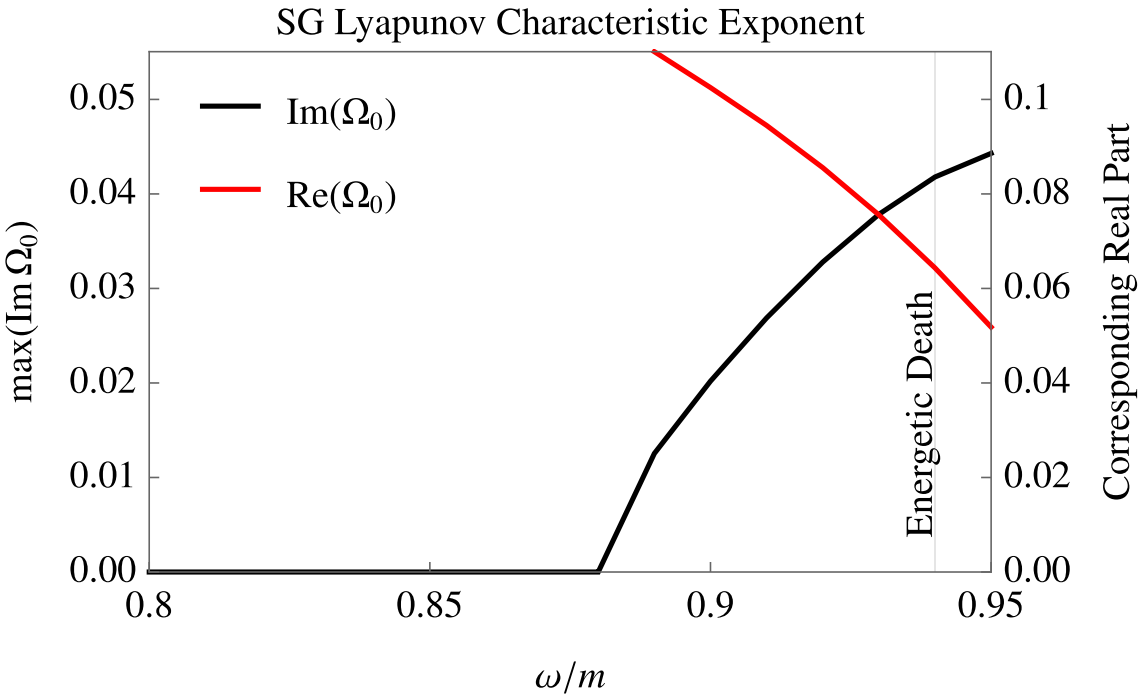

Figure 4.4a: The Lyapunov characteristic exponent (the eigenvalue Ω_0 of (4.25) with maximum imaginary part) for the sine-Gordon deformed physical quasibreather (with an error of ± 0.005). The perturbation $\delta\theta$ becomes linearly unstable at $\omega \approx 0.88$. The nearest asymptotically attractive quasibreather is always finitely far away from the oscillon. When $\omega > 0.88$, the linearly unstable mode is therefore *always* excited, leading to growing quasiperiodic oscillations on top of the deformed quasibreather background (see figure 4.4b). Note, throughout this band of linear instability, the mass energy $\int \mathrm{d}V \frac{1}{4} m^2 S_1^2$ is monotonically decreasing, in contradiction with [64]. On the plot, we denote the energetic death at $\omega \approx 0.94$, where the oscillon is forced off the quasibreather trajectory by energy conservation.

where $\mathbf{H}$ and $\mathbf{A}$ are Hermitian and anti-Hermitian matrices defined by

$$\mathbf{H} = \frac{1}{2\omega}\boldsymbol{\sigma}_z(\omega^2 - \nabla^2 + V_0'')\,, \qquad \mathbf{A} = \frac{\mathrm{i}}{2\omega}\boldsymbol{\sigma}_y V_2''\,. \tag{4.28}$$

In other words, the Ω_0 eigenvalues are the roots of the characteristic polynomial with all-real coefficients defined by the matrix with all-real entries $\mathbf{H} + \mathbf{A}$. Consider the case $\mathbf{A} = 0$; the eigenvalues Ω_0 are the eigenvalues of $\mathbf{H}$, which is composed of two mirrored copies of the real spectrum of the single-block operator $\frac{1}{2\omega}(\omega^2 - \nabla^2 + V_0'')$. The addition of $\mathbf{A}$ only introduces couplings between these two sectors; since it is also antisymmetric, these couplings are equal and opposite in sign. If we start from a spectrum of $\mathbf{H}$ with no overlap between its two sectors, the addition of $\mathbf{A}$ will bring the two mirrored 'ground states' together from $\Omega_0 = \pm E_{\text{ground}}$ to the value of $\Omega_0 = 0$. From the perspective of the characteristic polynomial, this corresponds to the two roots becoming degenerate

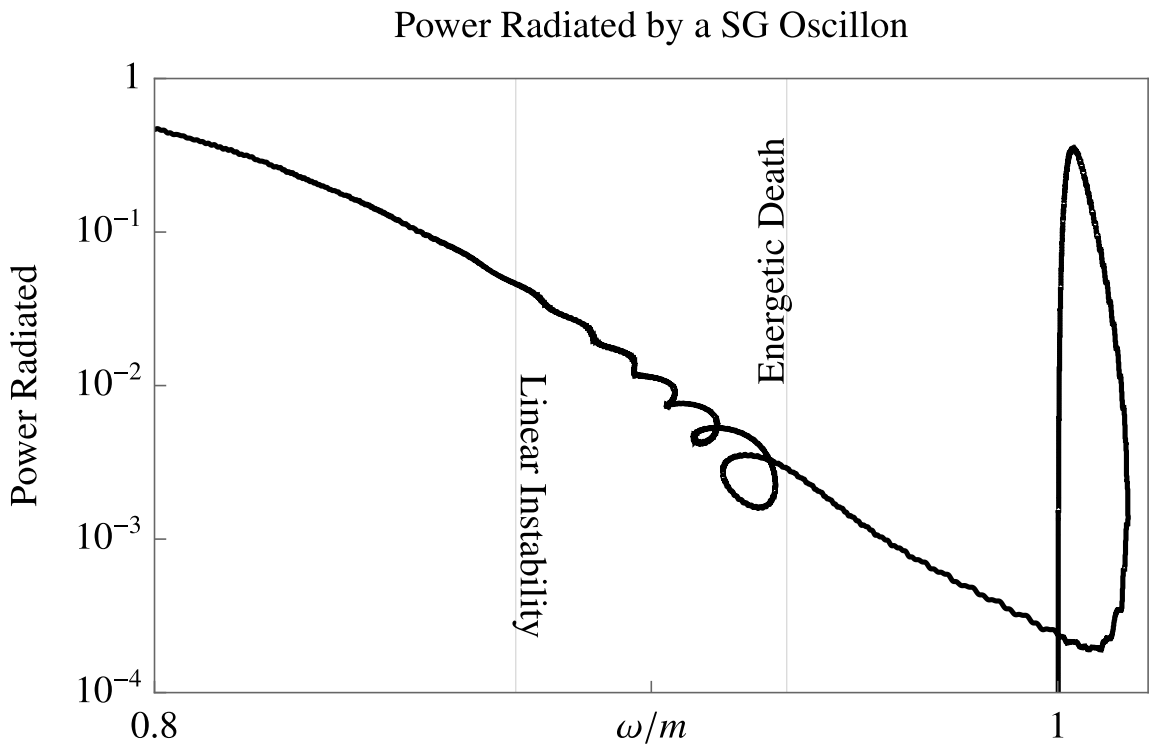

Figure 4.4b: The power radiated by a simulated sine-Gordon oscillon versus the central fundamental frequency. On this plot, we've indicated the onset of linear instability $\omega \approx 0.88$ calculated using our eigenvalue code described in appendix 4.3, and the instance of energetic death $\omega \approx 0.94$ described in appendix 4.1.4. This figure represents the a consequence of linear instability: growing quasiperiodic oscillations. The specific magnitude of this effect depends on initial conditions and environmental perturbations (see figure 2.11 for an example where oscillations are suppressed). Whether or not the unstable mode can become large enough to destroy the oscillon, the perturbation itself has a radiation component, which may significantly modify the lifetime. In this particular case, the unstable mode's frequency $\omega \pm \mathrm{Re}\Omega_0$ approaches the oscillon frequency ω towards the end of life, leading to growing beats (see figure 4.4a). The loop of death at the end of the evolution occurs because the central oscillon rapidly becomes a mix of first and third harmonic, causing the central frequency to be larger than 1.

before turning imaginary. In other words, complex eigenvalues must appear by first passing through an inter-block degeneracy. Therefore, the meeting of the two ground states defines the boundary between periodicity (i.e. an all-real spectrum) and instability (i.e. complex spectrum). If the spectrum of $\mathbf{H}$ is bounded below by 0, then the meeting of the two states will produce purely imaginary eigenvalues. This result should be compared to [64]. In general, the symmetries of (4.27) that led to this result are only approximate, and therefore we should expect the first nearly-stable eigenvalue to be close to zero in general.

However, because the oscillon lives in an open box, we must ensure that (4.25) is endowed with transparent boundary conditions. Such radiative boundary conditions depend on the momentum of the outgoing mode $\sqrt{(\Omega_0 + n\omega)^2 - 1}$. Eigenvalue problems with radiative boundary conditions have been studied in the non-relativistic limit in [233]. Crucially, the calculations of [233] depend on the existence of a uniformizing variable $u(\Omega_0)$ in which the outgoing momentum becomes a rational function of u. As far as we are aware, no such uniformization procedure is known for the relativistic case with two channels, or more generally for any case with more than two channels.

Using series approximations and a uniformizing variable $u(\Omega_0)$, we show in appendix 4.4.3 that it is possible to express the boundary condition as a polynomial for $|\Omega_0| < 1/2$ for $\omega > 1/2$ in the case of parity or $\omega > 3/4$ without parity. Using standard linearization techniques, we may reduce this polynomial eigenvalue problem to a generalized eigenvalue problem, for which numerical software is plentiful. This is the method applied to the stability analysis in Figure 4.4a.

4.3.2 Nonlinear stabilization

In the previous section, we laid out our numerical method for computing the linear stability of the homogeneous perturbation $\delta\theta$ in the background of the deformed physical quasibreather. Modulo technicalities at the boundary, we found that all linear perturbations either are oscillatory, or come in pairs of exponentially growing and decaying modes. The result is that stability, understood to mean that all homogeneous perturbations shrink, cannot be fully explained at the level of linear Floquet analysis.

Thus, stability must originate at higher order in perturbation theory, if it exists at all. In this section, we identify radiation as the mechanism of stabilization accessible to small oscillatory perturbations; specifically, modes which are periodic in the linear stability analysis will couple to radiative modes at higher orders, providing a channel for dissipation. Therefore, we conclude that a sufficient condition for full nonlinear stability is that all modes are oscillatory at the level of linear perturbation theory. Furthermore, we will see that linear instability does *not* imply nonlinear instability.

We will explore the effect of adding a nonlinear term to a Floquet-type problem by studying the toy example of the Mathieu equation with a quadratic nonlinear term. To simplify our analysis,

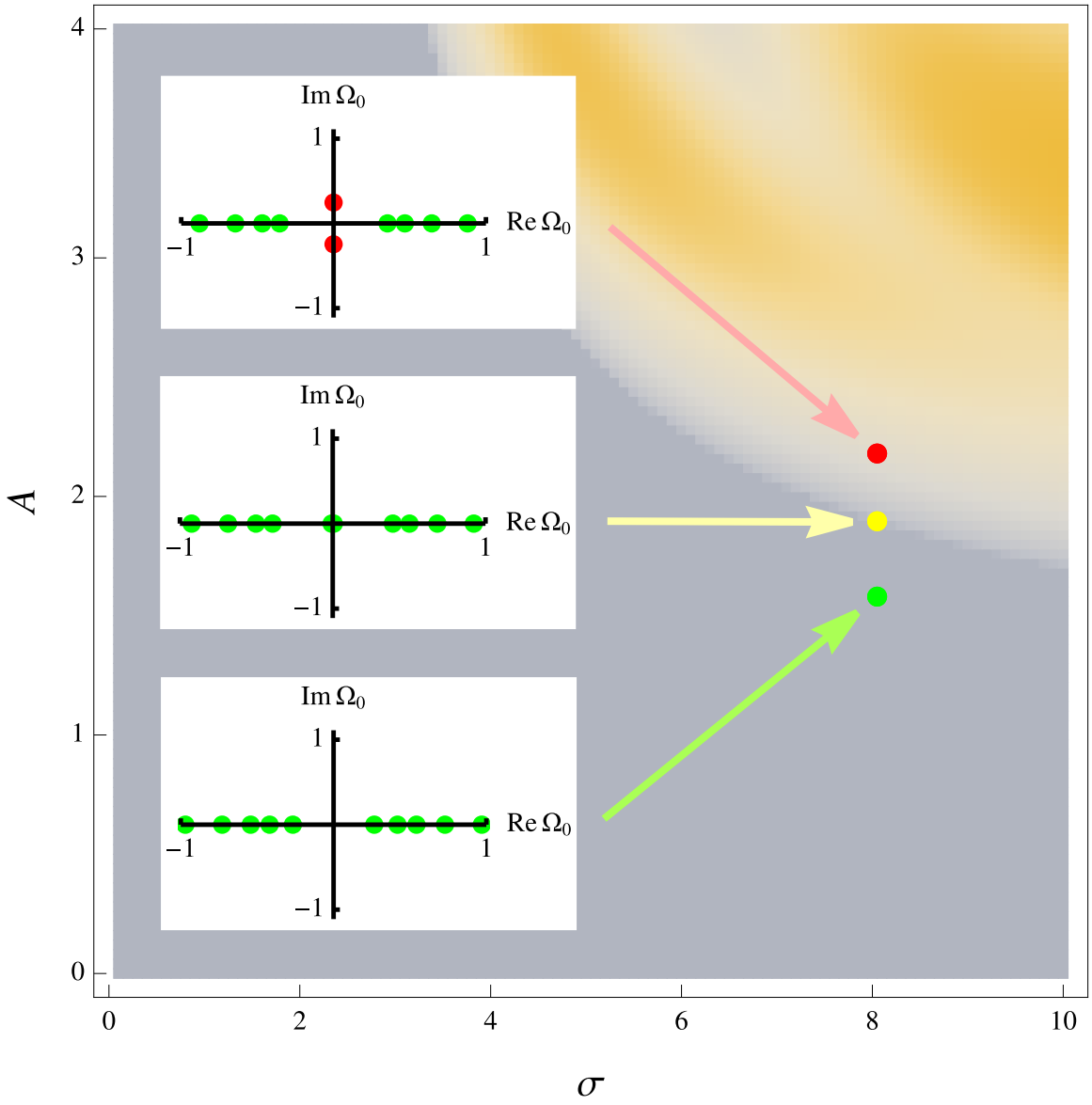

Figure 4.5: A visualization of how linear instability emerges in the simplified model of appendix 4.3. The boundary of stability is described by eigenvalues meeting at zero. The plot describes the solutions to the eigenvalue equation (4.27) in the case of a simple Gaussian background, in which the fundamental oscillon mode is taken to be $S_1(r) = A\exp\{-r^2/2\sigma^2\}$. The plot background describes stability as a function of the two Gaussian parameters, the oscillon amplitude A and width σ; for oscillons of sufficient width and amplitude, there are eigenvalues Ω_0 with negative imaginary part, and thus the oscillon is unstable. We show the eigenvalues nearest to zero for three points in this parameter space: stable (green), borderline unstable (yellow), and unstable (red). The real eigenvalues closest to the origin become degenerate at zero on the boundary of stability; they further split into purely imaginary conjugates in the instability region.

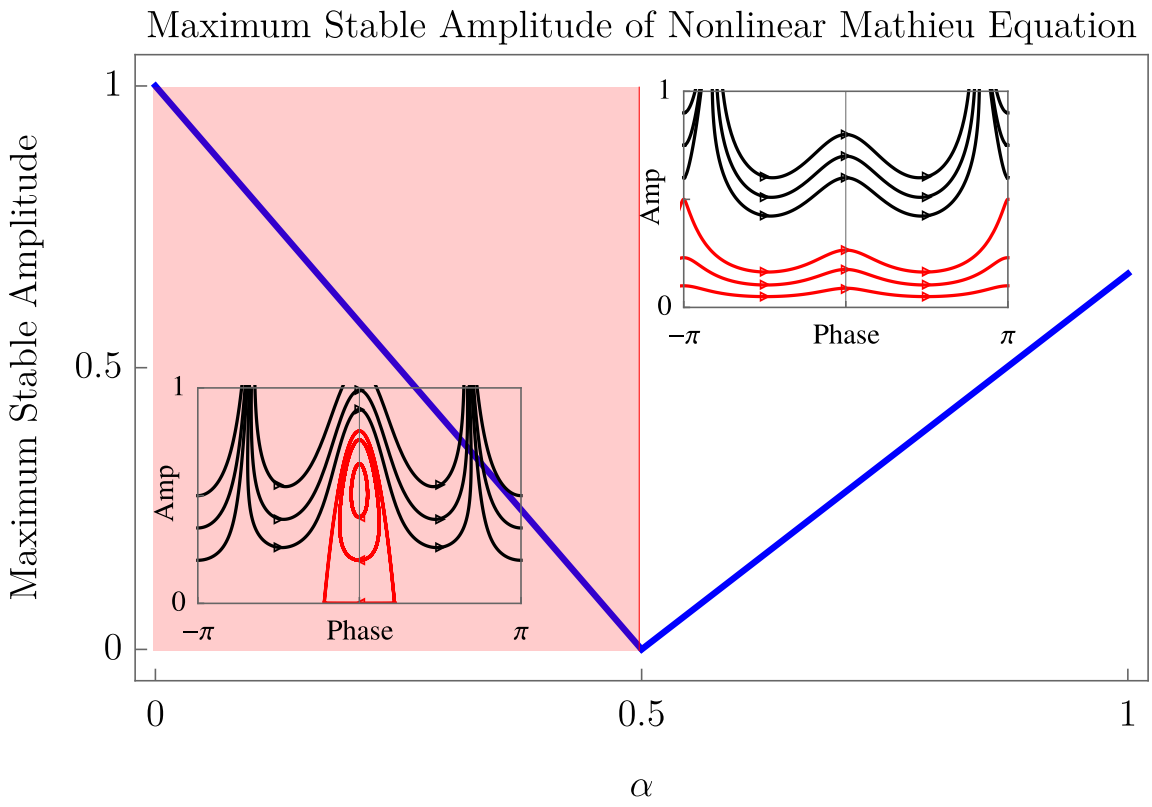

Figure 4.6: Here we plot the maximum stable amplitude of y in the nonlinear Mathieu equation (4.29) for small ϵ, and we've indicated the instability band of the linear Mathieu equation in red. Outside the red region, the nonlinear oscillations are centered on $y = 0$, representing that the oscillations stay bounded independent of phase. However, for $|\alpha| < 0.5$, only oscillations of a particular phase remain bounded, indicating that $y = 0$ has become hyperbolic (see left inset). Inset in the plot are two examples of the slow oscillation trajectories. For $|\alpha| < 0.5$, the red stable trajectories have amplitude larger than 0 and are restricted to a finite interval of phase. This generally nonlinear phenomenon represents a special region of stability within the otherwise unstable phase of the Mathieu parameter space. For $|\alpha| > 0.5$, the red stable oscillations are restricted to a finite amplitude, but are allowed to have any phase. In both cases, large enough amplitude perturbations grow without bound, represented by the black trajectories.

we begin by studying potentials with parity, so that the leading order oscillating contribution to $V''(\theta_{\mathrm{PQB}})$ is proportional to $\cos 2\omega t$. The leading nonlinear term is then proportional to $\sin \omega t$. Thus, we will study the nonlinear generalizations of the Mathieu equation of the form

$$0 = \ddot{y} + (1 + \epsilon(\alpha + \cos 2t + y \sin t))y \,. \tag{4.29}$$

In this toy problem, y represents the perturbation $\delta\theta$ to a physical quasibreather whose potential conserves parity. The fact that the linear term is proportional to $\cos 2t$ and the quadratic term y^2 is proportional to $\sin t$ is a consequence of the symmetry of the potential, which guarantees that polynomials in y of certain parity have the corresponding oscillatory terms.

A standard two-timing analysis, along the lines of [235], with $\epsilon \ll 1$ demonstrates that the Mathieu instability bifurcation at $|\alpha| = 1/2$ is unchanged by the nonlinearity around $y = 0$. However, one difference is the appearance of regions of stability inside the linearly unstable region $|\alpha| < 1/2$, although large enough y always implies instability, regardless of α [3]. When y is the smallest scale in the problem, we recover the usual Mathieu equation behavior (see figure 4.6). In summary, linear periodicity is unchanged for small enough y, although linearly unstable modes may become periodic.

Thus, we should expect that the oscillatory modes of the linear equation (4.25) remain oscillatory upon introduction of a nonlinear term as long as they are of small enough amplitude. Moreover, the nonlinear terms may convert an otherwise linearly unstable mode into an oscillatory one. Further, the nonlinear interactions of linearly oscillatory modes will necessarily produce radiation, carrying away energy, causing their amplitude to shrink. Thus, sufficiently small linearly oscillatory modes are stabilized by radiation.

4.3.3 Angular perturbations

In appendix 4.4.3, we develop a calculation scheme to solve for the perturbation $\delta\theta$ as a function of t and r. In order to obtain the perturbation equations for $\delta\theta$, we performed a spherical harmonic decomposition, resulting in a set of decoupled equations for each mode of angular momentum number ℓ. These equations differ by the coefficient of the angular momentum effective potential

$$V_{\mathrm{angular}} = \frac{\ell(\ell + d - 2)}{r^2} \,. \tag{4.30}$$

Because this potential is positive, it acts as a repulsive centrifugal term, reducing the perturbation density at the origin. Hence, we expect that perturbations with more angular momentum are typically *more linearly stable*, since less of the perturbation lies inside the oscillon bulk, although for low angular momentum, the conclusion is case-dependent. An intuition for this comes from applying

[3] Indeed, this example is illustrative for much of the behavior we observe in numerical simulations of oscillons. Large quasiperiodic oscillations, arising from a linear instability, do not blow up like the linear analysis would suggest, but rather persist because of nonlinear regions of stability.

the stability phases of the standard Mathieu equation (see figure 4.7).

A similar $1/r^2$ term appears in the effective potential for the perturbation upon removing the $(d-1)/r$ friction term through a change of variables $\delta\theta \to r^{(d-1)/2}\delta\theta$. This introduces the effective potential

$$V_{\text{geometric}} = -\frac{(d-1)(d-3)}{4r^2}\,. \tag{4.31}$$

This term differs from the angular momentum term in two important ways. First, it can be of either sign: for $d = 1, 3$ it vanishes, for $d = 2$, it is repulsive, and for $d \geq 4$ it is attractive. Second, it also influences the quasibreather background itself, whereas the angular momentum terms only influence the non-spherical perturbations. Because this potential influences both the background *and* the perturbation, its effect on stability depends on the specifics of the nonlinear potential.

4.4 Technical formulae

In this section, we provide a detailed description of the formulae and numerical techniques used to compute physical quasibreather properties.

4.4.1 Perturbative harmonic formulae

Once we have computed the oscillon's non-perturbative modes $S_{n<n_{\text{pert}}}, C_{n<n_{\text{pert}}}$ and their orthogonal deformations $c_{n<n_{\text{pert}}}, s_{n<n_{\text{pert}}}$, we may compute the perturbative modes $S_{n\geq n_{\text{pert}}}, C_{n\geq n_{\text{pert}}}$ and their orthogonal deformations $c_{n\geq n_{\text{pert}}}, s_{n\geq n_{\text{pert}}}$ using the procedure outlined in section 4.2.1. Here, we provide explicit formulae for the Sommerfeld matrix $\mathbf{S}$ and the block Laplacian operator $\boldsymbol{\nabla}^2$. Upon discretizing space such that $r = [0, \mathrm{d}r, \ldots, (N-1)\,\mathrm{d}r]$, the matrix $\mathbf{S}$ is comprised of all zeros, except for the lower right entry in each diagonal block. To describe this object, we introduce the following notation. The matrix $\mathbf{S}$ has four indices: two upper indices labelling the block, and two lower indices labeling the location within that block. In this notation, the entries in the matrix $\mathbf{S}$ in (4.21) may be written

$$\mathbf{S}^{nm}_{ab} = (-1)^n\sqrt{(n\omega)^2 - 1}\delta_{nm}\delta_{aN}\delta_{bN}\,. \tag{4.32}$$

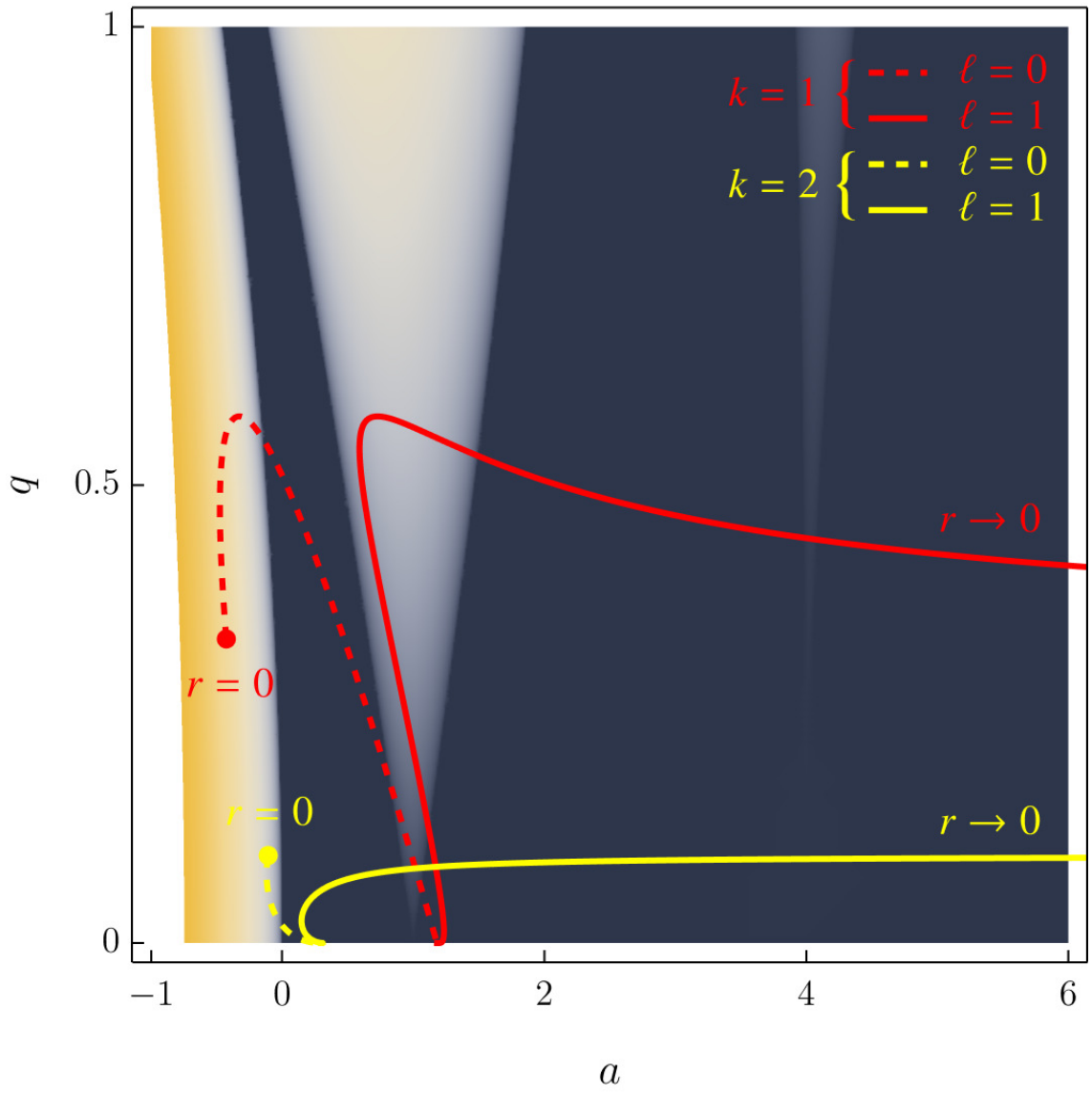

Figure 4.7: Effective Mathieu equation parameters $0 = \ddot{y} + (a - 2q\cos 2k\omega t)y$ for integer k, where we associate a pair (a_r, q_r) to each radius r of the sine-Gordon quasibreather background (4.25) for $\omega = 0.95$, ignoring the gradient term. This picture is meant to guide our intuition of the Mathieu equation into the less-familar Floquet problem (4.25). Intuitively, a mode can be understood as more unstable if more of its volume lies in the Mathieu instability bands. This plot, although not quantitatively precise, provides intuition for why the lowest angular momentum states are more susceptible to instabilities, since they have the most overlap with the dominant instability bands.

In the same notation, we may describe the Dirichlet-Neumann block Laplacian operator

$$[\boldsymbol{\nabla}^2]^{nm} = \frac{1}{\mathrm{d}r^2} \begin{pmatrix} -2 & 1 & & & \\ 1 & & & & \\ & & \ddots & 1 & \\ & & 1 & -2 & \mathrm{d}r \\ & & & 1 & -\mathrm{d}r \end{pmatrix} \delta_{nm} \,. \tag{4.33}$$

4.4.2 Potentials with parity

As described in section 2.4, the Fourier basis is a natural basis to describe any scalar potential, since it is not plagued by the same radius-of-convergence issues of, say, the Taylor basis. Here we provide the harmonic factorization of a general scalar potential with parity (2.43). Taking the first derivative of (2.43) with respect to θ, we arrive at the following expression for the self-interaction terms in the non-linear wave equation

$$V'(\theta) = \sum_{m=1}^{\infty} \frac{\mathcal{V}_m}{m} \sin m\theta \,. \tag{4.34}$$

This expression is specific to the case of a potential with 2π periodicity. To accommodate potentials without periodicity, simply replace $\theta \to \theta/\theta_{\max}$ where $\theta \in [-\pi\theta_{\max}, \pi\theta_{\max}]$ and $\sum \mathcal{V}_m = \theta_{\max}^2$. In order to keep the following expressions from getting any more unruly, we will present the explicit formulae for 2π-periodic potentials, since the reader may easily convert these expressions to accommodate general periodicity.

By virtue of the Jacobi-Anger expansion [236]

$$e^{\mathrm{i}a \sin b} = \sum_{k=-\infty}^{\infty} J_k(a) e^{\mathrm{i}kb} \,, \tag{4.35}$$

we may compute the harmonic expansion of the potential, evaluated as a function of the PQB harmonics

$$V'\left(\sum_{n=1}^{\infty} S_n \sin(n\omega t)\right) = \sum_{m=1}^{\infty} \frac{\mathcal{V}_m}{m} \sum_{\vec{k} \in \vec{\mathbb{Z}}} \left[\left(\prod_{n=1}^{\infty} J_{k_n}(mS_n) \right) \sin\left(\sum_{n=1}^{\infty} n k_n \omega t \right) \right] \,, \tag{4.36}$$

where $\vec{k} = (k_1, k_2, \dots)$. One may write this more compactly in terms of generalized Bessel functions [236]. From this formula, we obtain the expressions for V_{S_n} in (4.9)

$$V'(\theta) \equiv \sum_{n=1}^{\infty} V'_{S_n}(S_1, \dots,) \sin(n\omega t) \,. \tag{4.37}$$

In general, we may evaluate the full non-perturbative formulae for the mode-potential derivatives V'_{S_N} and V'_{c_N},

$$\begin{aligned} V'_{S_N} &= \sum_{m=1}^{\infty} \frac{\mathcal{V}_m}{m} \sum_{k_1^s,\ldots,k_1^c,\ldots} \left(\prod_{n=1}^{\infty} J_{k_n^s}(mS_n) J_{k_n^c}(mc_n) \right) \cos\left(\sum_{n=1}^{\infty} k_n^c \pi/2 \right) \\ &\quad \times \left[\delta\left(N - \sum_{n=1}^{\infty} n(k_n^s + k_n^c) \right) - \delta\left(-N - \sum_{n=1}^{\infty} n(k_n^s + k_n^c) \right) \right] , \\ V'_{c_N} &= \sum_{m=1}^{\infty} \frac{\mathcal{V}_m}{m} \sum_{k_1^s,\ldots,k_1^c,\ldots} \left(\prod_{n=1}^{\infty} J_{k_n^s}(mS_n) J_{k_n^c}(mc_n) \right) \sin\left(\sum_{n=1}^{\infty} k_n^c \pi/2 \right) \\ &\quad \times \left[\delta\left(N - \sum_{n=1}^{\infty} n(k_n^s + k_n^c) \right) + \delta\left(-N - \sum_{n=1}^{\infty} n(k_n^s + k_n^c) \right) \right] . \end{aligned} \tag{4.38}$$

Note, the δs in this equation are Kronecker δs, but we use a parenthetical argument to keep the expression readable. From these expressions, we may derive useful formulae for important cases of interest. Here, we present two examples for illustration, and because the reader may find them particularly useful in generating oscillon profiles of their own. First, in the case that the fundamental mode S_1 dominates and all other modes are perturbative, we have the following source term

$$\vec{\mathcal{J}}_{\vec{C}} = r^{(d-1)/2} \sum_{m=1}^{\infty} 2 \frac{\mathcal{V}_m}{m} \begin{pmatrix} J_3(mS_1) \\ J_5(mS_1) \\ \vdots \end{pmatrix} , \tag{4.39}$$

with $\vec{\mathcal{J}}_{\vec{s}} = 0$ and the following mass matrices

$$\begin{aligned} \mathbf{V}_{\vec{C}} &= \sum_{m=1}^{\infty} \mathcal{V}_m \begin{pmatrix} (J_{3-3}(mS_1) - J_{3+3}(mS_1)) & (J_{3-5}(mS_1) - J_{3+5}(mS_1)) & \cdots \\ (J_{5-3}(mS_1) - J_{5+3}(mS_1)) & (J_{5-5}(mS_1) - J_{5+3}(mS_1)) & \\ \vdots & & \ddots \end{pmatrix} , \\ \mathbf{V}_{\vec{s}} &= \sum_{m=1}^{\infty} \mathcal{V}_m \begin{pmatrix} (J_{3-3}(mS_1) + J_{3+3}(mS_1)) & (J_{3-5}(mS_1) + J_{3+5}(mS_1)) & \cdots \\ (J_{5-3}(mS_1) + J_{5+3}(mS_1)) & (J_{5-5}(mS_1) + J_{5+3}(mS_1)) & \\ \vdots & & \ddots \end{pmatrix} , \end{aligned} \tag{4.40}$$

to be inserted into equation (4.21). The case where S_1 and S_3 are non-perturbative and all other harmonics are perturbative everywhere has a similarly clean form

$$\mathbf{V} = \sum_{m=1}^{\infty} V_m \sum_{k=-\infty}^{\infty} J_k(mS_3) \begin{pmatrix} (J_{5-5-3k}(mS_1) \mp J_{5+5-3k}(mS_1)) & (J_{5-7-3k}(mS_1) \mp J_{5+7-3k}(mS_1)) & \cdots \\ (J_{7-5-3k}(mS_1) \mp J_{7+5-3k}(mS_1)) & (J_{7-7-3k}(mS_1) \mp J_{7+7-3k}(mS_1)) & \\ \vdots & & \ddots \end{pmatrix},$$

$$\vec{\mathcal{J}}_{\vec{C}} = r^{(d-1)/2} \sum_{m=1}^{\infty} \frac{V_m}{m} \sum_{k=-\infty}^{\infty} J_k(mS_3) \begin{pmatrix} J_{5-3k}(mS_1) - J_{-5-3k}(mS_1) \\ J_{7-3k}(mS_1) - J_{-7-3k}(mS_1) \\ \vdots \end{pmatrix},$$

$$\vec{\mathcal{J}}_{\vec{s}} = r^{(d-1)/2} c_3 \sum_{m=1}^{\infty} V_m \sum_{k=-\infty}^{\infty} J_{k-1}(mS_3) \begin{pmatrix} J_{5-3k}(mS_1) + J_{-5-3k}(mS_1) \\ J_{7-3k}(mS_1) + J_{-7-3k}(mS_1) \\ \vdots \end{pmatrix}, \tag{4.41}$$

with $-$ corresponding to $\mathbf{V}_{\vec{C}}$ and $+$ corresponding to $\mathbf{V}_{\vec{s}}$. The formulae when there are more non-perturbative harmonics follow the same pattern.

4.4.3 Formulae for linear stability analysis

Here we provide the mathematical details to accompany appendix 4.3. We restrict ourselves to $\omega > 1/2$ in the case of parity and $\omega > 3/4$ otherwise. This restriction is to ensure that the following series approximation converges on the disc $|\Omega_0| < 1/2$. If one is certain that the unstable eigenvalues occur in a smaller disc, the restrictions on ω may be weakened significantly, and indeed, this is often the case.

The outgoing boundary conditions depend on the momentum of the outgoing mode, which is an irrational function of Ω_0. In order to convert the irrational eigenvalue problem (4.25) into a polynomial eigenvalue problem that may be solved with standard techniques, we need to approximate the momentum $\sqrt{(\Omega_0 \pm n\omega)^2 - 1}$ by a polynomial. One's first intuition might be that the Taylor series of the momentum expanded about $\Omega_0 = 0$ would be a good approximation. This intuition is good for the higher harmonics, since Ω_0 is often much smaller than $n\omega$. However, this series only converges inside the disc $|\Omega_0| < 1 - \omega$ for $n = 1$, which is not sufficient to compute the Lyapunov exponent of the linear perturbation $\delta\theta$. A more sophisticated approximation is necessary in order to capture the behavior of the momentum as a function of Ω_0 on a disc that remains finite size as $\omega \to 1$.

To this end, we define

$$x = \Omega_0^2 - (1 - \omega)^2, \tag{4.42}$$

so that

$$\sqrt{(\Omega_0 \pm \omega)^2 - 1} = \sqrt{x + 2\omega(\omega - 1 \pm \Omega_0)}\,. \tag{4.43}$$

We then Taylor expand around $x = 0$, yielding the following series that converges on the disc of radius $1/2$ centered on $\Omega_0 = 0$ for $\omega > 1/2$

$$\begin{aligned}
\sqrt{(\Omega_0 \pm \omega)^2 - 1} &= \sqrt{2\omega(\omega - 1 \pm \Omega_0)} \left[1 - \sum_{j=0}^{\infty} \begin{pmatrix} 2j \\ j \end{pmatrix} \frac{1}{(j+1)2^{2j+1}} \left(\frac{(1-\omega)^2 - \Omega_0^2}{2\omega(\omega - 1 \pm \Omega_0)} \right)^{j+1} \right], \\
\sqrt{(\Omega_0 \pm n\omega)^2 - 1} &= \sqrt{(n\omega)^2 - 1} \left[1 - \sum_{j=0}^{\infty} \begin{pmatrix} 2j \\ j \end{pmatrix} \frac{1}{(j+1)2^{2j+1}} \left(-\frac{(\Omega_0 \pm n\omega)^2 - (n\omega)^2}{(n\omega)^2 - 1} \right)^{j+1} \right],
\end{aligned} \tag{4.44}$$

where the second equation is just the ordinary Taylor expansion centered on $\Omega_0 = 0$ for $n \geq 2$. The factor $\sqrt{2\omega(\omega - 1 \pm \Omega_0)}$ is not yet a polynomial. We utilize the technique of uniformization [233], where we define the complex variable u such that $\sqrt{2\omega(\omega - 1 \pm \Omega_0)}$ becomes a polynomial in u,

$$\Omega_0 = \frac{1 - \omega}{2} \left(u^2 + u^{-2} \right). \tag{4.45}$$

This definition turns (4.44) into rational functions of u, allowing us to rephrase (4.25) as a polynomial eigenvalue problem. The zero eigenvalues now live at the four roots of the equation $u^4 = -1$, around which we perform a small eigenvalue search using the Krylov subspace methods implemented in `Matlab`. Once the u eigenvalues and eigenvectors have been computed, we must convert back to check that they correspond to eigenvalues of the original irrational eigenvalue problem. In short, we have reduced the original irrational eigenvalue to a polynomial eigenvalue problem of degree at-least 4, depending on the degree of accuracy one wants to achieve.

Finally, we define the matrix $\mathbf{S}$ which encodes the non-derivative term in the Sommerfeld radiation condition, which can be written as a sum of the matrices $\hat{\mathbf{S}}_\lambda$, which are matrices of all zeros except for the lower right entry of the λth diagonal block, which is 1. This entry corresponds to the outer boundary of the grid, with λ ranging from $-L$ to L, and the upper left block corresponding to $\lambda = -L$, where L is the chosen order of the Floquet expansion. In this notation, the non-derivative part of the Sommerfeld boundary conditions may be written

$$\mathbf{S} = \sum_{\lambda=-\infty}^{\infty} \sqrt{(\Omega_0 + \lambda\omega)^2 - 1} \hat{\mathbf{S}}_\lambda \approx \sum_{\lambda=-L}^{L} \sum_{i=0}^{2M+1} c_{\lambda,i} u^i \hat{\mathbf{S}}_\lambda\,, \tag{4.46}$$

where $M = \min(2j_{\max,1} + 3, 4j_{\max,n} + 4)$, where $j_{\max,n}$ is the order of the Taylor expansion of the

nth momentum eigenvalue.

Collecting terms in (4.44), we have the following expressions for the coefficients of the $\hat{\mathbf{S}}_\lambda$ matrices, for $\lambda = 1$ and $\lambda = n > 1$ respectively

$$
\begin{aligned}
c_{\pm 1,i} = \sqrt{\pm\omega(1-\omega)}\,[(\delta_{1+M-i} \mp \delta_{-1+M-i}) - \\
- \sum_{j=0}^{j_{\max,1}} \begin{pmatrix} 2j \\ j \end{pmatrix} \frac{1}{(j+1)2^{2j+1}} \left(\pm\frac{\omega-1}{4\omega}\right)^{j+1} \sum_{k=0}^{2(j+1)} \begin{pmatrix} 2j+2 \\ k \end{pmatrix} (\pm 1)^k \left(\delta_{2(j-k)+3+M-i} \mp \delta_{2(j-k)+1+M-i}\right) \Bigg] \,, \\
c_{n,i} = \sqrt{(n\omega)^2 - 1} \Bigg[\delta_{i-M} - \sum_{j=0}^{j_{\max,n}} \frac{(2j)!}{(j!)^2} \frac{2^{-3j-2}}{(j+1)} \left(\frac{(1-\omega)^2}{1-(n\omega)^2}\right)^{j+1} \times \\
\sum_{k_{-4}+k_{-2}+k_0+k_2+k_4=j+1} \frac{(j+1)!}{k_{-4}!k_{-2}!k_0!k_2!k_4!} \left(\frac{1}{2}\right)^{k_4+k_{-4}} \left(\frac{2n\omega}{\omega-1}\right)^{k_2+k_{-2}} \delta_{4k_4-4k_{-4}+2k_2-2k_{-2}+M-i} \Bigg] \,.
\end{aligned}
\tag{4.47}
$$

Finally, we define the matrix of frequencies

$$
\mathbf{\Omega} = \begin{pmatrix} \ddots & & & & \\ & \omega & & & \\ & & 0 & & \\ & & & -\omega & \\ & & & & \ddots \end{pmatrix} , \tag{4.48}
$$

where the even entries are dropped when V has parity. These versions of $\mathbf{\Omega}$ and $\mathbf{S}$ are not to be confused with those used to solve for the physical quasibreather (4.21), as the correct version to use will always be clear from context.

With these definitions, the irrational eigenvalue problem (4.25) has been reduced to the polynomial eigenvalue problem

$$
0 = \sum_{i=0}^{N} u^i \mathbf{M}_i \,, \tag{4.49}
$$

where the matrices $\mathbf{M}_i$ are defined

$$\mathbf{M}_i = -\mathrm{i}\sum_{\lambda=-L}^{L} c_{\lambda,i}\hat{\mathbf{S}}_\lambda + \left[2\left(\frac{1-\omega}{2}\right)^2\mathbf{I} + \mathbf{\Omega}^2 + \mathbf{L}\right]\delta_{M-i} + \\ + \left(\frac{1-\omega}{2}\right)^2\mathbf{I}\left(\delta_{M+4-i} + \delta_{M-4-i}\right) + (1-\omega)\mathbf{\Omega}\left(\delta_{M+2-i} + \delta_{M-2-i}\right)\,, \tag{4.50}$$

$$\mathbf{L} = \boldsymbol{\nabla}^2 - \frac{\ell(\ell+d-2)}{r^2} + \frac{(d-1)(d-3)}{4r^2} - V_0'' - \\ - \frac{1}{2}\sum_{m\in\mathbb{N}_{\mathrm{even}}}^{\infty} V_m''\left(\mathbf{D}_{-m} + \mathbf{D}_m\right) - \frac{1}{2\mathrm{i}}\sum_{m\in\mathbb{N}_{\mathrm{odd}}}^{\infty} V_m''\left(\mathbf{D}_m - \mathbf{D}_{-m}\right)\,, \tag{4.51}$$

where displacement matrices $\mathbf{D}_m$ are the matrices consisting of all 1's on the diagonal of the mth block diagonal. Thus, we have reduced the computation of the Lyapunov exponents to computing the eigenvalues of the generalized eigenvalue problem

$$0 = \begin{pmatrix} u\mathbf{I} & -\mathbf{I} & & & & \\ & u\mathbf{I} & -\mathbf{I} & & & \\ & & \ddots & \ddots & & \\ & & & u\mathbf{I} & -\mathbf{I} & \\ \mathbf{M}_0 & \mathbf{M}_1 & \dots & \mathbf{M}_{N-2} & \mathbf{M}_{N-1} + u\mathbf{M}_N & \end{pmatrix}\begin{pmatrix} \delta\theta \\ u\delta\theta \\ \vdots \\ u^{N-1}\delta\theta \end{pmatrix}. \tag{4.52}$$

To summarize, the precision of this approximation can be increased to the desired level by

1. increasing the resolution of the radial grid by reducing $\mathrm{d}r$,
2. increasing the physical radius of the simulation r_{out},
3. increasing the number L of Floquet blocks kept in the expansion,
4. increasing the order $j_{\mathrm{max},\lambda}$ of the momentum expansions,
5. increasing the number of PQB harmonics kept in the background.

4.5 Explicit time evolution — numerical methods

Throughout the text, we refer to explicit numerical simulations for validation of our results. Here we outline the numerical setup used to compute the time evolution of the field θ in the equations of motion (2.2), and the methodology used to measure oscillon frequency ω and radiated power P.

The radial equation of motion for the field $\theta(t,r)$ in $3+1$ dimensions is

$$0 = \frac{\partial^2\theta(t,r)}{\partial t^2} - \frac{\partial^2\theta(t,r)}{\partial r^2} - \frac{2}{r}\frac{\partial\theta(t,r)}{\partial r} + F(\theta(t,r))\,. \tag{4.53}$$

We introduce the variable $v = r\theta$, which eliminates the friction term. We now discretize time and space, with time steps $\mathrm{d}t$ and radial steps $\mathrm{d}r$, and introduce the notation

$$v(N\,\mathrm{d}t, M\,\mathrm{d}r) = v_N(M) \tag{4.54}$$

Finally, we define the ratio $\xi \equiv (\mathrm{d}t/\,\mathrm{d}r)^2$. In this notation, the equations of motion lead to the following leading-order finite difference equation

$$\begin{aligned} v_{N+1}(M) = \xi(v_N(M+1) + v_N(M-1)) + 2(1-\xi)v_N(M) \\ - v_{N-1}(M) - (\mathrm{d}t^2\,\mathrm{d}rM)F(v_N(M)/(\mathrm{d}rM))\,. \end{aligned} \tag{4.55}$$

Dirichlet boundary conditions are imposed at the origin by fixing $v_N(0) = 0$. The oscillon is assumed to be evolving in empty space, and therefore the box size must be chosen large enough that the radiation from the oscillon reflected off the outer boundary does not propagate backwards and interfere with the oscillon itself.

The length scale of the nth harmonic is $2\pi/\sqrt{(n\omega)^2 - m^2}$. During an instance of destructive interference, typically the fifth harmonic dominates, and in rare cases the seventh may contribute significantly. Since $2\pi/\sqrt{7^2-1} \approx 0.9$, we choose a safe value of $\mathrm{d}r = 0.1/m$, about 10 times smaller than the length scale of radiation at the highest possible frequency. We find that $\xi = 1/4$ leads to stable evolution for $\mathrm{d}r$ of order $0.1/m$. To check that this choice of $\mathrm{d}r$ is good, we increased the resolution by a factor of 2 and 4 which resulted in marginal discrepancies.

The frequency of the oscillon is then measured by tracking the times at which $v_N(1)$ crosses through zero. The outgoing flux is measured outside the oscillon bulk, typically between 20 and 100 in units of the mass. We do not measure the flux too far from the source, since the different frequency modes travel at different velocities, and the PQB formalism does not account for this dispersion.

4.6 Mass vs. interaction basis

The ϕ_S and ϕ_L fields in Eq. 3.4 are not mass eigenstates (i.e. they are not stable under propagation in the non-interacting limit). They are, however, the natural basis in which to consider most of the early-time dynamics and the late-time signatures (since any couplings to the SM likely descend from the UV theory). In this appendix we clarify this point and include the transformation from the interaction basis (ϕ_S, ϕ_L) to the mass basis. For $\mathcal{F} \gg 1/(1-\mu^2)$ the two bases are quite similar and so this discussion has very little effect on the interpretation of the dynamics studied in this paper, although we have included it in our results where relevant.

We wish to find the propagation eigenstates of ϕ_L and ϕ_S. Expanding the potential of Eq. 3.4

to quadratic order yields a mass mixing matrix:

$$\begin{aligned} V(\phi_L,\phi_S) &\approx \frac{1}{2}m^2\left(\phi_S^2+\frac{1}{\mathcal{F}^2}\phi_L^2+\frac{2}{\mathcal{F}}\phi_S\phi_L+\mu^2\phi_L^2\right) \\ &= \frac{1}{2}m^2\begin{pmatrix}\phi_S & \phi_L\end{pmatrix}\begin{pmatrix}1 & \mathcal{F}^{-1}\\ \mathcal{F}^{-1} & \mu^2+\mathcal{F}^{-2}\end{pmatrix}\begin{pmatrix}\phi_S\\ \phi_L\end{pmatrix} \end{aligned} \tag{4.56}$$

which has off-diagonal elements suppressed by the ratio of decay constants. This matrix is easy to diagonalize, yielding the following basis of heavy and light fields ν_h and ν_l:

$$\nu_h \equiv \phi_S\cos\eta+\phi_L\sin\eta \tag{4.57}$$

$$\nu_l \equiv -\phi_S\sin\eta+\phi_L\cos\eta \tag{4.58}$$

$$m_h^2 = m_0^2+\Delta m^2 \tag{4.59}$$

$$m_l^2 = m_0^2-\Delta m^2 \tag{4.60}$$

$$m_0^2 \equiv \frac{1}{2}m^2(1+\mu^2+\mathcal{F}^{-2}) \tag{4.61}$$

$$\Delta m^2 = \frac{1}{2}m^2(1-\mu^2-\mathcal{F}^{-2})\sec 2\eta \tag{4.62}$$

$$\sin\eta \equiv \frac{1}{\sqrt{2}}\sqrt{1-\frac{1-\mu^2-\mathcal{F}^{-2}}{\sqrt{4\mathcal{F}^{-2}+(1-\mu^2-\mathcal{F}^{-2})^2}}} \tag{4.63}$$

For the late-time Newtonian evolution of the axion energy density, it is most useful to describe the system in this basis, since the energy densities in the fields ν_l and ν_h are constant in the small-amplitude limit. As mentioned above, for $\mathcal{F}\gg(1-\mu^2)^{-1}$ we have $\sin\eta\approx 0$ and so $\nu_l\approx\phi_L$ and $\nu_h\approx\phi_S$. The effects of this basis rotation are thus very slight for most of the parameter space discussed in this paper, but we nevertheless use this basis when performing the analysis of Sec. 3.2.4.

In rotating to the mass basis, we have also modified the quartic interactions

$$\begin{aligned} V_{\rm int}(\nu_h,\nu_l) = &\frac{1}{4!}\lambda_{hh}\nu_h^4+\frac{1}{3!}\lambda_{hhhl}\nu_h^3\nu_l+\frac{1}{4}\lambda_{hl}\nu_h^2\nu_l^2 \\ &+\frac{1}{3!}\lambda_{hlll}\nu_h\nu_l^3+\frac{1}{4!}\lambda_{ll}\nu_l^4\,, \end{aligned} \tag{4.64}$$

where the even-interactions are

$$\frac{f^2}{m^2}\lambda_{hh} = -b^4\mu^2\mathcal{F}^{-2}-(a+b\mathcal{F}^{-1})^4\,, \tag{4.65}$$

$$\frac{f^2}{m^2}\lambda_{hl} = -a^2b^2\mu^2(\mathcal{F}^{-2}+\mu^2)\,, \tag{4.66}$$

$$\frac{f^2}{m^2}\lambda_{ll} = -a^4\mu^2\mathcal{F}^{-2}-(b-a\mathcal{F}^{-1})^4\,, \tag{4.67}$$

with

$$a^2 = \cos^2\eta\,, \qquad b^2 = \sin^2\eta\,. \tag{4.68}$$

It turns out that the leading order self-interactions in the non-relativistic theory only come from those terms that conserve parity under $\nu_h \to -\nu_h$ and $\nu_l \to -\nu_l$ independently. Odd-parity interactions enter at the next-to-leading order in the non-relativistic approximation and so we do not take them into account in this work, but for completeness, we list them here:

$$\frac{f^2}{m^2}\lambda_{hhhl} = -(a+b\mathcal{F}^{-1})^3(a\mathcal{F}^{-1}-b) - ab^3\mu^2\mathcal{F}^{-2}\,, \tag{4.69}$$

$$\frac{f^2}{m^2}\lambda_{hlll} = -(a\mathcal{F}^{-1}-b)^3(a+b\mathcal{F}^{-1}) - a^3b\mu^2\mathcal{F}^{-2}\,. \tag{4.70}$$

4.7 A more detailed study of autoresonance

The dynamics of autoresonating axions are rich, and in this appendix we focus on building analytic intuition for their behavior. Even though the oscillators are quite nonlinear, it turns out that we can get good approximations for several interesting quantities by searching for stable autoresonant solutions and perturbing around them.

4.7.1 Adiabatic evolution of resonance curves

Here we review the details of the calculations behind the resonance curve results in Sec. 3.1. For this purpose, we are interested in the $\mathcal{F} \to \infty$ limit, for which Θ_L decouples from Θ_S and obeys a simple pendulum equation of motion:

$$\ddot{\Theta}_L + \frac{3}{2t}\dot{\Theta}_L + \mu^2 \sin\Theta_L = 0\,. \tag{4.71}$$

For small initial conditions $\sin\Theta_L \approx \Theta_L$, the solutions can be obtained analytically:

$$\Theta_L(t) = \Theta_L(0)\,\Gamma(5/4)2^{1/4}\frac{J_{1/4}(\mu t)}{(\mu t)^{1/4}}\,, \tag{4.72}$$

which, at late times, is approximately:

$$\Theta_L(t) = \frac{\Theta_L(0)\Gamma(\frac{5}{4})2^{3/4}}{\sqrt{\pi}}\frac{\sin\left(\mu t + \frac{\pi}{8}\right)}{(\mu t)^{3/4}}\,. \tag{4.73}$$

At large initial conditions comparable to π, this approximation fails and we must correct the initial amplitude $\Theta_L(0)$ to account for the delay in oscillations caused by the flatness of the cosine potential. To this end, we define the function $\Theta_{\text{lin}\to\cos}$, which takes as input the initial amplitude of a linear

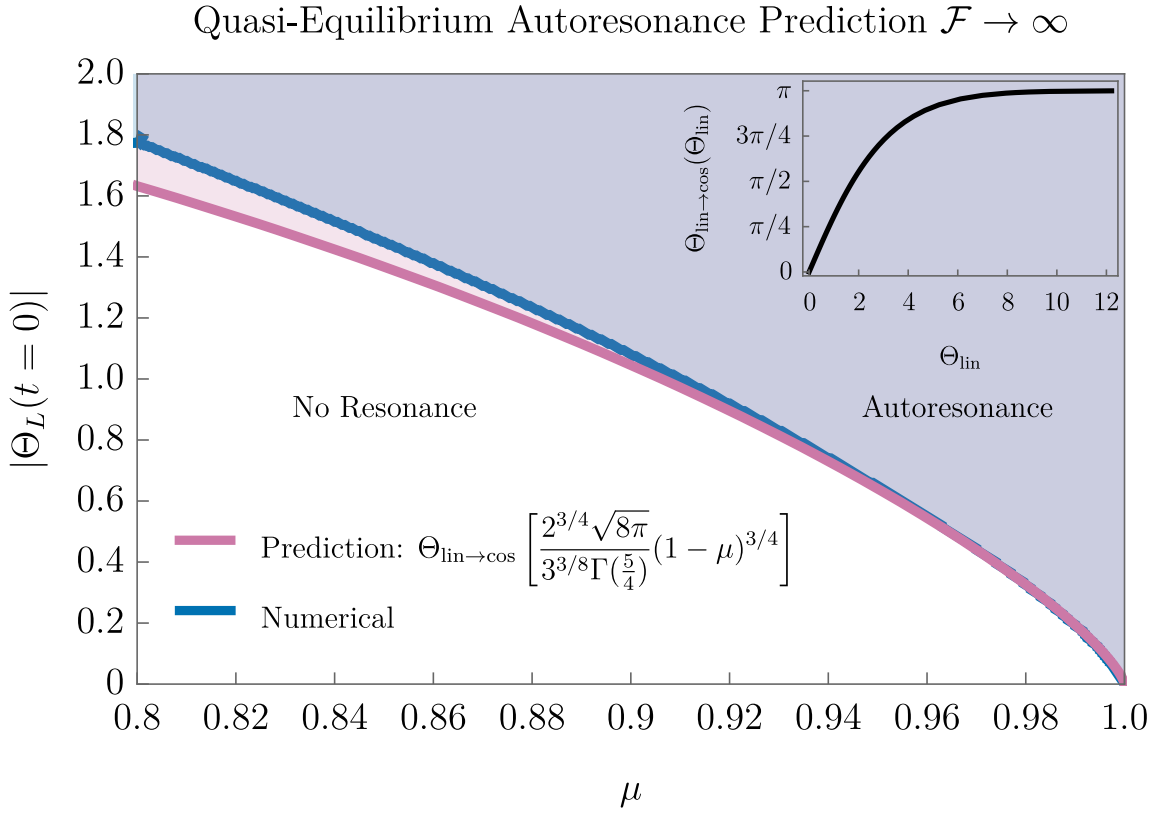

Figure 4.8: The set of parameters for which Θ_S ends up autoresonating for $\Theta_S(0) = 0$ in the $\mathcal{F} \to \infty$ limit. We compare a numerical evaluation (Blue) to the analytic adiabatic prediction of the critical driver amplitude. The numeric autoresonance region corresponds to those parameters for which Θ_S has finite amplitude as $t \to \infty$. The analytic contour is obtained as the minimum driver amplitude for which a quasi-equilibrium configuration connects the zero amplitude linear resonance at $t = 0$ with the finite amplitude nonlinear resonance at $t = \infty$ as in Fig. 3.3. Note that the analytic estimate improves as $\mu \to 1$, where the evolution of the resonance curve is slowest, and thus is most accurately described by an adiabatic approximation. **Inset:** A plot of the function $\Theta_{\text{lin}\to\cos}$, which takes as input the initial misalignment of a harmonic oscillator, and outputs the misalignment of a cosine oscillator that yields the same late-time relic abundance. Note that this function is the identity at small Θ_{lin}.

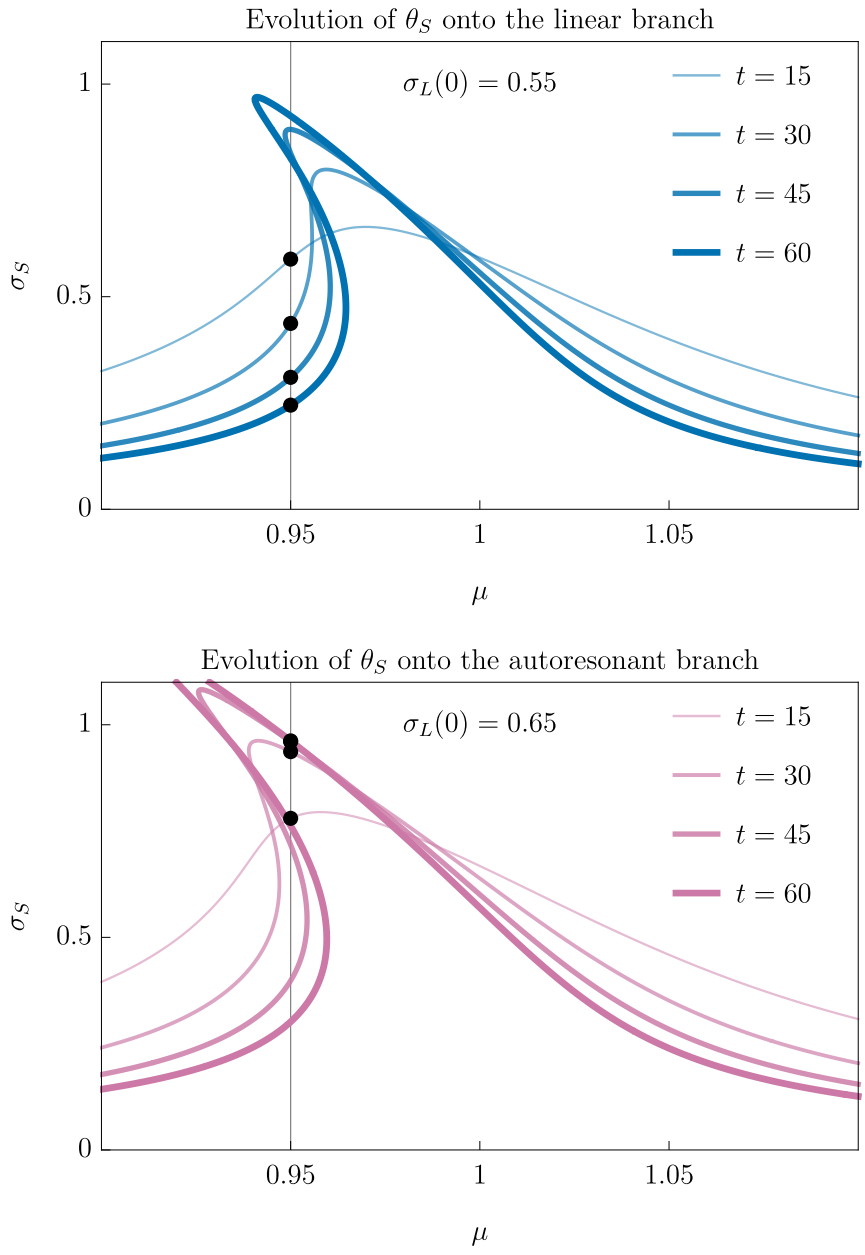

Figure 4.9: Short axion resonance curves over a sequence of times for two different values of initial long amplitude $\sigma_L(0)$. Black dots represent the adiabatic evolution of an axion system with $\mu = 0.95$. The short axion always begins on the linear branch at early times, but its final amplitude is determined by the evolution of the resonance curve. **Top:** For $\sigma_L(0) = 0.55$, the resonance curve "tongue" grows over the instantaneous equilibrium, leaving σ_S on the linear branch. **Bottom:** For $\sigma_L(0) = 0.65$, the resonance curve narrows under the instantaneous equilibrium, leaving σ_S elevated on the nonlinear branch (autoresonance). Note: these resonance curves are made using Eq. 3.15 to enable direct comparison with Fig. 3.3; utilizing Eq. 4.78 does not change the qualitative features of these two classes of evolution history.

oscillator, and returns the corresponding initial amplitude of a cosine oscillator which results in the same energy density at late times. This function is shown in the inset of Fig. 4.8. At small amplitudes it is approximately the identity, while at large amplitudes it asymptotes to π. The late-time amplitude of the full non-linear solution for Θ_L in the cosine potential can be written as:

$$\sigma_L(t) = \Theta^{-1}_{\text{lin}\to\cos}(\Theta_L(0))\frac{\Gamma(\frac{5}{4})2^{3/4}}{\sqrt{\pi}(\mu t)^{3/4}}\,. \tag{4.74}$$

This instantaneous amplitude σ_L will drive the short axion Θ_S at the long frequency μ. Specifically, the equation of motion for Θ_S, obtained in the small-Θ_L regime from Eq. 3.8, becomes:

$$\ddot{\Theta}_S + \frac{3}{2t}\dot{\Theta}_S + \sin\Theta_S = -\cos\Theta_S\,\sigma_L\cos(\mu t - \Phi)\,, \tag{4.75}$$

where Φ is the relative phase between Θ_S and Θ_L (which is constant at leading order in the adiabatic approximation). Note that compared to a standard driven pendulum (Eq. 3.13), the driver is suppressed by a $\cos\Theta_S$ correction. To leading order, the resonance curve can be obtained by only treating the terms oscillating at the driver frequency μ, which is equivalently thought of as the small-amplitude limit. We thus take $\Theta_S \approx \sigma_S\cos(\mu t)$ and expand $\sin\Theta_S$ and $\cos\Theta_S$ using the Jacobi-Anger formulae:

$$\cos(\sigma_S\cos\mu t) = J_0(\sigma_S) + 2\sum_{n=1}^{\infty}(-1)^n J_{2n}(\sigma_S)\cos(2n\mu t)\,, \tag{4.76a}$$

$$\sin(\sigma_S\cos\mu t) = 2\sum_{n=0}^{\infty}(-1)^n J_{2n+1}(\sigma_S)\cos((2n+1)\mu t)\,. \tag{4.76b}$$

Keeping only terms of frequency μ, we collect the terms proportional to $\sin\mu t$ and $\cos\mu t$, leading to the equations

$$-\mu^2\sigma_S + 2J_1(\sigma_S) + J_0(\sigma_S)\sigma_L\cos\Phi = 0\,, \tag{4.77a}$$

$$\frac{3\mu}{2t}\sigma_S - J_0(\sigma_S)\sigma_L\sin\Phi = 0\,, \tag{4.77b}$$

which, upon eliminating the phase shift Φ, lead to the condition defining the resonance curve:

$$\left(2J_1(\sigma_S) - \mu^2\sigma_S\right)^2 + \left(\frac{3\mu}{2t}\right)^2\sigma_S^2 = J_0(\sigma_S)^2\sigma_L^2\,. \tag{4.78}$$

Expanding the Bessel function to leading non-linear order we arrive at the following approximate small-amplitude resonance curve:

$$\sigma_S = \frac{\sigma_L(t)\left(1-\frac{\sigma_S^2}{4}\right)}{\sqrt{\left(1-\frac{\sigma_S^2}{8}-\mu^2\right)^2+\frac{9\mu^2}{4t^2}}}\,. \tag{4.79}$$

Given a fixed frequency μ, we are interested in tracking the equilibrium solution of σ_S given by this resonance condition when the driver amplitude σ_L also varies slowly with time, as given by Eq. 4.74.

At small t friction dominates, and there is only one real solution to Eq. 4.79. At large t, the curve narrows around the free frequency curve as shown in Fig. 3.2 and, over a range of frequencies $\mu < 1$, can support two stable solutions on either the nonlinear branch (which asymptotes to a finite amplitude $\sigma_S \approx 4\sqrt{(1-\mu)}$), or on the linear branch (which tends to zero). In this adiabatic view of the evolving resonance curve, *autoresonance* is considered to occur when the early-time solution, which starts on the linear branch, is continuously connected to a late-time solution on the upper, non-linear branch. Autoresonance does not happen if the system remains on the linear branch. To find the critical point between these two regimes, it suffices to look for the largest $\Theta_L(0)$ for which the linear branch at μ never becomes complex. Solving for this condition in Eq. 4.79 leads to the $\Theta_L(0)$ amplitude cutoff

$$\Theta_L(0) \geq \Theta_{\text{lin}\to\cos}\left[\frac{2^{3/4}\sqrt{8\pi}}{3^{3/8}\Gamma(\frac{5}{4})}(1-\mu)^{3/4}\right]. \tag{4.80}$$

We plot the resulting critical initial misalignment $\Theta_L(0)$ versus μ in Fig. 4.8, where we find excellent agreement between the analytical threshold (Magenta) and the numerical threshold (Blue). In Fig. 4.9 we show an explicit comparison between an initial $\Theta_L(0)$ amplitude that results in autoresonance and one that does not. The values are chosen to match those shown in Fig. 3.3.

4.7.2 Expected relic density ratio

In this section, we derive the maximum relic abundance ratio at the end of autoresonance. In essence, this calculation assumes that autoresonance carries on until θ_L is small enough that flavor oscillations dominate its energy density ρ_L. Thus our goal in this section is to calculate the minimal size of flavor oscillations.

To begin, consider the mass eigenstates ν_l and ν_h with masses m_l and m_h respectively (see App. 4.6). We will assume that the total energy density is fixed at a constant ρ_0:

$$\rho_0 = \frac{1}{2}\langle\dot{\nu}_l^2\rangle + \frac{1}{2}m_l^2\langle\nu_l^2\rangle + \frac{1}{2}\langle\dot{\nu}_h^2\rangle + \frac{1}{2}m_h^2\langle\nu_h^2\rangle \tag{4.81}$$

$$= m_l^2\langle\nu_l^2\rangle + m_h^2\langle\nu_h\rangle^2\,. \tag{4.82}$$

We will maximize the ratio ρ_S/ρ_L subject to fixed ρ_0. Using our definition of ρ_S and ρ_L in Eq. 3.19, expanding in the small Θ_S, Θ_L limit, and using the fact that $m_l \neq m_h$ so that $\langle \nu_l \nu_h \rangle = 0$, we have

$$\rho_S = \frac{1}{4}\langle \nu_l^2 \rangle \left(2(1-\sin(2\eta)) + m_l^2(1-\cos(2\eta))\right) + \frac{1}{4}\langle \nu_h^2 \rangle \left(2(1+\sin(2\eta)) + m_h^2(1+\cos(2\eta))\right) , \tag{4.83}$$

$$\rho_L = \frac{1}{2}\langle \nu_l^2 \rangle (m_l^2+\mu^2)\cos^2\eta + \frac{1}{2}\langle \nu_h^2 \rangle (m_h^2+\mu^2)\sin^2\eta \, . \tag{4.84}$$

One can check that the ratio ρ_S/ρ_L is maximized for $\nu_l = 0$ provided $\mu < 1$,

$$\max \frac{\rho_S}{\rho_L} = \frac{(1+m_h^2)\csc^2\eta + 2\cot\eta - m_h^2}{\mu^2 + m_h^2} \, . \tag{4.85}$$

Expanding for $\mathcal{F} \gg (1-\mu^2)^{-1}$ and $1-\mu \to 0$, we find

$$\max \frac{\rho_S}{\rho_L} \approx 4\mathcal{F}^2(1-\mu)^2 \, . \tag{4.86}$$

This estimate is essentially the envelope of the hourglass shape in Fig. 3.5. Our numeric results nearly saturate this bound, indicating that autoresonance transfers virtually all energy density out of the long field. An additional factor of $1/2$ appears to do a good job matching the measured final ratio:

$$\left.\frac{\rho_S}{\rho_L}\right|_{\text{observed}} \approx 2\mathcal{F}^2(1-\mu)^2 \, . \tag{4.87}$$

4.7.3 Stability of autoresonance

We now derive a set of equations for the amplitude and phase of both axions during autoresonance and use them to compute the evolution of excitations on top of the autoresonance solution. We begin with the coupled equations of motion of Eq. 3.8, where we are measuring time in units of m^{-1}. Because we are expecting approximately periodic solutions, we make the following ansatz for $\Theta_L(t)$ and $\Theta_S(t)$:

$$\Theta_S = \sigma_S \, \mathrm{Re}[e^{i\varphi_S}] \, , \tag{4.88a}$$

$$\Theta_L = \sigma_L \, \mathrm{Re}[e^{i\varphi_L}] \, . \tag{4.88b}$$

We will assume that $\sigma_S, \sigma_L, \dot{\varphi}_S, \dot{\varphi}_L$ (where dots denote time derivatives) all vary slowly compared to the oscillatory timescale $1/m$. We can then insert our ansatz into the equations of motion and expand, keeping only the lowest order in σ_L and only the lowest harmonics of φ_S to obtain:

$$\ddot{\sigma}_L + 2i\dot{\varphi}_L\dot{\sigma}_L + i\ddot{\varphi}_L\sigma_L - \dot{\varphi}_L^2\sigma_L + \frac{3}{2t}(\dot{\sigma}_L + i\dot{\varphi}_L\sigma_L) + (\mu^2 + \mathcal{F}^{-2})\sigma_L = -2\frac{1}{\mathcal{F}^2}J_1(\sigma_S)e^{i\Phi} \, , \tag{4.89a}$$

$$\ddot{\sigma}_S + 2i\dot{\varphi}_S\dot{\sigma}_S + i\ddot{\varphi}_S\sigma_S - \dot{\varphi}_S^2\sigma_S + \frac{3}{2t}(\dot{\sigma}_S + i\dot{\varphi}_S\sigma_S) + 2J_1(\sigma_S) = -\sigma_L J_0(\sigma_S)e^{-i\Phi}\,, \tag{4.89b}$$

where $\Phi \equiv \varphi_S - \varphi_L$ is the relative phase of the two oscillators, J_n are Bessel functions, and we have used the Jacobi-Anger identities Eq. 4.76. Note that from Eq. 4.89b we can see that if σ_S becomes so large that $J_0(\sigma_S) = 0$, then σ_S is no longer driven. This critical σ_S determines a critical driving frequency $\mu \approx 0.64$ below which autoresonance is no longer possible, given by the first zero of $J_0(4\sqrt{1-\mu})$.

Now we may take the real and imaginary parts of Eq. 4.89 to obtain a set of four coupled equations:

$$\ddot{\sigma}_L - \dot{\varphi}_L^2\sigma_L + \frac{3}{2t}\dot{\sigma}_L + (\mu^2 + \mathcal{F}^{-2})\sigma_L = -\frac{2}{\mathcal{F}^2}J_1(\sigma_S)\cos\Phi\,, \tag{4.90a}$$

$$\ddot{\varphi}_L + \left(\frac{3}{2t} + 2\frac{\dot{\sigma}_L}{\sigma_L}\right)\dot{\varphi}_L = -\frac{2}{\mathcal{F}^2}\frac{J_1(\sigma_S)}{\sigma_L}\sin\Phi\,, \tag{4.90b}$$

$$\ddot{\sigma}_S - \dot{\varphi}_S^2\sigma_S + \frac{3}{2t}\dot{\sigma}_S + 2J_1(\sigma_S) = -\sigma_L J_0(\sigma_S)\cos\Phi\,, \tag{4.90c}$$

$$\ddot{\varphi}_S + \left(\frac{3}{2t} + 2\frac{\dot{\sigma}_S}{\sigma_S}\right)\dot{\varphi}_S = \sigma_L\frac{J_0(\sigma_S)}{\sigma_S}\sin\Phi\,. \tag{4.90d}$$

These equations are interesting in their own right, and can be numerically integrated more efficiently than a rapidly-oscillating system such as Eq. 3.8, but for now we will focus on further simplification. We wish to find the state of the system when it is stably autoresonating, by which we mean we are looking for a solution for which σ_S is roughly constant and $\dot{\varphi}_S \approx \dot{\varphi}_L$ so the oscillators are synchronized with each other. We thus approximate $\dot{\sigma}_S \approx \ddot{\sigma}_S \approx \ddot{\varphi}_S \approx \ddot{\varphi}_L \approx 0$ and obtain:

$$(\dot{\varphi}_L^2 - \mu^2 - \mathcal{F}^{-2}) = \frac{3}{2t}\frac{\dot{\sigma}_L}{\sigma_L} + \frac{2}{\mathcal{F}^2}\frac{J_1(\sigma_S)}{\sigma_L}\cos\Phi\,, \tag{4.91a}$$

$$\left(\frac{3}{2t} + 2\frac{\dot{\sigma}_L}{\sigma_L}\right)\dot{\varphi}_L = -\frac{2}{\mathcal{F}^2}\frac{J_1(\sigma_S)}{\sigma_L}\sin\Phi\,, \tag{4.91b}$$

$$2\frac{J_1(\sigma_S)}{\sigma_S} - \dot{\varphi}_S^2 = -\sigma_L J_0(\sigma_S)\cos\Phi\,, \tag{4.91c}$$

$$\frac{3}{2t}\dot{\varphi}_S = \sigma_L\frac{J_0(\sigma_S)}{\sigma_S}\sin\Phi\,. \tag{4.91d}$$

From these equations we may read off a few things. First, provided $t \gg \sigma_L/\dot{\sigma}_L$ and $\mathcal{F}^2 \gg \sigma_L^{-1}$, the long oscillator undergoes roughly free motion at its fundamental frequency: $\dot{\varphi}_L^2 = \mu^2 + \mathcal{F}^{-2} \approx \mu^2$. If we demand that $\dot{\varphi}_S \approx \dot{\varphi}_L$ to ensure we are in autoresonance, that then implies that $\dot{\varphi}_S \approx \mu$, and from Eq. 4.91d we can read off an expression for the relative phase of the two oscillators:

$$\sin\bar{\Phi} \approx \frac{3\mu}{2t}\frac{\sigma_S}{\sigma_L}\frac{1}{J_0(\sigma_S)}\,, \tag{4.92}$$

where we have used the bar to denote the fact that this is the relative phase in steady-state autoresonance.

We now turn to the question of how excitations on top of this steady-state solution behave. This will provide an analytic justification for the numeric observation that autoresonance is a stable condition. We work in the limit $\mathcal{F} \to \infty$, which implies $\dot{\varphi}_L = \mu$ and $\dot{\sigma}_L/\sigma_L = -3/(4t)$. We may then combine Eqs. 4.90b, 4.90c, and 4.90d to obtain:

$$\ddot{\sigma}_S + \frac{3}{2t}\dot{\sigma}_S - \dot{\varphi}_S^2\sigma_S + 2J_1(\sigma_S) + \sigma_L \cos\Phi = 0\,, \tag{4.93a}$$

$$\ddot{\Phi} + \frac{3}{2t}\dot{\Phi} - \frac{\sigma_L}{\sigma_S}\sin\Phi + \frac{3\mu}{2t} + 2\dot{\varphi}_S\frac{\dot{\sigma}_S}{\sigma_S} = 0\,. \tag{4.93b}$$

We now perturb around the equilibrium autoresonance solution, defining:

$$\Phi \equiv \bar{\Phi} + \delta_\Phi\,, \tag{4.94a}$$

$$\sigma_S \equiv \bar{\sigma}_S + \delta_S\,, \tag{4.94b}$$

with $\bar{\Phi}$ defined in Eq. 4.92 and $\bar{\sigma}_S$ defined by the autoresonance condition:

$$\frac{2J_1(\bar{\sigma}_S)}{\bar{\sigma}_S} = \mu^2\,. \tag{4.95}$$

Expanding and linearizing yields the pair of equations:

$$\ddot{\delta}_S + \frac{3}{2t}\dot{\delta}_S - 2\mu\bar{\sigma}_S\dot{\delta}_\Phi - 2J_2(\bar{\sigma}_S)\delta_S - \frac{3\mu}{2t}\bar{\sigma}_S\delta_\Phi = -\sigma_L\cos\bar{\Phi}\,, \tag{4.96a}$$

$$\ddot{\delta}_\Phi + \frac{3}{2t}\dot{\delta}_\Phi - \frac{\sigma_L}{\bar{\sigma}_S}\cos\bar{\Phi}\delta_\Phi + 2\mu\frac{\dot{\delta}_S}{\bar{\sigma}_S} + \frac{3\mu}{2t}\frac{\delta_S}{\bar{\sigma}_S} = 0\,, \tag{4.96b}$$

where we have substituted in for $\sin\bar{\Phi}$ with Eq. 4.92 and approximated $J_0(\bar{\sigma}_S) \approx \bar{\sigma}_S$. For $t \gg 1$, we may neglect several terms, simplifying to:

$$\ddot{\delta}_S - 2J_2(\bar{\sigma}_S) - 2\mu\bar{\sigma}_S\dot{\delta}_\Phi - \frac{3\mu}{2t}\bar{\sigma}_S\delta_\Phi = 0\,, \tag{4.97a}$$

$$\ddot{\delta}_\Phi - \frac{\sigma_L}{\bar{\sigma}_S}\delta_\Phi + 2\mu\frac{\dot{\delta}_S}{\bar{\sigma}_S} + \frac{3\mu}{2t}.\frac{\delta_S}{\bar{\sigma}_S} = 0 \tag{4.97b}$$

To analyze the stability of autoresonance we can search for first-order perturbative solutions of the form:

$$\delta_S = |\delta_S|e^{i\omega_{\text{f.o.}}t} \qquad \delta_\Phi = |\delta_\Phi|e^{i\omega_{\text{f.o.}}t}\,, \tag{4.98}$$

where we will assume (and then confirm) that $|\omega_{\text{f.o.}}| \ll 1$. Plugging this into the above relations and

solving yields:

$$\omega_{\text{f.o.}} \overset{t\gg 1}{\approx} \left(\frac{2\sigma_L}{\bar{\sigma}_S}\frac{J_2(\bar{\sigma}_S)}{4\mu^2 - 2J_2(\bar{\sigma}_S)}\right)^{1/2} + i\frac{3}{4t}\,, \tag{4.99}$$

where the imaginary part in particular demonstrates that fluctuations about the autoresonant solution should damp away as $t^{-3/4}$ at large times. As predicted, $|\omega_{\text{f.o.}}| \ll 1$ so our approximations above were safe.

4.7.4 Chaotic parameter space

As we've discussed in the previous sections, there is a wide range of parameter space where the zero-mode is well-described by a slowly varying amplitude and phase. This description neglects the initial phase of transient oscillations, and as we have seen in App. 4.7.1, transients often do not play a significant role in the evolution of Θ_S. This is no longer true if the long axion delivers enough energy to the short axion that it can roll over many vacua, exploring the saddle points of the potential. If Θ_S happens to slow down near one of the saddle points, the direction it rolls off will depend sensitively on the details of its trajectory, and consequently, on its initial conditions. In other words, if Θ_L starts with enough energy, then the short axion exhibits classical chaos, leading to the intricate striations in Fig. 3.6 near $\Theta_L = \pi$. The possibility of chaotic evolution in this type of potential was first pointed out in Ref. [224, 226].

During chaotic evolution, the short axion receives substantial energy from the long axion, leading to many of the same signatures we have described in Sec. 3.3. In particular, the chaotic rolling of Θ_S necessarily delays the onset of near-harmonic oscillations, generating large Θ_S perturbations, as described in Sec. 3.2. Further, although it is no longer guaranteed, an $\mathcal{O}(1)$ fraction of chaotic initial conditions lead to autoresonance, and consequently enhanced direct detection prospects.

A new behavior is also possible for initial conditions sufficiently close to the boundary between striations in Fig. 3.6. For these initial conditions, Θ_S spends a long time very close to the apex of the saddle point, causing rapid perturbation growth. If Θ_S gets close enough to the hilltop for long enough, the axion field in different parts of space can roll off to either side, creating a network of vacuum bubbles. The cosmological implications of this scenario require further investigation.

4.8 Perturbations in detail

In this section, we provide the details of the perturbation growth rate calculations referenced in Sec. 3.2. We first review the general formalism to numerically compute the full spectrum of axion perturbations. We then go on to describe the analytic approximations made in Sec. 3.2.1 and Sec. 3.2.2.

4.8.1 General formalism

Consider a theory of N interacting axions $\phi_1, \ldots, \phi_N$ with scalar potential V

$$\mathcal{L}(\phi_1, \ldots, \phi_N) = \frac{1}{2}\left(\sum_{i=1}^{N} \partial_\mu \phi_i \partial^\mu \phi_i\right) - V(\phi_1, \ldots, \phi_N)\,. \tag{4.100}$$

To study the strongly self-interacting regime of this theory, it is helpful to change variables from the canonically normalized fields ϕ_i to the fields $\theta_i \equiv \phi_i/f_i$, where f_i is chosen so that $\theta_i \approx 1$ is the scale of self-interaction. In the two-axion model, there is no ambiguity regarding the choice of f_i. However, one generally must take more care in choosing the scales f_i if there are more instantons than axions [172].

The axion field evolves in the background of the perturbed FLRW metric Eq. 3.24 where $\Phi(t, \mathbf{x}) = \sum_{\mathbf{k}} \Phi_k(t, \mathbf{k}) e^{i\mathbf{k}\cdot\mathbf{x}}$ is the adiabatic scalar perturbation with spectral components given by Eq. 3.30. Breaking θ_i down into homogeneous modes Θ_i and perturbations $\delta\theta_i$

$$\theta_i(t, \mathbf{x}) = \Theta_i(t) + \sum_{\mathbf{k}} \delta\theta_i(t, \mathbf{k})\,, \tag{4.101}$$

we arrive at the following set of equations of motion

$$0 = \ddot{\Theta}_i + 3H\dot{\Theta}_i + \frac{1}{f_i^2}\frac{\partial V}{\partial \Theta_i}\,, \tag{4.102a}$$

$$\mathcal{S}_i = \delta\ddot{\theta}_i + 3H\delta\dot{\theta}_i + \frac{\tilde{k}^2}{t}\delta\theta_i + \frac{1}{f_i^2}\frac{\partial^2 V}{\partial\Theta_i \partial\Theta_j}\delta\theta_j\,, \tag{4.102b}$$

$$\mathcal{S}_i \equiv 2\left(\frac{t_k}{t}\frac{d\Phi_k}{dt_k}\dot{\Theta}_i - \Phi_k \frac{1}{f_i^2}\frac{\partial V}{\partial \Theta_i}\right)\,, \tag{4.102c}$$

where we've specialized to the case of radiation domination, and $\tilde{k}$ and t_k are defined in Eq. 3.26 and Eq. 3.30 respectively. For definiteness, we assume that inflation lasts long enough that the $\delta\theta_i$ initial conditions are well approximated as $\delta\theta_i = \delta\dot{\theta}_i = 0$.

4.8.2 Analytical approximations

Having reviewed the full set of perturbation equations, we now specialize to the case of the one-axion potential Eq. 3.23. As we have described in Sec. 3.2.1, perturbations do not grow at an appreciable rate until after the homogeneous oscillations have settled down near the vacuum. At this point, the potential is well approximated by the leading nonlinear terms

$$\frac{1}{f^2}V(f\theta) = \frac{1}{2}\theta^2 + \frac{1}{3!}A\theta^3 + \frac{1}{4!}B\theta^4\,, \tag{4.103}$$

where A and B are constants that may be determined from the full potential by Taylor expanding around the vacuum. The homogeneous mode Θ then satisfies the following equation of motion

$$0 = \ddot{\Theta} + \frac{3}{2t}\dot{\Theta} + \left(1 + \frac{1}{2}A\Theta + \frac{1}{3!}B\Theta^2\right)\Theta\,. \tag{4.104}$$

For Θ oscillating with small amplitude σ, its waveform and frequency at leading nontrivial order in σ are

$$\Theta(t) = -\frac{1}{4}A\sigma^2 + \sigma\cos\omega t + \frac{1}{12}A\sigma^2\cos 2\omega t\,, \tag{4.105}$$

$$\delta\omega = \frac{3B - 5A^2}{48}\sigma^2\,. \tag{4.106}$$

From these formulas, we see that the cubic and quartic interactions have qualitatively distinct effects on the Θ oscillations. The sign of B controls whether the quartic interaction is attractive or repulsive, leading to slower or faster oscillations respectively. On the other hand, A always works to decrease the fundamental frequency of the oscillations. For positive A, the cubic interaction is repulsive for positive Θ and attractive for negative Θ, ultimately causing Θ to spend more time at negative values where it is oscillating slower. For negative A the sides are switched, but in either case the net effect is to decrease the oscillator's frequency.

In the background of the homogeneous Θ oscillations, the equation of motion for the perturbation $\delta\theta$ is

$$\mathcal{S} = \delta\ddot{\theta}(t,\tilde{k}) + \frac{3}{2t}\delta\dot{\theta}(t,\tilde{k}) + \left(1 + \frac{\tilde{k}^2}{t} + A\Theta + \frac{1}{2}B\Theta^2\right)\delta\theta(t,\tilde{k})\,, \tag{4.107a}$$

$$\mathcal{S} \equiv 2\left[\frac{t_k}{t}\frac{d\Phi_k}{dt_k}\dot{\Theta} + \Phi_k\left(\Theta + \frac{1}{2}A\Theta^2 + \frac{1}{3!}B\Theta^3\right)\right]\,. \tag{4.107b}$$

The source $\mathcal{S}$ provides the axion with the initial fluctuations that will grow because of parametric resonance. Soon after the exponential growth starts, $\mathcal{S}$ becomes irrelevant and the perturbation growth rate may be computed from the homogeneous equation

$$0 \approx \delta\ddot{\theta} + \frac{3}{2t}\delta\dot{\theta} + \left(1 + \frac{\tilde{k}^2}{t} + A\Theta + \frac{1}{2}B\Theta^2\right)\delta\theta\,. \tag{4.108}$$

Modes will only grow once Hubble friction is small $H \ll 1$, i.e. once $t \gg 1$. This allows us to treat the time variation of the Hubble friction, the zero-mode amplitude $\sigma \propto t^{-3/4}$, and the changing frequency $\delta\omega \propto \sigma^2 \propto t^{-3/2}$ adiabatically. Thus, we may change variables

$$\delta\theta = e^{-\frac{3}{4t}}\psi\,, \tag{4.109}$$

so that ψ obeys the frictionless version of Eq. 4.108 up to order t^{-2}. Inserting the known zero-mode

evolution Eq. 4.105, we arrive at the following equation for ψ

$$0 = \ddot{\psi} + (1 + \alpha + 2\beta\cos t + 2\gamma\cos 2t)\psi\,, \tag{4.110}$$

where

$$\alpha = \frac{\tilde{k}^2}{t} - \frac{1}{24}\left(A^2 - 3B\right)\sigma^2\,, \tag{4.111a}$$

$$\beta = \frac{1}{2}A\sigma\,, \tag{4.111b}$$

$$\gamma = \frac{1}{24}\left(A^2 + 3B\right)\sigma^2\,. \tag{4.111c}$$

This Mathieu-type equation can be solved directly by applying a Fourier transformation $t \to \omega_t$:

$$0 = -\omega_t^2\psi(\omega_t) + (1+\alpha)\psi(\omega_t) + \beta(\psi(\omega_t+1) + \psi(\omega_t-1)) + \gamma(\psi(\omega_t+2) + \psi(\omega_t-2))\,. \tag{4.112}$$

In this equation, only frequencies related by integer multiples of m couple to one another, and thus this problem can be rephrased in terms of an infinite matrix. To see this, we define $\Gamma_\psi \in [0,1) + \mathrm{i}\mathbb{R}$, so that its real part represents the non-integer real part of ω_t. We can then label harmonics as:

$$\psi_n(\Gamma_\psi) \equiv \psi(\Gamma_\psi + n) = \psi(\omega_t)\,. \tag{4.113}$$

The Fourier transformed Eq. 4.112 is thus equivalent to the matrix equation

$$0 = \left(-(\Gamma_\psi + n)^2 + 1 + \alpha\right)\psi_n + \beta\left(\psi_{n+1} + \psi_{n-1}\right) + \gamma\left(\psi_{n+2} + \psi_{n-2}\right)\,.$$

The eigenvalues Γ_ψ characterize the growth-rate $\mathrm{Im}\,\Gamma_\psi$ and frequency $\mathrm{Re}\,\Gamma_\psi$ of the ψ oscillations.

To solve for Γ_ψ, we look for solutions with $|\Gamma_\psi| \to 0$, which corresponds to the principal instability branch of the Mathieu-type equation Eq. 4.110. Thus, we approximate $(\Gamma_\psi + n)^2 \approx 2n\Gamma_\psi + n^2$, leading to the following eigenvalue problem

$$0 = \det \begin{pmatrix} \ddots & & & & & & \\ & -4+4\Gamma_\psi+1+\alpha & \beta & \gamma & & & \\ & \beta & -1+2\Gamma_\psi+1+\alpha & \beta & \gamma & & \\ & \gamma & \beta & 1+\alpha & \beta & \gamma & \\ & & \gamma & \beta & -1-2\Gamma_\psi+1+\alpha & \beta & \\ & & & \gamma & \beta & -4-4\Gamma_\psi+1+\alpha & \\ & & & & & & \ddots \end{pmatrix}. \tag{4.114}$$

By truncating Eq. 4.114 at the leading 5×5 elements, we arrive at the following expression for the ψ growth rate

$$\begin{aligned} \Gamma_\psi &= -\mathrm{i}\sqrt{\left(\frac{\gamma^2}{4} - \frac{\alpha^2}{4}\right) + \left(\frac{\alpha}{3} - \frac{\gamma}{2}\right)\beta^2 + \frac{5}{36}\beta^4 + \mathcal{O}(\sigma^5)}\,, \\ &= -\mathrm{i}|\delta\omega|\sqrt{1 - \left(1 + \frac{\tilde{k}^2}{2t_m\delta\omega}\right)^2}\,, \end{aligned} \tag{4.115}$$

to order σ^4 in the root (using the fact that $\tilde{k}^2/t \sim \sigma^2$), and where $\delta\omega$ is as in Eq. 4.106. Re-introducing the $-3/4t$ term we had absorbed into ψ, we arrive at Eq. 3.34 for the growth rate of $\delta\theta$: $\Gamma = \mathrm{Re}(-3/4t + \mathrm{i}\Gamma_\psi)$.

The perturbations begin growing when $\Gamma \geq 0$, which we define as the time t_{init}. Prior to $t = t_{\mathrm{init}}$, the source term $\mathcal{S}$ holds $\delta\theta$ at an approximately constant initial amplitude given by Eq. 3.36, and thus we arrive at the expression Eq. 3.35 for the amplitude of $\delta\theta$, which we reproduce here for ease of reference:

$$\langle \delta\theta(t,\tilde{k})^2 \rangle \approx \langle \delta\theta(t_{\mathrm{init}},\tilde{k})^2 \rangle \exp\left[2\int_{t_{\mathrm{osc}}}^{t} \mathrm{d}t' \Gamma(t',\tilde{k})\right], \tag{4.116a}$$

$$\langle \delta\theta(t,\tilde{k})^2 \rangle \approx \frac{\Phi_{k,0}^2}{\left(1 + \frac{mt\tilde{k}^2}{\pi^2}\right)^2}\,. \tag{4.116b}$$

The integral in Eq. 4.116a can be evaluated exactly, but the resulting expression is hardly useful. To make clean analytic progress, it is helpful to first compute the integral by ignoring Hubble friction, and then to re-introduce Hubble friction at the end by adding $-(3/4)\log(t_{\mathrm{end}}/t_{\mathrm{init}})$. Because Θ is oscillating at the bottom of the potential with decaying amplitude proportional to $t^{-3/4}$, the frequency shift is $\delta\omega = \delta\omega_{\mathrm{osc}}(t/t_{\mathrm{osc}})^{-3/2}$, where t_{osc} represents the time at which the zero-mode

amplitude starts decaying as $\sigma \propto t^{-3/4}$, and thus $t_{\rm osc} = t_{\rm init}$ for the single axion model. In the case of autoresonant axions, $t_{\rm osc}$ is the time at which autoresonance ends, which is in general much larger than the time $t_{\rm init}$ when perturbations start growing. Substituting our expression for $\delta\omega$ into Eq. 4.115 and plugging into Eq. 4.116a we arrive at the integrated growth rate (neglecting Hubble friction):

$$\int_{t_{\rm osc}}^{\infty} {\rm d}t' \, {\rm Re}\left(\Gamma(t', \tilde{k}) + \frac{3}{4t_m}\right) = 2\tilde{k}^2 \left(\left(\frac{4(1-\mu)t_{\rm osc}}{\tilde{k}^2} - 1\right)^{1/2} - {\rm arccot}\left[\left(\frac{4(1-\mu)t_{\rm osc}}{\tilde{k}^2} - 1\right)^{-1/2}\right]\right). \tag{4.117}$$

The parametric resonance ends at the time

$$t_{\rm end} = \frac{t_{\rm osc}^3 \delta\omega_{\rm osc}}{(\tilde{k}/2)^4}\,, \tag{4.118}$$

so we add $-(3/4)\log\left(t_{\rm osc}^2 \delta\omega_{\rm osc}/(\tilde{k}/2)^4\right)$ to account for Hubble damping.

We have thus accounted for perturbation growth in the single-particle model Eq. 3.23. As we discussed in Sec. 3.2.2, this calculation carries through unchanged in the two-axion model (Eq. 3.5) for the perturbations of θ_S that accrue after the end of autoresonance, where $\delta\omega = (\mu-1)(t/t_{\rm osc})^{-3/2}$. Further, the same physics applies to perturbations that grow during autoresonance, except that $\delta\omega(t)$ is simply constant, fixed by the frequency shift between the long axion and short axion $\delta\omega(t) = \mu - 1$. In our approximate treatment of Hubble friction, the integrated growth rate during autoresonance turns out to be exactly one half the integrated growth rate after autoresonance, although this growth occurs over only roughly 2% of the time.

4.9 Simulations of non-perturbative structure growth during radiation domination

In Sec. 3.2.3, we outlined the results of $3+1d$ numerical simulations in which the collapse of non-perturbative fluctuations lead to the breakdown of autoresonance. In this appendix, we provide the details of these simulations and outline improvements that can be made in future work.

4.9.1 Metric perturbations and the equations of motion

In this first section, we review the equations of motion for a set of scalar particles $\phi_1, \ldots, \phi_n$ in a potential $V(\phi_1, \ldots, \phi_n)$ in the background of an FLRW spacetime in the presence of adiabatic scalar perturbations $\Phi(t, \mathbf{x})$ Eq. 3.24. As in previous sections, we work in terms of the variables

$\theta_i(t,\mathbf{x}) = \phi_i(t,\mathbf{x})/f_i$, where f_i is the scale of self-interaction for ϕ_i. Treating the metric perturbations at first order, the θ_i equations of motion are

$$0 = \left[(1-2\Phi)\,\partial_t^2 + \left(3H\,(1-2\Phi) - 4\dot{\Phi}\right)\partial_t - (1+2\Phi)\,\frac{1}{a^2}\nabla^2\right]\theta_i + \frac{1}{f_i^2}\frac{\partial V}{\partial \theta_i}\,. \tag{4.119}$$

The axion fields θ_i are endowed with order 1 initial misalignment and homogeneous initial conditions by a sufficiently long period of inflation.

Unlike in the linearized equations, where each wavelength of θ_i evolves independently, large θ_i fluctuations couple different modes, and therefore the relative size of perturbations on different scales becomes important. In other words, we may no longer be agnostic to the phase and amplitude of the metric perturbations Φ_k: a particular realization of the metric perturbation Φ must be generated from its dimensionless power spectrum inside our integration volume.

Our simulation takes place inside a symmetric box of size $2L$ and resolution dL, corresponding to a momentum resolution of $k_{\rm max} = \pi/dL$ and $dk = \pi/L$. The dimensionless metric power spectrum is defined in terms of Φ_k as

$$\mathcal{P}_\Phi(k) = \left(\frac{k}{k_0}\right)^{n_s-1}\Phi_k^2\,, \tag{4.120a}$$

$$\mathcal{P}_{\dot{\Phi}}(k) = \left(\frac{k}{k_0}\right)^{n_s-1}\left(\frac{t_k}{2t}\right)^2\left(\frac{d\Phi_k}{dt_k}\right)^2\,, \tag{4.120b}$$

(see discussion around Eq. 3.30 for definitions of Φ_k, n_s, and t_k). The dimensionful power spectrum P is defined in terms of the dimensionless power spectrum $\mathcal{P}$ as

$$P = \frac{2\pi^2}{k^3}\mathcal{P}\,. \tag{4.121}$$

A particular realization of the field is then generated from the dimensionful power spectrum with the procedure of Ref. [237]. First, for each point $\mathbf{k}$ in the momentum grid, generate two random numbers $R_1(\mathbf{k})$ and $R_2(\mathbf{k})$ uniformly distributed on the interval $[0,1]$. Then define

$$\rho_{\mathbf{k}} = -2\log R_1(\mathbf{k})\,, \qquad \varphi_{\mathbf{k}} = 2\pi R_2(\mathbf{k})\,. \tag{4.122}$$

A particular realization of the Φ and $\dot{\Phi}$ Fourier coefficients is then computed as

$$\Phi_{\mathbf{k}}(t) = s\sqrt{V\rho_{\mathbf{k}}P_\Phi(t,\mathbf{k})}e^{\mathrm{i}\varphi_{\mathbf{k}}}\,, \tag{4.123a}$$

$$\dot{\Phi}_{\mathbf{k}}(t) = s'\sqrt{V\rho_{\mathbf{k}}P_{\dot{\Phi}}(t,\mathbf{k})}e^{\mathrm{i}\varphi_{\mathbf{k}}}\,, \tag{4.123b}$$

where s and s' denote the signs of $\Phi_k(t_k)$ and $d\Phi_k(t_k)/dt_k$ respectively and $V = (2L)^3$ is the

comoving integration volume. The zero-momentum terms represent a constant shift of $\Phi_{\mathbf{k}}$ and $\dot{\Phi}_{\mathbf{k}}$, which we remove by setting $\Phi_{\mathbf{0}} = \dot{\Phi}_{\mathbf{0}} = 0$. The real-space fields $\Phi(t, \mathbf{x})$ and $\dot{\Phi}(t, \mathbf{x})$ are then

$$\Phi(t, \mathbf{x}) = \mathrm{Re}\left(\frac{dk}{2\pi}\right)^3 \sum_{\mathbf{k}} \Phi_{\mathbf{k}}(t) e^{-\mathrm{i}\mathbf{k}\cdot\mathbf{x}}\,, \tag{4.124a}$$

$$\dot{\Phi}(t, \mathbf{x}) = \mathrm{Re}\left(\frac{dk}{2\pi}\right)^3 \sum_{\mathbf{k}} \dot{\Phi}_{\mathbf{k}}(t) e^{-\mathrm{i}\mathbf{k}\cdot\mathbf{x}}\,. \tag{4.124b}$$

These expressions can be written in terms of the fast Fourier transform (FFT), or `fftn(fftshift(`Φ_k`))` in `Matlab`.

Finally, we discuss the process of measuring the power spectrum of a real field $F(\mathbf{x})$ at an instant in time. Measuring the density power spectrum is especially important when verifying the $3+1d$ code, since the density power spectrum can be directly compared to the output of the linearized theory of Sec. 4.8.

In order to measure the power spectrum of a real field $F(\mathbf{x})$, we first compute its Fourier transform

$$F_{\mathbf{k}} = dL^3 \sum_{\mathbf{k}} F(\mathbf{x}) e^{-\mathrm{i}\mathbf{k}\cdot\mathbf{x}}\,. \tag{4.125}$$

The power spectrum of $F(\mathbf{x})$ is the average of $F_{\mathbf{k}}^2$ over concentric spherical momentum shells. The fact that small $|\mathbf{k}|$ shells contain fewer momentum grid points means that the one should not trust the the low-frequency power spectrum to reflect the statistical properties of the field. Define the magnitude of the momentum vector $k_r = \sqrt{\mathbf{k}^2}$. Let $k_r(n) = k_r$ when k_r is in the interval $[(n-1), n]dk$, and zero otherwise. Let N_n be the number of non-zero elements in $k_r(n)$. The power spectrum is then

$$P_F(n\,dk) = \sum_{k \in k_r(n)} \frac{|F_k|^2}{N_n V}\,. \tag{4.126}$$

4.9.2 Numerical methods

To evolve the equations of motion Eq. 4.119, we use Runge-Kutta 4th-order (RK4) time-integration, with pseudospectral derivative operators. Here, we provide a brief review of pseudospectral methods.

The Laplacian operator in Eq. 4.119 poses a computational challenge: in position space, it represents matrix multiplication, which can be an inefficient process. The pseudospectral method recognizes that the potential is best computed in position-space, where it acts as a pointwise operator, and derivatives are best computed in momentum space, where they acts as pointwise operators. The pseudospectral algorithm to compute derivatives is as follows:

1. compute the FFT of θ_i,
2. apply the derivative operator in momentum space (pointwise multiplication),
3. compute the inverse FFT (IFFT).

We note that the pseudospectral method is well suited to GPU acceleration, since it makes use of pointwise matrix multiplication and the FFT, both of which have efficient GPU implementations. Because the FFT is an extremely optimized algorithm, converting between position space and momentum space is an extremely efficient process, in essence making the pseudospectral method an efficient implementation of multiplication that would otherwise need to take place to compute the action of a differential operator. The numerical Laplacian is computed as:

$$\nabla^2\theta = \frac{1}{V}\sum_{\mathbf{k}}(-\mathbf{k}^2)e^{-i\mathbf{k}\cdot\mathbf{x}}\sum_{\mathbf{k}}\theta e^{i\mathbf{k}\cdot\mathbf{x}}\,. \tag{4.127}$$

We note that to ensure convergence of the pseudospectral method, it is often helpful to suppress the numerical instability of high-frequency modes by truncating momentum space somewhat below the maximum possible resolution of the spatial grid ($k_{\max} = \pi/dL$). In our calculations, we take this cutoff to be $k_{\max}/2$.

4.9.3 Future directions

While our preliminary simulations shed some light on the possible consequences of nonlinear fluctuations during autoresonance, we recognize an opportunity to develop higher resolution simulations in order to reach a definitive conclusion. In particular, our simulations are limited in the range of comoving momenta they can resolve, $|\tilde{\mathbf{k}}| \in [m, 30m]$, which is particularly restrictive at the time of oscillon formation. Because our simulations take place on a comoving grid, oscillons, whose physical size does not redshift, appear to get smaller, requiring higher and higher momenta to fully resolve. This, combined with the fact that oscillons already have very broad momentum spectra, means that our simulations are substantially less reliable after oscillons have formed, and our observation that autoresonance is terminated by oscillon formation may not hold up to higher resolution simulations.

We end on a tangentially related note that there are additional questions which will only be resolved by $3+1d$ simulations. In particular, it need not be the case that the axion rolls to the true vacuum. For example, the potential Eq. 3.23 will in general have many false vacua, and it may be more likely that the axion rolls there than the true vacuum. In this case, there are two possibilities. First, the axion can quantum tunnel out of the false vacuum into the true vacuum, nucleating vacuum bubbles that quickly expand to fill the universe. Second, the axion can *classically* tunnel out of the false vacuum, also nucleating vacuum bubbles that expand to fill the universe, but potentially on a very different timescale. Classical tunnelling occurs when the axion perturbations become large enough that the field must explore adjacent vacua, and the rapid perturbation growth experienced

in potentials such as Eq. 3.23 may make this the dominant tunneling mechanism. Both classical and quantum tunnelling require detailed simulations to resolve signatures such as gravitational wave production and the matter power spectrum.

Bibliography

[1] Jan Olle, Oriol Pujolas, and Fabrizio Rompineve. Recipes for oscillon longevity. *arXiv preprint arXiv:2012.13409*, 2020.

[2] Ciaran O'Hare. cajohare/axionlimits: Axionlimits, July 2020.

[3] Ciaran O'Hare. Axion limits. `https://github.com/cajohare/AxionLimits`. Accessed: 2021-07-11.

[4] Vid Iršič, Matteo Viel, Martin G. Haehnelt, James S. Bolton, and George D. BECker. First constraints on fuzzy dark matter from Lyman-α forest data and hydrodynamical simulations. *Phys. Rev. Lett.*, 119:031302, Jul 2017.

[5] Eric Armengaud, Nathalie Palanque-Delabrouille, Christophe Yèche, David JE Marsh, and Julien Baur. Constraining the mass of light bosonic dark matter using SDSS Lyman-α forest. *Monthly Notices of the Royal Astronomical Society*, 471(4):4606–4614, 2017.

[6] Katelin Schutz. Subhalo mass function and ultralight bosonic dark matter. *Phys. Rev. D*, 101:123026, Jun 2020.

[7] María Benito, Juan Carlos Criado, Gert Hütsi, Martti Raidal, and Hardi Veermäe. Implications of milky way substructures for the nature of dark matter. *Phys. Rev. D*, 101:103023, May 2020.

[8] Keir K Rogers and Hiranya V Peiris. Strong bound on canonical ultralight axion dark matter from the Lyman-alpha forest. *Physical Review Letters*, 126(7):071302, 2021.

[9] Manuel A Buen-Abad, JiJi Fan, and Chen Sun. Constraints on axions from cosmic distance measurements. *arXiv preprint arXiv:2011.05993*, 2020.

[10] Christopher S Reynolds, MC David Marsh, Helen R Russell, Andrew C Fabian, Robyn Smith, Francesco Tombesi, and Sylvain Veilleux. Astrophysical limits on very light axion-like particles from chandra grating spectroscopy of ngc 1275. *The Astrophysical Journal*, 890(1):59, 2020.

[11] MC David Marsh, Helen R Russell, Andrew C Fabian, Brian R McNamara, Paul Nulsen, and Christopher S Reynolds. A new bound on axion-like particles. *Journal of Cosmology and Astroparticle Physics*, 2017(12):036, 2017.

[12] Christopher Dessert, Joshua W Foster, and Benjamin R Safdi. X-ray searches for axions from super star clusters. *Physical Review Letters*, 125(26):261102, 2020.

[13] Denis Wouters and Pierre Brun. Constraints on axion-like particles from x-ray observations of the hydra galaxy cluster. *The Astrophysical Journal*, 772(1):44, 2013.

[14] Francesca Calore, Pierluca Carenza, Maurizio Giannotti, Joerg Jaeckel, and Alessandro Mirizzi. Bounds on axionlike particles from the diffuse supernova flux. *Physical Review D*, 102(12):123005, 2020.

[15] Adrian Ayala, Inma Dominguez, Maurizio Giannotti, Alessandro Mirizzi, and Oscar Straniero. Revisiting the bound on axion-photon coupling from globular clusters. *Physical review letters*, 113(19):191302, 2014.

[16] Núria Vinyoles, Aldo Serenelli, Francesco L Villante, Sarbani Basu, Javier Redondo, and Jordi Isern. New axion and hidden photon constraints from a solar data global fit. *Journal of Cosmology and Astroparticle Physics*, 2015(10):015, 2015.

[17] Marco Regis, Marco Taoso, Daniel Vaz, Jarle Brinchmann, Sebastiaan L Zoutendijk, Nicolas F Bouché, and Matthias Steinmetz. Searching for light in the darkness: Bounds on ALP dark matter with the optical muse-faint survey. *Physics Letters B*, 814:136075, 2021.

[18] Daniel Grin, Giovanni Covone, Jean-Paul Kneib, Marc Kamionkowski, Andrew Blain, and Eric Jullo. Telescope search for decaying relic axions. *Physical Review D*, 75(10):105018, 2007.

[19] Davide Cadamuro and Javier Redondo. Cosmological bounds on pseudo Nambu-Goldstone bosons. *Journal of Cosmology and Astroparticle Physics*, 2012(02):032, 2012.

[20] Michael A Fedderke, Peter W Graham, and Surjeet Rajendran. Axion dark matter detection with CMB polarization. *Physical Review D*, 100(1):015040, 2019.

[21] Saptarshi Chaudhuri. DMRadio-GUT: Probing gut-scale QCD axion dark matter. `https://www.snowmass21.org/docs/files/summaries/CF/SNOWMASS21-CF2_CF0-IF1_IF0_Saptarshi_Chaudhuri-219.pdf`. Accessed: 2021-08-11.

[22] David Alesini, Danilo Babusci, Daniele Di Gioacchino, Claudio Gatti, Gianluca Lamanna, and Carlo Ligi. The KLASH proposal. *arXiv preprint arXiv:1707.06010*, 2017.

[23] Ian Stern. ADMX status. *arXiv preprint arXiv:1612.08296*, 2016.

[24] The BRASS experiment. `https://www1.physik.uni-hamburg.de/iexp/gruppe-horns/forschung/brass.html`. Accessed: 2021-08-11.

[25] Robert Lasenby. Microwave cavity searches for low-frequency axion dark matter. *Physical Review D*, 102(1):015008, 2020.

[26] Asher Berlin, Raffaele Tito D'Agnolo, Sebastian AR Ellis, Christopher Nantista, Jeffrey Neilson, Philip Schuster, Sami Tantawi, Natalia Toro, and Kevin Zhou. Axion dark matter detection by superconducting resonant frequency conversion. *Journal of High Energy Physics*, 2020(7):1–42, 2020.

[27] Asher Berlin, Raffaele Tito d'Agnolo, Sebastian AR Ellis, and Kevin Zhou. Heterodyne broadband detection of axion dark matter. *arXiv preprint arXiv:2007.15656*, 2020.

[28] Hongwan Liu, Brodi D Elwood, Matthew Evans, and Jesse Thaler. Searching for axion dark matter with birefringent cavities. *Physical Review D*, 100(2):023548, 2019.

[29] Yuta Michimura, Yuka Oshima, Taihei Watanabe, Takuya Kawasaki, Hiroki Takeda, Masaki Ando, Koji Nagano, Ippei Obata, and Tomohiro Fujita. Dance: Dark matter axion search with ring cavity experiment. In *Journal of Physics: Conference Series*, volume 1468, page 012032. IOP Publishing, 2020.

[30] J. L. Ouellet. Probing the QCD axion with DMRadio-m^3. `https://www.snowmass21.org/docs/files/summaries/CF/SNOWMASS21-CF2_CF0-IF1_IF0_Ouellet-217.pdf`. Accessed: 2021-08-11.

[31] S Beurthey, N Böhmer, P Brun, A Caldwell, L Chevalier, C Diaconu, G Dvali, P Freire, E Garutti, C Gooch, et al. Madmax status report. *arXiv preprint arXiv:2003.10894*, 2020.

[32] Masha Baryakhtar, Junwu Huang, and Robert Lasenby. Axion and hidden photon dark matter detection with multilayer optical haloscopes. *Physical Review D*, 98(3):035006, 2018.

[33] Koji Nagano, Tomohiro Fujita, Yuta Michimura, and Ippei Obata. Axion dark matter search with interferometric gravitational wave detectors. *Physical review letters*, 123(11):111301, 2019.

[34] Ben T McAllister, Graeme Flower, Eugene N Ivanov, Maxim Goryachev, Jeremy Bourhill, and Michael E Tobar. The ORGANexperiment: An axion haloscope above 15 ghz. *Physics of the dark universe*, 18:67–72, 2017.

[35] Jan Schütte-Engel, David JE Marsh, Alexander J Millar, Akihiko Sekine, Francesca Chadha-Day, Sebastian Hoof, Mazhar Ali, Kin-Chung Fong, Edward Hardy, and Libor Šmejkal. Axion quasiparticles for axion dark matter detection. *arXiv preprint arXiv:2102.05366*, 2021.

[36] Mengjiao Xiao, Kerstin M. Perez, Maurizio Giannotti, Oscar Straniero, Alessandro Mirizzi, Brian W. Grefenstette, Brandon M. Roach, and Melania Nynka. Constraints on Axionlike Particles from a Hard X-Ray Observation of Betelgeuse. *Phys. Rev. Lett.*, 126(3):031101, 2021.

[37] Denis Wouters and Pierre Brun. Constraints on Axion-like Particles from X-Ray Observations of the Hydra Galaxy Cluster. *Astrophys. J.*, 772:44, 2013.

[38] M. C. David Marsh, Helen R. Russell, Andrew C. Fabian, Brian P. McNamara, Paul Nulsen, and Christopher S. Reynolds. A New Bound on Axion-Like Particles. *JCAP*, 12:036, 2017.

[39] Francesca Calore, Pierluca Carenza, Maurizio Giannotti, Joerg Jaeckel, and Alessandro Mirizzi. Bounds on axionlike particles from the diffuse supernova flux. *Phys. Rev. D*, 102(12):123005, 2020.

[40] M. Ajello et al. Search for Spectral Irregularities due to Photon–Axionlike-Particle Oscillations with the Fermi Large Area Telescope. *Phys. Rev. Lett.*, 116(16):161101, 2016.

[41] M. Meyer, M. Giannotti, A. Mirizzi, J. Conrad, and M. A. Sánchez-Conde. Fermi Large Area Telescope as a Galactic Supernovae Axionscope. *Phys. Rev. Lett.*, 118(1):011103, 2017.

[42] Manuel Meyer and Tanja Petrushevska. Search for Axionlike-Particle-Induced Prompt γ-Ray Emission from Extragalactic Core-Collapse Supernovae with the *Fermi* Large Area Telescope. *Phys. Rev. Lett.*, 124(23):231101, 2020. [Erratum: Phys.Rev.Lett. 125, 119901 (2020)].

[43] A. Abramowski et al. Constraints on axionlike particles with H.E.S.S. from the irregularity of the PKS 2155-304 energy spectrum. *Phys. Rev. D*, 88(10):102003, 2013.

[44] Adrian Ayala, Inma Domínguez, Maurizio Giannotti, Alessandro Mirizzi, and Oscar Straniero. Revisiting the bound on axion-photon coupling from Globular Clusters. *Phys. Rev. Lett.*, 113(19):191302, 2014.

[45] Hai-Jun Li, Jun-Guang Guo, Xiao-Jun Bi, Su-Jie Lin, and Peng-Fei Yin. Limits on axionlike particles from Mrk 421 with 4.5-year period observations by ARGO-YBJ and Fermi-LAT. *Phys. Rev. D*, 103(8):083003, 2021.

[46] Joshua W. Foster, Yonatan Kahn, Oscar Macias, Zhiquan Sun, Ralph P. Eatough, Vladislav I. Kondratiev, Wendy M. Peters, Christoph Weniger, and Benjamin R. Safdi. Green Bank and Effelsberg Radio Telescope Searches for Axion Dark Matter Conversion in Neutron Star Magnetospheres. *Phys. Rev. Lett.*, 125(17):171301, 2020.

[47] Jeremy Darling. Search for Axionic Dark Matter Using the Magnetar PSR J1745-2900. *Phys. Rev. Lett.*, 125(12):121103, 2020.

[48] Jeremy Darling. New Limits on Axionic Dark Matter from the Magnetar PSR J1745-2900. *Astrophys. J. Lett.*, 900(2):L28, 2020.

[49] J. Jaeckel, P. C. Malta, and J. Redondo. Decay photons from the axionlike particles burst of type II supernovae. *Phys. Rev. D*, 98(5):055032, 2018.

[50] Alexandre Payez, Carmelo Evoli, Tobias Fischer, Maurizio Giannotti, Alessandro Mirizzi, and Andreas Ringwald. Revisiting the SN1987A gamma-ray limit on ultralight axion-like particles. *JCAP*, 02:006, 2015.

[51] Jun Seok Lee. Revisiting supernova 1987a limits on axion-like-particles. *arXiv preprint arXiv:1808.10136*, 2018.

[52] Christopher Dessert, Joshua W. Foster, and Benjamin R. Safdi. X-ray Searches for Axions from Super Star Clusters. *Phys. Rev. Lett.*, 125(26):261102, 2020.

[53] Daniel Grin, Giovanni Covone, Jean-Paul Kneib, Marc Kamionkowski, Andrew Blain, and Eric Jullo. A Telescope Search for Decaying Relic Axions. *Phys. Rev. D*, 75:105018, 2007.

[54] Charles Thorpe-Morgan, Denys Malyshev, Andrea Santangelo, Josef Jochum, Barbara Jäger, Manami Sasaki, and Sara Saeedi. THESEUS insights into axionlike particles, dark photon, and sterile neutrino dark matter. *Phys. Rev. D*, 102(12):123003, 2020.

[55] Davide Cadamuro and Javier Redondo. Cosmological bounds on pseudo Nambu-Goldstone bosons. *JCAP*, 02:032, 2012.

[56] Paul Frederik Depta, Marco Hufnagel, and Kai Schmidt-Hoberg. Robust cosmological constraints on axion-like particles. *JCAP*, 05:009, 2020.

[57] Marco Regis, Marco Taoso, Daniel Vaz, Jarle Brinchmann, Sebastiaan L. Zoutendijk, Nicolas F. Bouché, and Matthias Steinmetz. Searching for light in the darkness: Bounds on ALP dark matter with the optical MUSE-faint survey. *Phys. Lett. B*, 814:136075, 2021.

[58] V. Anastassopoulos et al. New CAST Limit on the Axion-Photon Interaction. *Nature Phys.*, 13:584–590, 2017.

[59] Asimina Arvanitaki, Savas Dimopoulos, Marios Galanis, Luis Lehner, Jedidiah O. Thompson, and Ken Van Tilburg. Large-misalignment mechanism for the formation of compact axion structures: Signatures from the QCD axion to fuzzy dark matter. *Phys. Rev. D*, 101(8):083014, 2020.

[60] Pierre-Henri Chavanis and Luca Delfini. Mass-radius relation of newtonian self-gravitating Bose-Einstein condensates with short-range interactions. ii. numerical results. *Phys. Rev. D*, 84:043532, Aug 2011.

[61] L Zhong, S Al Kenany, KM Backes, BM Brubaker, SB Cahn, G Carosi, YV Gurevich, WF Kindel, SK Lamoreaux, KW Lehnert, et al. Results from phase 1 of the haystac microwave cavity axion experiment. *Physical Review D*, 97(9):092001, 2018.

[62] Ken Van Tilburg, Anna-Maria Taki, and Neal Weiner. Halometry from astrometry. *Journal of Cosmology and Astroparticle Physics*, 2018(07):041–041, jul 2018.

[63] Liang Dai and Jordi Miralda-Escudé. Gravitational lensing signatures of axion dark matter minihalos in highly magnified stars. *The Astronomical Journal*, 159(2):49, jan 2020.

[64] Mustafa A Amin and David Shirokoff. Flat-top oscillons in an expanding universe. *Physical Review D*, 81(8):085045, 2010.

[65] David Cyncynates and Tudor Giurgica-Tiron. Structure of the oscillon: The dynamics of attractive self-interaction. *Physical Review D*, 103(11):116011, 2021.

[66] David Cyncynates, Tudor Giurgica-Tiron, Olivier Simon, and Jedidiah O Thompson. Resonant nonlinear pairs in the axiverse and their late-time direct and astrophysical signatures. *Physical Review D*, 105(5):055005, 2022.

[67] Roberto D Peccei and Helen R Quinn. Constraints imposed by cp conservation in the presence of pseudoparticles. *Physical Review D*, 16(6):1791, 1977.

[68] Georg G Raffelt. Astrophysical axion bounds. In *Axions*, pages 51–71. Springer, 2008.

[69] V Anastassopoulos, S Aune, K Barth, A Belov, H Bräuninger, Giovanni Cantatore, JM Carmona, JF Castel, SA Cetin, F Christensen, et al. New cast limit on the axion–photon interaction. *Nature Physics*, 13(6):584, 2017.

[70] Jae Hyeok Chang, Rouven Essig, and Samuel D McDermott. Supernova 1987a constraints on sub-gev dark sectors, millicharged particles, the qcd axion, and an axion-like particle. *Journal of High Energy Physics*, 2018(9):1–45, 2018.

[71] Frank Wilczek. Problem of strong p and t invariance in the presence of instantons. *Physical Review Letters*, 40(5):279, 1978.

[72] Steven Weinberg. A new light boson? *Physical Review Letters*, 40(4):223, 1978.

[73] Asimina Arvanitaki, Savas Dimopoulos, Sergei Dubovsky, Nemanja Kaloper, and John March-Russell. String axiverse. *Physical Review D*, 81(12):123530, 2010.

[74] John Preskill, Mark B Wise, and Frank Wilczek. Cosmology of the invisible axion. *Physics Letters B*, 120(1-3):127–132, 1983.

[75] Laurence F Abbott and P Sikivie. A cosmological bound on the invisible axion. *Physics Letters B*, 120(1-3):133–136, 1983.

[76] Michael Dine and Willy Fischler. The not-so-harmless axion. *Physics Letters B*, 120(1-3):137–141, 1983.

[77] Michael S Turner. Windows on the axion. *Physics Reports*, 197(2):67–97, 1990.

[78] Pierre Sikivie. Axion cosmology. In *Axions*, pages 19–50. Springer, 2008.

[79] Alberto Salvio, Alessandro Strumia, and Wei Xue. Thermal axion production. *Journal of Cosmology and Astroparticle Physics*, 2014(01):011, 2014.

[80] Giovanni Grilli di Cortona, Edward Hardy, Javier Pardo Vega, and Giovanni Villadoro. The qcd axion, precisely. *Journal of High Energy Physics*, 2016(1):34, 2016.

[81] Lawrence J Hall, Keisuke Harigaya, et al. Axion kinetic misalignment mechanism. *Physical review letters*, 124(25):251802, 2020.

[82] Lam Hui, Jeremiah P Ostriker, Scott Tremaine, and Edward Witten. Ultralight scalars as cosmological dark matter. *Physical Review D*, 95(4):043541, 2017.

[83] Vid Iršič, Matteo Viel, Martin G Haehnelt, James S Bolton, and George D Becker. First constraints on fuzzy dark matter from lyman-α forest data and hydrodynamical simulations. *Physical review letters*, 119(3):031302, 2017.

[84] Katelin Schutz. Subhalo mass function and ultralight bosonic dark matter. *Physical Review D*, 101(12):123026, 2020.

[85] María Benito, Juan Carlos Criado, Gert Hütsi, Martti Raidal, and Hardi Veermäe. Implications of milky way substructures for the nature of dark matter. *Physical Review D*, 101(10):103023, 2020.

[86] Lam Hui. Wave dark matter. *arXiv preprint arXiv:2101.11735*, 2021.

[87] Ethan O Nadler, Simon Birrer, Daniel Gilman, Risa H Wechsler, Xiaolong Du, Andrew Benson, Anna M Nierenberg, and Tommaso Treu. Dark matter constraints from a unified analysis of strong gravitational lenses and milky way satellite galaxies. *arXiv preprint arXiv:2101.07810*, 2021.

[88] Xiaolong Du, Christoph Behrens, and Jens C Niemeyer. Substructure of fuzzy dark matter halos. *Monthly Notices of the Royal Astronomical Society*, page stw2724, 2016.

[89] Jiajun Zhang, Hantao Liu, and Ming-Chung Chu. Cosmological simulation for fuzzy dark matter model. *Frontiers in Astronomy and Space Sciences*, 5:48, 2019.

[90] Matteo Nori, Riccardo Murgia, Vid Iršič, Marco Baldi, and Matteo Viel. Lyman α forest and non-linear structure characterization in fuzzy dark matter cosmologies. *Monthly Notices of the Royal Astronomical Society*, 482(3):3227–3243, 2019.

[91] Andreas Burkert. Fuzzy dark matter and dark matter halo cores. *The Astrophysical Journal*, 904(2):161, 2020.

[92] Prateek Agrawal, Anson Hook, and Junwu Huang. A cmb millikan experiment with cosmic axiverse strings. *Journal of High Energy Physics*, 2020(7):1–38, 2020.

[93] Edward W Kolb and Igor I Tkachev. Axion miniclusters and bose stars. *Physical review letters*, 71(19):3051, 1993.

[94] Malte Buschmann, Joshua W Foster, and Benjamin R Safdi. Early-universe simulations of the cosmological axion. *Physical review letters*, 124(16):161103, 2020.

[95] Nikita Blinov, Matthew J Dolan, and Patrick Draper. Imprints of the early universe on axion dark matter substructure. *Physical Review D*, 101(3):035002, 2020.

[96] Pierre-Henri Chavanis. Phase transitions between dilute and dense axion stars. *Physical Review D*, 98(2):023009, 2018.

[97] Eric Braaten and Hong Zhang. Axion stars. *arXiv preprint arXiv:1810.11473*, 2018.

[98] Luca Visinelli, Sebastian Baum, Javier Redondo, Katherine Freese, and Frank Wilczek. Dilute and dense axion stars. *Physics Letters B*, 777:64–72, 2018.

[99] Gyula Fodor, Péter Forgács, Philippe Grandclément, and István Rácz. Oscillons and quasi-breathers in the ϕ 4 klein-gordon model. *Physical Review D*, 74(12):124003, 2006.

[100] AE Kudryavtsev. Solitonlike solutions for a higgs scalar field. Technical report, Institute of Theoretical and Experimental Physics, 1975.

[101] VG Makhankov. Dynamics of classical solitons (in non-integrable systems). *Physics reports*, 35(1):1–128, 1978.

[102] J Geicke. Cylindrical pulsons in nonlinear relativistic wave equations. *Physica Scripta*, 29(5):431, 1984.

[103] Marcelo Gleiser. Pseudostable bubbles. *Physical Review D*, 49(6):2978, 1994.

[104] Edward W Kolb and Igor I Tkachev. Nonlinear axion dynamics and the formation of cosmological pseudosolitons. *Physical Review D*, 49(10):5040, 1994.

[105] Edmund J Copeland, Marcello Gleiser, and H-R Müller. Oscillons: Resonant configurations during bubble collapse. *Physical Review D*, 52(4):1920, 1995.

[106] Ethan P Honda and Matthew W Choptuik. Fine structure of oscillons in the spherically symmetric φ 4 klein-gordon model. *Physical Review D*, 65(8):084037, 2002.

[107] Paul M Saffin and Anders Tranberg. Oscillons and quasi-breathers in d+ 1 dimensions. *Journal of High Energy Physics*, 2007(01):030, 2007.

[108] Gyula Fodor, Peter Forgacs, Zalan Horvath, and Arpad Lukacs. Small amplitude quasi-breathers and oscillons. *Physical Review D*, 78(2):025003, 2008.

[109] Gyula Fodor, Péter Forgács, Zalán Horváth, and Márk Mezei. Radiation of scalar oscillons in 2 and 3 dimensions. *Physics Letters B*, 674(4-5):319–324, 2009.

[110] Marcelo Gleiser and David Sicilia. General theory of oscillon dynamics. *Physical Review D*, 80(12):125037, 2009.

[111] Mustafa A Amin, Richard Easther, Hal Finkel, Raphael Flauger, and Mark P Hertzberg. Oscillons after inflation. *Physical review letters*, 108(24):241302, 2012.

[112] Erik Alexander Andersen and Anders Tranberg. Four results on ϕ 4 oscillons in d+ 1 dimensions. *Journal of High Energy Physics*, 2012(12):16, 2012.

[113] Petja Salmi and Mark Hindmarsh. Radiation and relaxation of oscillons. *Physical Review D*, 85(8):085033, 2012.

[114] Kyohei Mukaida, Masahiro Takimoto, and Masaki Yamada. On longevity of i-ball/oscillon. *Journal of High Energy Physics*, 2017(3):122, 2017.

[115] Gyula Fodor. A review on radiation of oscillons and oscillatons. *arXiv preprint arXiv:1911.03340*, 2019.

[116] Marcelo Gleiser and Max Krackow. Resonant configurations in scalar field theories: Can some oscillons live forever? *Physical Review D*, 100(11):116005, 2019.

[117] Jan Ollé, Oriol Pujolas, and Fabrizio Rompineve. Oscillons and dark matter. *Journal of Cosmology and Astroparticle Physics*, 2020(02):006, 2020.

[118] Hong-Yi Zhang, Mustafa A Amin, Edmund J Copeland, Paul M Saffin, and Kaloian D Lozanov. Classical decay rates of oscillons. *Journal of Cosmology and Astroparticle Physics*, 2020(07):055, 2020.

[119] Masahiro Kawasaki, Wakutaka Nakano, and Eisuke Sonomoto. Oscillon of ultra-light axion-like particle. *Journal of Cosmology and Astroparticle Physics*, 2020(01):047, 2020.

[120] Mark P Hertzberg. Quantum radiation of oscillons. *Physical Review D*, 82(4):045022, 2010.

[121] Jan Ollé, Oriol Pujolàs, Tanmay Vachaspati, and George Zahariade. Quantum evaporation of classical breathers. *Physical Review D*, 100(4):045011, 2019.

[122] Tomasz Romańczukiewicz and Yakov Shnir. Oscillons in the presence of external potential. *Journal of High Energy Physics*, 2018(1):1–24, 2018.

[123] Patrick Dorey, Tomasz Romańczukiewicz, and Yakov Shnir. Staccato radiation from the decay of large amplitude oscillons. *Physics Letters B*, 806:135497, 2020.

[124] Ken Van Tilburg, Anna-Maria Taki, and Neal Weiner. Halometry from astrometry. *Journal of Cosmology and Astroparticle Physics*, 2018(07):041, 2018.

[125] Anirudh Prabhu and Nicholas M Rapidis. Resonant conversion of dark matter oscillons in pulsar magnetospheres. *Journal of Cosmology and Astroparticle Physics*, 2020(10):054, 2020.

[126] Anirudh Prabhu. Optical lensing by axion stars: Observational prospects with radio astrometry. *arXiv preprint arXiv:2006.10231*, 2020.

[127] Masahiro Kawasaki, Wakutaka Nakano, Hiromasa Nakatsuka, and Eisuke Sonomoto. Probing oscillons of ultra-light axion-like particle by 21cm forest. *arXiv preprint arXiv:2010.13504*, 2020.

[128] Mustafa A Amin and Zong-Gang Mou. Electromagnetic bursts from mergers of oscillons in axion-like fields. *Journal of Cosmology and Astroparticle Physics*, 2021(02):024, 2021.

[129] Mustafa A Amin, Andrew J Long, Zong-Gang Mou, and Paul Saffin. Dipole radiation and beyond from axion stars in electromagnetic fields. *arXiv preprint arXiv:2103.12082*, 2021.

[130] James H Buckley, PS Bhupal Dev, Francesc Ferrer, and Fa Peng Huang. Fast radio bursts from axion stars moving through pulsar magnetospheres. *Physical Review D*, 103(4):043015, 2021.

[131] Philip B Burt. Exact, multiple soliton solutions of the double sine gordon equation. *Proceedings of the Royal Society of London. A. Mathematical and Physical Sciences*, 359(1699):479–495, 1978.

[132] BMAG Piette and WJ Zakrzewski. Metastable stationary solutions of the radial d dimensional sine-gordon model. Technical report, SCAN-9809075, 1997.

[133] Steven H Schot. Eighty years of sommerfeld's radiation condition. *Historia mathematica*, 19(4):385–401, 1992.

[134] Eva Silverstein and Alexander Westphal. Monodromy in the cmb: gravity waves and string inflation. *Physical Review D*, 78(10):106003, 2008.

[135] Sergei Dubovsky, Albion Lawrence, and Matthew M Roberts. Axion monodromy in a model of holographic gluodynamics. *Journal of High Energy Physics*, 2012(2):53, 2012.

[136] Nemanja Kaloper and Albion Lawrence. London equation for monodromy inflation. *Physical Review D*, 95(6):063526, 2017.

[137] R. D. Peccei and Helen R. Quinn. CP conservation in the presence of pseudoparticles. *Phys. Rev. Lett.*, 38:1440–1443, Jun 1977.

[138] R. D. Peccei and Helen R. Quinn. Constraints imposed by CP conservation in the presence of pseudoparticles. *Phys. Rev. D*, 16:1791–1797, Sep 1977.

[139] Steven Weinberg. A new light boson? *Phys. Rev. Lett.*, 40:223–226, Jan 1978.

[140] F. Wilczek. Problem of strong p and t invariance in the presence of instantons. *Phys. Rev. Lett.*, 40:279–282, Jan 1978.

[141] Edward Witten. Some Properties of O(32) Superstrings. *Phys. Lett. B*, 149:351–356, 1984.

[142] Tom Banks and Michael Dine. Couplings and scales in strongly coupled heterotic string theory. *Nuclear Physics B*, 479(1):173–196, 1996.

[143] Peter Svrcek and Edward Witten. Axions In String Theory. *JHEP*, 06:051, 2006.

[144] John Preskill, Mark B. Wise, and Frank Wilczek. Cosmology of the Invisible Axion. *Phys. Lett. B*, 120:127–132, 1983.

[145] L. F. Abbott and P. Sikivie. A Cosmological Bound on the Invisible Axion. *Phys. Lett. B*, 120:133–136, 1983.

[146] Michael Dine and Willy Fischler. The Not So Harmless Axion. *Phys. Lett. B*, 120:137–141, 1983.

[147] Michael S. Turner. Coherent scalar-field oscillations in an expanding universe. *Phys. Rev. D*, 28:1243–1247, Sep 1983.

[148] Wayne Hu, Rennan Barkana, and Andrei Gruzinov. Fuzzy cold dark matter: The wave properties of ultralight particles. *Phys. Rev. Lett.*, 85:1158–1161, Aug 2000.

[149] Alan H. Guth, Mark P. Hertzberg, and C. Prescod-Weinstein. Do dark matter axions form a condensate with long-range correlation? *Phys. Rev. D*, 92:103513, Nov 2015.

[150] David JE Marsh. Axion cosmology. *Physics Reports*, 643:1–79, 2016.

[151] Mark P. Hertzberg. Quantum and classical behavior in interacting bosonic systems. *Journal of Cosmology and Astroparticle Physics*, 2016(11):037–037, nov 2016.

[152] Edward W. Kolb and Michael S. Turner. *The Early Universe*, volume 69. Addison-Wesley Publishing Company, 1990.

[153] Andrei D. Linde. Inflationary Cosmology. *Lect. Notes Phys.*, 738:1–54, 2008.

[154] Andrew Eberhardt, Alvaro Zamora, Michael Kopp, and Tom Abel. On the single classical field description of interacting scalar fields. *arXiv preprint arXiv:2111.00050*, 2021.

[155] Mark Srednicki. Axion Couplings to Matter. 1. CP Conserving Parts. *Nucl. Phys. B*, 260:689–700, 1985.

[156] Peter W. Graham and Surjeet Rajendran. New Observables for Direct Detection of Axion Dark Matter. *Phys. Rev. D*, 88:035023, 2013.

[157] P. A. Zyla et al. Review of Particle Physics. *PTEP*, 2020(8):083C01, 2020.

[158] Raymond T. Co, Eric Gonzalez, and Keisuke Harigaya. Axion Misalignment Driven to the Bottom. *JHEP*, 05:162, 2019.

[159] Raymond T Co, Eric Gonzalez, and Keisuke Harigaya. Axion misalignment driven to the hilltop. *arXiv preprint arXiv:1812.11192*, 2018.

[160] Peter W Graham and Adam Scherlis. Stochastic axion scenario. *Physical Review D*, 98(3):035017, 2018.

[161] Fuminobu Takahashi, Wen Yin, and Alan H. Guth. QCD axion window and low-scale inflation. *Phys. Rev. D*, 98(1):015042, 2018.

[162] Fuminobu Takahashi and Wen Yin. QCD axion on hilltop by a phase shift of π. *JHEP*, 10:120, 2019.

[163] Junwu Huang, Amalia Madden, Davide Racco, and Mario Reig. Maximal axion misalignment from a minimal model. *JHEP*, 10:143, 2020.

[164] Ben Freivogel. Anthropic Explanation of the Dark Matter Abundance. *JCAP*, 03:021, 2010.

[165] Asimina Arvanitaki and Sergei Dubovsky. Exploring the String Axiverse with Precision Black Hole Physics. *Phys. Rev. D*, 83:044026, 2011.

[166] Michael S. Turner. Cosmic and local mass density of "invisible" axions. *Phys. Rev. D*, 33:889–896, Feb 1986.

[167] D. H. Lyth. Axions and inflation: Vacuum fluctuations. *Phys. Rev. D*, 45:3394–3404, May 1992.

[168] Karl Strobl and Thomas J. Weiler. Anharmonic evolution of the cosmic axion density spectrum. *Phys. Rev. D*, 50:7690–7702, 1994.

[169] Takeshi Kobayashi, Ryosuke Kurematsu, and Fuminobu Takahashi. Isocurvature Constraints and Anharmonic Effects on QCD Axion Dark Matter. *JCAP*, 09:032, 2013.

[170] Kyu Jung Bae, Ji-Haeng Huh, and Jihn E. Kim. Update of axion CDM energy. *JCAP*, 09:005, 2008.

[171] Luca Visinelli and Paolo Gondolo. Dark Matter Axions Revisited. *Phys. Rev. D*, 80:035024, 2009.

[172] Viraf M Mehta, Mehmet Demirtas, Cody Long, David JE Marsh, Liam McAllister, and Matthew J Stott. Superradiance in string theory. *arXiv preprint arXiv:2103.06812*, 2021.

[173] Igor E. Halperin and Ariel Zhitnitsky. Axion potential, topological defects and CP odd bubbles in QCD. *Phys. Lett. B*, 440:77–88, 1998.

[174] Richard Easther and Liam McAllister. Random matrices and the spectrum of n-flation. *Journal of cosmology and astroparticle physics*, 2006(05):018, 2006.

[175] Thomas C. Bachlechner, Cody Long, and Liam McAllister. Planckian Axions and the Weak Gravity Conjecture. *JHEP*, 01:091, 2016.

[176] Thomas C Bachlechner. Axionic band structure of the cosmological constant. *Physical Review D*, 93(2):023522, 2016.

[177] Thomas C Bachlechner, Kate Eckerle, Oliver Janssen, and Matthew Kleban. Multiple-axion framework. *Physical Review D*, 98(6):061301, 2018.

[178] Mehmet Demirtas, Cody Long, Liam McAllister, and Mike Stillman. The Kreuzer-Skarke axiverse. *Journal of High Energy Physics*, 2020(4):1–34, 2020.

[179] Viraf M Mehta, Mehmet Demirtas, Cody Long, David JE Marsh, Liam McAllister, and Matthew J Stott. Superradiance exclusions in the landscape of type iib string theory. *arXiv preprint arXiv:2011.08693*, 2020.

[180] James Halverson, Cody Long, Brent Nelson, and Gustavo Salinas. Towards string theory expectations for photon couplings to axionlike particles. *Physical Review D*, 100(10):106010, 2019.

[181] V. A. Veksler. Concerning some new methods of acceleration of relativistic particles. *Physical Review*, 69:244–244, 1946.

[182] Edwin M. McMillan. The synchrotron—a proposed high energy particle accelerator. *Phys. Rev.*, 68:143–144, Sep 1945.

[183] D. Bohm and L. Foldy. The theory of the synchrotron. *Phys. Rev.*, 70:249–258, Sep 1946.

[184] L. D. Landau and E. M. Lifshitz. *Mechanics*, volume 1 of *Course of Theoretical Physics*, chapter V. Elsevier, 3rd edition, 1976.

[185] N. N. Bogoliubov and Y. A. Mitropolsky. *Asymptotic Methods in the Theory of Non-Linear Oscillations*. Hindustan Publishing Corporation, 1961.

[186] S. Rajasekar and M. A. F. Sanjuan. *Nonlinear Resonances.*, chapter Autoresonance. Springer Series in Synergetics. Springer, Cham, 2016.

[187] Sergey G. Glebov, Oleg M. Kiselev, and Nikolai N. Tarkhanov. *Nonlinear equations with small parameter*, volume Volume 1 Oscillations and Resonances, chapter Autoresonances in nonlinear systems. De Gruyter, 2017.

[188] J. Fajans and L. Frièdland. Autoresonant (nonstationary) excitation of pendulums, plutinos, plasmas, and other nonlinear oscillators. *American Journal of Physics*, 69(10):1096–1102, 2001.

[189] L. Friedland. Autoresonance in nonlinear systems. *Scholarpedia*, 4(1):5473, 2009. revision #126610.

[190] B. Meerson and L. Friedland. Strong autoresonance excitation of rydberg atoms: The rydberg accelerator. *Phys. Rev. A*, 41:5233–5236, May 1990.

[191] G. Marcus, L. Friedland, and A. Zigler. From quantum ladder climbing to classical autoresonance. *Phys. Rev. A*, 69:013407, Jan 2004.

[192] L. Friedland. Multidimensional autoresonant mode conversion. *Physics of Plasmas*, 2(5):1393–1397, 1995.

[193] J. Fajans, E. Gilson, and L. Friedland. Autoresonant (nonstationary) excitation of the diocotron mode in non-neutral plasmas. *Phys. Rev. Lett.*, 82:4444–4447, May 1999.

[194] Chapman Docteur Thomas. *Autoresonance in Stimulated Raman Scattering*. Theses, Ecole Polytechnique X, November 2011.

[195] Liu Chen and Fulvio Zonca. Physics of alfvén waves and energetic particles in burning plasmas. *Reviews of Modern Physics*, 88(1):015008, 2016.

[196] S. V. Batalov, A. G. Shagalov, and L. Friedland. Autoresonant excitation of bose-einstein condensates. *Phys. Rev. E*, 97:032210, Mar 2018.

[197] Aleksandr L Fradkov. Application of cybernetic methods in physics. *Physics-Uspekhi*, 48(2):103, 2005.

[198] O. Naaman, J. Aumentado, L. Friedland, J. S. Wurtele, and I. Siddiqi. Phase-locking transition in a chirped superconducting josephson resonator. *Phys. Rev. Lett.*, 101:117005, Sep 2008.

[199] Changyao Chen, Damián H. Zanette, Jeffrey R. Guest, David A. Czaplewski, and Daniel López. Self-sustained micromechanical oscillator with linear feedback. *Phys. Rev. Lett.*, 117:017203, Jul 2016.

[200] A. Kovaleva. Control of autoresonance in mechanical and physical models. *Philosophical Transactions of the Royal Society A: Mathematical, Physical and Engineering Sciences*, 375(2088):20160213, mar 2017.

[201] Avishek Chowdhury, Marcel G. Clerc, Sylvain Barbay, Isabelle Robert-Philip, and Remy Braive. Weak signal enhancement by nonlinear resonance control in a forced nano-electromechanical resonator. *Nature Communications*, 11(1):2400, 2020.

[202] Jihn E. Kim. Weak-interaction singlet and strong CP invariance. *Phys. Rev. Lett.*, 43:103–107, Jul 1979.

[203] M.A. Shifman, A.I. Vainshtein, and V.I. Zakharov. Can confinement ensure natural cp invariance of strong interactions? *Nuclear Physics B*, 166(3):493–506, 1980.

[204] Michael Dine, Willy Fischler, and Mark Srednicki. A simple solution to the strong cp problem with a harmless axion. *Physics Letters B*, 104(3):199–202, 1981.

[205] Masaharu Tanabashi, K Hagiwara, K Hikasa, Katsumasa Nakamura, Y Sumino, F Takahashi, J Tanaka, K Agashe, G Aielli, Claude Amsler, et al. Review of particle physics. *Physical Review D*, 98(3), 2018.

[206] Nabila Aghanim, Yashar Akrami, M Ashdown, J Aumont, C Baccigalupi, M Ballardini, AJ Banday, RB Barreiro, N Bartolo, S Basak, et al. Planck 2018 results-vi. cosmological parameters. *Astronomy & Astrophysics*, 641:A6, 2020.

[207] Ui-Han Zhang and Tzihong Chiueh. Evolution of linear wave dark matter perturbations in the radiation-dominated era. *Phys. Rev. D*, 96:023507, Jul 2017.

[208] Ui-Han Zhang and Tzihong Chiueh. Cosmological perturbations of extreme axion in the radiation era. *Phys. Rev. D*, 96:063522, Sep 2017.

[209] William H Press and Paul Schechter. Formation of galaxies and clusters of galaxies by self-similar gravitational condensation. *The Astrophysical Journal*, 187:425–438, 1974.

[210] James M Bardeen, JR Bond, Nick Kaiser, and AS Szalay. The statistics of peaks of gaussian random fields. *The Astrophysical Journal*, 304:15–61, 1986.

[211] Gaia Collaboration, Brown, A. G. A., et al. Gaia data release 2 - summary of the contents and survey properties. *A&A*, 616:A1, 2018.

[212] A. Bellini, J. Anderson, R. P. van der Marel, L. L. Watkins, I. R. King, P. Bianchini, J. Chanamé, R. Chandar, A. M. Cool, F. R. Ferraro, H. Ford, and D. Massari. Hubble Space Telescope Proper Motion (HSTPROMO) Catalogs of Galactic Globular Clusters. I. Sample Selection, Data Reduction, and NGC 7078 Results. *The Astrophysical Journal*, 797(2):115, December 2014.

[213] The Theia Collaboration, Celine Boehm, Alberto Krone-Martins, et al. Theia: Faint objects in motion or the new astrometry frontier, 2017.

[214] Robyn E. Sanderson, Andrea Bellini, Stefano Casertano, Jessica R. Lu, Peter Melchior, Mattia Libralato, David Bennett, Michael Shao, Jason Rhodes, Sangmo Tony Sohn, Sangeeta Malhotra, Scott Gaudi, S. Michael Fall, Ed Nelan, Puragra Guhathakurta, Jay Anderson, and Shirley Ho. Astrometry with the wide-field infrared space telescope, 2019.

[215] E. Fomalont and M. Reid. Microarcsecond astrometry using the ska. *New Astronomy Reviews*, 48(11):1473–1482, 2004. Science with the Square Kilometre Array.

[216] Warren Skidmore and. Thirty meter telescope detailed science case: 2015. *Research in Astronomy and Astrophysics*, 15(12):1945–2140, dec 2015.

[217] Ya. B. Zeldovich. Generation of Waves by a Rotating Body. *Journal of Experimental and Theoretical Physics Letters*, 14:180, 1971.

[218] Richard Brito, Vitor Cardoso, and Paolo Pani. Black holes as particle detectors: evolution of superradiant instabilities. *Class. Quant. Grav.*, 32(13):134001, 2015.

[219] Asimina Arvanitaki, Masha Baryakhtar, and Xinlu Huang. Discovering the QCD Axion with Black Holes and Gravitational Waves. *Phys. Rev. D*, 91(8):084011, 2015.

[220] Richard Brito, Vitor Cardoso, and Paolo Pani. Superradiance. *Lect. Notes Phys.*, 906:pp.1–237, 2015.

[221] Vitor Cardoso, Óscar J. C. Dias, Gavin S. Hartnett, Matthew Middleton, Paolo Pani, and Jorge E. Santos. Constraining the mass of dark photons and axion-like particles through black-hole superradiance. *JCAP*, 03:043, 2018.

[222] Masha Baryakhtar, Marios Galanis, Robert Lasenby, and Olivier Simon. Black hole superradiance of self-interacting scalar fields. *Phys. Rev. D*, 103(9):095019, 2021.

[223] JiJi Fan. Ultralight repulsive dark matter and BEC. *Physics of the Dark Universe*, 14:84–94, 2016.

[224] Ryuji Daido, Naoya Kitajima, and Fuminobu Takahashi. Domain wall formation from level crossing in the axiverse. *Physical Review D*, 92(6):063512, 2015.

[225] Naoya Kitajima and Fuminobu Takahashi. Resonant conversions of QCD axions into hidden axions and suppressed isocurvature perturbations. *Journal of Cosmology and Astroparticle Physics*, 2015(01):032, 2015.

[226] Ryuji Daido, Naoya Kitajima, and Fuminobu Takahashi. Level crossing between the QCD axion and an axionlike particle. *Physical Review D*, 93(7):075027, 2016.

[227] Shu-Yu Ho, Ken'ichi Saikawa, and Fuminobu Takahashi. Enhanced photon coupling of ALP dark matter adiabatically converted from the QCD axion. *Journal of Cosmology and Astroparticle Physics*, 2018(10):042, 2018.

[228] L Friedland and AG Shagalov. Emergence and control of multiphase nonlinear waves by synchronization. *Physical review letters*, 90(7):074101, 2003.

[229] L Friedland and AG Shagalov. Excitation of multiphase waves of the nonlinear schrödinger equation by capture into resonances. *Physical Review E*, 71(3):036206, 2005.

[230] Chia-Feng Chang and Yanou Cui. New perspectives on axion misalignment mechanism. *Physical Review D*, 102(1):015003, 2020.

[231] Joseph Ford. Equipartition of energy for nonlinear systems. *Journal of Mathematical Physics*, 2(3):387–393, 1961.

[232] Françoise Tisseur and Karl Meerbergen. The quadratic eigenvalue problem. *SIAM review*, 43(2):235–286, 2001.

[233] George V Sitnikov and Oleg I Tolstikhin. Siegert pseudostate formulation of scattering theory: two-channel case. *Physical Review A*, 67(3):032714, 2003.

[234] Valentin N Ostrovsky and Nils Elander. Scattering resonances and background associated with an asymmetric potential barrier via siegert pseudostates. *Physical Review A*, 71(5):052707, 2005.

[235] VS Jordan. Two-timing solution of mathieu equation to second order. *Quarterly of Applied Mathematics*, 31(1):147–149, 1973.

[236] Giuseppe Dattoli and Amalia Torre. Theory and applications of generalized bessel functions. Aracne Rome, 1996.

[237] Ue-Li Pen. Generating cosmological gaussian random fields. *The Astrophysical Journal Letters*, 490(2):L127, 1997.